

The Role of Chemical Activation in the Formation and Loss of Atmospheric Carbonyl Species

James Philip Andrew Lockhart

Submitted in accordance with requirements for the degree of
Doctor of Philosophy

August 2014

The University of Leeds,
School of Chemistry

The candidate confirms that the work submitted is his own. Where work which has formed part of a jointly-authored publication has been included, the contribution of this candidate to this work has been explicitly indicated overleaf. The candidate confirms that appropriate credit has been given where reference has been made to the work of others.

This copy has been supplied on the understanding that it is copyright material and that no quotation from the thesis may be published without proper acknowledgement.

The right of James Philip Andrew Lockhart to be identified as Author of this work has been asserted by him in accordance with the Copyright, Designs and Patents Act 1988.

Summary of my contributions to published work

Glowacki, D. R.; Lockhart, J.; Blitz, M. A.; Klippenstein, S. J.; Pilling, M. J.; Robertson, S. H.; Seakins, P. W., Interception of Excited Vibrational Quantum States by O₂ in Atmospheric Association Reactions. *Science* 2012, 337, 1066 – 1069.

Lockhart, J.; Blitz, M. A.; Heard, D. E.; Seakins, P. W.; Shannon, R. J., Mechanism of the Reaction of OH with Alkynes in the Presence of Oxygen. *Journal of Physical Chemistry A* 2013, 117, 5407 – 5418.

Lockhart, J.; Blitz, M. A.; Heard, D. E.; Seakins, P. W.; Shannon, R. J., Kinetic Study of the OH + Glyoxal Reaction: Experimental Evidence and Quantification of Direct OH Recycling. *Journal of Physical Chemistry A* 2013, 117, 11027 – 11037.

I carried out all the experimental work presented in these publications, and the material from these papers is presented in detail in chapters 3, 4, and 6.

Acknowledgements

I would like to thank several individuals whose support over the past four years has made it possible to complete this thesis. First and foremost I would like to thank my darling wife Sami. Her love, patience, compassion and sanity have all been tested since meeting me, but perhaps most rigorously over the course of my PhD, and yet she has withstood this trial with grace, elegance, and kindness. I can only hope that when she comes to undertake her doctoral training, I can offer the same level of support. It is to her that I dedicate this thesis, despite the fact that she will likely never read it.

My family have always been very supportive of my decision to return to University as a twenty four year old mature student, although, at the time, I don't think they could foresee that I would remain a student until the tender age of thirty two. I hope they're now proud of my first tentative step into the real world.

I owe a great thanks to both of my supervisors, Professors Paul Seakins and Dwayne Heard; I found their encouragement and passion for the subjects of reaction kinetics and atmospheric chemistry both inspiring and infectious. Paul deserves special thanks for his patience whilst reading a great many of my poorly written reports and thesis chapters over the past four years.

Dr Mark Blitz oversaw the running of the Dainton Laboratory at the University of Leeds, where all the experimental work presented in this thesis was carried out. I would not have been able to carry out any of the work presented here without his help and guidance.

Both Sami and I count ourselves very lucky for the time we have spent in Leeds, as it has provided us the opportunity to make friends with some very special people. In no particular order, Robin and Clare, Fred and Jess, Rebecca and Tim, Tom and Jo, Ros, Owen, Luke, Charlotte and Tom; I've tried to indoctrinate you all with my vinyl and, well, hopefully you enjoyed the beers even if you thought the records were lousy.

Last but by no means least, a big thank you to Elaine for the Nick Cave t-shirts!

Abstract

The Earth's atmosphere is often compared to a low temperature combustion system in which solar energy drives radical oxidation of trace gases. The OH radical is the key daytime radical oxidant and reacts rapidly with the majority of the anthropogenic and biogenic volatile organic compounds (VOCs) released to the atmosphere. Over the past two decades, field campaigns in remote regions, characterised by high concentrations of hydrocarbons, such as isoprene, but relatively low concentrations of NO_x (NO + NO₂) have highlighted significant discrepancies between measured and modelled concentrations of OH; with modelled OH concentrations underestimating the measured daytime values by up to an order of magnitude. Consequently, a number of experimental and theoretical studies have sought novel OH generating reactions that are currently not implemented into atmospheric models. One such suggestion is that under low NO_x conditions (sub 100 pptv), certain peroxy radical species, formed following the addition of O₂ to radicals produced through OH initiated VOC oxidation, might undergo unimolecular dissociation reactions that regenerate OH. In this thesis, a number of OH initiated oxidation systems have been studied which produce radical intermediates that recycle OH in the presence of O₂. These systems have been investigated experimentally by monitoring the OH directly using laser flash photolysis coupled with laser induced fluorescence (LFP – LIF). By monitoring the OH kinetics directly, it is possible to quantify the yield of OH recycled in the presence of O₂ as a function of pressure, temperature, and O₂ concentration from the ratio of rate coefficients measured in the presence and absence of O₂; this OH cycling methodology was used extensively in the work presented here.

The first experimental work presented in this thesis focused on the OH initiated oxidation of a series of alkynes (acetylene, propyne, and 2-butyne). These reactions proceed initially via OH addition across the alkyne triple bond, to generate an adduct that exists in two energetically distinct conformations. These adducts react rapidly with O₂ to generate a bicarbonyl species and recycle OH, or an organic acid and acyl radical as first generation products; with product branching ratios dictated by the stereochemistry of the adduct at the point of reaction with O₂. The nascent adduct forms following the OH + alkyne reaction with excess energy. It is widely accepted that at pressures relevant to the troposphere, any

excess energy in reaction products is dissipated through inelastic collisions prior to the onset of secondary bimolecular chemistry. However, experimental and theoretical work presented here suggests that under atmospheric conditions, a significant fraction of the total product yield associated with the OH + alkyne/O₂ systems, form before the internal quantum states of the adducts have fully relaxed. The product branching observed for the OH + alkyne/O₂ system is said to be influenced by *chemical activation*, whereby the exothermicity of an initial reaction is utilised by the products to undergo secondary reactions not accessible to the thermalised products.

Attention then turns to OH oxidation reactions that proceed via a hydrogen-atom abstraction channel. Abstraction reactions are often considered to deposit the majority of the available reaction exothermicity into the newly formed bond, particularly if the reaction involved has an early transition state. Experimental evidence presented here suggests that some atmospherically relevant carbonyl reactions, that are considered to proceed via direct hydrogen-atom abstraction, partition a significant fraction of the reaction exothermicity into the radical fragment. The OH + acetaldehyde, CH₃CHO, reaction is considered an archetypal abstraction reaction. The acetyl, CH₃CO, produced is known to react with O₂ at low pressures to generate OH, with a unity yield at zero pressure. However, the pressure dependent OH yields observed for the OH + CH₃CHO/O₂ system suggest that ~15% of the CH₃CO produced through the OH + CH₃CHO reaction dissociates promptly to CH₃ + CO. CH₃CO fragmentation requires more than 50% of the total exothermicity of the OH + CH₃CHO reaction to be channelled into the CH₃CO.

The second hydrogen-abstraction channel considered here is the OH + glyoxal, (HCO)₂, reaction that results in production of the HC(O)CO radical. HC(O)CO chemistry is governed by a competition between unimolecular dissociation, and bimolecular association with O₂. Recent calculations have suggested that the HC(O)CO + O₂ reaction proceeds directly to OH + CO + CO₂. This channel has been verified here through experiment, with OH yields associated with the OH + (HCO)₂/O₂ reaction quantified for the first time as a function of pressure (5 – 80 Torr), temperature (212 – 295 K), and O₂ concentration. The OH yields increase with O₂ concentration under all experimental conditions, as the bimolecular HC(O)CO + O₂ reaction increasingly competes with unimolecular HC(O)CO decomposition,

but converge on a limiting yield under high O₂ conditions, suggesting that a fraction of the HC(O)CO produced following the OH + (HCO)₂ reaction dissociates promptly to HCO + CO.

In the final experimental section of this thesis a laser system was developed to detect HCO via LIF. Attempts were made to monitor both prompt and growth HCO signal following the Cl + (HCO)₂ reaction, and quantify the rate of thermal HC(O)CO decomposition as a function of pressure at low temperatures (212 K). However, rapid HCO removal was observed at the low experimental temperatures required. Further experimental evidence suggested that HCO reacts rapidly with (HCO)₂ and other aldehydes at 212 K. Quantitative studies focused on the reaction of HCO with formaldehyde, HCHO, and acetaldehyde, CH₃CHO, with rate coefficients of (3.44 ± 0.15) and $(1.24 \pm 0.05) \times 10^{-11} \text{ cm}^3 \text{ molecule}^{-1} \text{ s}^{-1}$ measured, respectively.

Table of Contents

Chapter 1 Introduction	1
1.1 Basic Atmospheric Chemistry	1
1.2 HO_x Concentrations in Remote Forested Regions	4
1.3 Chemical Kinetics	10
1.4 Temperature Dependence	11
1.5 Theories of Chemical Reactions	11
1.5.1 Collision Theory	11
1.5.2 Transition State Theory (TST)	13
1.5.3 Barrierless Reactions	15
1.5.4 Pressure Dependent Reactions	16
1.5.5 Association Reactions	19
1.5.6 Development of the Lindemann Theory	20
1.5.7 Rice, Ramsperger, Kassel and Marcus (RRKM) Theory	24
1.6 Energy Grained Master Equation (EGME)	25
1.7 Chemical Activation	27
1.8 Electronic States in Atoms and Molecules	30
1.8.1 Angular momentum	31
1.8.2 Spin Angular Momentum	32
1.8.3 Total Electronic Angular Momentum and Term Symbols	33
1.8.4 Diatomic Term Symbols	34
1.9 Overview of this Thesis	35
1.10 References	37
Chapter 2 Experimental Techniques	42
2.1 Laser Flash Photolysis - Laser Induced Fluorescence (LFP-LIF)	42
2.2 The Principles of Laser Action	45
2.2.1 Absorption and Emission of Radiation	45
2.2.2 Population inversion	49
2.2.3 Optical Cavity	50
2.2.4 Excimer or Exciplex Laser (Lambda Physik, Compex or LPX 100)	51
2.2.5 Nd: YAG laser (Spectra- Physics, Quanta-Ray GCR 100-series)	54
2.2.6 Q-Switching	55
2.2.7 Dye Laser (Spectra-Physics, Quanta Ray PDL-3 and Lambda Physik, FL 2002)	57
2.3 OH Spectroscopy	60
2.4 Detection Technique – Photomultiplier Tube	60
2.5 Alternative Detection Techniques	61
2.5.1 Ultraviolet and Infrared Absorption	62
2.5.2 Mass Spectrometry	64

2.6	Alternative Kinetic Techniques	65
2.6.1	Discharge Flow	65
2.6.2	Shock Tube	67
2.6.3	Relative Rates Method	68
2.7	Details of the Apparatus and Kinetic Methods used during this Work	71
2.7.1	Reaction Cells	71
2.7.2	Gas Flows	73
2.7.3	Pressure Readings	74
2.8	Experimental Gas-Phase Kinetics	74
2.8.1	Isolation Method	74
2.8.2	Data Collection and Analysis	77
2.9	References	80

Chapter 3 Kinetic Study of the OH + Acetylene Reaction in the Presence and Absence of O₂

86

3.1	Abstract	82
3.2	Background and Previous Work	83
3.3	Experimental	87
3.4	OH + C₂H₂ Pressure Dependence in Nitrogen Bath Gas	89
3.5	Branching Ratios from Kinetic Studies in Excess O₂	92
3.6	Error in OH Yield Measurements	94
3.7	Experimental OH yields for the OH + C₂H₂/O₂ Reaction	95
3.8	Temperature Dependent OH yields for the OH + C₂H₂/O₂ Reaction	98
3.9	Theoretical Treatment of the OH + C₂H₂/O₂ Reaction	100
3.9.1	Master Equation (ME) Model	102
3.9.2	Master Equation Sensitivity Analysis	107
3.10	Biexponential OH decay Traces Kinetics of the adduct + O₂	109
3.11	Isotopic Studies on the OH + C₂H₂/O₂ System	112
3.11.1	Pressure Dependence in the OD + C ₂ H ₂ Reaction	114
3.11.2	Kinetic OD Yields	117
3.12	Conclusions	124
3.13	References	125

Chapter 4 Experimental OH Yields following OH initiated Oxidation of Higher Alkynes

129

4.1	Abstract	129
4.2	Background and Previous Work	130
4.3	Experimental	137
4.4	Kinetics of the Reactions of OH with propyne and 2-butyne	139

4.5	Product Yields for the OH initiated oxidation of Propyne and 2-Butyne _____	142
4.6	Kinetics of the Alkyne-OH Adduct + O ₂ Reaction _____	149
4.7	Conclusions _____	154
4.8	References _____	156
Chapter 5 Products of the OH + Acetaldehyde Reaction _____		159
5.1	Abstract _____	159
5.2	Background and Previous Work _____	160
5.3	Experimental _____	165
5.4	OH + CH ₃ CHO Temperature Dependence in Nitrogen Bath Gas _____	167
5.5	OH Yields from kinetic Analysis of the OH + CH ₃ CHO Reaction with and without Excess O ₂ 169	
5.6	Photoionisation Mass Spectrometry (PIMS) Measurements _____	178
5.7	Discussion _____	Error! Bookmark not defined.
5.8	References _____	187
Chapter 6 Kinetic Study of the OH + Glyoxal Reaction _____		190
6.1	Abstract _____	190
6.2	Background and Previous work _____	191
6.3	Experimental _____	194
6.4	OH + (HCO) ₂ Temperature Dependence in Nitrogen Bath Gas _____	197
6.5	Generation of OH from the HC(O)CO + O ₂ Reaction _____	199
6.6	Experimental OH Yields for the OH + (HCO) ₂ /O ₂ Reaction _____	202
6.7	Ambient OH yields _____	211
6.8	Evidence for Nonthermal Rate Behaviour _____	Error! Bookmark not defined.
6.9	Linear Dependence of [CO]/[CO ₂] Products as a Function of 1/[O ₂] _____	216
6.10	Comparison of the OH/Glyoxal/O ₂ and OH/Methyl-glyoxal/O ₂ Systems _____	219
6.11	Atmospheric Implications _____	220
6.12	References _____	222
Chapter 7 Some Known and Novel HCO Chemistry _____		226
7.1	Abstract _____	226
7.2	Background _____	227
7.3	Experimental _____	229
7.4	Room temperature kinetics of the Reactions of HCO with O ₂ , NO and NO ₂ _____	230

7.4.1	Kinetics of the Reactions of HCO with O ₂ and NO	232
7.4.2	Kinetic Study of the HCO + NO ₂ Reaction	235
7.5	HC(O)CO Decomposition Kinetics	238
7.6	Kinetics of the HCO + HCHO Reaction	244
7.7	Kinetics of the HCO + CH₃CHO Reaction	246
7.8	Discussion	248
7.9	References	250
Chapter 8 Summary and Future Work		253
8.1	Synopsis	253
8.2	Implications	256
8.2.1	Combustion Chemistry	256
8.2.2	Atmospheric Chemistry	258
8.3	Future Work	259
8.4	References	261
Appendix A: Published Papers		263

Table of Figures

Chapter 1

Figure 1: Schematic of the atmospheric oxidation steps for a general saturated hydrocarbon RH in the presence of NO_x. _____ 3

Figure 2: Comparison of measured OH concentrations over Borneo measured during the OP3 campaign in 2008 (black line) with values calculated using the photostationary steady state approximation constrained to the measured total OH reactivity, k'_{total} , for the loss term and with various OH source terms included. The grey shading represents the 1 σ standard deviation of the averaged OH profile. _____ 8

Figure 3: Potential energy surface for a decomposition reaction at total energy E. Reaction requires a minimum amount of energy, E_0 , to be partitioned within the reactive mode, the remainder, E' , is distributed throughout the activated complex. _____ 25

Figure 4: Representation of the energy grained master equation model for an association reaction between reactants A and B, with two wells and an irreversible product channel. _____ 26

Figure 5: Chemical activation by an exothermic (a) and endothermic (b) reaction; X^\ddagger represents the activated complex for the activating reaction, and Y^\ddagger represents the activated complex for subsequent reaction of the chemically activated species (Redrawn from Robinson and Holbrook). 28

Chapter 2

Figure 1: Schematic diagram of laser flash photolysis, laser induced fluorescence (LFP-LIF) apparatus for the study of OH radicals with acetylene, C₂H₂. _____ 44

Figure 2: Typical OH decay trace measured in the presence of 2.12×10^{16} molecules cm⁻³ of C₂H₂ at 295 K under 25 Torr of N₂ using the LFP-LIF technique. _____ 44

Figure 3: Schematic diagram of the radiative transitions associated with stimulated absorption (a), stimulated emission (b) and spontaneous emission (c). _____ 47

Figure 4: Schematic diagram of the energy levels and transitions involved in a three and four level laser system. _____ 50

Figure 5: Schematic diagram of an optically pumped laser cavity. _____	51
Figure 6: Schematic energy level diagram for the KrF laser. _____	52
Figure 7: Schematic energy level diagram for a Nd: YAG laser. _____	54
Figure 8: Schematic of the Q-switch used in the Nd: YAG cavity to enable short high power laser pulses; denoting horizontal (H), circular (C) and vertically (V) polarized light. _____	58
Figure 9: Jablonski diagram for a laser dye. The solid vertical arrows show the transitions involved in laser action, and the dashed arrows illustrate some of the competing transitions. _____	58
Figure 10: Set up of the Quanta Ray PDL-3 dye laser _____	59
Figure 11: Schematic energy level diagram showing the transitions relevant to off- (A) and on-resonant (B) fluorescence of the OH radical following the A – X electronic transition. Collisional energy transfer processes are presented in blue. _____	60
Figure 12: Schematic diagram of a photomultiplier tube (PMT). _____	61
Figure 13: Schematic diagram of laser flash photolysis, absorption spectroscopy apparatus required for the study of CH ₃ radical recombination kinetics. _____	63
Figure 14: Schematic diagram of the flash photolysis, photoionisation mass spectrometry (PIMS) apparatus. _____	65
Figure 15: Schematic diagram of a discharge flow apparatus for the study of OH reactions with laser induced fluorescence (LIF) detection. _____	66
Figure 16: Plot of the competitive loss C ₂ H ₂ and CH ₃ OCH ₃ following exposure to OH radicals at 296 K in 750 Torr of O ₂ (◇), 400 Torr of air (△), 200 Torr of air (▲), and 25 Torr of O ₂ (●) using equation E17. ²² _____	70
Figure 17: Schematic of the high temperature (295 – 498 K) reactor used in this thesis. _____	72
Figure 18: Schematic of the low temperature (195 – 295 K) cell used in this thesis _____	73
Figure 19: Typical raw experimental signal of both OH fluorescence and laser power (a); pseudo-first-order OH decay measured in the presence of excess (HCO) ₂ (6.66×10^{14} molecule cm ⁻³) at 295 K under 40 Torr of nitrogen, normalised for laser power, the fit using equation E19 corresponds to a	

pseudo-first-order decay coefficient of $(7000 \pm 75) \text{ s}^{-1}$ (b); the corresponding residuals to the exponential fit (c). _____ 78

Figure 20: Bimolecular plot for the $\text{OH} + (\text{HCO})_2 \rightarrow \text{HC(O)CO} + \text{H}_2\text{O}$ reaction at room temperature in 40 Torr of nitrogen, for which a bimolecular rate coefficient of $(9.95 \pm 0.10) \times 10^{-12} \text{ cm}^3 \text{ molecule}^{-1} \text{ s}^{-1}$ was observed (where the error bar is purely statistical at the 2σ level). _____ 79

Chapter 3

Figure 1: Main stationary points on the potential energy surface for the $\text{HO-C}_2\text{H}_2 + \text{O}_2$ reaction. ___ 86

Figure 2: Typical bimolecular plot for the $\text{OH} + \text{C}_2\text{H}_2 \rightarrow \text{HO-C}_2\text{H}_2$ reaction at 295 K and 10 Torr total pressure in pure nitrogen; corresponding to an experimental k_1 value of $(3.79 \pm 0.03) \times 10^{-13} \text{ cm}^3 \text{ molecule}^{-1} \text{ s}^{-1}$. The inset shows a typical experimental OH decay trace measured in the presence of C_2H_2 ($1.11 \times 10^{16} \text{ molecule cm}^{-3}$) using pure N_2 bath gas; the fit to equation E1 corresponds to a pseudo-first-order decay coefficient of $(4610 \pm 30) \text{ s}^{-1}$. _____ 89

Figure 3: Pressure dependence of the bimolecular rate coefficient, k_1 , for the $\text{OH} + \text{C}_2\text{H}_2$ reaction measured during this work in pure N_2 (■), by Sorensen et al. in air (●); Wahner and Zetzsch in N_2 (▲) McKee et al. in N_2 (◆); and Bohn et al. in N_2 (◀). The solid line shows the best fit though the data points collected during this work using MESMER at 295 K using N_2 bath gas. _____ 90

Figure 4: Bimolecular Plots for the $\text{OH} + \text{C}_2\text{H}_2 \rightarrow \text{Products}$ reaction at 10 Torr total pressure and 295 K: in pure N_2 bath gas (■), 2% O_2 and 98% N_2 (●), and in 94% O_2 and 6% N_2 (▲). Error bars are purely statistical at the 1σ level. _____ 94

Figure 5: Dependence of the OH Yield, Φ_{OH} , for the $\text{OH} + \text{C}_2\text{H}_2/\text{O}_2$ reaction at 295 K as a function of oxygen fraction, $f\text{-O}_2$, at total pressures of 10 (■), 25 (●), and 75 Torr (▲). The error bars are purely statistical at the 1σ level. The line shows the fit obtained from the ME/VRC-TST calculations (details are included in the text). _____ 95

Figure 6: Acetylene atmospheric oxidation mechanism, including a schematic of the potential energy surface for the $\text{OH} + \text{C}_2\text{H}_2$ addition step, and an illustration of the vibrationally quantum state distribution (denoted by *) in the nascent cis- and trans-adduct isomers as they relax to thermal equilibrium. All energy units are in kJ mol^{-1} . _____ 98

Figure 7: Variation of the OH Yield, Φ_{OH} , for the OH + C₂H₂/O₂ reaction with temperature at oxygen fractions, f-O₂, of 0.01 (■), 0.20 (●), and 0.90 (▲). The error bars are purely statistical at the 1 σ level. The lines show the results obtained from the corresponding ME/VRC-TST calculations. _____ 99

Figure 8: VRC-TST thermal rate coefficients for the O₂ association reaction with cis- (■) and trans-adduct conformers (●) based on CASPT2(7,5)/aug-cc-pVDZ orientation samplings coupled with one-dimensional corrections along the MEP based on CI+QC(9,7)CBS estimates which include geometry relaxation effects. _____ 102

Figure 9: Results from ME-VRC/TST calculations at 298 K and 760 Torr showing evolution of the vibrational state distributions in cis- and trans-adduct isomers, as a function of both energy and time. (A and B) show results with f-O₂ = 0.01 for cis- and trans-adduct, respectively, (C and D) show results with f-O₂ = 0.90 for cis- and trans-adduct, respectively. _____ 105

Figure 10: Schematic of the ME/VRC-TST results used to determine the fraction of each adduct conformer intercepted by O₂ before complete of vibrational deactivation at 298 K and 760 Torr. The top panel shows the average adduct energy as a function of time with the irreversible bimolecular loss channels turned off. As indicated, the system reaches thermal equilibrium at ~17 ns. The bottom panel shows the species profiles obtained from a separate simulation with the loss channels turned on at 298 K and 760 Torr using f-O₂ of 0.21. The profiles shows that upon completion of vibrational deactivation ~25% of the total cis- and trans-adduct population has gone to O₂ addition products. _____ 107

Figure 11: χ^2 surface showing the fitting produced by the ME model to the experimental data points (shown in Figures 5 and 7) as both ΔE_{down} and the $E_{trans} - E_{cis}$ adduct energy difference are varied. 108

Figure 12: Experimental OH decays in the presence of acetylene with and without trace amounts of O₂ at 295 K and 10 Torr total pressure: oxygen free conditions (■), 2.30×10^{14} molecule cm⁻³ (▲), 5.1×10^{14} molecule cm⁻³ (■), and 1.02×10^{15} molecule cm⁻³ of O₂ (◆); each fit using equation E15. ___ 109

Figure 13: Temperature dependence of the bimolecular rate coefficient, k_2 , for the HO-C₂H₂ + O₂ → products reaction, measured at 10 Torr total pressure and 295 (■) and 212 K (●), corresponding to k_2 values (6.15 ± 0.27) and $(19.29 \pm 0.12) \times 10^{-12}$ cm³ molecule⁻¹ s⁻¹, respectively. The error bars are purely statistical at the 2 σ level. _____ 112

Figure 14: Theoretical pathways leading to glyoxal and formic acid production through the OH initiated oxidation of acetylene. _____ 113

Figure 15: Typical bimolecular plot for the $\text{OD} + \text{C}_2\text{H}_2 \rightarrow \text{DO-C}_2\text{H}_2$ reaction at 295 K and 10 Torr total pressure in pure nitrogen; corresponding to an experimental k_6 value of $(5.39 \pm 0.08) \times 10^{-13} \text{ cm}^3 \text{ molecule}^{-1} \text{ s}^{-1}$. A typical experimental OD decay trace and fit to equation E1 and corresponding to a pseudo-first-order decay coefficient of $(1239 \pm 285) \text{ s}^{-1}$ is included in the insert. _____ 114

Figure 16: Pressure dependence of the bimolecular rate coefficients k_1 (■) and k_6 (●) for the respective addition of OH and OD radicals to acetylene in pure N_2 bath gas at 295 K, measured during this work; included are the pressure dependent bimolecular rate coefficients, k_1 , for the OH + C_2H_2 reaction measured by Sorensen et al. in air (●); Wahner and Zetzsch in N_2 (▲), McKee et al. in N_2 (◆), and Bohn et al. in N_2 (▲). The solid lines show the best fit though the experimental k_1 (black) and k_6 (red) values measured here using MESMER at 295 K using N_2 bath gas. _____ 115

Figure 17: Bimolecular Plots for the $\text{OD} + \text{C}_2\text{H}_2 \rightarrow \text{Products}$ reaction at 10 Torr total pressure and 295 K: in pure N_2 bath gas (■), 1% O_2 and 99% N_2 (●), and in 90% O_2 and 10% N_2 (▲). Error bars are purely statistical at the 1σ level. _____ 118

Figure 18: Room temperature Φ_{OH} for the $\text{OH} + \text{C}_2\text{H}_2/\text{O}_2$ reaction (■) and Φ_{OD} for the $\text{OD} + \text{C}_2\text{H}_2/\text{O}_2$ reaction (●) at 10 Torr total pressure as a function of $f\text{-O}_2$. _____ 119

Figure 19: Experimental radical profiles during the $\text{OD} + \text{C}_2\text{H}_2/\text{O}_2$ reaction showing OD decay (■) and OH growth (▲) occurring on the same timescale at 10 Torr and 295 K; included is the OH profile in the absence of O_2 (◆). _____ 121

Figure 20: Radical profiles of OD (■) and OH (▲) observed during the $\text{OD} + \text{C}_2\text{H}_2/\text{O}_2$ reaction using acetone-d6 as OD precursor at 295 K and 10 Torr total pressure, using an $f\text{-O}_2$ of 0.07, with the excimer laser operating at a pulse repetition rate of 1Hz. Included is the OH profile observed in the absence of acetylene (▼). _____ 123

Chapter 4

Figure 1: Schematic mechanism for the OH-initiated oxidation of 2-butyne. _____ 135

Figure 2: Diagram of the relative energies of the reactants, intermediates and products associated with the OH initiated oxidation of alkynes (redrawn from Yeung et al.) _____ 136

Figure 3: Typical bimolecular plot for the OH + C₃H₄ reaction at 295 K under 10 Torr of nitrogen; corresponding to a k_1 value of $(3.88 \pm 0.03) \times 10^{-12} \text{ cm}^3 \text{ molecule}^{-1} \text{ s}^{-1}$ (where the error is purely statistical at the 2σ level). The inset shows a typical experimental OH decay trace in the presence of propyne ($1.27 \times 10^{15} \text{ molecule cm}^{-3}$) using pure N₂ bath gas that corresponds to a pseudo-first-order decay constant of $(5140 \pm 50) \text{ s}^{-1}$. _____ 138

Figure 4: Pressure dependence of the bimolecular rate coefficients, k_1 , for the OH + C₃H₄ reaction using pure nitrogen bath gas at 295 K. The error bars include both the statistical (2σ) and estimated systematic errors (10%). _____ 139

Figure 5: Temperature dependence of the bimolecular rate coefficients, k_4 , measured during this work for the OH + C₄H₆ reaction using pure nitrogen bath gas over a range of temperatures from 212 to 498 K (■). Included for comparison are the direct measurements of k_4 by Boodaghians et al. (●) at temperatures ranging between 253 and 343 K using helium bath gas, and the room temperature measurement by Hatakeyama et al (▲) using synthetic air bath gas. _____ 142

Figure 6: Bimolecular plots for the OH + C₃H₄ → Products reaction at 295 K and 10 Torr total pressure: using pure nitrogen bath gas (■), 48% nitrogen and 52% oxygen (●), and 2% oxygen and 98% nitrogen (▲). Error bars are purely statistical at the 2σ level. _____ 143

Figure 7: (a) Dependence of the OH yield for the OH + C₃H₄/O₂ reaction as a function of oxygen fraction, $f\text{-O}_2$, and total pressure at 295 K and 5 (■), 10 (●), 25 (▲) and 75 Torr (▼). (b) Dependence of the OH yield for the OH + C₄H₆/O₂ reaction as a function of oxygen fraction, $f\text{-O}_2$, and total pressure at 295 K at 5 (■), 10 (●) and 25 Torr (▲). _____ 144

Figure 8: (a) Temperature dependence of the OH yield for the OH + C₃H₄/O₂ reaction measured at 10 Torr total pressure using 0.04 (■), 0.20 (●), and 0.80 oxygen fractions, $f\text{-O}_2$ (▲). (b) Temperature dependence of the OH yield for the OH + C₄H₆/O₂ reaction measured at 10 Torr total pressure using 0.04 (■), 0.20 (●) and 0.80 oxygen fractions, $f\text{-O}_2$ (▲). _____ 148

Figure 9: Bimolecular plot for the HO-C₄H₆ + O₂ → Products reaction at 10 Torr pressure and 295 K, corresponding to a k_5 value of $(6.45 \pm 0.22) \times 10^{-12} \text{ cm}^3 \text{ molecule}^{-1} \text{ s}^{-1}$. A typical biexponential OH decay trace is included in the inset, with OH monitored in the presence of $\sim 1.41 \times 10^{15} \text{ molecule cm}^{-3}$ of 2-butyne and $\sim 8.3 \times 10^{14} \text{ molecule cm}^{-3}$ of oxygen; under these conditions a pseudo-first-order rate coefficient of $(8940 \pm 540) \text{ s}^{-1}$ was observed. _____ 151

Figure 10: Experimental OH decay profile associated with the reaction of OH with 2-butyne (1.41×10^{15} molecule cm^{-3}) in the presence of trace oxygen (8.3×10^{14} molecule cm^{-3}). Simulated OH decay profiles under identical conditions are included using a k_5 rate coefficient value of either 7.03×10^{-13} cm^3 molecule $^{-1}$ s $^{-1}$ (blue line), determined by Yeung et al., or 6.45×10^{-12} cm^3 molecule $^{-1}$ s $^{-1}$ (red line), measured here. _____ 153

Chapter 5

Figure 1: Bimolecular plot for the OH + CH₃CHO reaction at 212 K at pressures ranging from between 1 and 10 Torr; least squares linear analysis through all data points yields a bimolecular rate coefficient of $(2.07 \pm 0.02) \times 10^{-11}$ cm^3 molecule $^{-1}$ s $^{-1}$; a typical experimental OH decay trace at 212 K fit using equation E1 is included in the inset. _____ 167

Figure 2: Arrhenius plot of the experimental rate coefficients, $k_1(T)$, for the OH + CH₃CHO → Products reaction, measured during this work. $k_1(T)$ measurements reported by other studies are included for comparison. The data of Taylor et al. 1996 were not tabulated in their publication and were therefore taken from their Arrhenius plot. The error bars quoted by Sivakumaran and Crowley, Zhu et al., and Taylor et al., 2006 are purely statistical (2σ). The error bars quoted by Atkinson and Pitts, and Semmes et al. combine both the statistical (2σ) and estimated systematic errors. ____ 168

Figure 3: Bimolecular plots for the OH + CH₃CHO → Products reaction at 295 K using both pure nitrogen bath gas (■), and in the presence of excess O₂ at total pressures of 10 (◆), 5 (▼), 2 (▲) and 1 Torr (●). A typical OH decay trace at this temperature is included in the inset. _____ 171

Figure 4: Stern-Volmer Plots of reciprocal OH yield against total pressure for the OH + CH₃CHO → Products reaction at 212 (▲), 295 (■) and 385 K (●); error bars a purely statistical (2σ). Weighted least squares linear regression fits through the data with 1σ confidence intervals are included. The magnified intercept is included in the inset. _____ 173

Figure 5: Overlaid plots of acetyl (-■-) and methyl radical (-●-) signals from the same experiments demonstrating they are produced on identical timescales. _____ 179

Figure 6: Methyl-to-acetyl signal ratios observed following reaction of OH (■) and Cl-atoms (●) with acetaldehyde at 295 K. _____ 180

Figure 7: Behaviour of acetyl, methyl and lactone signals in an OH/CH₃CHO/O₂ system. The solid points are the experimental data and the lines are a numerical simulation using Kintecus. _____ 181

Chapter 6

Figure 1: Schematic of the potential energy surface showing the initial addition of O₂ followed by an internal H transfer and then elimination of CO. The COOH rapidly dissociates to OH and CO₂. Adapted with permission from da Silva. _____ 193

Figure 2: Typical UV-vis absorption spectra for an (HCO)₂ sample (a) and corresponding glyoxal fraction, f-(HCO)₂, as a function of wavelength (b); analysis of this spectra results in an f-(HCO)₂ of 0.033 ± 0.005, the error is statistical at the 1σ level. _____ 195

Figure 3: Typical bimolecular plot for the OH + (HCO)₂ → HC(O)CO + H₂O reaction measured at 295 K under 20 Torr total pressure of pure N₂; corresponding to an experimental k₁ value of (9.37 ± 0.08) × 10⁻¹² molecule cm⁻³ s⁻¹. The outer lines show the confidence intervals at the 2σ level. A typical experimental OH decay trace measured in the presence of 1.67 × 10¹⁴ molecule cm⁻³ of glyoxal is included in the inset, the fit to equation E1 corresponds to a pseudo-first-order rate coefficient of (2030 ± 20) s⁻¹. _____ 197

Figure 4: Temperature dependence of the OH + (HCO)₂ rate coefficient, k₁(T), measured between 5 and 80 Torr total pressure using N₂ bath gas (■); the error bars include both statistical (2σ level) and estimated systematic error. The k₁(T) values measured by Feierabend et al. (●) and the room temperature k₁(296 K) relative rate value reported by Plum et al. (▲) are included for comparison. _____ 198

Figure 5: Experimental OH profile (open circles) following the Cl + (HCO)₂ reaction in the presence of 1.04 × 10¹⁷ molecules cm⁻³ O₂ at 295 K and 10 Torr total pressure, using initial Cl-atom and (HCO)₂ concentrations of 0.1 and 2.7 × 10¹⁴ molecules cm⁻³, respectively. Two model simulations are included. The red solid line using the OH pathways proposed by da Silva²¹ and the Cl + (HCO)₂ rate coefficient reported by Niki et al., the blue dashed-dot line shows a simulation based on the Niki et al. mechanism for OH formation. _____ 200

Figure 6: Bimolecular plots for the $\text{OH} + (\text{HCO})_2 \rightarrow \text{products}$ reaction at 212 K and 40 Torr; in pure N_2 (■) and in the presence of 869 mTorr of O_2 (●), corresponding to rate coefficients (16.68 ± 0.07) and $(11.45 \pm 0.12) \times 10^{-12} \text{ molecule cm}^{-3} \text{ s}^{-1}$; giving an experimental Φ_{OH} of 0.31. The outer lines show the confidence intervals at the 2σ level. _____ 204

Figure 7: Experimental OH yields, Φ_{OH} , for the $\text{OH} + (\text{HCO})_2/\text{O}_2$ reaction at 295 K as a function of oxygen fraction, $f\text{-O}_2$, at total pressures of 5 (■), 10 (●), 20 (▲), 40 (◄) and 80 Torr (▼) total pressure. The dashed line shows the predicted Φ_{OH} dependence on $f\text{-O}_2$ at 760 Torr. The error bars include both the statistical (2σ level) and estimated systematic errors. Included are fits through each total pressure data set using the extended Lindemann-Hinshelwood model (See text for details). 205

Figure 8: Experimental OH yields, Φ_{OH} , for the $\text{OH} + (\text{HCO})_2/\text{O}_2$ reaction at 250 K as a function of oxygen concentration at total pressures of 5 (■), 10 (●), 20 (▲), 40 (◄) and 80 Torr (▼). The errors include both the statistical (2σ) and estimated systematic errors. _____ 210

Figure 9: Experimental OH yields, Φ_{OH} , for the $\text{OH} + (\text{HCO})_2/\text{O}_2$ reaction at 212 K as a function of oxygen concentration at total pressures of 5 (■), 10 (●), 20 (▲), 40 (◄) and 80 Torr (▼). The error bars include both the statistical (2σ level) and estimated systematic errors. _____ 210

Figure 10: OH yields, Φ_{OH} , as a function of total pressure at 295 (black line), 250 (red line), and 212 K (blue line) and atmospheric oxygen fractions ($f\text{-O}_2 = 0.21$); included are Φ_{OH} predicted at 295 K in pure O_2 (dashed line). _____ 212

Figure 11: Ratios of the observed $\text{OH}_{\text{limit}}/\Phi_{\text{OH}}$ ratio following glyoxal oxidation as a function of the inverse O_2 concentration at total pressures of 5 (■), 40 (◄) and 80 Torr (▼) and 295 K; the small error bars are purely statistical (2σ level); the larger error bars include the estimated systematic error. _____ 213

Figure 12: The observed k_2/k_5 pressure dependence on total pressure (5 – 80 Torr) at 295 K. The solid line is the k_2/k_5 calculated using MESMER based on thermal rate coefficients for k_2 and k_5 suggesting a linear dependence to pressures of ~ 1 Torr. _____ 214

Figure 13: The observed k_2/k_5 pressure dependence on total pressure (5 – 80 Torr) at 250 K. The solid line is the k_2/k_5 calculated using MESMER based on thermal rate coefficients for k_2 and k_5 . 215

Figure 14: The observed k_2/k_5 pressure dependence on total pressure (5 – 80 Torr) at 212 K. The solid line is the k_2/k_5 calculated using MESMER based on thermal rate coefficients for k_2 and k_5 . 216

Figure 15: Observed $[\text{CO}]/[\text{CO}_2]$ ratios from glyoxal oxidation as a function of inverse O_2 partial pressure and temperature at 700 Torr total pressure; with data obtained from the photolysis of $\text{Cl}_2/\text{glyoxal}/\text{O}_2/\text{N}_2$ mixtures (squares), from the photolysis of $\text{Cl}_2/\text{glyoxal}/\text{NO}/\text{O}_2/\text{N}_2$ mixtures (circles), from the photolysis of $\text{C}_2\text{H}_5\text{ONO}/\text{glyoxal}/\text{NO}/\text{O}_2/\text{N}_2$ mixtures (triangles), from the photolysis of $\text{Cl}_2/\text{glyoxal}/\text{NO}_2/\text{O}_2/\text{N}_2$ mixtures. (Redrawn from Orlando and Tyndall). _____ 217

Chapter 7

Figure 1: Bimolecular plot for the $\text{HCO} + \text{O}_2$ reaction at 295 K and 10 (■) and 30 Torr (●) total pressure using N_2 bath gas corresponding to a k_1 value of $(5.27 \pm 0.01) \times 10^{-12} \text{ cm}^3 \text{ molecule}^{-1} \text{ s}^{-1}$. A typical experimental HCO decay trace is included in the inset, measured in the presence of $6.95 \times 10^{14} \text{ molecule cm}^{-3}$ of O_2 and corresponding to a pseudo-first-order decay constant of $(3550 \pm 50) \text{ s}^{-1}$. _____ 233

Figure 2: Bimolecular plot for the $\text{HCO} + \text{NO}$ reaction at 295 K and 10 (■) and 30 Torr (●) total pressure using N_2 bath gas corresponding to a k_9 value of $(12.96 \pm 0.29) \times 10^{-12} \text{ cm}^3 \text{ molecule}^{-1} \text{ s}^{-1}$. A typical experimental HCO decay trace is included in the inset, measured in the presence of $1.24 \times 10^{15} \text{ molecule cm}^{-3}$ of NO and corresponding to a pseudo-first-order decay constant of $(17655 \pm 300) \text{ s}^{-1}$. _____ 234

Figure 3: Bimolecular plot for the $\text{HCO} + \text{NO}_2 \rightarrow \text{Products}$ reaction at 295 K under 10 Torr of N_2 , corresponding to a k_{10} value of $(6.99 \pm 0.16) \times 10^{-11} \text{ cm}^3 \text{ molecule}^{-1} \text{ s}^{-1}$, where the error is purely statistical at the 2σ level. Included is a typical biexponential HCO decay trace measured in the presence of $4.48 \times 10^{13} \text{ molecule cm}^{-3}$ of NO_2 , corresponding to a pseudo-first-order HCO decay coefficient of $(3865 \pm 340) \text{ s}^{-1}$. _____ 236

Figure 4: Simulated HCO profiles following the $\text{Cl} + (\text{HCO})_2$ reaction at 295 (black), 250 (red), and 212 K (blue) under 5 Torr of nitrogen. The green line shows the model HCO profile at 212 K under 10 Torr total pressure. These model profiles are all based on initial $(\text{HCO})_2$ and Cl-atom concentrations of $3 \times 10^{14} \text{ molecule cm}^{-3}$ and $1 \times 10^{13} \text{ molecule cm}^{-3}$, respectively. _____ 239

Figure 5: Bimolecular plot for the $\text{Cl} + (\text{HCO})_2 \rightarrow \text{HCO} + \text{CO}$ reaction at 295 K under 5 Torr of nitrogen, corresponding to a k_{15} value of $(3.88 \pm 0.12) \times 10^{-11} \text{ cm}^3 \text{ molecule}^{-1} \text{ s}^{-1}$; the quoted error is purely statistical at the 2σ level. Included in the inset is a typical experimental HCO growth profile

measured in the presence of 3.83×10^{14} molecule cm^{-3} of $(\text{HCO})_2$ corresponding to a pseudo-first-order growth constant of $(17500 \pm 800) \text{ s}^{-1}$. _____ 242

Figure 6: Experimental HCO decay profile observed in the in the presence of $\sim 3 \times 10^{14}$ molecule cm^{-3} of $(\text{HCO})_2$ at 212 K under 10 Torr of N_2 . Included is an exponential decay fit through these data using equation E1, corresponding to a pseudo-first-order decay coefficient of $(10300 \pm 265) \text{ s}^{-1}$. _____ 244

Figure 7: Bimolecular plot for the $\text{Cl} + \text{HCHO}$ reaction at 295 K and 10 Torr total pressure used to characterize the experimental HCHO bulb concentration. A typical experimental HCO growth profile is included in the inset, measured in the presence of 8.72×10^{13} molecule cm^{-3} of HCHO corresponding to a pseudo-first-order growth constant of $(7340 \pm 350) \text{ s}^{-1}$. _____ 245

Figure 8: Bimolecular plot for the $\text{HCO} + \text{HCHO} \rightarrow \text{Products}$ reaction at 212 K under 10 (■) and 30 Torr (●) of nitrogen; corresponding to a k_{17} value of $(3.44 \pm 0.15) \times 10^{-11} \text{ cm}^3 \text{ molecule}^{-1} \text{ s}^{-1}$. Included in the inset is a typical HCO decay profile measured at 10 Torr total pressure in the presence of 2.14×10^{14} molecule cm^{-3} of HCHO corresponding to a pseudo-first-order decay constant of $(7435 \pm 180) \text{ s}^{-1}$. _____ 246

Figure 9: Bimolecular plot for the $\text{HCO} + \text{CH}_3\text{CHO} \rightarrow \text{Products}$ reaction at 212 K under 10 Torr of nitrogen, corresponding to k_{18} value of $(1.24 \pm 0.05) \times 10^{-11} \text{ cm}^3 \text{ molecule}^{-1} \text{ s}^{-1}$. A typical experimental HCO decay trace measured in the presence of 3.87×10^{14} molecule cm^{-3} is included in the inset. The experimental HCHO concentration used to generate HCO was $(1.6 \pm 0.1) \times 10^{14}$ molecule cm^{-3} and consistent with the intercept observed. _____ 247

Chapter 8

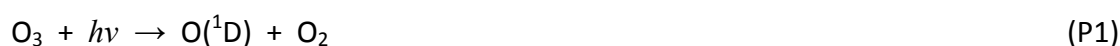
Figure 1: Room temperature bimolecular plots measured for the $\text{OH} + \text{C}_2\text{H}_4 \rightarrow \text{Products}$ reaction carried out under 10 Torr of pure N_2 bath gas (■), and in the presence of $\sim 1.35 \times 10^{17}$ molecule cm^{-3} of O_2 (●), and correspond to bimolecular rate coefficients of (4.48 ± 0.04) and $(3.64 \pm 0.05) \times 10^{-12} \text{ cm}^3 \text{ molecule}^{-1} \text{ s}^{-1}$, respectively; (where the errors are purely statistical at the 2σ level). A typical OH decay trace measured in the presence of $\sim 7.29 \times 10^{14}$ molecule cm^{-3} of C_2H_4 in pure N_2 bath gas, corresponding to a pseudo-first-order decay coefficient of $(3925 \pm 30) \text{ s}^{-1}$ is included in the inset. 260

Chapter 1 Introduction

The opening chapter of this thesis provides a brief introduction to atmospheric chemistry, and the importance of the hydroxyl radical, OH, in removing atmospheric trace gas species. Attention then turns to recent OH field measurements which may suggest significant misunderstanding with regard to volatile organic compound (VOC) oxidation in remote atmospheric regions. The second half of this chapter highlights the importance of kinetic studies to atmospheric science and provides a concise introduction to gas-phase kinetics and the development of theoretical methods used to describe these reaction systems. This chapter concludes with an overview of the subsequent chapters presented in this thesis.

1.1 Basic Atmospheric Chemistry

A number of significant environmental concerns, such as photochemical smog, global climate change, and stratospheric ozone depletion, relate directly to perturbations in the chemical composition of the atmosphere. Resolving these issues requires a detailed understanding of the ways in which chemical emissions are processed in the atmosphere. Trace gases of both anthropogenic and biogenic origin, are for the most part removed from the Earth's troposphere via radical-chain oxidation.¹ The initial step in these radical-mediated pathways is predominantly through reaction with the hydroxyl radical, OH. The primary source of tropospheric OH is through photolysis of ozone in the presence of water vapour:

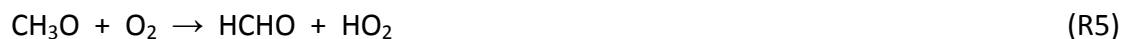


The OH radical is the dominant day-time tropospheric oxidant and reacts rapidly with the majority of volatile organic compounds (VOCs) emitted to the atmosphere. Saturated hydrocarbons (such as methane, CH₄) react with OH to generate alkyl radicals and

water vapour, subsequent pressure-dependent addition of molecular oxygen, O₂, produces the respective alkyl peroxy radical. The initial steps in the atmospheric oxidation of CH₄ are given below, where M represents an atmospheric third body, typically a nitrogen or oxygen molecule, which removes excess energy from the nascent peroxy radical through collisional deactivation:



The chemistry which follows peroxy radical formation is largely dictated by the concentration of various oxides of nitrogen that are present. Consequently the chemistry associated with polluted industrial regions, where NO and NO₂ (collectively termed NO_x) are relatively abundant, differs markedly from remote, clean regions where NO_x concentrations are relatively low. Alkyl radicals react rapidly with NO to produce alkoxy radicals and NO₂. The alkoxy radical can then react with O₂ to form a carbonyl species and an HO₂ radical. Continuing with the simple methane oxidation example, equations describing the reaction of the methylperoxy with NO (R4), and subsequent reaction of the methoxy radical with O₂ (R5) are given below:



The HO₂ radical produced during methane oxidation (R5) can then react with NO to complete the oxidative chain process and regenerate OH (R6):



The OH and HO₂ radicals are often collectively termed HO_x. The NO₂ produced during these atmospheric degradation cycles is the only recognised means of generating ground-level ozone, a significant pollutant:



The cyclic radical reactions and first generation products associated with the atmospheric oxidation of a generic unsaturated hydrocarbon, RH, are highlighted in Figure 1.

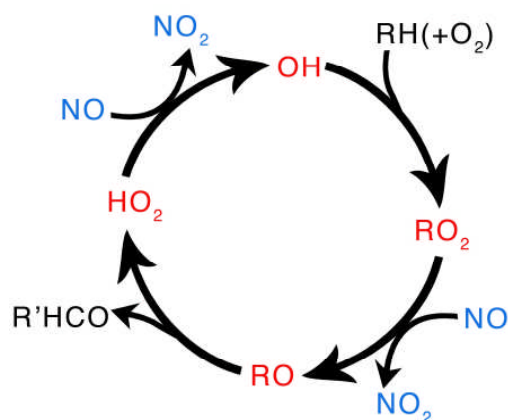


Figure 1: Schematic of the atmospheric oxidation steps for a general saturated hydrocarbon RH in the presence of NOx.

In the absence of NO, peroxy radicals can undergo self- and cross-peroxy radical reactions, forming organic peroxides and acids; the major atmospheric sinks of methylperoxy and HO₂ radicals are given below:



In remote regions these radical termination channels are important radical loss processes; although recent experimental and theoretical studies have shown cross reactions of carbonyl containing RO₂ species with HO₂ also generates OH.^{2,3}

Alkenes and alkynes also react rapidly with OH, but via addition across the unsaturated bond, which generates hydroxyl substituted radicals. Subsequent reaction of alkene derived HO-adducts with molecular oxygen yields peroxy radicals, with subsequent chemistry analogous with that of the peroxy radicals derived from alkanes. Unlike other RO₂ species, the peroxy radicals formed following reaction of the alkyne derived HO-adduct

radicals with molecular oxygen are unstable with respect to two product forming channels, leading to dicarbonyl + OH or organic acid + acyl radical.⁴⁻⁶

Acetylene is the most abundant alkyne in the troposphere, and has been detected in both urban and remote regions, and at high altitudes.⁷⁻⁹ It is released primarily through biomass burning and automobile exhaust,¹⁰⁻¹⁴ and is consequently used as an atmospheric marker of anthropogenic activity.¹⁵ OH initiated oxidation of acetylene is studied in detail in chapter 3 of this thesis, and results in the formation of either glyoxal, (HCO)₂, and OH, or formic acid and a formyl radical.⁴ Acetylene oxidation represents a significant source of atmospheric (HCO)₂, second only to isoprene oxidation, and accounts for 20% of the global (HCO)₂ budget.¹⁶ (HCO)₂ has been implicated as a likely precursor of secondary organic aerosol (SOA), which can potentially influence atmospheric chemistry, air quality and climate.¹⁷⁻¹⁹ The total continental source of (HCO)₂ is constrained by satellite measurements to range from 94 to 108 tg yr⁻¹,²⁰ however, only around 50% of the total (HCO)₂ budget is accounted for by recognised sources.^{16, 21} (HCO)₂ has recently been detected in the marine boundary layer (MBL), in concentrations ranging from 25 to 140 pptv, although the source remains uncertain.^{22, 23}

1.2 HOx Concentrations in Remote Forested Regions

Due to its decisive role in the removal of atmospheric trace gases, the oxidative capacity of Earth's atmosphere is largely governed by the atmospheric concentration of OH. Accurate future predictions of stratospheric ozone recovery, or changes in global mean surface temperature demand detailed accounts of the atmospheric lifetimes of the significant species involved, including CFC replacements (HCFCs and HFCs) and greenhouse gases (CH₄, O₃). Accurate derivations of these lifetimes are dependent on the accurate quantification of both the atmospheric OH radical concentration and the relevant rate coefficients.

In remote forested regions large quantities of VOCs such as isoprene (C₅H₈) are released from the biosphere (~1000 TgC yr⁻¹).²⁴ Biogenic hydrocarbons are known to react rapidly with OH, indeed, the OH + C₅H₈ reaction proceeds with a near gas kinetic rate

coefficient of $(1.11 \pm 0.23) \times 10^{-10} \text{ cm}^3 \text{ molecule}^{-1} \text{ s}^{-1}$ under ambient conditions;²⁵ and therefore act as efficient OH sinks. In the absence of appreciable NO_x, atmospheric global models predict that biogenic VOCs should rapidly sequester OH, reducing the oxidising capacity of the atmosphere in these regions and thereby extending the atmospheric lifetimes of less reactive hydrocarbons, such as CH₄. However, several recent field measurements in pristine forested environments contradict these model predictions, and report OH concentrations far higher than those simulated by chemical models.²⁶⁻³¹ Furthermore, the disparity between measurement and prediction is observed to correlate with isoprene emission;²⁹ suggesting either a significant fault in the current understanding of VOC oxidation in clean air masses, or systematic errors in HO_x field measurements in these environments. The latter has been suggested by Mao et al.,³² following the comparison of recent OH field measurements made above a Californian forest using two different detection techniques. OH was detected by on-resonance laser induced fluorescence (LIF) using either the traditional fluorescence assay by gas expansion (FAGE) technique, or by chemical modulation based on the signal difference with and without the addition of a highly reactive OH scavenger prior to LIF detection. The diurnal OH concentrations measured by Mao et al. using chemical modulation were consistently between 40 and 60% lower than the values measured by FAGE.³² Mao and co-workers concluded that the chemical modulation technique provided a quantitative measure of the real atmospheric OH concentration, based partly on their ability to model the daytime OH concentrations measured using this technique, and that the high bias observed using their FAGE instrument was a result of an unknown OH source within the FAGE cell. It is worthwhile to note there is also indirect evidence that indicates elevated OH concentrations in remote forested regions. Recent (HCO)₂ measurements above the tropical rainforest in Borneo, using differential optical absorption spectroscopy (DOAS), have reported peak concentrations of ~1.6 ppb.³³ Modelling studies have shown (HCO)₂ concentrations of this magnitude are consistent with (HCO)₂ production via isoprene oxidation using the elevated OH concentrations reported in this region using the FAGE technique; indicating that the uncertainty rests in our understanding of radical chemistry in these regions.

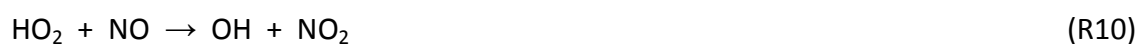
In an effort to resolve the discrepancy between measured and modelled OH concentrations in clean air regions rich in biogenic VOCs, the scientific community has recently re-examined its understanding of VOC oxidation under low NO_x conditions, and sought novel OH forming channels currently not implemented into atmospheric models. One such reaction, the aforementioned OH product channel following reactions of HO₂ with RO₂ radicals was first proposed by Lelieveld et al.,²⁸ and recently observed directly by Dillon and Crowley,³ and inferred by product studies,^{2, 34-37} although these radical propagating channels have only been observed for RO₂ species containing acyl, carbonyl, hydroxyl or alkoxy functionalities.

An alternative suggestion described OH regeneration through epoxide formation during isoprene oxidation.³⁸ Conventional chemistry for isoprene oxidation under low NO_x conditions predicts the formation of hydroxyl-hydroperoxides from the cross reaction of isoprene derived peroxy radicals with HO₂. Paulot and colleagues proposed that oxidation of these hydroxyl-hydroperoxides by OH results predominantly in the formation of epoxides and OH. Theoretical calculations supporting epoxide formation were performed alongside chamber experiments, during which both the isoprene derived hydroxyl-hydroperoxides and the epoxides were identified as ion-molecule clusters using chemical ionisation mass spectrometry (CIMS).

Theoretical studies of the OH initiated oxidation of isoprene have also been carried out to investigate the potential for OH recycling. Density functional theory (DFT) calculations carried out independently by da Silva et al.³⁹ and Peeters et al.,⁴⁰ have reported the possibility of OH formation following decomposition of alkoxy radicals formed following intramolecular rearrangement of certain peroxy radicals derived from isoprene; although the isomerisation rate is not expected to compete with peroxy radical loss through reactions with NO and HO₂.³⁹ In addition, Peeters and co-workers suggested that isomerisation of other isoprene derived peroxy radicals could lead to the formation of resonance stabilised alkoxy radicals which might react with oxygen to generate HO₂ and an unsaturated hydroperoxy-aldehyde (HPALD); these carbonyl species are expected to then photolyse rapidly in daylight to give further OH, and thereby increase the concentration of both OH and HO₂.⁴⁰⁻⁴²

All of the suggestions proposed in the literature to explain the systematic model underestimation of OH concentrations in remote forested regions have recently been assessed by Whalley et al.,³¹ using HOx measurements made over Borneo during the OP3 campaign in 2008 to determine the current understanding of oxidation chemistry in pristine environments. OH and HO₂ concentrations were measured using the fluorescence assay by gas expansion (FAGE) technique. The mean diurnal OH concentration profile constructed from 25 days of OH measurements is shown by the solid black line in Figure 2. Whalley and co-workers carried out simultaneous field measurements of both the OH concentration and the total OH reactivity, and by treating OH in photo-stationary steady state, were able to compare their measured OH concentrations with values calculated from their total OH reactivity measurements and the various recognised, and postulated OH sources reported in the literature.

OH concentrations calculated assuming OH is formed solely from ozone photolysis in the presence of water vapour are plotted as the yellow line in Figure 2, while the brown line also includes other known OH sources, such as the reactions of HO₂ with NO (R10) and ozone (R11), the reaction of ozone with isoprene, C₅H₈, (R12), and peroxide photolysis.⁴³⁻⁴⁶



The OH concentrations calculated using all established OH sources underestimate the observed OH concentration by an order of magnitude at midday (Figure 2); and highlight a significant missing photochemical OH source, consistent with previous studies.

Including OH generation following OH initiated oxidation of C₅H₈, as suggested by the calculations of da Silva and Peeters et al.,^{39, 40} and experimentally by Paulot and co-workers³⁸ brings a marked improvement in the agreement between the measured and modelled OH concentrations (Figure 2); although the green line showing the OH concentrations calculated using an OH yield of unity associated with C₅H₈ oxidation chemistry, still fails to satisfactorily reconcile the measured and calculated OH profiles.

Stavrakou et al. have suggested that rapid photolysis of the co-products generated using the Peeters et al. oxidation mechanism, could generate up to 3 OH radicals for every isoprene molecule oxidised.⁴⁷ While the OH concentrations calculated using an OH yield of 2.7 brings the measured and modelled OH concentrations in closer agreement (blue line in Figure 2), the Peeters et al. mechanism is found to introduce a high bias in the modelled HO₂ concentration; suggesting that if the isoprene chemistry proposed by Peeters and co-workers is significant in these regions, then additional chemistry is required to convert HO₂ to OH.^{30, 31}

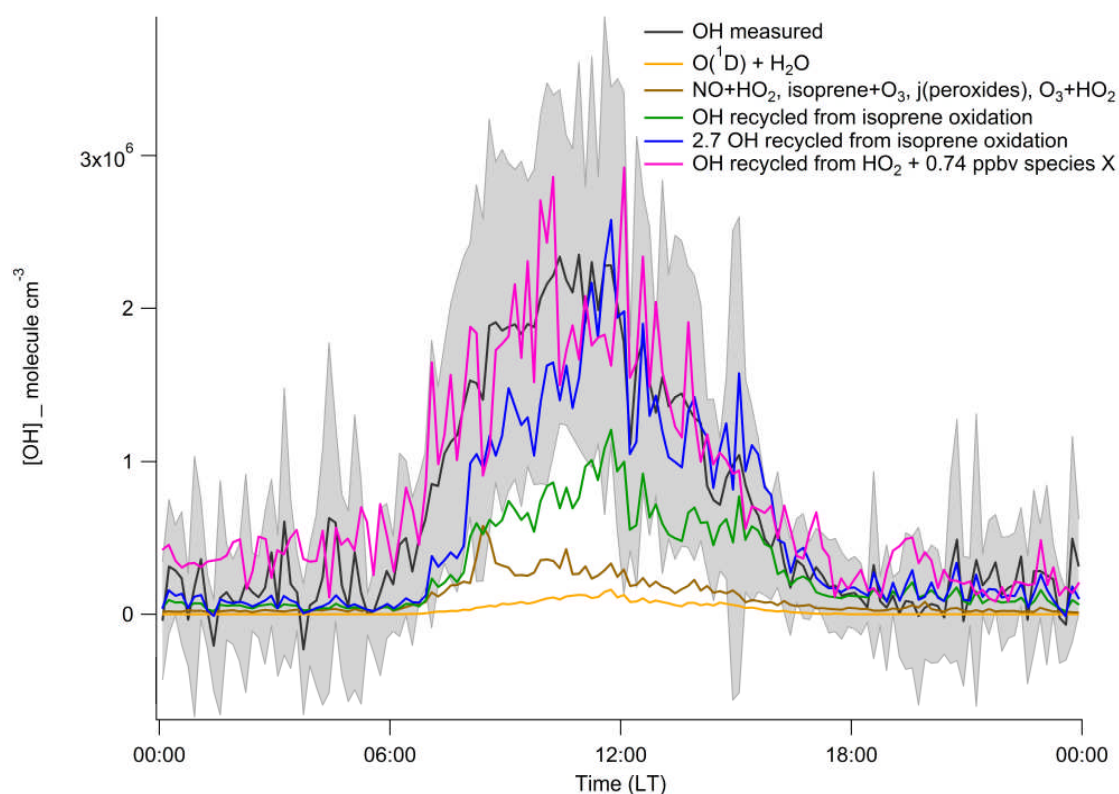


Figure 2: Comparison of measured OH concentrations over Borneo measured during the OP3 campaign in 2008 (black line) with values calculated using the photostationary steady state approximation constrained to the measured total OH reactivity, k'_{total} , for the loss term and with various OH source terms included. The grey shading represents the 1σ standard deviation of the averaged OH profile.³¹

It has been suggested that including an unknown reagent that can convert HO₂ to OH can reconcile the measured and modelled HOx concentrations in remote forested regions.⁴⁸ Indeed, Whalley et al.³¹ found that by including an unknown species X that reacts rapidly with HO₂ to generate OH, they were able to model both OH and HO₂ concentrations observed during the OP3 campaign, without including novel isoprene chemistry (pink line in Figure 2). However, their satisfactory HOx simulation required a species X concentration of 0.74 ppbv and an HO₂ to OH conversion rate comparable to NO. Currently, only carbonyl containing peroxy radical species have been shown through experiment to convert HO₂ to OH,^{3, 34-36} and none generate OH in sufficient yield to model the HOx concentration observed during the OP3 campaign. In conclusion, none of the mechanistic alterations proposed in the literature were found to result in a satisfactory simulation of the observed HOx concentrations, as reactions are required that increase the OH-to-HO₂ ratio.

It is possible that under low NOx conditions, a number of peroxy radicals derived from OH initiated VOC oxidation, either convert HO₂ to OH, or decompose and recycle OH directly, and that collectively, these reactions significantly increase the OH-to-HO₂ ratio. Recent calculations by da Silva has suggested that HC(O)CO radical, produced following the OH initiated oxidation of (HCO)₂ (R13) reacts with O₂ to generate OH directly (R14).⁴⁹ A detailed investigation of glyoxal oxidation is presented in chapter 6 of this thesis.



The uncertainty associated with measured and modelled HOx concentrations in remote forested regions highlights a recent area of scientific research that has demanded the concerted efforts of field studies, laboratory experiments, and theoreticians. While the issues surrounding VOC oxidation chemistry in remote forested regions remain unresolved, the efforts to date suggest reactions are required that either convert HO₂ to OH, or that recycle OH without also generating HO₂. The majority of work presented in this thesis centres on OH recycling chemistry, and involved quantifying OH yields based on the detailed kinetic study of elementary reactions. The remainder of this chapter provides a brief introduction to chemical kinetics.

1.3 Chemical Kinetics

Kinetics is a field of chemistry concerned primarily with quantifying the rates at which reactions proceed. Reactions are fundamental to all chemistry and an understanding of kinetics is essential for a wide range of significant issues, from the catalysts used in industrial synthesis, to the atmospheric processes related to tropospheric air quality, stratospheric ozone recovery, and global climate change. Experimental kinetic studies provide reaction rate coefficients which in turn can provide insight into the mechanism by which reactions proceed. Rate coefficients are required as primary inputs in the Master Chemical Mechanism (MCM), a model developed at the University of Leeds to describe the chemical degradation of tropospheric organic compounds and provide accurate information concerning the role of specific organic compounds in ground level ozone formation in relation to European air quality policy development (<http://mcm.leeds.ac.uk/MCM/>).

For the theoretical reaction:



The rate equation can be expressed as follows:

$$-\frac{d[A]}{dt} = k[A]^\alpha [B]^\beta \quad (\text{E1})$$

where [A] and [B] are the concentrations of reactants A and B, respectively, and α and β are experimental quantities known as the order of reaction with respect to reactants A and B, and the proportionality constant, k , is known as the reaction rate coefficient. An elementary reaction is one in which one or more chemical species react directly to form products in a single step. The term molecularity refers to the number of reactant species involved in an elementary step. All the reactions considered in this thesis are either unimolecular or bimolecular (involve one or two reactant species, respectively) elementary reactions for which molecularity and order are identical.

1.4 Temperature Dependence

A great many chemical reactions demonstrate positive temperature dependence, such that experimental rate coefficients are observed to increase with temperature. This temperature dependence can be explained by the existence of an energy barrier between the reactants and products that must be overcome prior to reaction. At higher temperatures more thermal energy is supplied to the system and an increased fraction of collisions occur with sufficient energy to form products. This temperature dependence was empirically quantified by the famous Arrhenius equation:

$$k(T) = A \exp(-E_{\text{act}}/RT) \quad (\text{E2})$$

where the activation energy, E_{act} , can be considered as the energy required to reach the reaction transition state (J mol^{-1}), $k(T)$ is the temperature dependent rate coefficient, A is a pre-exponential factor, R is the gas constant ($8.315 \text{ J K}^{-1} \text{ mol}^{-1}$), and T is temperature (K).

Not all reaction rate coefficients exhibit positive temperature dependence. Many reactions do not exhibit a significant activation energy on path to products and may even have wells in energy such that reactants pass through an energy minimum on route to products. Negative temperature dependent kinetic behaviour has recently been observed at the University of Leeds for the reactions of OH with oxygenated organic compounds.⁵⁰⁻⁵³ Rate coefficients for the reactions of OH with methanol, acetone and dimethyl ether were all observed to increase significantly as temperatures decrease below 100 K, relative to their well established room temperature values. Experimental and theoretical evidence support the formation of hydrogen bound complexes prior to products in these systems; with stabilisation into the pre-reactive complex increasingly favoured at low temperatures.

1.5 Theories of Chemical Reactions

1.5.1 Collision Theory

Collision theory was the first theory proposed to explain and quantify the rates of gas-phase chemical reactions, and follows the same assumptions made in deriving the kinetic theory of gases. Collision theory was devised independently by Trautz and by Lewis

in the early 1900s and treats molecules as impenetrable spheres, and assumes that no molecular interaction occurs prior to collision. The collision theory expression adopts the same form as the Arrhenius equation, with an exponential term that defines the fraction of collisions that occur with enough energy to overcome the barrier to reaction, but quantifies the Arrhenius pre-exponential A -factor in terms of the collision frequency. The collision frequency, Z , can be calculated from the collision cross section and the average speed of the reactants. The collision cross section, σ , for the reaction is given by:

$$\sigma = \pi b_{\max}^2 \quad (\text{E3})$$

where b_{\max} represents the maximum separation between the centres of two reacting molecules which still results in collision; for collision between two reactants A and B, with radii r_A and r_B , respectively, $b_{\max} = r_A + r_B$. The average speed of the reactants \bar{v} is then determined from the Maxwell-Boltzmann distribution of kinetic energies:

$$\bar{v} = \left(\frac{8k_B T}{\pi \mu} \right)^{\frac{1}{2}} \quad (\text{E4})$$

where μ is the reduced mass, $m_A m_B / (m_A + m_B)$, and occurs in the equation because we are interested in the relative speed of approach. Combining the collision frequency with the fraction of molecules which collide with sufficient energy to react, gives the collision theory expression for the bimolecular rate coefficient, k_{CT} :

$$\begin{aligned} k_{\text{CT}} &= \pi b_{\max}^2 \left(\frac{8k_B T}{\pi \mu} \right)^{\frac{1}{2}} \exp(-E_{\text{act}} / RT) \\ &= Z \exp(-E_{\text{act}} / RT) \end{aligned} \quad (\text{E5})$$

While the collision theory expression conforms to that of the empirical Arrhenius equation and provides some physical significance to the pre-exponential A -factor and the importance of reactants colliding, it completely ignores the internal energies of the reactants involved, and the manner by which a reaction complex evolves on route to products. In addition, it makes no account of the importance of the orientation of the collision leading to products, or of the intermolecular forces involved during reaction. A

more sophisticated theoretical model known as Transition State Theory (TST), developed in the 1930s by Wigner and Pilzer⁵⁴ and later by Eyring,^{55, 56} is required to accurately predict reaction rates.

1.5.2 Transition State Theory (TST)

Transition State Theory (TST) has long been synonymous with the theoretical treatment of elementary reactions, with reactants passing through an activated complex on route to products, across a path defined by the potential energy surface of the reaction.⁵⁷ Returning to the hypothetical bimolecular reaction:



the differential rate law for product formation can be expressed as:

$$\frac{d[\text{Products}]}{dt} = k_{15}[A][B] \quad (\text{E6})$$

TST assumes that the reaction between species A and B proceeds through an activated complex, or transition state, and that this activated complex can dissociate by unimolecular decay either back to reactants or into products; as shown in the fictional reaction scheme presented below:



The overall rate of forming products is given by:

$$\frac{d[\text{Products}]}{dt} = k_b[AB^\ddagger] \quad (\text{E7})$$

As this model assumes a pre-equilibrium exists between the reactants and the activated complex, the concentration of AB^\ddagger can be expressed in terms of the equilibrium constant K^\ddagger for the formation of AB^\ddagger from reactants A and B as follows:

$$[AB^\ddagger] = K^\ddagger[A][B] \quad (E8)$$

Substituting equation E8 into equation E7 it follows that:

$$k_{15} = k_b K^\ddagger \quad (E9)$$

The equilibrium constant, K^\ddagger , can be re-written in terms of the molecular partition functions of species A and B and the AB activated complex, giving:

$$k_{15} = k_b \left(\frac{Q_{AB}}{Q_A Q_B} \right) \exp(-\Delta H^\ddagger / RT) \quad (E10)$$

where Q_A , Q_B and Q_{AB} correspond to the molecular partition functions of species A, B and the activated complex AB^\ddagger , respectively.

One of the vibrational frequencies of the activated complex is not a true vibration as it corresponds to translation about the reaction coordinate. This degree of freedom can be defined using vibrational partition function q^* in which the vibrational frequency ν tends towards zero:

$$q^* = \frac{1}{1 - \exp(-h\nu/k_B T)} \approx \frac{1}{1 - (1 - h\nu/k_B T)} \approx \frac{k_B T}{h\nu} \quad (E11)$$

The rate constant is now given by:

$$k_{15} = \frac{k_b k_B T}{h\nu} \left(\frac{Q_{AB}^\ddagger}{Q_A Q_B} \right) \exp(-\Delta H^\ddagger / RT) \quad (E12)$$

where Q_{AB}^\ddagger is now one less degree of freedom corresponding to the reaction coordinate. The frequency ν corresponds to its decomposition to products, and therefore is equal to the first-order rate coefficient k_b . Consequently the TST expression for the experimental rate coefficient k_{15} is given by:

$$k_{15}(T) = \frac{k_B T}{h} \left(\frac{Q_{AB}^\ddagger}{Q_A Q_B} \right) \exp(-\Delta H^\ddagger / RT) \quad (E13)$$

Equation E13 is in canonical form and expresses the rate coefficient as a function of temperature, $k_{15}(T)$. Properties of the reactants and transition state can be determined from spectroscopic or thermodynamic data, if available, or from electronic structure calculations.

1.5.3 Barrierless Reactions

Conventional TST assumes that the reaction flux passing through the transition state does so once, and does not cross back over to reactants; consequently TST is often considered to provide an upper limit of the true reaction rate coefficient. The *no-recrossing* assumption is valid for reactions where the activation barrier is high compared with the thermal energy available to reactants; for these reactions the transition state can be located from the stationary point along the intrinsic reaction coordinate, and equation E13 can be used to derive accurate rate coefficients. However, none of the reactions investigated in this thesis have appreciable barriers between reactants and products, moreover, some, such as the association of the HO-C₂H₂ radical with O₂, proceed to products across a barrierless potential energy surface; these reactions rely on variational transition state theory (VTST) to locate the transition state.⁵⁸ By treating the effective frequency with which activated complexes are converted to products as $k_B T/h$; equation E9 can be re-written in the form:

$$k_{15} = \left(\frac{k_B T}{h} \right) K^\ddagger \quad (\text{E14})$$

where K^\ddagger denotes the equilibrium constant for formation of the activated complex, with the imaginary frequency corresponding to the reaction coordinate removed. The equilibrium constant K^\ddagger can be expressed in terms of the Gibbs energy of activation, G^\ddagger , as follows:

$$\Delta G^\ddagger = -RT \ln K^\ddagger \quad (\text{E15})$$

It follows from equations E14 and E15 that the rate coefficient k_{15} can be written in terms of the change in Gibbs free energy as follows:

$$k_{15} = \left(\frac{k_B T}{h} \right) \exp(-\Delta G^\ddagger/RT) \quad (\text{E16})$$

At constant temperature, the change in free energy is dependent on the changes in enthalpy and entropy according to equation E17:

$$\Delta G^\ddagger = \Delta H^\ddagger - T\Delta S^\ddagger \quad (\text{E17})$$

The VTST method defines the transition state by varying the reactant parameters to give the maximum ΔG^\ddagger . For a barriered reaction surface the enthalpy term in equation E17 will dominate, and the maximum ΔG^\ddagger value becomes closely approximated by ΔH^\ddagger . For barrierless surface the entropic term in equation E17 becomes significant. There is often a negative change in entropy associated with formation of an activated complex. For bimolecular reactions, the complex forms following the association of two species, corresponding to a loss of three translational, and at least one rotational degree of freedom. The VTST method adjusts the location of the transition state to give the maximum ΔG^\ddagger . The variable calculations involved in VTST demand a highly detailed potential energy surface for the reaction of interest; consequently, the calculations are often limited by the level of theory used to calculate the reaction surface.

1.5.4 Pressure Dependent Reactions

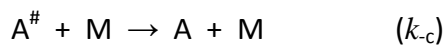
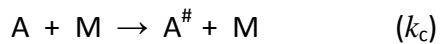
Under certain conditions, some reaction rate expressions depend on pressure as well as temperature. Unimolecular decomposition and bimolecular association reactions are prevalent in gas-phase chemistry, and rate coefficients for both these classes of reaction depend critically on pressure, and, furthermore, have reaction orders that vary with pressure. Unimolecular decomposition reactions are intuitively expected to demonstrate first-order kinetics, although under certain pressure regimes second-order behaviour is observed. A qualitative explanation for this kinetic dichotomy was provided in 1921 by Frederick Lindemann. The mechanism proposed almost a century ago by Frederick Lindemann to explain gas-phase decomposition reactions formed the basis for much of our current understanding of gas-phase chemical kinetics. For the hypothetical unimolecular reaction:



the rate of product formation can be expressed by the following rate law:

$$\frac{d[\text{Products}]}{dt} = k_{16}[\text{A}] \quad (\text{E18})$$

The Lindemann model breaks reaction R16 down into a series of elementary reactions, and defines the phenomenological rate coefficient, k_{16} , in terms of the rate constants assigned to each of the elementary steps. The Lindemann model provides a qualitative description for the unimolecular decomposition of A (R16) using the following reaction scheme:



where species A can collide with bath gas molecules, M, to give the energised intermediate $\text{A}^\#$ (k_c). This intermediate can then either dissociate to products (k_d) or be stabilised through further bath gas collisions to give A (k_{-c}). If the energised intermediate $\text{A}^\#$ is considered highly reactive, then after a short induction period, the concentration of $\text{A}^\#$ is expected to reach a steady state, at which point the rate of change in $[\text{A}^\#]$ can be considered zero, for as soon as $\text{A}^\#$ is formed it reacts and is removed. Under these conditions, the steady state concentration of intermediate $\text{A}^\#$ can be expressed as follows:

$$[\text{A}^\#]_{ss} = \left(\frac{k_c}{k_{-c}[\text{M}] + k_d} \right) [\text{A}][\text{M}] \quad (\text{E19})$$

The rate of product formation can be expressed as follows:

$$\frac{d[\text{Products}]}{dt} = k_d[\text{A}^\#] \quad (\text{E20})$$

where substitution of equation E19 into E20 gives:

$$\frac{d[\text{Products}]}{dt} = \left(\frac{k_d k_c}{k_{-c}[\text{M}] + k_d} \right) [\text{A}][\text{M}] \quad (\text{E21})$$

To a first approximation, equation E21 can be seen to conform to two extreme limits at high and low pressure. At the so called *high-pressure limit*, collisional deactivation dominates the removal of intermediate $A^\#$ and the $k_c[M]$ term in the denominator of equation E21 becomes much greater than k_d ; consequently the rate law reduces to:

$$\frac{d[\text{Products}]}{dt} = \left(\frac{k_d k_c}{k_c} \right) [A] \quad (\text{E22})$$

with a first-order rate coefficient independent of total pressure. At extreme low pressures bimolecular excitation of reactant A becomes rate limiting and the k_d term in the denominator of equation E21 becomes much greater than $k_c[M]$; under these conditions the rate law reduces to:

$$\frac{d[\text{Products}]}{dt} = k_c [A][M] \quad (\text{E23})$$

and the overall rate coefficient is pressure dependent.

The high and low pressure limiting behaviour of the Lindemann mechanism can be described generally by equation E24:

$$k_x = \frac{[M]}{\frac{1}{k_x^0} + \frac{[M]}{k_x^\infty}} \quad (\text{E24})$$

where k_x^∞ and k_x^0 denote the pressure dependent reaction rate coefficient k_x at the high and low pressure limit, respectively, and $[M]$ is the total gas number density. Equation E24 is used in chapter 6 to describe the unimolecular dissociation of the HC(O)CO radical produced following the reaction of OH with $(\text{HCO})_2$:



While the Lindemann mechanism provides a qualitative explanation of pressure dependent kinetics, its quantitative description is limited by neglecting the effect of the internal energy distribution within reactant molecules. The total energy of a polyatomic molecule is distributed amongst translational, rotational and vibrational modes. The

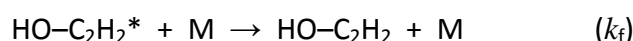
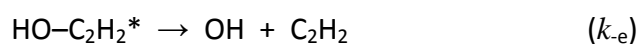
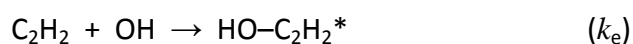
Lindemann model fails to account for the contribution made by this internal vibrational energy to the rate of activation and, consequently, systematically underestimates the bimolecular rate k_c . In addition, certain reactions will require reactant energy to be partitioned in specific modes before products form rapidly. Therefore a distinction must be made between reactant molecules with sufficient energy to undergo reaction, and those which yield products rapidly due to energy residing in a reactive mode.

1.5.5 Association Reactions

A second important class of pressure dependent gas-phase reactions involve three different chemical species. These processes are referred to as association or termolecular reactions, and involve the formation of an energetically activated complex which requires collisional stabilisation from a third body; these reactions are significant to atmospheric, combustion and interstellar chemistry. A detailed kinetic study of the OH initiated oxidation of acetylene, C_2H_2 , is presented in chapter 3 of this thesis, and for which the initial step is an association reaction between OH and the alkyne (R18):



Orders for association reactions characteristically depend on pressure, being third order at low pressures and second order at high total pressures. A Lindemann scheme can be applied to reaction R18 to provide a qualitative explanation of the pressure sensitive kinetics:



In this scheme OH adds across the C_2H_2 triple bond to generate an energetically activated $HO-C_2H_2^*$ intermediate (k_e), which can either dissociate back to reactants (k_{-e}) or be stabilized through collisions with bath gas molecules ($k_f[M]$). The rate of adduct formation can be expressed as follows:

$$\frac{d[\text{HO}-\text{C}_2\text{H}_2]}{dt} = k_f[\text{HO}-\text{C}_2\text{H}_2^*][\text{M}] \quad (\text{E25})$$

Treating the activated intermediate $\text{HO}-\text{C}_2\text{H}_2^*$ in steady state ($d[\text{HO}-\text{C}_2\text{H}_2^*]/dt = 0$) allows $[\text{HO}-\text{C}_2\text{H}_2^*]$ to be defined as:

$$[\text{HO}-\text{C}_2\text{H}_2^*]_{ss} = \left(\frac{k_e}{k_f[\text{M}] + k_{-e}} \right) [\text{OH}][\text{C}_2\text{H}_2] \quad (\text{E26})$$

Substituting equation E26 into E25 yields the following expression for the observed rate coefficient k_{18} :

$$k_{18} = \left(\frac{k_f k_e}{k_f[\text{M}] + k_{-e}} \right) [\text{OH}][\text{C}_2\text{H}_2][\text{M}] \quad (\text{E27})$$

Equation E27 can be seen to conform to two extreme pressure limits; analogous to the Lindemann description of unimolecular dissociation kinetics. At the high pressure limit, equation E27 reduces to:

$$k_{18}^\infty = k_f[\text{OH}][\text{C}_2\text{H}_2] \quad (\text{E28})$$

Under these conditions the formation of the association complex is rate determining, the rate adduct formation is independent of total pressure, and second order kinetics are observed. At limiting low pressures equation E27 reduces to:

$$k_{18}^0 = \left(\frac{k_f k_e}{k_{-e}} \right) [\text{OH}][\text{C}_2\text{H}_2][\text{M}] \quad (\text{E29})$$

Under low pressure conditions the rate of adduct formation is dependent on the equilibrium established between OH and C_2H_2 , and the activated association complex. The rate of adduct formation scales with pressure and third order kinetics are observed.

1.5.6 Development of the Lindemann Theory

The first flaw in the Lindemann model was addressed by Cyril Hinshelwood who treated the internal vibrational modes of the hypothetical molecule A as being s equivalent

simple harmonic oscillators, all of frequency ν , and used statistical methods to determine the probability of molecule A being energised to A^\ddagger following a collision.

The degeneracy, g_ν , for a set of molecules distributing ν vibrational quanta amongst s oscillators can be expressed as follows:

$$g_\nu = \frac{(\nu + s - 1)!}{\nu!(s - 1)!} \quad (\text{E30})$$

For a polyatomic molecule with ν quanta of vibrational energy and s harmonic oscillators of frequency ν , the fraction of molecules in state ν is given by the Boltzmann distribution:

$$n_\nu/N = g_\nu \exp(-\nu h\nu/k_B T)/Q \quad (\text{E31})$$

where the vibrational partition function, Q , now becomes $(1 - (\exp(-h\nu/k_B T)))^{-s}$.

Hinshelwood invoked the *strong collision assumption* which infers the state of the molecule after a collision is totally uncorrelated to its state prior to collision, and that the probability of any collision deactivating A^\ddagger was unity, consequently the bimolecular rate of deactivation, k_c , in the Lindemann reaction scheme becomes equal to the collision frequency, Z . As collisions promote equilibrium, the probability of forming state ν following a collision is given by the Boltzmann distribution for that state, therefore the rate of activation to state ν , $k_c(\nu)$, is given by:

$$k_c(\nu) = Zg_\nu \exp(-\nu h\nu/k_B T)/Q \quad (\text{E32})$$

Since chemical energies are generally much greater than the thermal energy ($k_B T$) available, the major contribution to the vibrational partition function comes from states below the critical energy for reaction, consequently, the probability of deactivating the energised intermediate A^\ddagger upon collision is effectively one. The overall rate of activation, k_c , is given by summing $k_c(\nu)$ over all energy levels with energy greater than the minimum energy required for reaction, E_0 :

$$k_c = \sum_{\nu=m}^{\infty} Zg_\nu \exp(-\nu h\nu/k_B T)/Q \quad (\text{E33})$$

where $mh\nu = E_0$. Hinshelwood developed equations for the case in which the energy levels can be assumed to be continuous ($k_B T > h\nu$); under these conditions Equation E33 becomes:

$$dk_c = Z\rho(E) \exp(-E/k_B T) dE/Q \quad (E34)$$

where $\rho(E) dE$ is the number of energy levels in the range $E-(E + dE)$, $\rho(E)$ is the density of states, and dk_c is the rate of activation into this energy region. The total rate of activation is then determined by integrating equation E34 over all energies greater than E_0 :

$$k_c = (Z/(s - 1)!)(E_0/k_B T)^{s-1} \exp(-E_0/k_B T) \quad (E35)$$

Equation E35 differs from the collision theory expression for the rate of activation by the factor:

$$\frac{(E_0 / k_B T)^{s-1}}{(s - 1)!} \quad (E36)$$

Under most conditions, the minimum energy required for reaction (E_0) is much larger than the available thermal energy ($k_B T$), and consequently the Hinshelwood modification leads to a significant increase in the theoretical rate of activation. In addition, the increased rate of activation, k_a , will be more pronounced for larger molecules which have a greater number of vibrational modes (s); this is exactly what is required to overcome the first failure in the simple Lindemann model.

Building on the earlier work by Hinshelwood, Rice, Ramsperger and Kassel modified the Lindemann mechanism further with quantitative efforts that focused on the rate at which the energised intermediate $A^\#$ dissociates.⁵⁹⁻⁶¹ The Rice, Ramsperger and Kassel (RRK) theory distinguishes the generally energised intermediate $A^\#$ from the activated complex A^\ddagger , which possesses sufficient energy in the required degree of freedom to dissociate promptly to products; adopting the following reaction sequence to describe the transition from the energised molecule $A^\#$ to products:



The first-order rate coefficient k^\ddagger is of the order of a vibrational frequency, while k_d is significantly slower. Applying the steady state approximation to A^\ddagger it can be shown that:

$$k_d = k^\ddagger[A^\ddagger]/[A^\#] \quad (\text{E37})$$

The degeneracy, g_v , for a set of molecules distributing v vibrational quanta amongst s oscillators can be expressed by equation E30. Assuming that formation of the activated complex A^\ddagger requires that at least m quanta of the total vibrational energy be partitioned in one specific mode, then the options for distributable quanta reduces to $(v - m)$. It follows that the degeneracy for a set of molecules partitioning v quanta of vibrational energy amongst s oscillators, while retaining m quanta in one specific mode can be expressed as follows:

$$g_v = \frac{(v - m + s - 1)!}{(v - m)!(s - 1)!} \quad (\text{E38})$$

The probability, P^\ddagger that a molecule with v vibrational quanta has at least m in the reactive mode is simply the ratio of E38/E30:

$$P^\ddagger = \frac{(v - m + s - 1)!v!}{(v - m)!(v + s - 1)!} \quad (\text{E39})$$

The quantum states involved are very large, allowing the application of Sterling's approximation to the factorials in equation E39, then from subsequent use of a Taylor expansion it can be shown that:

$$P^\ddagger = \left(\frac{v - m}{v} \right)^{s-1} \quad (\text{E40})$$

Since $E = v h \nu$ and $E_0 = m h \nu$, equation E40 can be re-written in terms of energies:

$$P_{EO}^E = \left(1 - \frac{E_0}{E} \right)^{s-1} \quad (\text{E41})$$

RRK theory assumes that the molecular vibrations are coupled, and that energy can flow freely from one vibrational mode to another, and that energy randomization takes place

sufficiently rapidly for the vibrational energy to be distributed statistically; therefore it follows that:

$$k_d(E) = k^\ddagger \left(1 - \frac{E_0}{E}\right)^{s-1} \quad (\text{E42})$$

where $k_d(E)$ denotes the dependence of k_d on the energy of the reacting molecule. Energy dependence in k_d is expected given that as the energy of the system increases, so does the probability of partitioning adequate quanta for reaction in the reactive mode. In addition, equation E42 shows k_d to decrease as the number of oscillators s increases. Again this is expected as for a given energy, increasing s provides more modes in which to partition the energy, thereby reducing the probability that a certain number of quanta will reside in one specific mode.

1.5.7 Rice, Ramsperger, Kassel and Marcus (RRKM) Theory

The Hinshelwood – RRK treatment of unimolecular reactions has proven a defining stage in developing our physical understanding of reaction kinetics. Further development at the time was limited by the computational technology available, forcing gross approximations to be made; specifically that all molecular vibrations are identical and oscillate at low frequencies.

More recent developments, which date from the work of Marcus,⁶² were reliant on computational methods and can result in stronger agreement between theory and experiment. This approach is named after the theoreticians responsible Rice, Ramsperger, Kassel and Marcus, and often abbreviated simply to RRKM Theory.

In RRKM theory the real frequencies of the molecule are used to evaluate $\rho(E)$, using *direct count* methods. The energy dependent unimolecular dissociation rate coefficient, $k_d(E)$, is adapted from equation E42 to give the famous, energy resolved, RRKM rate equation for unimolecular reactions, $k(E)$:

$$k(E) = \frac{W(E')}{h\rho(E)} \quad (\text{E43})$$

where $\rho(E)$ is the density of states of the reactant molecule at energy E , h is Planck's constant, and $W(E')$ is the sum of states at the activated complex for energy E . E' is the energy that remains in the activated complex after surmounting the reaction barrier, thus $E' = E - E_0$, and $W(E')$ is simply the number of ways of distributing throughout the activated complex (Figure 3).

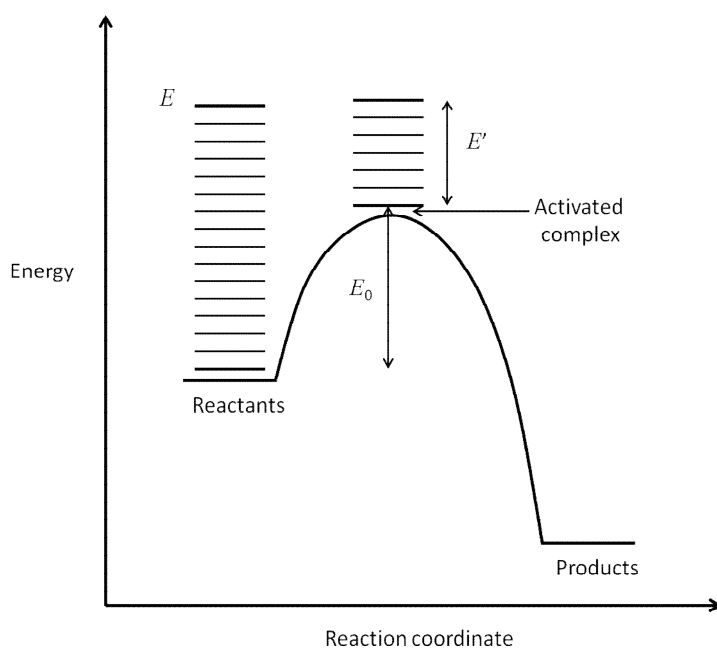


Figure 3: Potential energy surface for a decomposition reaction at total energy E . Reaction requires a minimum amount of energy, E_0 , to be partitioned within the reactive mode, the remainder, E' , is distributed throughout the activated complex.

1.6 Energy Grained Master Equation (EGME)

TST can be used to provide an accurate, quantitative description of a reaction rate at thermal equilibrium, when relaxation is fast compared to the timescale of reaction. Equally, when relaxation is slow compared with the reaction rate, energy resolved, RRKM theory becomes suitable. However, much of the chemistry considered in this thesis occurs over the intermediate relaxation regime, and demands the use of an Energy Grained Master Equation (EGME) to accurately describe the kinetics. This approach requires a detailed

potential energy surface (PES) for the reaction to be calculated, from which all the stationary points (transition states and energy wells) that separate the reactants, intermediates, and products are partitioned into energy grains of set energy width. A typical EGME description of the stationary points of a PES for a typical gas phase reaction is provided in Figure 4, for which the initial step is a bimolecular association reaction, which is followed by a sequence of unimolecular reactions involving two potential energy wells, and an irreversible product channel.

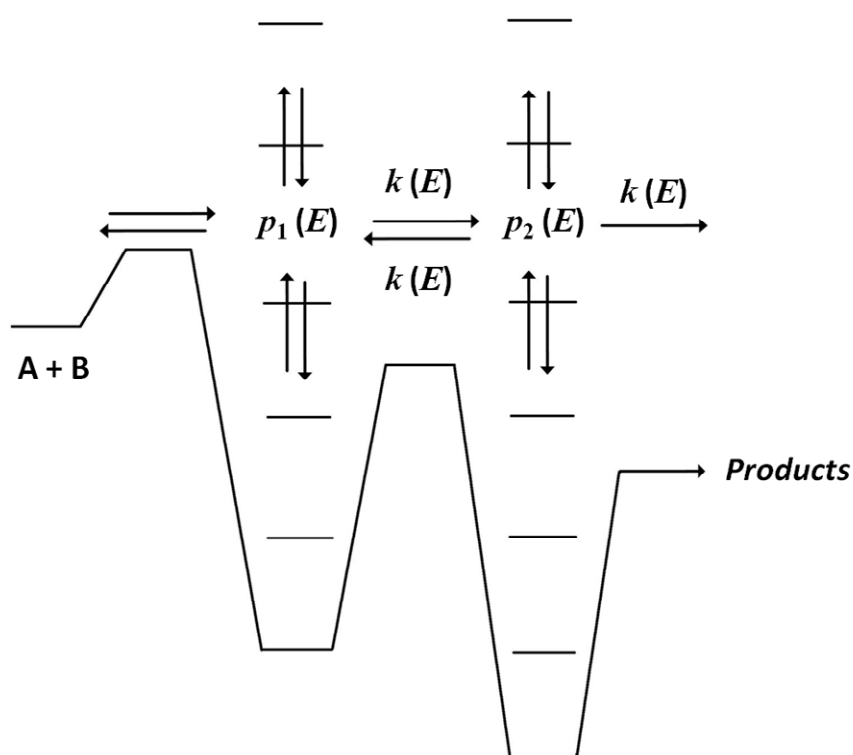


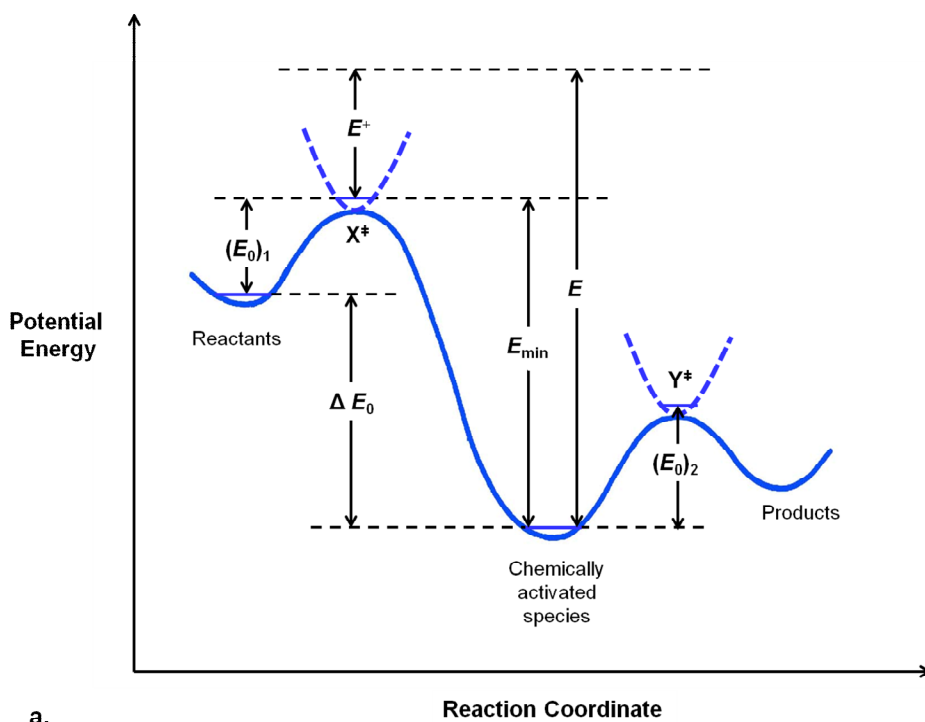
Figure 4: Representation of the energy grained master equation model for an association reaction between reactants A and B, with two wells and an irreversible product channel.

The population of any given energy grain can change as a function of time due either to collisional stabilization or activation, or from chemical reaction, into or out of the grain. An accurate theoretical description of these systems requires both the energy resolved microcanonical rate coefficients, $k(E)$, and a collisional energy transfer model. These are

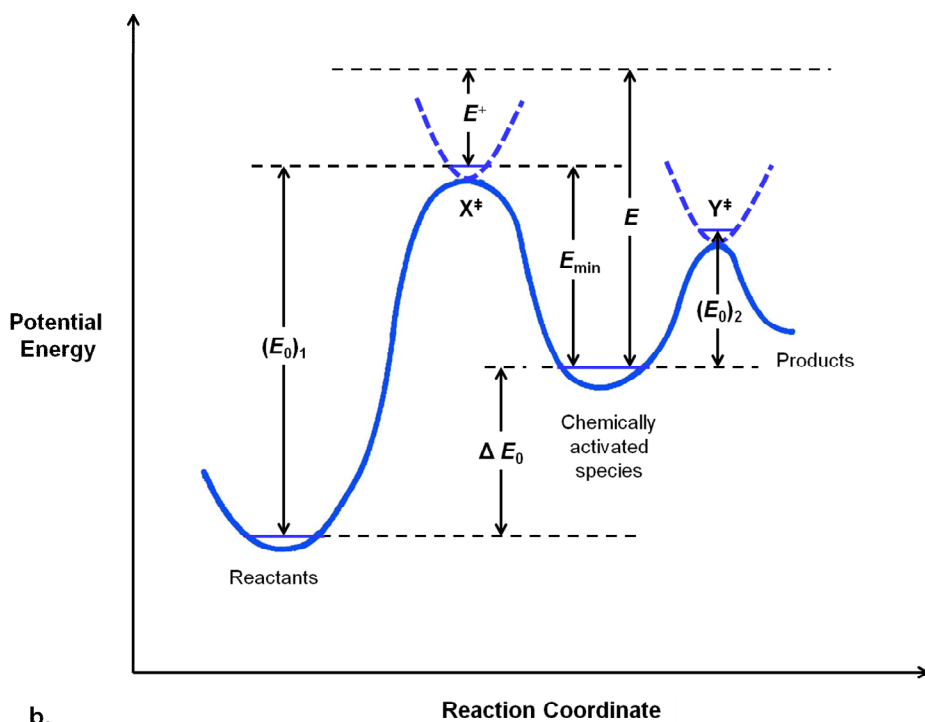
combined to construct a Master Equation (ME) model of the system that describes the evolution of each grain population. The coupled differential equations describing the relative change in population of each energy grain are then solved using numerical matrix methods. The energy grained master equation solver MESMER (Master Equation Solver for Multiple Energy-well Reactions) developed at the University of Leeds was used to fit experimental data sets presented in chapters 3, 4 and 5.⁶³ The relevant microcanonical rate coefficients were calculated using RRKM theory, and an exponential down model implemented into the MESMER code was used to calculate collisional energy transfer probabilities.

1.7 Chemical Activation

It has been shown that bimolecular association reactions result in formation of a nascent energised complex, and that in the absence of an additional exit channel, this energy is dissipated by molecular collisions which promote a thermal distribution of quantum states. However, when additional exit channels are available, then this excess energy can drive further chemistry. In cases such as this, where the energy is provided by virtue of the energy change involved in a preceding chemical reaction, the process is known as *chemical activation*. Reaction of these activated species can influence both the kinetics and product branching of chemical systems under both laboratory and atmospheric conditions. Figure 5 shows hypothetical potential energy surfaces for two chemically activated reactions where the activated complex forms as a result of a preceding exothermic (Fig. 5a) or endothermic reaction (Fig. 5b). Figure 5 shows clearly that if the critical energy for generating the chemically activated intermediate species is $(E_0)_1$, and the difference in zero point energies between reactants and the activated species is ΔE_0 , then the intermediate will form with a minimum excess energy $E_{\min} = (E_0)_1 - \Delta E_0$, where ΔE_0 is negative or positive depending upon whether the reaction is exothermic or endothermic. If the critical energy required for a subsequent reaction $(E_0)_2$ is less than E_{\min} then reactant molecules can proceed directly to products provided the excess energy is not removed through inert bath gas collisions.



a.



b.

Figure 5: Chemical activation by an exothermic (a) and endothermic (b) reaction; X^\ddagger represents the activated complex for the activating reaction, and Y^\ddagger represents the activated complex for subsequent reaction of the chemically activated species (Redrawn from Robinson and Holbrook).⁶⁴

Several studies have reported chemical activation to influence the product branching associated with a unimolecular exit channel in systems where the unimolecular path must compete with collisional stabilisation.⁶⁵⁻⁶⁸ These effects are often limited to low pressure conditions when thermal equilibrium is attained less rapidly. Chemical activation has been reported to influence the products observed following reaction of the methoxymethyl radical, CH₃OCH₂, with O₂ (R19):^{66, 68}



In a recent study, Eskola et al., generated CH₃OCH₂ by 248 nm photolysis of CH₃OCH₂Br (P3), and monitored the kinetics and yield of OH produced following reaction R19 over a range of temperatures (195 – 600 K) and pressures (5 – 500 Torr) by LIF.⁶⁹



The OH yields measured by Eskola et al. for reaction R19 were pressure dependent, with OH produced near exclusively as pressure is reduced close to zero. Eskola and co-workers complemented their experimental results with theory and argued convincingly that reaction R19 proceeds via a chemically activated association complex that can either dissociate to 2HCHO + OH (R19a), or become stabilised through inert bath gas collisions (R19b); an analogous chemical scheme has been used to describe OH production following the acetyl + O₂ reaction (R20).⁶⁵



While chemical activation has been shown to facilitate unimolecular exit channels, the role of activation in bimolecular exit channels is less well established.⁷⁰ Oxygen is the dominant bimolecular reaction partner for radicals produced in the atmosphere, where reactions are generally thought to involve thermally equilibrated reactants. However, in chapters 3 and 4 strong evidence is used to argue that the product distributions observed following the OH initiated oxidation of alkynes are strongly dependent on the internal

energy of the HO-alkyne adduct at the point of reaction with O₂, and that under atmospheric conditions, a significant fraction of the total product yield is formed before the internal quantum states of the adducts have fully relaxed.

All of the chemically activated species discussed in the preceding section have been generated following an association reaction; far less attention has focused on the possibility of energising a reactive intermediate via an abstraction channel. Hydrogen atom abstractions by OH result in formation of the thermodynamically stable H₂O molecule, and consequently dominate OH abstraction chemistry in the atmosphere. The widely accepted Polanyi rules state that abstraction reactions channel the exothermicity predominantly into the newly formed bond,⁷¹ consequently, secondary chemistry associated with the H₂O co-fragment is not expected to be influenced by chemical activation. However, this established rule is inconsistent with a study of the reaction of OH with methyl glyoxal, CH₃C(O)CHO (R21), by Baeza-Romero et al.⁷² Reaction R21 proceeds via hydrogen atom abstraction at the aldehydic hydrogen:



Baeza-Romero studied the OH kinetics associated with reaction R21 and in the presence of O₂ observed pressure dependent OH regeneration consistent with acetyl + O₂ chemistry, suggesting a significant fraction of the nascent CH₃C(O)CO population dissociates to give CH₃CO + CO following reaction R21. The role of chemical activation in abstraction channels is discussed in chapters 5 and 6.

1.8 Electronic States in Atoms and Molecules

Fluorescence detection techniques rely on the transition of an electron between states in the species of interest. The quantum mechanical model of an electron orbiting a nucleus is defined using a wavefunction. There are essentially three elements to an electronic wavefunction; some fundamental physical constants (c , h , π etc); parameters specific to the system such as an electrons radial distance from the nucleus; and a set of four quantum numbers (n , l , m_l and m_s). The principle quantum number, n , determines the orbitals distance from the nucleus and therefore the orbital energy level of the electron and

can take integer values from 1 to ∞ . The orbital quantum number, l , governs the shape and angular momentum of an orbital, and can take any integer value between 0 and $(n - 1)$. Each value is assigned to a particular type of atomic orbital; such that values 0, 1, 2 and 3 correspond to s , p , d and f -orbitals, respectively. The orbital magnetic quantum number, m_l , determines the direction of the orbital and the electron's behaviour in a magnetic field, and can take integer values ranging from $+l$ to $-l$. Finally, the spin magnetic quantum number, m_s , identifies the orientation of the intrinsic motion of an electron about its axis relative to those of other electrons in the system, and can take values $\pm\frac{1}{2}$ only.

For an open-shell atom there will be several possible ways in which the valence electrons can be arranged in the outer sub-shell, each unique configuration is known as a *microstate*, and defined by four unique quantum numbers in accordance with the *Pauli Exclusion Principle*. Individual microstates may have different energies as each represents a different spatial distribution of electrons within the atom, subject to different inter-electronic repulsions; for simplicity, each state can be represented in abbreviated form by a *term symbol*.

1.8.1 Angular momentum

An object orbiting on a circular path acquires angular momentum, defined as the product of its mass and angular velocity (degree rad s^{-1}). An electron orbiting a nucleus possesses both orbital and spin angular momentum, both of which are quantised, vector properties. The magnitude of the orbital angular momentum, I , of an electron can be calculated from the orbital quantum number, l , as follows:

$$I = \hbar\sqrt{l(l+1)} \quad (\text{E44})$$

where \hbar is the reduced Planck constant, $h/2\pi$. The direction of the orbital momentum is dependent on the magnetic quantum number, m_l . Once a reference direction has been specified, quantum law dictates that the orbital momentum can point such that the magnitude of its component vector in the reference direction can take values of $m_l\hbar$ only; providing $(2l + 1)$ possible orientations. When several valence electrons are present in an

atom, their orbital momenta combine to give a resultant total orbital momentum, \mathbf{L} . The magnitude of this vector can be calculated as follows:

$$\mathbf{L} = \hbar\sqrt{L(L+1)} \quad (\text{E45})$$

where L is the total orbital momentum quantum number, and can take positive integer values only, including 0. The value of L depends on the relative direction of the component momenta, and allow $(2L + 1)$ possible orientations of \mathbf{L} . Historically, upper-case Roman letters are used to express L , analogous to the lower-case Roman letters used to denote atomic orbitals; such that L values 0, 1, 2 and 3 are signified by the letters S, P, D and F, respectively.

1.8.2 Spin Angular Momentum

In addition to the momentum associated with orbital motion, the electron itself acquires spin momentum, \mathbf{s} , due to its intrinsic rotation about its own axis. The magnitude of the spin momentum of a single electron can be calculated using the spin quantum number, s , which takes the value $+\frac{1}{2}$ only, as follows:

$$\mathbf{s} = \hbar\sqrt{s(s+1)} = 0.866 \hbar \quad (\text{E46})$$

As with orbital momentum, quantisation limits the possible orientations of \mathbf{s} such that it can only adopt one of two directions, distinguished by the spin magnetic quantum number, m_s (spin up or spin down). The value of m_s signifies the component of its spin momentum in the reference direction. When several electrons are present in the valence shell of an atom, their spin momenta combine to give a resultant total spin momentum, \mathbf{S} . The magnitude of this vector can be calculated as follows:

$$\mathbf{S} = \hbar\sqrt{S(S+1)} \quad (\text{E47})$$

where S is the total spin momentum quantum number, which can take positive integer or half integer values, including 0; depending on the number of electrons contributing to the atomic spin momentum, and the relative direction of the component spin momenta. The quantity $(2S + 1)$ is known as the *multiplicity* of a term, and terms for which $(2S + 1)$ equals

1, 2, 3 and 4 are referred to as *singlets*, *doublets*, *triplets* and *quartets*, respectively. The multiplicity is of particular significance to *spectroscopists* as selection rules forbid transitions occurring between states of different multiplicity.

1.8.3 Total Electronic Angular Momentum and Term Symbols

The combination of the orbital and spin momenta provide an atom with a total angular momentum, \mathbf{J} . Electronic orbital and spin motions can be considered classically as rotating charges that generate magnetic fields, and therefore allow weak field interactions referred to as spin-orbit coupling. If the spin-orbit coupling is weak then the field interaction only becomes significant when both the orbital and spin momenta are operating collectively; as defined by the quantum numbers L and S , respectively. When more than one electron is present in the valence shell of an atom, the total angular momentum, \mathbf{J} , can be calculated by first adding the individual orbital angular momentum to give \mathbf{L} , then adding the individual spin angular momenta to give \mathbf{S} , with final summation of \mathbf{L} and \mathbf{S} to give \mathbf{J} . This method is known as the *Russell-Saunders coupling scheme*, and has proved a suitable approximation for light atoms (atomic number, $Z < 35$).

As with the component orbital and spin momentum vectors, the magnitude of the resultant total angular momentum, \mathbf{J} , can be calculated as follows:

$$\mathbf{J} = \hbar\sqrt{J(J+1)} \quad (\text{E48})$$

where J is the total angular momentum quantum number, and can take positive values only, including 0.

Degenerate states are grouped together into *terms*. Given that there are $(2L + 1)$ possible orientations of \mathbf{L} , and $(2S + 1)$ possible orientations of \mathbf{S} , it follows that the total number of states for any term given L and S is $(2L + 1)(2S + 1)$. Each term may be represented in abbreviated form by a *term symbol* which conventionally takes the form:

$$\text{Term Symbol} = {}^{(2S+1)}L_J$$

1.8.4 Diatomic Term Symbols

Many of the rules used to assign term symbols to electrons in atoms can be applied to electrons in molecules. For diatomic molecules the reference direction used to assign the atomic orbital angular momentum vector is specified by the bond axis. In addition, the electric field generated along the bond axis by the two nuclei, make different \mathbf{I} components of molecular orbital angular momentum different in energy. The axial component of angular momentum is denoted by the symbol λ , and can take either positive integer values or is zero. Greek letters corresponding to the letters s, p, d, \dots are used to designate the λ state of an electron in a molecule:

$$l_z = 0, \pm 1, \pm 2, \pm 3, \dots$$

$$\lambda = 0, 1, 2, 3, \dots$$

$$\sigma, \pi, \delta, \phi, \dots$$

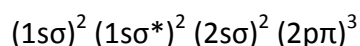
The axial component of the total orbital angular momentum is of greatest significance due to strong orbital-axial coupling, and is denoted by the symbol Λ , and calculated simply from the sum of the individual axial components, λ :

$$\Lambda = \left| \sum \lambda_i \right|$$

with Λ state values of 0, 1, 2, ... designated by the capital Greek letters $\Sigma, \Pi, \Delta, \dots$

Electron spin momentum are not strongly affected by the force field generated between the two nuclear charges, therefore the notation used to describe electronic spin momentum in atoms, also applies to electronic spin in molecules.

The majority of kinetic experiment work presented here involved monitoring the OH radical by laser induced fluorescence (LIF). The OH radical has a total of nine electrons, with the ground state configuration:



Conventionally, the electronic ground state of a species is assigned the prefix X and consequently this configuration of OH corresponds to a $X^2\Pi$ term. Absorption at ~ 282 nm

results in excitation to the $v' = 1$ level of the first upper electronic OH state, conventionally assigned the prefix *A*. This transition corresponds to excitation of an electron from the $2s\sigma$ orbital to the unpaired $2p\pi$ orbital; leaving the unpaired electron in the $2s\sigma$ orbital with no axial component of angular momentum ($\Lambda = 0$), and therefore corresponds to a $A^2\Sigma$ term.

1.9 Overview of this Thesis

The majority of the experimental work presented in this thesis focuses on reaction systems initiated by OH that result in formation of reactive intermediates which potentially recycle OH in the presence of O_2 . By monitoring OH directly by laser induced fluorescence (LIF) it is possible to quantify the OH yield for these systems directly from the ratio of rate coefficients measured with and without O_2 . A summary of the following chapters presented in this thesis is provided below:

Chapter 2 introduces the laser flash photolysis laser induced fluorescence (LFP-LIF) technique used throughout this thesis to quantify bimolecular gas-phase reaction kinetics. Some alternative radical detection techniques and kinetic methods are also briefly discussed. Finally the details of the specific apparatus used throughout this thesis are provided.

Chapter 3 gives a detailed experimental and theoretical study of the association reaction between OH and acetylene, C_2H_2 . The resulting HO- C_2H_2 adducts react rapidly with O_2 to generate either glyoxal, $(HCO)_2$, and recycle OH, or formic acid and a formyl radical. Experimental and theoretical evidence confirm that the branching between the bicarbonyl and organic acid channels is controlled by the stereochemistry of the adduct and the point of reaction with O_2 .

Chapter 4 build on the work presented in chapter 3 and reports an experimental study of the reaction of OH with the propyne and 2-butyne. The OH yields are determined as a function of pressure and temperature using OH cycling methods. The OH yields measured for the higher alkynes considered in this chapter demonstrate qualitatively similar behaviour to the OH + C_2H_2/O_2 system.

In chapter 5, experiments were carried out to quantify the acetyl, CH_3CO , yield associated with the $\text{OH} + \text{acetaldehyde}$, CH_3CHO , reaction by investigating the pressure dependent OH yield associated with the subsequent reaction of CH_3CO with O_2 . Stern-Volmer analyses of the OH yields measured suggest that ~15% of the acetyl formed following reaction of OH with acetaldehyde dissociates to $\text{CH}_3 + \text{CO}$. These indirect measurements were complemented by a photoionisation mass spectrometry (PIMS) study that confirmed CH_3 and CO as primary products of the $\text{OH} + \text{CH}_3\text{CHO}$ reaction.

Recent theoretical and experimental evidence have suggested the HC(O)CO radical produced following the reaction of OH with glyoxal, $(\text{HCO})_2$, can react with O_2 and generate OH . In chapter 6 experiments generating HC(O)CO via reaction of chlorine atoms with $(\text{HCO})_2$ in the presence of O_2 confirm this. Experimental OH yields for the $\text{OH} + (\text{HCO})_2/\text{O}_2$ system are quantified for the first time as a function of pressure and temperature.

In Chapter 7 attention turns to developing a laser system suitable for formyl radical, HCO , detection. The system is characterised by measuring room temperature rate coefficients for the reactions of HCO with O_2 , NO and NO_2 . This chapter reports, for the first time, experimental evidence suggesting that the HCO radical reacts rapidly with a range of aldehyde species. Bimolecular rate coefficients for the reaction of HCO with HCHO and CH_3CHO are quantified and the reaction products inferred from the observed temperature dependence.

The final chapter provides a summary of all the experimental work presented in this thesis, together with its scientific significance.

1.10 References

1. Wayne, R. P., *Chemistry of Atmospheres*. 3rd ed.; Oxford University Press: New York, 2000.
2. Le Crane, J. P.; Rayez, M. T.; Rayez, J. C.; Villenave, E., A reinvestigation of the kinetics and the mechanism of the $\text{CH}_3\text{C}(\text{O})\text{O}_2 + \text{HO}_2$ reaction using both experimental and theoretical approaches. *Physical Chemistry Chemical Physics* 2006, 8, 2163-2171.
3. Dillon, T. J.; Crowley, J. N., Direct detection of OH formation in the reactions of HO_2 with $\text{CH}_3\text{C}(\text{O})\text{O}_2$ and other substituted peroxy radicals. *Atmospheric Chemistry and Physics* 2008, 8, 4877-4889.
4. Hatakeyama, S.; Washida, N.; Akimoto, H., Rate constants and mechanisms for the reaction of OH (OD) radicals with acetylene, propyne, and 2-butyne in air at 297 +/- 2K. *Journal of Physical Chemistry* 1986, 90, 173-178.
5. Bohn, B.; Siese, M.; Zetzsch, C., Kinetics of the $\text{OH} + \text{C}_2\text{H}_2$ reaction in the presence of O_2 . *Journal of the Chemical Society-Faraday Transactions* 1996, 92, 1459-1466.
6. Yeung, L. Y.; Pennino, M. J.; Miller, A. M.; Elrod, M. J., Kinetics and mechanistic studies of the atmospheric oxidation of alkynes. *Journal of Physical Chemistry A* 2005, 109, 1879-1889.
7. Greenberg, J. P.; Zimmerman, P. R., Nonmethane Hydrocarbons in Remote Tropical, Continental, and Marine Atmospheres. *Journal of Geophysical Research-Atmospheres* 1984, 89, 4767-4778.
8. Fischer, H.; Brunner, D.; Harris, G. W.; Hoor, P.; Lelieveld, J.; McKenna, D. S.; Rudolph, J.; Scheeren, H. A.; Siegmund, P.; Wernli, H.; Williams, J.; Wong, S., Synoptic tracer gradients in the upper troposphere over central Canada during the Stratosphere-Troposphere Experiments by Aircraft Measurements 1998 summer campaign. *Journal of Geophysical Research-Atmospheres* 2002, 107.
9. Whalley, L. K.; Lewis, A. C.; McQuaid, J. B.; Purvis, R. M.; Lee, J. D.; Stemmler, K.; Zellweger, C.; Ridgeon, P., Two high-speed, portable GC systems designed for the measurement of non-methane hydrocarbons and PAN: Results from the Jungfraujoch High Altitude Observatory. *Journal of Environmental Monitoring* 2004, 6, 234-241.
10. Blake, D. R.; Smith, T. W.; Chen, T. Y.; Whipple, W. J.; Rowland, F. S., Effects of biomass burning on summertime nonmethane hydrocarbon concentrations in the Canadian wetlands. *Journal of Geophysical Research-Atmospheres* 1994, 99, 1699-1719.
11. Blake, N. J.; Blake, D. R.; Sive, B. C.; Chen, T. Y.; Rowland, F. S.; Collins, J. E.; Sachse, G. W.; Anderson, B. E., Biomass burning emissions and vertical distribution of atmospheric methyl halides and other reduced carbon gases in the South Atlantic region. *Journal of Geophysical Research-Atmospheres* 1996, 101, 24151-24164.
12. Greenberg, J. P.; Zimmerman, P. R.; Heidt, L.; Pollock, W., Hydrocarbon and carbon-monoxide emissions from biomass burning in Brazil. *Journal of Geophysical Research-Atmospheres* 1984, 89, 1350-1354.
13. Hegg, D. A.; Radke, L. F.; Hobbs, P. V.; Rasmussen, R. A.; Riggan, P. J., Emissions of Some Trace Gases from Biomass Fires. *Journal of Geophysical Research-Atmospheres* 1990, 95, 5669-5675.
14. Fraser, M. P.; Cass, G. R.; Simoneit, B. R. T., Gas-phase and particle-phase organic compounds emitted from motor vehicle traffic in a Los Angeles roadway tunnel. *Environmental Science & Technology* 1998, 32, 2051-2060.
15. Hopkins, J. R.; Jones, I. D.; Lewis, A. C.; McQuaid, J. B.; Seakins, P. W., Non-methane hydrocarbons in the Arctic boundary layer. *Atmospheric Environment* 2002, 36, 3217-3229.
16. Fu, T. M.; Jacob, D. J.; Wittrock, F.; Burrows, J. P.; Vrekoussis, M.; Henze, D. K., Global budgets of atmospheric glyoxal and methylglyoxal, and implications for formation of secondary organic aerosols. *Journal of Geophysical Research-Atmospheres* 2008, 113.
17. Hastings, W. P.; Koehler, C. A.; Bailey, E. L.; De Haan, D. O., Secondary organic aerosol formation by glyoxal hydration and oligomer formation: Humidity effects and equilibrium shifts during analysis. *Environmental Science & Technology* 2005, 39, 8728-8735.

18. Kroll, J. H.; Ng, N. L.; Murphy, S. M.; Varutbangkul, V.; Flagan, R. C.; Seinfeld, J. H., Chamber studies of secondary organic aerosol growth by reactive uptake of simple carbonyl compounds. *Journal of Geophysical Research-Atmospheres* 2005, 110.
19. Liggio, J.; Li, S. M.; McLaren, R., Reactive uptake of glyoxal by particulate matter. *Journal of Geophysical Research-Atmospheres* 2005, 110.
20. Stavrou, T.; Müller, J.-F.; Smedt, I. D.; Roozendaal, M. V.; Kanakidou, M.; Vrekoussis, M.; Wittrock, F.; Richter, A.; Burrows, J., The continental source of glyoxal estimated by the synergistic use of spaceborne measurements and inverse modelling. *Atmospheric Chemistry and Physics* 2009, 9, 8431-8446.
21. Myriokefalitakis, S.; Vrekoussis, M.; Tsigaridis, K.; Wittrock, F.; Richter, A.; Bruhl, C.; Volkamer, R.; Burrows, J. P.; Kanakidou, M., The influence of natural and anthropogenic secondary sources on the glyoxal global distribution. *Atmospheric Chemistry and Physics* 2008, 8, 4965-4981.
22. Sinreich, R.; Coburn, S.; Dix, B.; Volkamer, R., Ship-based detection of glyoxal over the remote tropical Pacific Ocean. *Atmospheric Chemistry and Physics* 2010, 10, 11359-11371.
23. Mahajan, A. S.; Prados-Roman, C.; Hay, T. D.; Lampel, J.; Pöhler, D.; Großmann, K.; Tschirner, J.; Friess, U.; Platt, U.; Johnston, P., Glyoxal observations in the global marine boundary layer. *Journal of Geophysical Research: Atmospheres* 2014.
24. Goldstein, A. H.; Galbally, I. E., Known and unexplored organic constituents in the earth's atmosphere. *Environmental Science & Technology* 2007, 41, 1514-1521.
25. McQuaid, J. B.; Stocker, D. W.; Pilling, M. J., Kinetics of the reactions of OH with 3-methyl-2-cyclohexen-1-one and 3,5,5-trimethyl-2-cyclohexen-1-one under simulated atmospheric conditions. *International Journal of Chemical Kinetics* 2002, 34, 7-11.
26. Carslaw, N.; Creasey, D. J.; Harrison, D.; Heard, D. E.; Hunter, M. C.; Jacobs, P. J.; Jenkin, M. E.; Lee, J. D.; Lewis, A. C.; Pilling, M. J.; Saunders, S. M.; Seakins, P. W., OH and HO₂ radical chemistry in a forested region of north-western Greece. *Atmospheric Environment* 2001, 35, 4725-4737.
27. Ren, X. R.; Olson, J. R.; Crawford, J. H.; Brune, W. H.; Mao, J. Q.; Long, R. B.; Chen, Z.; Chen, G.; Avery, M. A.; Sachse, G. W.; Barrick, J. D.; Diskin, G. S.; Huey, L. G.; Fried, A.; Cohen, R. C.; Heikes, B.; Wennberg, P. O.; Singh, H. B.; Blake, D. R.; Shetter, R. E., HO_x chemistry during INTEX-A 2004: Observation, model calculation, and comparison with previous studies. *Journal of Geophysical Research-Atmospheres* 2008, 113.
28. Lelieveld, J.; Butler, T. M.; Crowley, J. N.; Dillon, T. J.; Fischer, H.; Ganzeveld, L.; Harder, H.; Lawrence, M. G.; Martinez, M.; Taraborrelli, D.; Williams, J., Atmospheric oxidation capacity sustained by a tropical forest. *Nature* 2008, 452, 737-740.
29. Kubistin, D.; Harder, H.; Martinez, M.; Rudolf, M.; Sander, R.; Bozem, H.; Eerdeken, G.; Fischer, H.; Gurk, C.; Klüpfel, T., Hydroxyl radicals in the tropical troposphere over the Suriname rainforest: comparison of measurements with the box model MECCA. *Atmospheric Chemistry and Physics* 2010, 10, 9705-9728.
30. Stone, D.; Evans, M. J.; Edwards, P. M.; Commane, R.; Ingham, T.; Rickard, A. R.; Brookes, D. M.; Hopkins, J.; Leigh, R. J.; Lewis, A. C.; Monks, P. S.; Oram, D.; Reeves, C. E.; Stewart, D.; Heard, D. E., Isoprene oxidation mechanisms: measurements and modelling of OH and HO₂ over a South-East Asian tropical rainforest during the OP3 field campaign. *Atmospheric Chemistry and Physics* 2011, 11, 6749-6771.
31. Whalley, L. K.; Edwards, P. M.; Furneaux, K. L.; Goddard, A.; Ingham, T.; Evans, M. J.; Stone, D.; Hopkins, J. R.; Jones, C. E.; Karunaharan, A.; Lee, J. D.; Lewis, A. C.; Monks, P. S.; Moller, S. J.; Heard, D. E., Quantifying the magnitude of a missing hydroxyl radical source in a tropical rainforest. *Atmospheric Chemistry and Physics* 2011, 11, 7223-7233.
32. Mao, J.; Ren, X.; Zhang, L.; Van Duin, D.; Cohen, R.; Park, J.-H.; Goldstein, A.; Paulot, F.; Beaver, M.; Crouse, J., Insights into hydroxyl measurements and atmospheric oxidation in a California forest. *Atmospheric Chemistry and Physics* 2012, 12, 8009-8020.

33. MacDonald, S. M.; Oetjen, H.; Mahajan, A. S.; Whalley, L. K.; Edwards, P. M.; Heard, D. E.; Jones, C. E.; Plane, J. M. C., DOAS measurements of formaldehyde and glyoxal above a south-east Asian tropical rainforest. *Atmospheric Chemistry and Physics* 2012, 12, 5949-5962.
34. Jenkin, M. E.; Hurley, M. D.; Wallington, T. J., Investigation of the radical product channel of the $\text{CH}_3\text{C}(\text{O})\text{CH}_2\text{O}_2 + \text{HO}_2$ reaction in the gas phase. *Physical Chemistry Chemical Physics* 2008, 10, 4274-4280.
35. Jenkin, M. E.; Hurley, M. D.; Wallington, T. J., Investigation of the radical product channel of the $\text{CH}_3\text{C}(\text{O})\text{O}_2 + \text{HO}_2$ reaction in the gas phase. *Physical Chemistry Chemical Physics* 2007, 9, 3149-3162.
36. Jenkin, M. E.; Hurley, M. A.; Wallington, T. J., Investigation of the Radical Product Channel of the $\text{CH}_3\text{OCH}_2\text{O}_2 + \text{HO}_2$ Reaction in the Gas Phase. *Journal of Physical Chemistry A* 2010, 114, 408-416.
37. Hasson, A. S.; Tyndall, G. S.; Orlando, J. J., A product yield study of the reaction of HO_2 radicals with ethyl peroxy ($\text{C}_2\text{H}_5\text{O}_2$), acetyl peroxy ($\text{CH}_3\text{C}(\text{O})\text{O}_2$), and acetonyl peroxy ($\text{CH}_3\text{C}(\text{O})\text{CH}_2\text{O}_2$) radicals. *Journal of Physical Chemistry A* 2004, 108, 5979-5989.
38. Paulot, F.; Crouse, J. D.; Kjaergaard, H. G.; Kurten, A.; St Clair, J. M.; Seinfeld, J. H.; Wennberg, P. O., Unexpected Epoxide Formation in the Gas-Phase Photooxidation of Isoprene. *Science* 2009, 325, 730-733.
39. da Silva, G.; Graham, C.; Wang, Z. F., Unimolecular beta-Hydroxyperoxy Radical Decomposition with OH Recycling in the Photochemical Oxidation of Isoprene. *Environmental Science & Technology* 2010, 44, 250-256.
40. Peeters, J.; Nguyen, T. L.; Vereecken, L., HOx radical regeneration in the oxidation of isoprene. *Physical Chemistry Chemical Physics* 2009, 11, 5935-5939.
41. Peeters, J.; Muller, J. F., HOx radical regeneration in isoprene oxidation via peroxy radical isomerisations. II: experimental evidence and global impact. *Physical Chemistry Chemical Physics* 2010, 12, 14227-14235.
42. Peeters, J.; Son Vinh, N.; Muller, J.-F.; Thanh Lam, N., Hydroxyl radical regeneration in isoprene oxidation: The Leuven isoprene mechanism. *Abstracts of Papers of the American Chemical Society* 2012, 244.
43. Bardwell, M. W.; Bacak, A.; Raventos, M. T.; Percival, C. J.; Sanchez-Reyna, G.; Shallcross, D. E., Kinetics of the $\text{HO}_2 + \text{NO}$ reaction: A temperature and pressure dependence study using chemical ionisation mass spectrometry. *Physical Chemistry Chemical Physics* 2003, 5, 2381-2385.
44. Herndon, S. C.; Villalta, P. W.; Nelson, D. D.; Jayne, J. T.; Zahniser, M. S., Rate constant measurements for the reaction of HO_2 with O_3 from 200 to 300 K using a turbulent flow reactor. *The Journal of Physical Chemistry A* 2001, 105, 1583-1591.
45. Lewin, A. G.; Johnson, D.; Price, D. W.; Marston, G., Aspects of the kinetics and mechanism of the gas-phase reactions of ozone with conjugated dienes. *Physical chemistry chemical physics* 2001, 3, 1253-1261.
46. Lee, M.; Heikes, B. G.; O'Sullivan, D. W., Hydrogen peroxide and organic hydroperoxide in the troposphere: a review. *Atmospheric Environment* 2000, 34, 3475-3494.
47. Stavrou, T.; Peeters, J.; Muller, J. F., Improved global modelling of HOx recycling in isoprene oxidation: evaluation against the GABRIEL and INTEX-A aircraft campaign measurements. *Atmospheric Chemistry and Physics* 2010, 10, 9863-9878.
48. Hofzumahaus, A.; Rohrer, F.; Lu, K.; Bohn, B.; Brauers, T.; Chang, C.-C.; Fuchs, H.; Holland, F.; Kita, K.; Kondo, Y., Amplified trace gas removal in the troposphere. *science* 2009, 324, 1702-1704.
49. da Silva, G., Hydroxyl radical regeneration in the photochemical oxidation of glyoxal: kinetics and mechanism of the $\text{HC}(\text{O})\text{CO} + \text{O}_2$ reaction. *Physical Chemistry Chemical Physics* 2010, 12, 6698-6705.
50. Shannon, R. J.; Taylor, S.; Goddard, A.; Blitz, M. A.; Heard, D. E., Observation of a large negative temperature dependence for rate coefficients of reactions of OH with oxygenated volatile organic compounds studied at 86-112 K. *Physical Chemistry Chemical Physics* 2010, 12, 13511-13514.

51. Shannon, R. J.; Blitz, M. A.; Goddard, A.; Heard, D. E., Accelerated chemistry in the reaction between the hydroxyl radical and methanol at interstellar temperatures facilitated by tunnelling. *Nature chemistry* 2013.
52. Shannon, R. J.; Caravan, R. L.; Blitz, M.; Heard, D. E., A combined experimental and theoretical study of reactions between the hydroxyl radical and oxygenated hydrocarbons relevant to astrochemical environments. *Physical Chemistry Chemical Physics* 2014, 16, 3466-3478.
53. Gómez Martín, J.; Caravan, R. L.; Blitz, M. A.; Heard, D. E.; Plane, J. M. C., Low Temperature Kinetics of the $\text{CH}_3\text{OH} + \text{OH}$ Reaction. *The Journal of Physical Chemistry A* 2014, 118, 2693-2701.
54. Pelzer, H.; Wigner, E., The speed constants of the exchange reactions. *Z Phys Chem B* 1932, 15, 445.
55. Eyring, H., The activated complex in chemical reactions. *The Journal of Chemical Physics* 1935, 3, 107-115.
56. Eyring, H., The activated complex and the absolute rate of chemical reactions. *Chemical Reviews* 1935, 17, 65-77.
57. Pechukas, P., Transition-State Theory. *Annual Review of Physical Chemistry* 1981, 32, 159-177.
58. Truhlar, D. G.; Garrett, B. C., Variational transition state theory. *Annual Review of Physical Chemistry* 1984, 35, 159-189.
59. Rice, O. K.; Ramsperger, H. C., Theories of unimolecular gas reactions at low pressures. *Journal of the American Chemical Society* 1927, 49, 1617-1629.
60. Rice, O. K.; Ramsperger, H. C., Theories of unimolecular gas reactions at low pressures II. *Journal of the American Chemical Society* 1928, 50, 617-620.
61. Kassel, L. S., Studies in homogeneous gas reactions I. *Journal of Physical Chemistry* 1928, 32, 225-242.
62. Marcus, R. A., Unimolecular Dissociations and Free Radical Recombination Reactions. *Journal of Chemical Physics* 1952, 20, 359-364.
63. Glowacki, D. R.; Liang, C. H.; Morley, C.; Pilling, M. J.; Robertson, S. H., MESMER: An Open-Source Master Equation Solver for Multi-Energy Well Reactions. *Journal of Physical Chemistry A* 2012, 116, 9545-9560.
64. Robinson, P. J.; Holbrook, K. A., *Unimolecular reactions*. Wiley-Interscience New York: 1972.
65. Carr, S. A.; Glowacki, D. R.; Liang, C. H.; Baeza-Romero, M. T.; Blitz, M. A.; Pilling, M. J.; Seakins, P. W., Experimental and Modeling Studies of the Pressure and Temperature Dependences of the Kinetics and the OH Yields in the Acetyl + O_2 Reaction. *Journal of Physical Chemistry A* 2011, 115, 1069-1085.
66. Carr, S. A.; Still, T. J.; Blitz, M. A.; Eskola, A. J.; Pilling, M. J.; Seakins, P. W.; Shannon, R. J.; Wang, B.; Robertson, S. H., Experimental and Theoretical Study of the Kinetics and Mechanism of the Reaction of OH Radicals with Dimethyl Ether. *Journal of Physical Chemistry A* 2013, 117, 11142-11154.
67. Romero, M. T. B.; Blitz, M. A.; Heard, D. E.; Pilling, M. J.; Price, B.; Seakins, P. W., OH formation from the $\text{C}_2\text{H}_5\text{CO} + \text{O}_2$ reaction: An experimental marker for the propionyl radical. *Chemical Physics Letters* 2005, 408, 232-236.
68. Eskola, A. J.; Carr, S. A.; Blitz, M. A.; Pilling, M. J.; Seakins, P. W., Kinetics and yields of OH radical from the $\text{CH}_3\text{OCH}_2 + \text{O}_2$ reaction using a new photolytic source. *Chemical Physics Letters* 2010, 487, 45-50.
69. Eskola, A. J.; Carr, S. A.; Shannon, R.; Wang, B.-S.; Blitz, M. A.; Pilling, M. J.; Seakins, P.; Robertson, S. H., Analysis of the Kinetics and Yields of OH Radical from the $\text{CH}_3\text{OCH}_2 + \text{O}_2$ Reaction in the Temperature Range 195–650 K: an Experimental and Computational Study. *The Journal of Physical Chemistry A* 2014.
70. Olzmann, M., On the role of bimolecular reactions in chemical activation systems. *Physical Chemistry Chemical Physics* 2002, 4, 3614-3618.

71. Polanyi, J. C., Some concepts in reaction dynamics *Science* 1987, 236, 680-690.
72. Baeza-Romero, M. T.; Glowacki, D. R.; Blitz, M. A.; Heard, D. E.; Pilling, M. J.; Rickard, A. R.; Seakins, P. W., A combined experimental and theoretical study of the reaction between methylglyoxal and OH/OD radical: OH regeneration. *Physical Chemistry Chemical Physics* 2007, 9, 4114-4128.

Chapter 2 Experimental Techniques

This chapter begins by introducing the laser flash photolysis, laser induced fluorescence (LFP-LIF) technique, used throughout this thesis, for quantifying gas-phase reaction rate coefficients. A brief introduction to the principles of laser action and the ways in which laser light has transformed experimental gas-phase kinetic studies is provided. Some alternative techniques for detecting short lived radical species and quantifying rate coefficients are also discussed. The final section of this chapter provides details of the specific apparatus and method of data collection and analysis used during this work.

2.1 Laser Flash Photolysis - Laser Induced Fluorescence (LFP-LIF)

Many of the elementary reactions which drive atmospheric chemistry involve extremely short lived radical and atomic species. Meaningful kinetic experiments require sensitive detection techniques and accurate resolution over microsecond or shorter timescales. The development of laser, optical and electronic technologies have led to significant advances in the field of chemical kinetics. Laser light has several properties which complement its use as an experimental radiation source. The high degree of monochromaticity associated with laser radiation allows specific electronic and rovibrational states to be probed selectively; furthermore, the appropriate laser medium can provide light with sufficient energy to cleave chemical bonds and initiate chemistry with extremely accurate time resolution.¹ Kinetic studies involving radical species often couple pulsed laser flash photolysis with laser induced fluorescence (LFP – LIF) as a means of initiating chemistry and monitoring radical concentration profiles with accurate resolution over short timescales. The flash photolysis technique of initiating chemistry using a short pulse of intense light was pioneered by R. G. W. Norrish and G. Porter in Cambridge during the late 1940s.² This method extended the experimental timescale resolution from the millisecond to the microsecond range, and earned the co-workers the Nobel Prize for Chemistry in 1967. The flash lamps used as the light source in early flash photolysis experiments have been in the main superseded by short pulse duration lasers that allow experimental measurements

on the sub-nanosecond timescale. The improved time resolution is not the only advantage of using pulsed laser radiation as the light source in flash photolysis experiments. High pulse energies mean a significant quantity of radical species can be generated using low experimental precursor concentrations, helping limit the contribution made by precursor reactions to the overall chemistry inside the reaction cell. Operating lasers at high pulse repetition rates allow data to be collected quickly. The data acquisition rate is limited only by the requirement that a fresh sample of gas be present in the cell for each photolysis laser pulse, so as to avoid the effects of secondary chemistry.

The LFP – LIF method involves premixing the reagent and a suitable radical precursor before the mixture is flowed into a reaction cell at the desired experimental pressure. A photolysis laser pulse is fired through the cell generating radical species *in situ* and defining the experimental time, t_0 . At a preset time following the photolysis laser pulse, a dye laser pulse is fired through the cell to electronically excite the radical. The excited electron can return to the ground state with conserved multiplicity via emission of a photon (fluorescence). The fluorescent photon can either oscillate at the same frequency as the light absorbed during the transition between electronic states (on-resonant), or at a lower frequency (off-resonant) following collisional stabilisation within the excited electronic state. The fluorescent emission can be monitored using a photomultiplier tube (PMT). As the fluorescence signal is proportional to the radical concentration, a radical concentration profile can be built as a function of time by varying the delay time between the photolysis and probe laser pulses. A schematic diagram of LFP-LIF apparatus setup for monitoring OH radicals in the presence of acetylene, C_2H_2 , is provided in Figure 1.

The UV-visible LIF technique is often used to detect short-lived radical and atomic species of atmospheric importance; such as OH (chapters 3 – 6 of this thesis), HCO (chapter 7 of this thesis), Cl, NO, NO_3 , $O(^1D)$.³⁻¹¹ A typical experimental OH radical decay trace in the presence of C_2H_2 is provided in Figure 2.

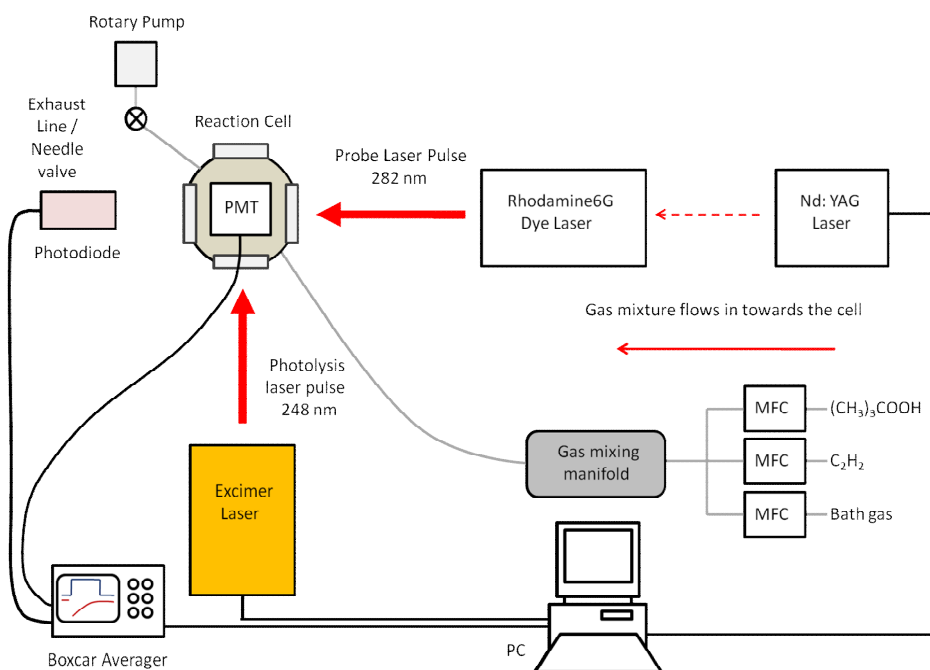


Figure 1: Schematic diagram of laser flash photolysis, laser induced fluorescence (LFP-LIF) apparatus for the study of OH radicals with acetylene, C_2H_2 .

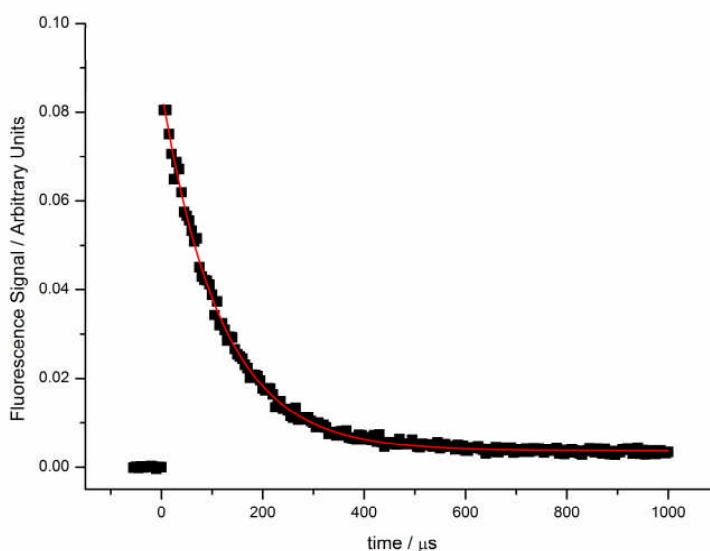


Figure 2: Typical OH decay trace measured in the presence of 2.12×10^{16} molecules cm^{-3} of C_2H_2 at 295 K under 25 Torr of N_2 using the LFP-LIF technique.

The ability to tune dye laser emission mean these systems offer extreme selectivity when used as probe light sources, as a wavelength corresponding to a transition between specific rovibrational states within the electronic bands of individual species can be generated. The full range of commercial dyes offer an output range of 320 nm – 1 μm , although the conversion efficiency depends on the specific dye and pump light source. This wavelength range, coupled with conventional frequency conversion techniques, provide the probe light required to monitor a variety of transient atmospheric species. Moreover, the dye can be replaced with another type in order to generate light of a different wavelength without the inconvenience of replacing the laser; although this process may also require changing other optical components of the laser.

Low radical concentration ($[R] < 1 \times 10^{12}$ molecule cm^{-3}) are often required during kinetic studies in order to simplify the chemistry, maintain *pseudo-first-order* conditions, and avoid unwanted radical-radical chemistry. Consequently, sensitive detection techniques are necessary to monitor time resolved radical concentration profiles. Fortunately, the defined spatial profile of laser light can be exploited to improve the sensitivity of radical detection. Conventionally the photolysis and dye laser beams enter the reaction cell at right angles to one another; with the PMT housed above the cell perpendicular to both laser beams. Fluorescent emission occurs in random directions and this orthogonal arrangement helps distinguish the fluorescence signal from the background scattered probe light. The signal-to-noise ratio can be further increased by monitoring the off-resonant fluorescence through an interference filter and averaging the signal over several photolysis laser pulses; this approach allows the signal observed using fluorescent techniques to be measured relative to a near zero background.

2.2 The Principles of Laser Action

2.2.1 Absorption and Emission of Radiation

Quantum theory stipulates that atoms and molecules possess distinct sets of energy levels. The relative populations of these states at equilibrium can be described

mathematically using the Maxwell-Boltzmann distribution. For a non-degenerate system at absolute temperature, T :

$$\frac{N_n}{N_m} = \exp(-\Delta E/k_B T) \quad (E1)$$

where N_n and N_m are the populations of the higher and lower energy states, respectively; ΔE is the difference in energy between the two states, and k_B is the Boltzmann constant, $1.381 \times 10^{-23} \text{ J K}^{-1}$. Light also exists in discrete energy quanta known as photons. The energy of a photon, E , is proportional to its frequency, ν , by Planck's constant, h ($E = h\nu$). When a photon of light is absorbed by an atom or molecule the energy of the photon can be transferred and result in excitation, provided the energy of the photon exactly matches the energy difference between the lower and excited atomic or molecular quantum states involved in the transition, $\Delta E = h\nu$. This process is known as *stimulated absorption*. Einstein derived a mathematical expression for the rate of stimulated absorption between lower and excited states m and n , respectively, as follows:

$$\text{Stimulated Absorption transition rate} = N_m \rho_\nu B_{mn} \quad (E2)$$

where ρ_ν is the photon energy density at frequency ν , and the constant of proportionality B_{mn} is the Einstein coefficient of stimulated absorption from state m to n . The subsequent relaxation from the excited state n to the lower energy state m can be accompanied by spontaneous emission of a photon of frequency ν . Spontaneous emission occurs in random directions at a rate proportional to the population of the excited state n :

$$\text{Spontaneous Emission transition rate} = N_n A_{nm} \quad (E3)$$

where A_{nm} is the Einstein coefficient of spontaneous emission from state n to m . Alternatively, species populating the excited state n can return to the lower energy state m when a photon of frequency ν stimulates the emission of a second photon of identical frequency to that initiating the transition. This process requires an external photon to initiate radiation and is therefore referred to as *stimulated emission*. The stimulated emission transition rate is proportional to the population of the excited state and the photon energy density at frequency ν , as follows:

Consequently the probability of stimulated emission decreases significantly as light frequencies increase; due to the onset of spontaneous emission. The rate of change in photon density, N_v , along the laser axis can be closely approximated by the difference between the rates of stimulated emission and absorption (equations E4 and E2); as spontaneous emission radiates in random directions, its contribution to light travelling along the laser axis can be considered negligible.

$$\frac{dN_v}{dt} = (N_n - N_m) B \rho_v \quad (E6)$$

If we consider a beam of laser light, travelling through a cell containing a laser medium. As light passes through the medium its speed will slow to velocity c' :

$$c' = \frac{c}{\eta} \quad (E7)$$

where c is the speed of light in a vacuum, and η is the refractive index of the medium. If we consider the intensity of light propagating along the laser axis in terms of irradiance, I_v , defined as the light energy of frequency ν , per unit cross sectional area, per second (J/m^2s), then I_v may be expressed in terms of either the photon energy density, ρ_v or the photon density, N_v at frequency ν as follows:

$$I_v = \rho_v c' \quad (E8)$$

$$I_v = N_v h \nu c' \quad (E9)$$

Rearranging equation E9 for N_v , and differentiating with respect to time, t provides an alternative expression for the rate of change in N_v :

$$\frac{dN_v}{dt} = \left(\frac{1}{h \nu c'} \right) \frac{dI_v}{dt} \quad (E10)$$

Equating the right hand sides of equations E6 and E10, and expressing ρ_v in terms of I_v and c' , it can be shown that the rate of change in I_v is equal to:

$$\frac{dI_v}{dt} = (N_n - N_m) B I_v h \nu \quad (E11)$$

It follows that an exponential increase in irradiance, I_ν is allowed only when the population of the excited state, N_n , exceeds that of the lower energy state, N_m . This non-equilibrium behaviour is known as a *population inversion*, and is essential in order to achieve laser action. Energy is required to perturb the system from equilibrium, in a process typically referred to as *pumping*.

2.2.2 Population inversion

A population inversion is unattainable with the simple two level model used so far to describe the interaction of radiation with a laser medium. Optically pumping the system will promote species from the lower to the excited state, but stimulated absorption will eventually reach equilibrium with the relaxation processes spontaneous and stimulated emission. Directly pumping from lower to excited states can potentially result in equally populated lower and excited states, but not allow the non-equilibrium conditions required for laser action. A population inversion requires indirect means of populating the excited state involved in the lasing transition, which in turn requires additional energy levels. The simplest example is provided by a three-level laser system. Figure 4 illustrates the energy levels and transitions involved in a three-level laser system. Using an appropriate pumping mechanism to excite from the ground state (E_0) to the second excited state (E_2), subsequent relaxation populates the first excited (E_1) state. Provided the rate of laser emission is slow compared to relaxation from the E_2 to the E_1 state, a population inversion forms between the E_1 and E_0 states involved in lasing, and is maintained by further pump transitions. One of the problems with a three-level laser system is that the lasing transition acts to populate the ground state, and therefore disrupts the population inversion. This problem can be overcome by introducing a fourth state to the system (Figure 4). In a four-level laser system the lasing transition occurs not between an excited state and the ground state, but between two excited states. Provided relaxation from the lower of the two states involved in lasing and the ground state is fast, a population inversion between the lasing states is retained. A range of substances have been shown to provide the non-equilibrium conditions demanded by laser action, and are collectively referred to as the *active medium*.

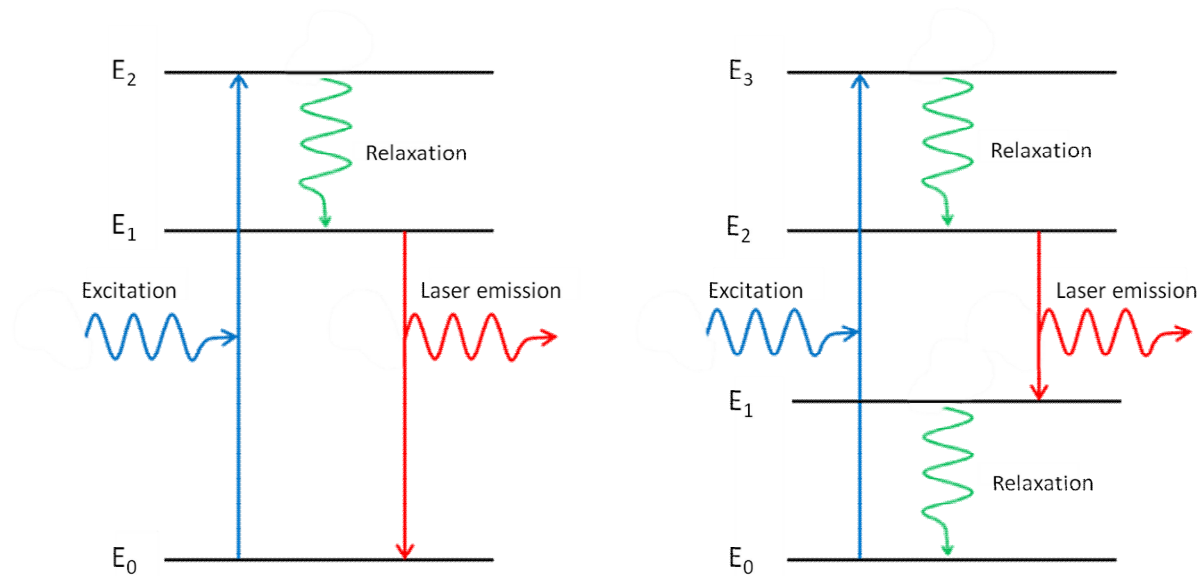


Figure 4: Schematic diagram of the energy levels and transitions involved in a three and four level laser system.

2.2.3 Optical Cavity

Optically pumping the active medium has been shown to provide a population inversion, and the onset of spontaneous emission between lasing states provides photons at the frequency required for stimulated emission. However, the rate at which light intensity is amplified is proportional to the initial intensity (equation E11), which, when relying on spontaneous emission, is not expected to be very great; therefore an optical cavity is employed to improve the light intensity traversing the active medium (Figure 5). This can be achieved by placing parallel mirrors at either end of the active medium, so that light travelling along the axis perpendicular to the mirrors is reflected back and forth indefinitely, growing in intensity with each pass. In practice only one of the end-mirrors is fully reflective; the other is partially transmissive in order to allow laser output from the resonator.

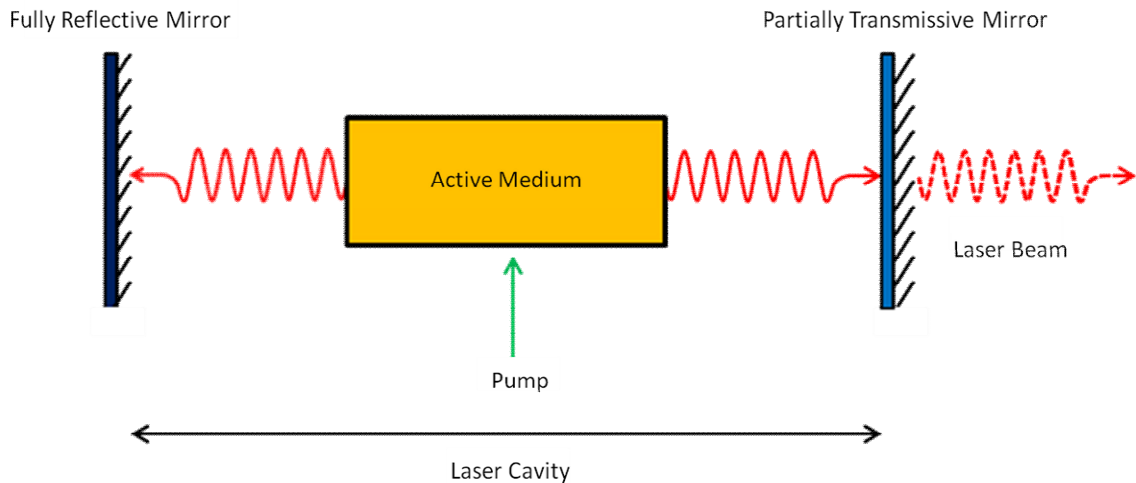


Figure 5: Schematic diagram of an optically pumped laser cavity.

Various chemical media have proven suitable for generating laser light, and encompass solid, liquid and gaseous phases. A range of laser systems were used to generate the radiation required during the experimental work presented in this thesis; specifically, a KrF (Lambda Physik, Compex) and a XeCl (Lambda Physik, LPX 100) excimer laser, a Nd: YAG laser (Spectra-Physics, Quanta-Ray GCR 100-series), a dye laser (Spectra-Physics, Quanta Ray PDL-3) operating on either Rhodamine6G or pyromethene 597, and a second dye laser (Lambda Physik, FL 2002) operating on Coumarin 307 dye.

2.2.4 Excimer or Exciplex Laser (Lambda Physik, Compex or LPX 100)

Exciplex lasers rely on an electronically excited diatomic complex, known as an *exciplex*, to generate laser light; though they are often referred to as Excimer lasers. The complex must only exist as a stable bound species when in the excited state; the ground state must be repulsive, with no significant potential energy minimum. Potential energy curves for the KrF states involved in laser action are illustrated in Figure 6.

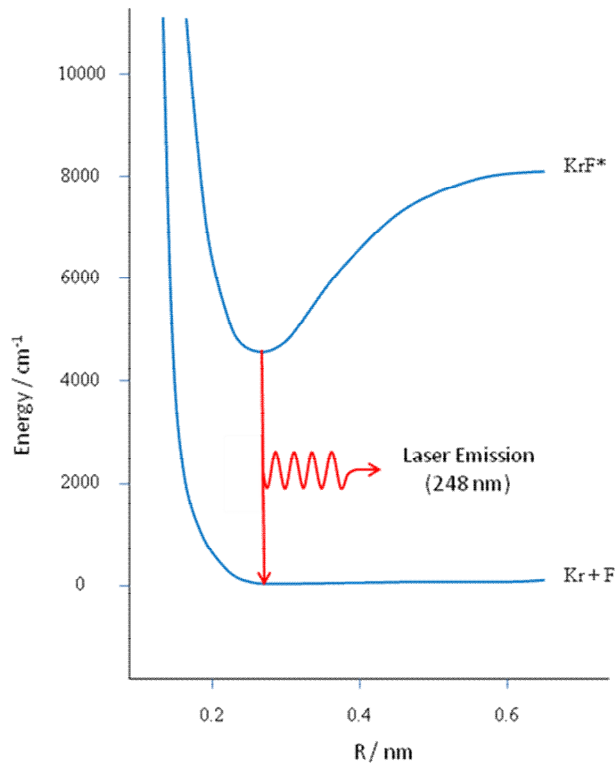


Figure 6: Schematic energy level diagram for the KrF laser.

The KrF excimer system consists of a gaseous mixture of krypton, fluorine and neon contained within a sealed cavity at a pressure of 2.5 – 3 Bar. An electrical discharge is used to generate krypton and fluoride ions, which react to form KrF* in accordance with the following reaction scheme:



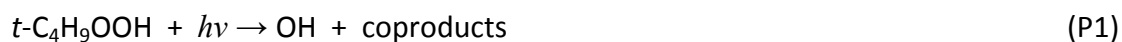
The electronically excited KrF* complex has a short lifetime of approximately 2.5 ns, and decays by photon emission to the ground state. The repulsive force operating between the atoms in the ground state cause the complex to rapidly dissociate to its constituent atoms within a few picoseconds. Consequently, the ground state never becomes significantly occupied and a population inversion exists between the ground and the higher energy excited states of the complex.

The excimer radiation is pulsed, and typically achieves pulse durations of 10 – 20 ns with repetition frequencies ranging from 1 to several hundred Hz. Excimer lasers can run on a variety of combinations of rare gas and halide to give different output wavelengths, the main gas mixtures and corresponding wavelengths and energies are listed in Table 1.

Exciplex	Wavelength / nm	Photon Energy / kJ mol ⁻¹
ArF	193	621
KrCl	222	540
KrF	248	483
XeCl	308	389
XeF	351	342

Table 1: Excimer laser wavelengths and energies

The photon energies generated using excimer lasers are comparable to typical bond dissociation energies (300 – 500 kJ mol⁻¹); absorption of a photon at these wavelengths can often result in chemical bond cleavage. Consequently, kinetic studies often use an excimer laser as photolytic light source to generate labile radical species from stable chemical precursors. A KrF excimer laser was used as photolytic light source in all the experimental work reported in this thesis, with the majority of the reaction systems investigated involving chemistry initiated through reaction with the OH radical. The OH radical was generated predominantly through the photolysis of *tertiary*-butyl hydroperoxide, *t*-C₄H₉OOH, at 248 nm (Photolysis P1), although alternative radical precursors were also used.



2.2.5 Nd: YAG laser (Spectra- Physics, Quanta-Ray GCR 100-series)

The Nd: YAG is a solid-state laser which uses neodymium ions embedded in a yttrium aluminium garnet crystal as lasing medium. The energy levels of the Nd^{3+} ions are split through interaction with the crystal field, allowing transitions between components of the ${}^4F_{3/2}$ and ${}^4I_{11/2}$ states forbidden in the free-state (Figure 7).

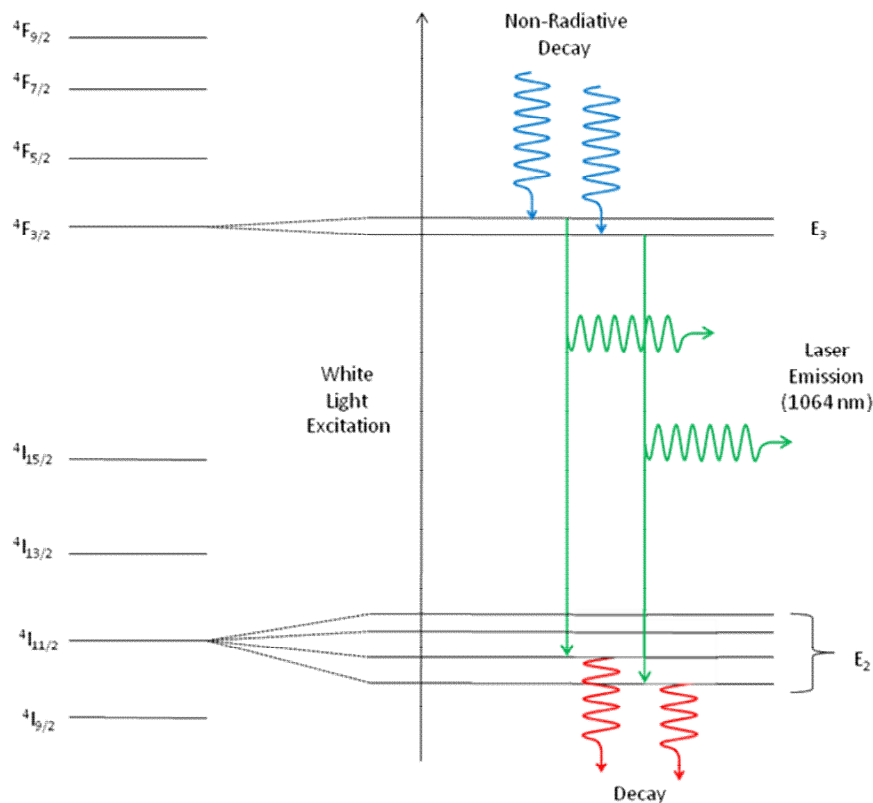


Figure 7: Schematic energy level diagram for a Nd: YAG laser.

A population inversion is achieved by optically pumping the Nd: YAG laser with high-pressure xenon flash lamps. The ${}^4F_{3/2}$ levels become populated from non-radiative decay from higher energy levels following excitation from the flash lamps. The ${}^4F_{3/2} \rightarrow {}^4I_{11/2}$ transition occurs with 1064 nm photon emission. Since the ${}^4I_{11/2}$ state is not the lowest lying energy level it rapidly decays to the ${}^4I_{9/2}$ ground state; it is this transition that maintains the population inversion between the ${}^4F_{3/2}$ and ${}^4I_{11/2}$ states involved in lasing.

The wavelength range accessible using conventional laser light sources can be greatly extended by exploiting a non-linear optical process known as *frequency doubling* or *second harmonic generation*. Two photons of frequency ν are absorbed by a non-linear media and one photon of frequency ν' is emitted. This concerted two photon process can only take place in crystalline material that lack a centre of symmetry, and a KDP (KH_2PO_4) doubling crystal is often used. The 1064 nm laser light generated by the Nd: YAG laser was frequency doubled to 532 nm, and then used to pump the Rhodamine6G (Pyromethene 597) dye used to generate OH (OD) probe radiation.

2.2.6 Q-Switching

When pumping the active medium of a laser, the population inversion will ultimately reach a steady-state, dependent on the pumping rate to, and decay rate from the upper and lower energy states involved in lasing. During this time, the laser beam grows until it reaches a saturation intensity; provided the gain is high enough to overcome cavity loss processes and the gain duration is long enough. For most solid-state lasers, including Nd: YAG lasers, the lifetime of the upper lasing state is longer than the time required for the population inversion to reach steady-state, consequently the laser output achieves its saturation intensity long before the population inversion has attained its maximum potential. However, a technique known as Q-switching allows the active medium to achieve the optimum population inversion before laser oscillation within the cavity; this process results in production of pulsed laser light with high pulse energies and short pulse durations. The Q-factor of a laser is proportional to the ratio of energy stored to the energy dissipated within the cavity per optical cycle; a high Q-factor corresponds to low energy loss per round-trip of radiation, while a low Q-factor signifies significant energy loss from the system per optical cycle. If a shutter is housed within the laser cavity that acts to increase the radiative loss within the cavity per cycle (low Q-factor), then a significant population inversion can be achieved within the active medium before the onset of stimulated emission. If light is then allowed to resonate within the cavity, the energy stored in the medium can be released as a single nanosecond pulse of highly intense light (high Q-factor). The term Q-switching refers to a process whereby the Q-factor of the laser cavity is first reduced and then rapidly

increased. The electro-optical shutter used during this work used a Pockels cell combined with a polarizer and quarter wave plate; a schematic diagram of how the Q-switch operates is presented in Figure 8. Light coming from the Nd: YAG crystal is horizontally polarized by the polarizer and then rotated to circularly polarized light by the quarter wave plate following the first pass. At zero volts the Pockels cell is transparent and the reflected light is converted to vertically polarized light following the second pass through the quarter wave plate, and subsequently reflected by the polarizer and no oscillation within the cavity occurs. When the maximum population inversion has built within the Nd³⁺ ions (~285 μs after the flash lamps fire) a voltage is applied to the Pockels cell. With voltage applied the Pockels cell add 45 degrees rotation with each pass, which combined with the quarter wave plate convert the initially horizontal beam to vertically and then back to horizontally polarized light. The horizontal light is transmitted by the polarizer allowing oscillation within the laser cavity.

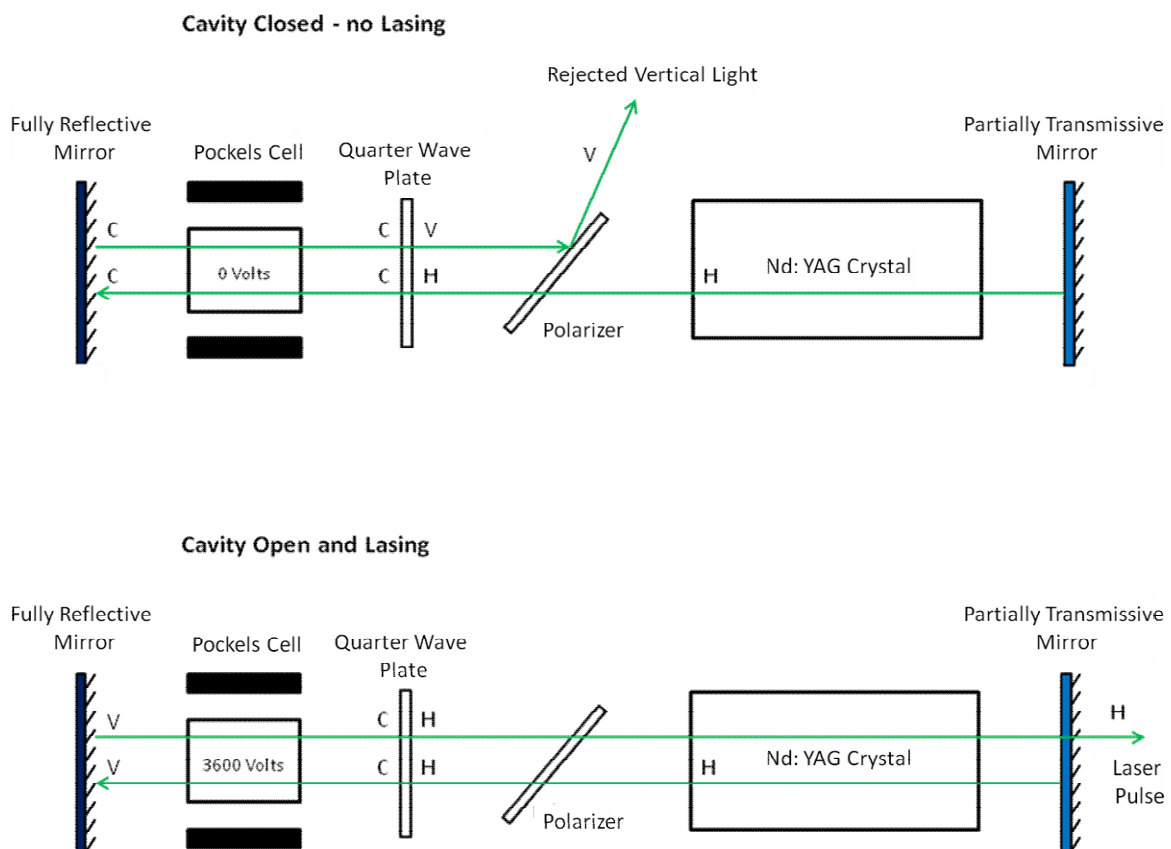


Figure 8: Schematic of the Q-switch used in the Nd: YAG cavity to enable short high power laser pulses; denoting horizontal (H), circular (C) and vertically (V) polarized light.

2.2.7 Dye Laser (Spectra-Physics, Quanta Ray PDL-3 and Lambda Physik, FL 2002)

Dye lasers use an organic dye as laser medium, usually dissolved in a suitable solvent such as water or an alcohol. Dye lasers can be used to provide tuneable laser radiation across a wavelength range of several 10 nm. Tuneable laser output is desirable for spectroscopic application as it allows selective excitation of specific ro-vibrational transitions of many chemical species. Many dyes have been used successfully to generate laser light and all share two common properties, a strong absorption band in the ultraviolet or visible spectral region, and a broad fluorescent spectrum at longer wavelengths. Typically, these conditions are satisfied by large, polyatomic, conjugated molecules with extensive electron delocalization and substantial vibrational modes of freedom. There are two sets of electronic energy levels within which excitation and relaxation can occur, referred to as the singlet and triplet energy manifold. In the singlet states the spin of the excited electron is antiparallel with the spin of the remaining molecule ($2S + 1 = 1$), while in the triplet states the spins are parallel ($2S + 1 = 3$). The energies of the extensive vibrational modes of these molecules become broadened and overlap in solution, such that an energy continuum exists for each electronic state. Electronic excitation can result in excitation from the ground singlet state continuum S_0 to the first excited singlet state S_1 . Subsequent rapid non-radiative decay to the lowest energy level of the S_1 continuum occurs within 20 ps; and precedes radiative transitions from the S_1 state to lower states within the S_0 continuum. Further decay within the S_0 continuum follow the radiative transition, and ensure a population inversion is maintained between the S_1 and S_0 states involved in lasing. In essence the dye laser represents a simple four-level system, though this simple system is complicated by competing processes (Figure 9); the most significant being *intersystem crossing*, whereby energy is transferred from the excited singlet state S_1 to the ground triplet state T_1 . The rate for this formally spin-forbidden transition is slow but significant, as it acts to disrupt the population inversion of the lasing states. The T_1 state can decay to the S_0 state by phosphorescent emission or non-radiative intersystem crossing; although both of these processes are also formally spin-forbidden and occur slowly. Alternatively, the T_1 state population may advance to higher energy states within the triplet manifold by absorbing light at the frequencies involved in lasing. The effects of *Intersystem crossing* can be limited by operating dye lasers in pulsed mode with pulse durations shorter than the time taken for

a significant population to build in the T_1 state. In addition to the processes described previously, the lasing transition must also compete with both non-radiative internal conversion between S_1 and S_0 states, and radiative excitation from the S_1 state to higher energy states within the singlet manifold. All competing processes act to reduce the laser efficiency. Furthermore, the heat released following non-radiative decay transitions can rapidly degrade the dye. Fortunately these problems can be significantly reduced by continuously circulating the dye through the amplified region of the laser cavity. This process not only delivers singlet state molecules and purge triplet state molecules from the beam path, but also allows effective cooling to take place.

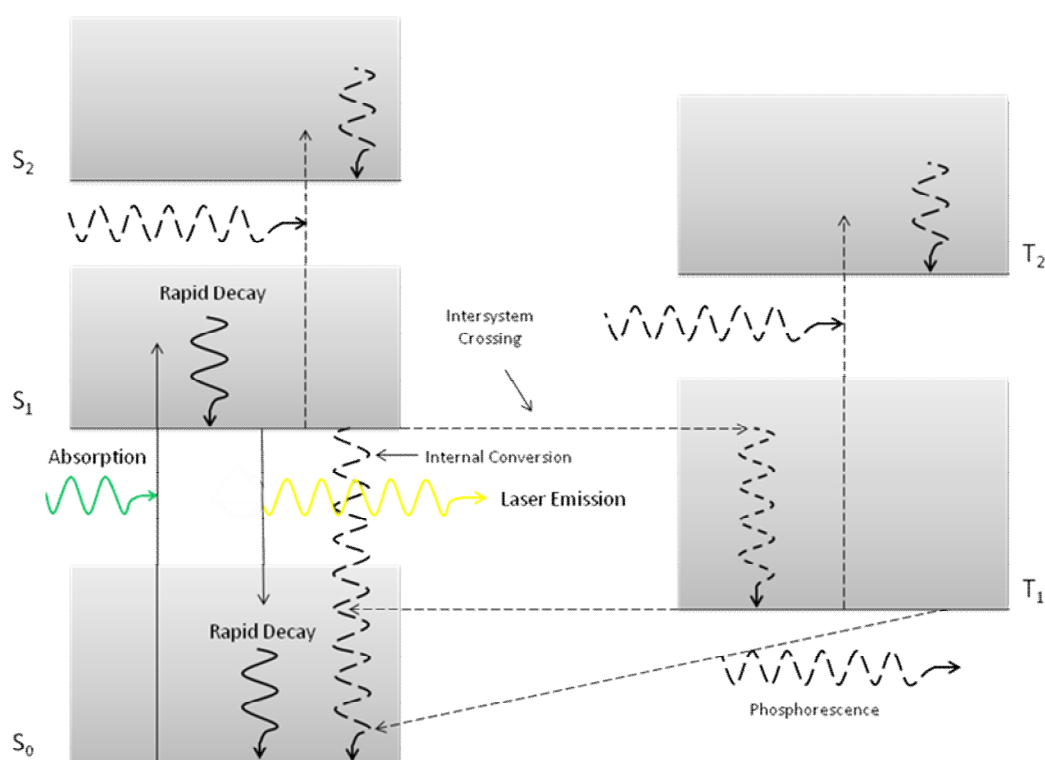


Figure 9: Jablonski diagram for a laser dye. The solid vertical arrows show the transitions involved in laser action, and the dashed arrows illustrate some of the competing transitions.

The effect of solvent interactions on the energy levels of the singlet states of the dye molecule result in fluorescent emission over a range of wavelengths. Monochromatic

tunable laser emission requires dispersive optics within the laser cavity, such as a diffraction grating or etalon. The experimental set up of the Quanta Ray PDL – 3 laser used during this work is presented in Figure 10. A diffraction grating was used to tune the output of the oscillator. In order to maximise the effect of the grating and minimise the wavelength output bandwidth, a prism telescope is used to expand the incident beam across the grating. The output of the oscillator is then amplified by a subsequent dye cell, such that the optical loss in the dispersive oscillator has minimal effect on the overall laser power. The doubled output of a pulsed Nd: YAG laser can be used to stimulate both the oscillator and amplifier dye cells by including a beam splitter; only 10 to 20 percent of the pump laser light is used to drive the oscillator, the remainder is used to pump the amplifier cell.

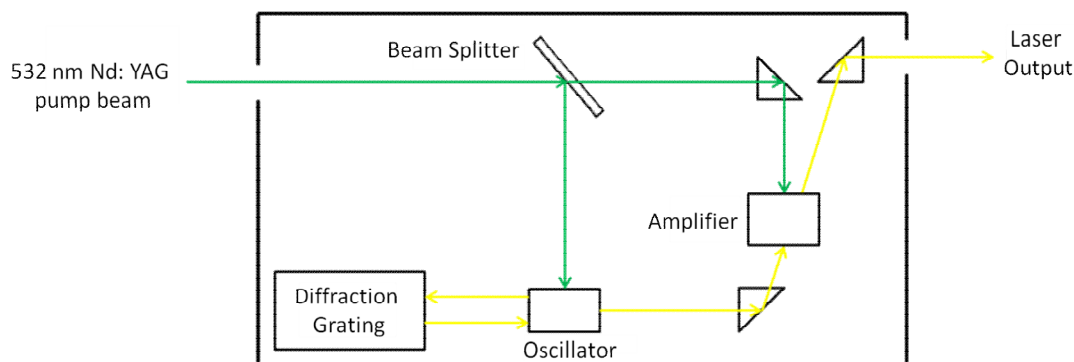


Figure 10: Set up of the Quanta Ray PDL-3 dye laser

A solution of Rhodamine6G in methanol pumped using the secondary harmonics of a ND: YAG laser is often used as it offers both high efficiency (~ 20 %) and a broad tuning range (570 – 660 nm). The Quanta-Ray PDL – 3 used during the work presented in this thesis operated on either Rhodamine6G or pyrromethene 597 dyes; the dye laser output was doubled to ~282 and ~287 nm using a KDP crystal and used to probe OH and OD radicals, respectively. The Lambda Physik, FL 2002 laser used during this work operated on Coumarin 307 dye; the doubled output allowed electronic excitation of HCO radicals at ~258 nm.

2.3 OH Spectroscopy

The majority of experimental work presented in this thesis involved monitoring the OH radical via off-resonance laser induced fluorescence (LIF), with excitation taking place at ~ 282 nm ($A^2\Sigma(v=1) \leftarrow X^2\Pi(v=0), Q_1(1)$) with the fluorescence being observed at ~ 308 nm. Schemes detailing the pertinent transitions involved in on- and off-resonance OH fluorescence are presented in Figure 11.

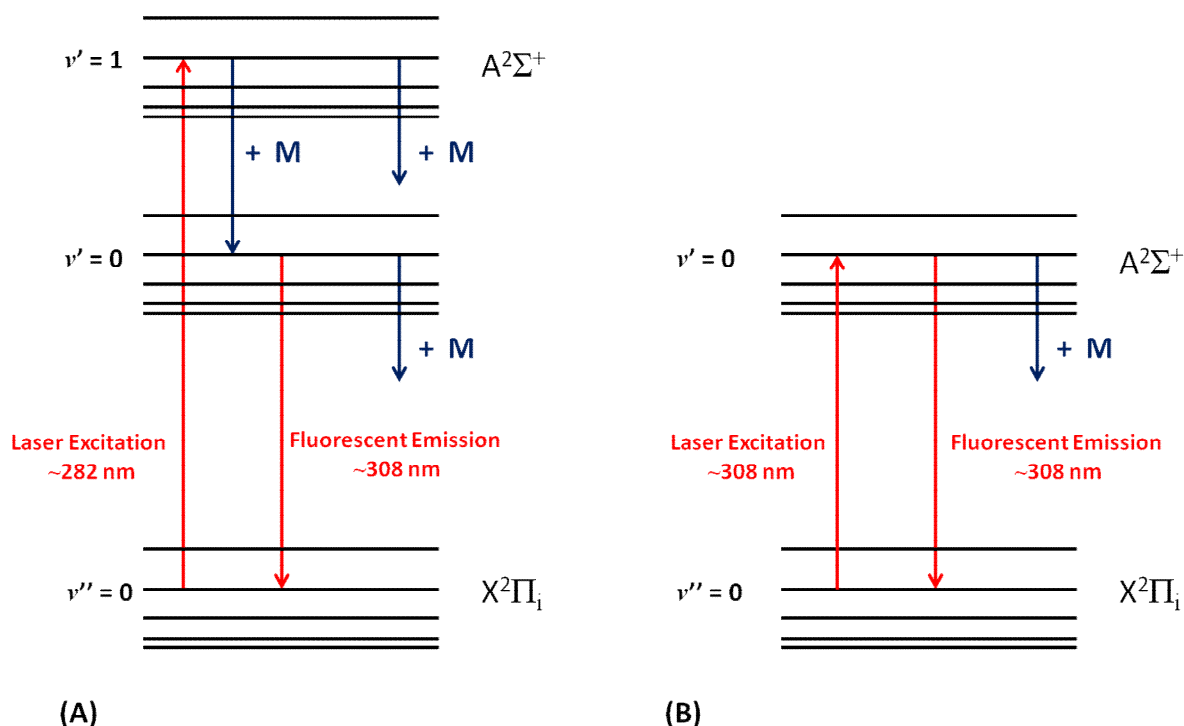


Figure 11: Schematic energy level diagram showing the transitions relevant to off- (A) and on-resonant (B) fluorescence of the OH radical following the A – X electronic transition. Collisional energy transfer processes are presented in blue.

2.4 Detection Technique – Photomultiplier Tube

A photomultiplier tube (PMT) is an instrument used to sensitively detect light or fluorescence by significantly amplifying the incident signal. The PMT consists of a photosensitive cathode, several dynodes and an anode, housed inside a glass vacuum tube. Incident photons strike the photocathode which emits electrons in accordance with the photoelectric effect. The electrons are then directed towards a series of dynodes by the

focusing electrode. Each dynode in the series is held at slightly higher voltage than the electrode preceding it. As the incident electrons move towards the first dynode they are accelerated by the electric field. Upon striking the dynode, more low energy electrons are emitted by secondary emission, which in turn are then accelerated towards the second dynode. A positive feedback operates, generating large numbers of electrons which eventually reach the anode plate, resulting in a large and easily detected surge in current. The pulse current signal is typically detected within a nanosecond of the photon striking the photocathode using this apparatus. A schematic diagram of the inner workings of a PMT is provided below:

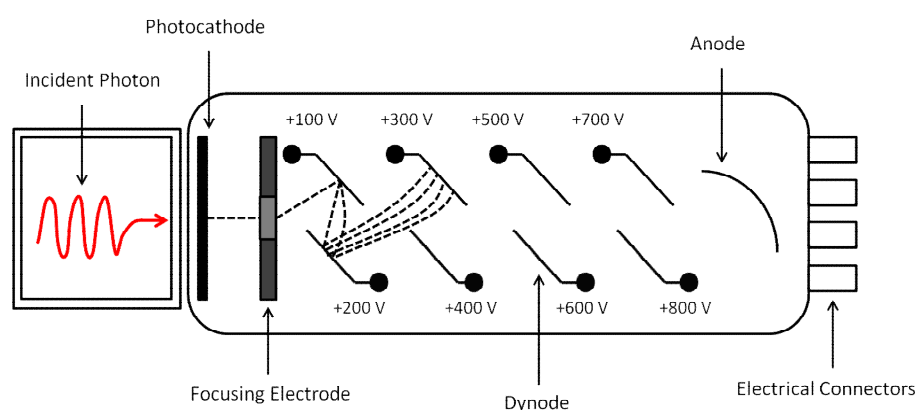


Figure 12: Schematic diagram of a photomultiplier tube (PMT).

2.5 Alternative Detection Techniques

Excimer lasers are used extensively as the photolysis light source in flash photolysis experiments, owing to their short pulse duration, ability to operate at high repetition rates, defined spatial profile, and associated photon energies. However, once a transient species of interest has been generated, a variety of different techniques can be used for detection. The following section discusses the merits and shortcomings of some alternative radical detection techniques.

2.5.1 Ultraviolet and Infrared Absorption

Absorption techniques provide an important means of detecting short lived radical species. Broadband lamps can be used to generate light at a frequency absorbed by the reactant radical. The light is passed through the reaction cell, and a monochromator is used to direct only light of frequency pertinent to radical absorption to a PMT for detection. An excimer laser can be used to generate radicals in the cell. After the excimer laser fires the light intensity detected by the PMT will immediately decrease owing to absorption from the radicals formed, then the signal starts to build as radicals in the cell are lost through reaction. The intensity of incident and absorbed light are related by the Beer-Lambert law:

$$I_{\text{abs}} = I_0(1 - \exp(-\sigma cl)) \quad (\text{E12})$$

where I_{abs} is the measured change in light intensity, I_0 is the incident light intensity, σ is the wavelength specific radical absorption cross section, c is the radical concentration and l is the optical path length. If the exponent term in equation E12 is small, then the exponential term can be expanded giving:

$$I_{\text{abs}} \approx I_0 \sigma cl \quad (\text{E13})$$

If the absorption cross section and path length are known then the radical concentration can be calculated directly. This allows a complete decay trace to be compiled using absolute radical concentrations in real time following each photolysis laser pulse, and for data acquisition to occur far more efficiently using absorption detection, than by using fluorescent methods. However, care must be taken when using absorption techniques to ensure that only the species of interest absorbs at the monitored wavelength. A schematic diagram illustrating the apparatus required to study the recombination of methyl, CH_3 , radicals is provided in Figure 13.

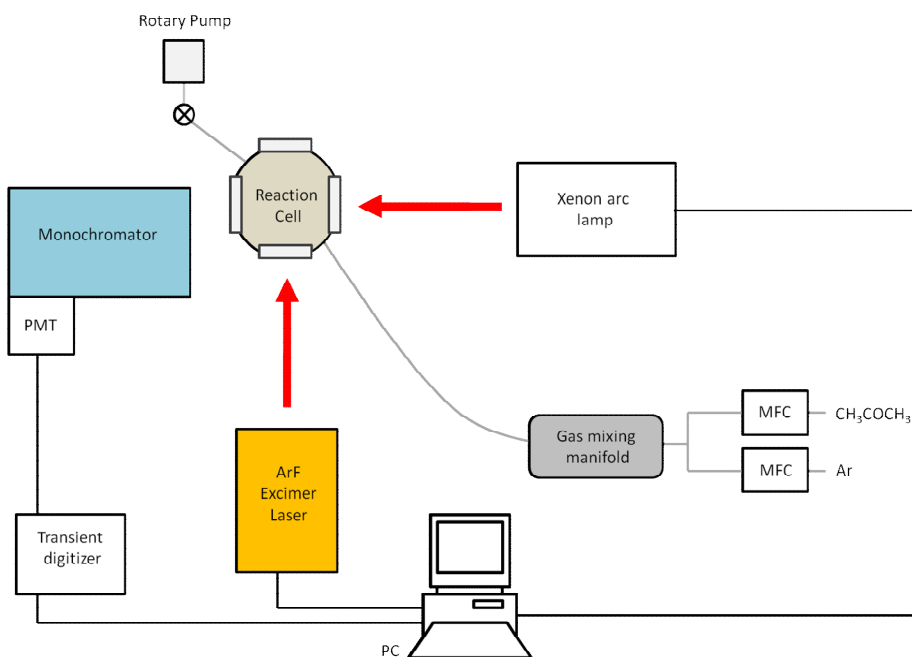


Figure 13: Schematic diagram of laser flash photolysis, absorption spectroscopy apparatus required for the study of CH_3 radical recombination kinetics.

Experimental investigations of radical-molecule kinetics, during which the radical species is observed directly, tend to generate the radical species in low concentrations to minimise the contribution of radical-radical chemistry to the observed kinetics. Absorption techniques demand accurate measurement of the light intensity passing through the reaction cell both prior to, I_0 , and following the onset of radical absorption, I_{abs} , which under low radical concentrations will correspond to a small perturbation in light intensity. Therefore absorption detection techniques often result in a poor signal-to-noise ratio when compared to fluorescent detection methods which monitor the radical signal relative to a near zero background.

In addition to the broadband flash lamps described previously, laser radiation can also be used as the probe light source in absorption experiments. The output of a dye laser can be tuned to a specific absorption line without the need of a monochromator. Moreover, a multipass instrument can be constructed by fitting highly reflective mirrors at either side of the absorption region, to magnify the experimental path length and greatly improve the sensitivity of the absorption technique.

2.5.2 Mass Spectrometry

Mass spectrometry (MS) is a powerful analytical technique that identifies molecules based on the mass-to-charge ratio of charged particles. All MS measurements rely on a familiar series of distinct stages; a gaseous sample is introduced through an inlet, ions are generated and then filtered based on their specific mass-to-charge ratios, before finally being detected. A range of different techniques have proven suitable for generating ions from a parent molecule in MS studies, including collision with a beam of high energy (~70 eV) electrons, photoionisation using a high energy (vacuum UV) laser pulse, and chemical ionisation which generates ions through collision of the analyte with the ions of a reagent gas. The ionisation process can result in significant fragmentation of the parent molecule, and samples containing complex mixtures of gaseous species often demand soft ionisation techniques to limit complications in the resulting mass spectra.

A quadrupole can be used to selectively detect ions by only offering ions of certain mass an undisturbed path to the detector.¹² The ions are filtered as they pass through a radio frequency (RF) quadrupole field generated by four parallel metal rods by applying an oscillating electric field. Ions can be selectively provided with a clear trajectory to the detector by adjusting the direct voltage applied to the RF field, while all others are lost through collision with the surface of the rods.

A time-of-flight (TOF) instrument is often used to distinguish the ions generated in a MS experiment.¹³ The TOF analyser uses an electric field to accelerate the ions through the same potential towards a detector. Provided the ions are all of the same charge, the kinetic energies will be identical and the time taken for each ion to reach the detector will depend only on their mass. The TOF technique allows all the ions generated to be observed, and therefore can offer an experimental advantage over the ion selective quadrupole filter.

In chapter 5 of this thesis, laser flash photolysis is coupled with photoionisation mass spectrometry (LFP-PIMS) to investigate the products of the OH and Cl-atom initiated oxidation of acetaldehyde. A brief description of this method is provided here. The flows of radical precursor, substrate and bath gas are allowed to mix and pass into a stainless steel flowtube. An excimer laser positioned such that the laser beam irradiates the length of the flowtube is fired, generating a uniform concentration of radicals along the flowtube. A 1 mm

diameter pin hole located in the wall of the flowtube allows a sample aliquot of gas to exit the flowtube and pass into a vacuum chamber, maintained at a pressure of less than 10^{-5} Torr using a diffusion pump. At some known time following the excimer laser pulse, a VUV laser pulse is fired through the vacuum chamber, photoionising species present in the vacuum chamber. The ions generated following the VUV laser pulse are focused into a TOF mass spectrometer and detected via dynode detectors. Ion signals can be monitored on a digital oscilloscope before being passed to a PC for analysis. A schematic diagram of the LFP-PIMS apparatus is provided in Figure 14.

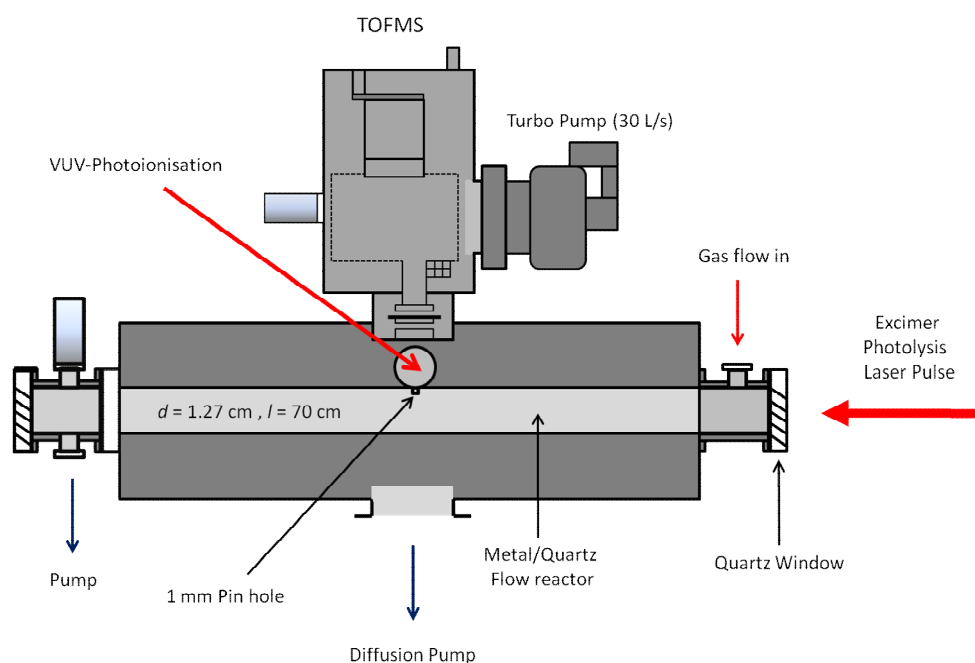


Figure 14: Schematic diagram of the flash photolysis, photoionisation mass spectrometry (PIMS) apparatus.

2.6 Alternative Kinetic Techniques

2.6.1 Discharge Flow

In the discharge flow technique transient reactants are generated indirectly, for example OH radicals can be produced by initially generating hydrogen atoms from the

microwave discharge of a mixture of molecular hydrogen in helium diluents, the hydrogen atoms react rapidly in the presence of NO₂ to give OH (R4):



The flow of each radical precursor is controlled such that *pseudo-first-order* conditions in the OH are maintained. The OH radicals are then passed into a flow tube. The substrate is introduced to the flow tube via a mobile injector, and at a well defined distance down the flow tube, the OH is detected by laser induced fluorescence (LIF). If the flow velocity of the gas mixture, v , and the distance between mobile injection and OH detection, d , are known, the reaction time, t , can be calculated from equation E14:

$$t = \frac{d}{v} \quad (\text{E14})$$

A schematic diagram of the discharge flow apparatus is provided in Figure 15.

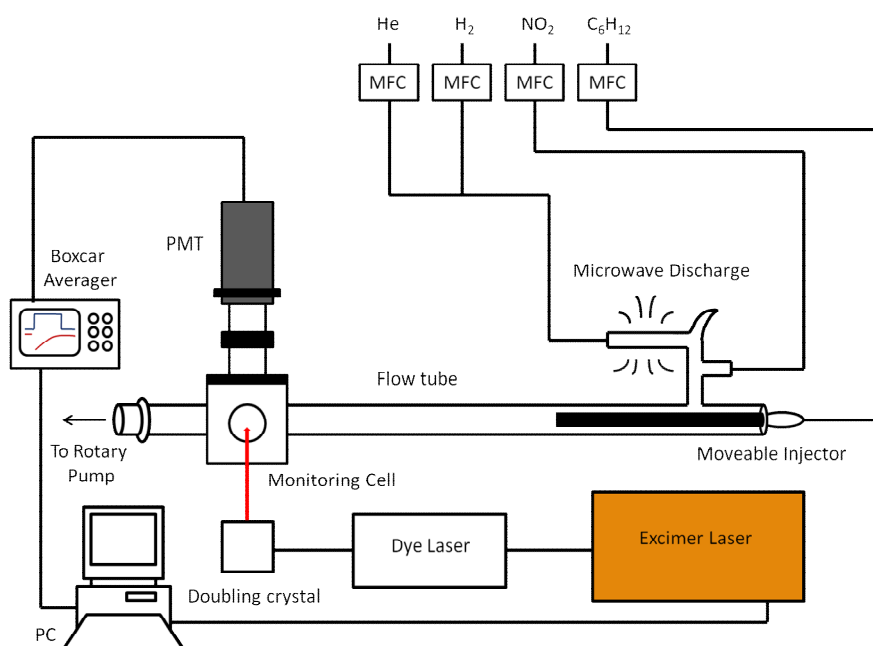


Figure 15: Schematic diagram of a discharge flow apparatus for the study of OH reactions with laser induced fluorescence (LIF) detection.

The injection site is then adjusted so that the OH signal corresponding to a different reaction time can be detected. Repeating this method allows an OH decay trace in the presence of the substrate to be constructed as a function of reaction time. The slope of a linear plot of the natural logarithm OH signal against time provides the *pseudo-first-order* rate coefficient, k' . Repeat experiments using various substrate concentrations allow the bimolecular rate coefficient to be determined from a linear plot of k' against substrate concentration. The discharge flow technique has been used to study OH kinetics following reaction with NO, NO₂, and a range of hydrocarbons.¹⁴⁻¹⁶

A significant limitation in the discharge flow technique is the time taken to achieve a uniform concentration of reactants in the flow tube following expulsion from the injector tip (typically a fraction of a millisecond at 1×10^2 Pa); consequently, discharge flow experiments do not provide a viable method of measuring rate coefficients for reactions which occur on a faster timescale than this. Traditional flow tube experiments were constrained to total pressures lower than 20 Torr in order to achieve a stable gas flow velocity across the entire cross section of the flow tube, and to temperatures greater than 250 K to avoid complication through heterogeneous chemistry associated with flow tube walls. Recent developments with this technique have shown by incorporating fast and turbulent flow conditions, both the experimental temperature ($T > 180$ K) and pressure range (70 – 760 Torr) achievable using the flow tube method can be greatly extended.^{17, 18} Flash photolysis experiments generate radical species in situ and therefore require detection methods that operate on the same timescale as the photolytic light source. Discharge flow methods generate radicals indirectly, and consequently offer greater flexibility in the methods used to generate radicals; furthermore, the detection technique employed is only limited by the rate of reaction and are less susceptible to secondary chemistry.

2.6.2 Shock Tube

The shock tube technique is often used to study reaction kinetics and mechanisms under conditions relevant to combustion.¹⁹ Conventional shock tube (ST) apparatus consists of a rectangular or circular metal tube, in which gas at low (driven) and high pressure (driver) can be separated by a diaphragm. The inert driver gas is maintained at high pressure

on one side of the diaphragm, while a dilute reactant gas mixture is partitioned at low pressure on the other. The diaphragm is burst causing a shock wave to propagate through the low pressure region and eventually reflect off the end wall of the ST. Gases behind the incident and reflected shock waves are subject to rapidly elevated pressures and temperatures. These extreme conditions can be used to initiate chemical processes significant to combustion, using apparatus which also allows the reactants and/or products to be monitored directly using a range of detection techniques. The opening of the diaphragm has a large effect on the development of the shock wave, and the conditions generated behind the incident and reflected shock waves are dependent on both the manner by which the diaphragm breaks and on the ratio of the driver-to-driven gas pressures. The variability introduced through rupturing the diaphragm results in significant uncertainty in the postshock conditions generated using conventional ST apparatus; consequently each ST experiment must be considered as a unique event, making signal averaging of repeat experiments under near identical conditions impossible.

The experimental limitations associated with the shock waves generated by breaking conventional ST diaphragms can be largely avoided following the design and development of a novel diaphragmless shock tube (DFST) by Dr Robert Tranter and colleagues at Argonne National laboratories, in which the conventional diaphragm breaker assembly is replaced with a fast valve system.²⁰ The DFST has been shown to generate highly reproducible shock waves, making a wide range of defined postshock conditions routinely achievable. The DFST design has recently been implemented into a miniature shock tube for use at synchrotron facilities, which can operate at high repetition rates (4 Hz) and generate experimental temperatures above 600 K and pressures of up to 100 bar.²¹

2.6.3 Relative Rates Method

This robust technique monitors the competitive loss rates of both the substrate, for which the rate coefficient is desired, and a reference species, for which the rate coefficient is known, through reaction with a common reactant, such as OH.^{22, 23} If the only experimental sinks for both substrate and reference species is through reaction with OH, then a linear plot can be constructed based on the relative loss of both reference and

substrate species with a slope equal to the ratio of rate coefficients. For the theoretical relative rates system:



If the concentration of OH inside the reactor is in steady state, then the integrated rate laws can be written in the form:

$$\ln\left(\frac{[\text{substrate}]_t}{[\text{substrate}]_0}\right) = -k_S[\text{OH}]_{ss}t \quad (\text{E15})$$

$$\ln\left(\frac{[\text{reference}]_t}{[\text{reference}]_0}\right) = -k_R[\text{OH}]_{ss}t \quad (\text{E16})$$

where k_S and k_R are bimolecular rate coefficients for reactions of substrate and reference species with OH, respectively, and $[\text{OH}]_{ss}$ is the steady state concentration of OH. If sample aliquots are removed from the reactor at various times following the onset of reaction, and the concentrations of both substrate and reference species determined relative to their initial concentrations, then equations E15 and E16 can be combined to give the linear expression:

$$\ln\left(\frac{[\text{substrate}]_t}{[\text{substrate}]_0}\right) = \frac{k_S}{k_R} \times \ln\left(\frac{[\text{reference}]_t}{[\text{reference}]_0}\right) \quad (\text{E17})$$

Relative concentrations of substrate and reference species are often determined by gas chromatography,²³ and provided the reference rate coefficient is known, the substrate rate coefficient can be determined using the experimental gradient of equation E17.

Soresnon and co-workers recently used the relative rate technique to measure room temperature rate coefficients for the reaction of OH with C₂H₂ (R8) at pressures ranging from 25 to 8000 Torr.²² Removal of C₂H₂ was measured relative to the loss of dimethyl ether, CH₃OCH₃ (R9), using either Fourier transform infrared (FTIR) spectroscopy or gas chromatography, flame ionisation detection (GC-FID). The relative rate plot based on the measurements by Soresnon and co-workers is presented in Figure 16.

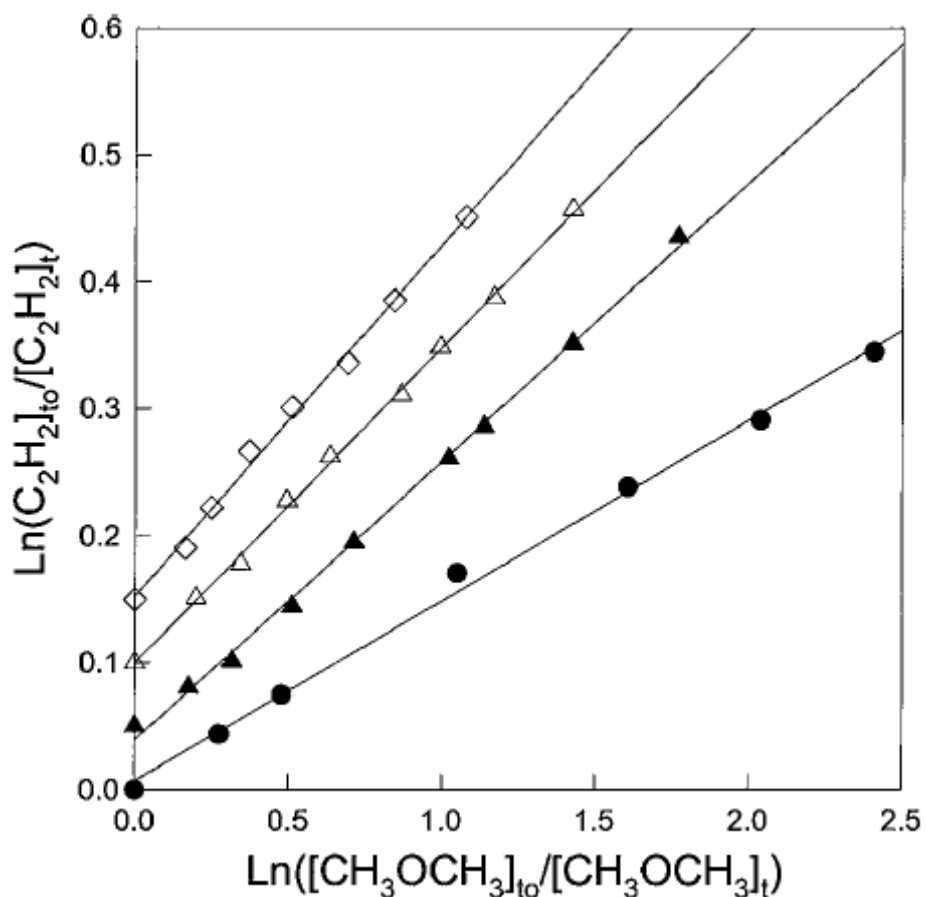


Figure 16: Plot of the competitive loss C_2H_2 and CH_3OCH_3 following exposure to OH radicals at 296 K in 750 Torr of O_2 (\diamond), 400 Torr of air (\triangle), 200 Torr of air (\blacktriangle), and 25 Torr of O_2 (\bullet) using equation E17.²²

Figure 16 shows strongly linear behaviour can be achieved using the relative rate technique, provided that only one reactant is responsible for the removal of both the substrate and reference molecule. The relative rates technique avoids the often arduous task of monitoring highly reactive species, such as radicals, as this method only requires the relative change in concentration of the typically stable co-reagent to be measured. Another

advantage of relative rate measurements is that they are typically conducted at pressures and temperatures directly pertinent to the troposphere. A major disadvantage of this technique is that some knowledge of the reaction mechanism is required to ensure there is no influence from secondary chemistry. In addition this technique relies on an alternative method to measure the reference rate coefficient absolutely, the uncertainty in which provides the major source of error in relative rate measurements.

2.7 Details of the Apparatus and Kinetic Methods used during this Work

Clearly, kinetic studies require the concentration of the co-reagent to be known, which in turn require an accurate measure of the pressure and temperature inside the cell. The following sections provide details of the specific apparatus used during this work, such as the reactors, and the means of measuring temperature and pressure inside the cell, and the pressure on the vacuum glass line used to prepare gas sample bulbs.

2.7.1 Reaction Cells

The experimental work presented in this thesis was carried out at temperatures ranging from 195 to 498 K. Two different reaction cells were required in order to achieve this experimental temperature range. Schematic diagrams of both the high and low temperature reaction cells are given in Figures 17 and 18, respectively.

High temperature experiments were carried out using a stainless steel reactor which could be heated to 700 K using cartridge resistance heaters mounted within the reactors metal casing. A commercial temperature controller was used to vary the current applied to the resistance heaters, and calibrated using a K-type thermocouple positioned in the centre of the reactor.

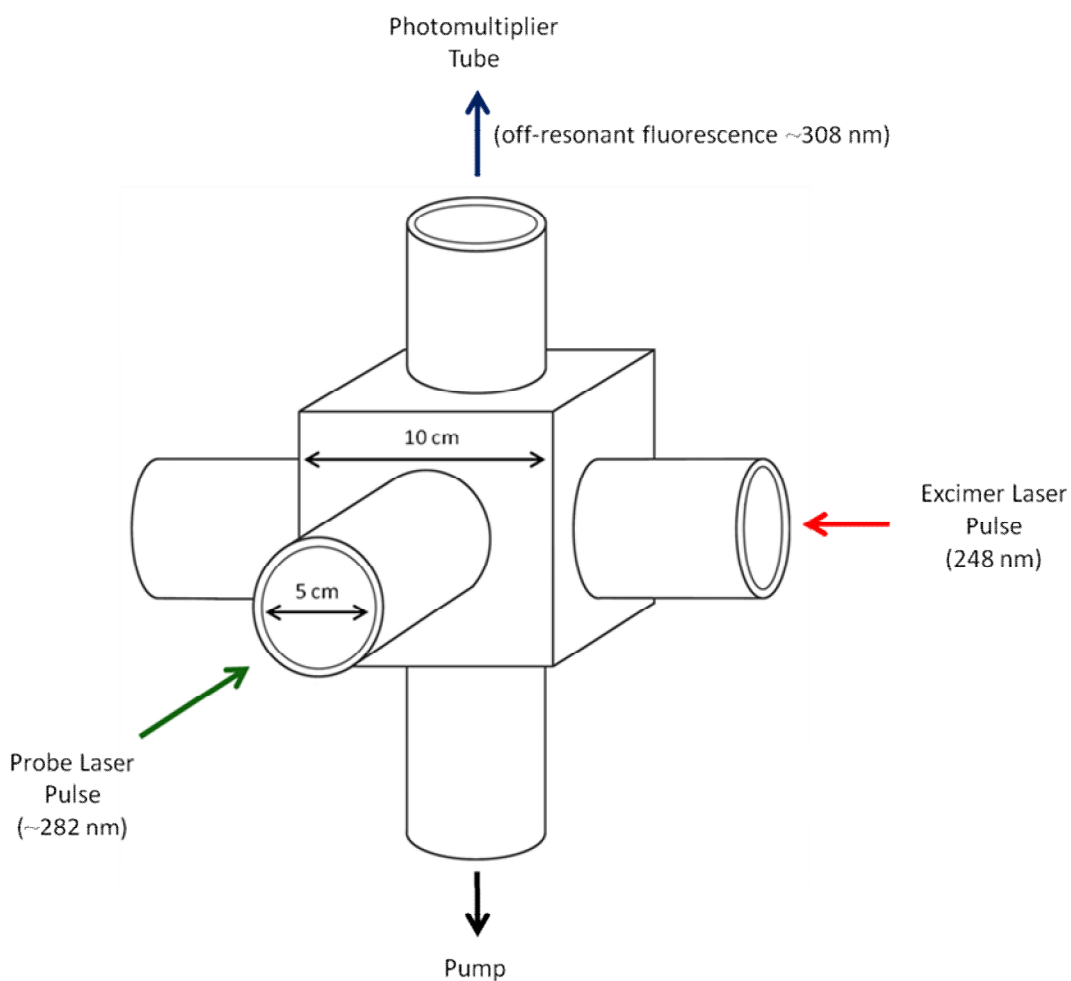


Figure 17: Schematic of the high temperature (295 – 498 K) reactor used in this thesis.

Subambient temperatures were achieved by cryogenically cooling a second, low temperature, stainless steel reactor, which had been welded into a bath. Temperatures ranging from 195 to 273 K were achieved by filling the bath with a suitable coolant. The windows of the cell were heated electrically to avoid condensation, and the walls of the bath were insulated using polystyrene. The temperature inside the bath was measured using a K-type thermocouple. All of the subambient temperature experiments carried out and presented in this thesis were undertaken at total bath pressures of 80 Torr or below, at these pressures the temperature inside the reactor is indistinguishable from the temperature of the bath.

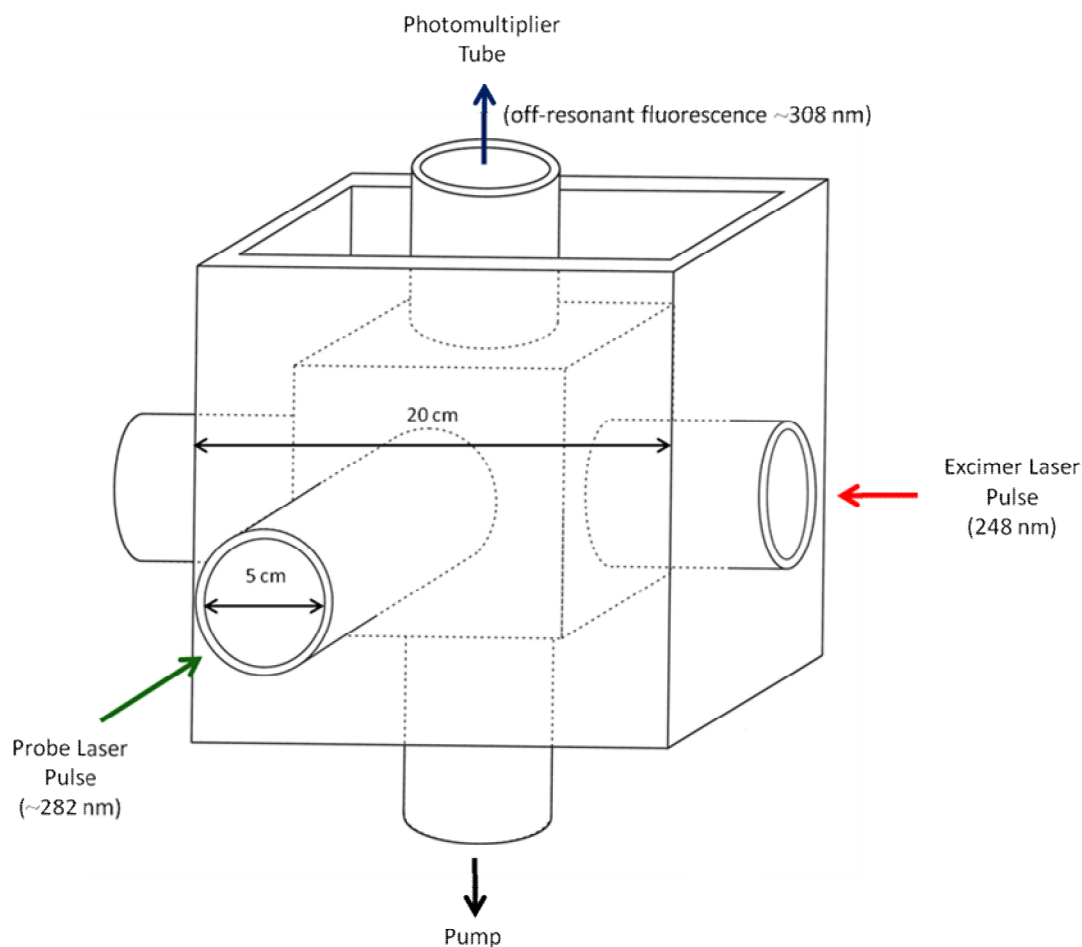


Figure 18: Schematic of the low temperature (195 – 295 K) cell used in this thesis

2.7.2 Gas Flows

The concentration of reactant molecules present in the reaction cell for each experiment was calculated from the total number density of gas molecules present and from the concentrations and relative flow rates of the gases used. The former was calculated using the ideal gas law. Reagent sample bulbs were prepared on a glass vacuum line with concentrations determined barometrically. Mass flow controllers (MKS) were used to regulate the flows of each gas into the cell. Each of the MFCs were connected to a digital readout box and calibrated by monitoring the displacement of bubbles through a flowtube. The MFCs were arranged such that the bath gas (N_2 and/or O_2) flushed both the precursor and substrate gas into a stainless steel gas mixing manifold before the gas flowed into the reaction cell, to ensure all the gases were well mixed prior to photolysis. The gas flow into

the reaction cell was kept sufficient to ensure a fresh gas sample was present in the cell for each photolysis laser pulse.

2.7.3 Pressure Readings

Pressures of between 2 and 300 Torr in the reactor (Leybold CERAVAV and MKS Baratron), and pressures up to 1300 Torr in the vacuum line were measured using capacitance manometers. These gauges contain a two plate capacitor; variations in pressure perturb one of the plates and alter the capacitance. Careful calibration allows the backing pressure to be determined from the capacitance reading. The low (sub mTorr) pressures of the vacuum line were measured using Pirani thermal-conductivity type gauges. These gauges contain a filament heated by constant current. The thermal conductivity of a gas scales with pressure, and these gauges monitor the change in temperature based on the change in resistivity of the wire.

2.8 Experimental Gas-Phase Kinetics

The final section of this chapter introduces the isolation method and the means of data analysis used throughout this thesis to determine bimolecular rate coefficients.

2.8.1 Isolation Method

The principal aim of chemical kinetics is to quantify the rate at which a chemical reaction proceeds. The following section describes the *isolation method* used during this work to measure bimolecular rate coefficients. For the theoretical unimolecular elementary reaction:



The reaction is first-order with respect to A and the rate law can be expressed in the form:

$$-\frac{d[A]}{dt} = k[A] \quad (\text{E18})$$

As this reaction proceeds, the decrease in concentration of species A may be temporally resolved by integrating the differential rate law (E18) between an initial time 0 and a subsequent time t , when concentrations of species A are $[A]_0$ and $[A]_t$, respectively. For a first order reaction, the integrated rate law is:

$$[A]_t = [A]_0 \exp(-kt) \quad (\text{E19})$$

Consequently, first-order decay is an exponential process. The dimensionless nature of the quotient term of the integrated rate law means absolute measurements of reactant or product concentrations are unnecessary, and that any detectable property proportional to concentration, such as fluorescence, may be used to quantify the rate coefficient.

Experimentally determining the rate equation for elementary reactions involving multiple reactants can become complicated due to the concentrations of several chemical species changing simultaneously. These complications can be limited by the isolation method. If the experimental conditions are controlled so that all but one of the reactants are present in great excess, then their concentrations can be considered effectively constant throughout the course of the reaction. Under these conditions the rate equation can be simplified and shown to conform to *pseudo-first-order* kinetics. If we consider the theoretical bimolecular elementary reaction (R8):



The differential rate law can be written as follows:

$$-\frac{d[A]}{dt} = k[A][B] \quad (\text{E20})$$

If the concentrations of reactants A and B are controlled such that species B is in great excess over A, then the rate equation can be simplified to:

$$-\frac{d[A]}{dt} = k'[A] \quad (\text{E21})$$

where $k' = k[B]$. Under *pseudo-first-order* conditions species A decays exponentially, and the *pseudo-first-order* rate coefficient, k' , can be determined by fitting experimental decay data for species A using equation E19.

The majority of experiments reported in this thesis involved monitoring OH decay in the presence of a stable co-reagent under *pseudo-first-order* conditions. Typical initial OH concentrations, $[OH]_0$, inside the reaction cell can be calculated using an approximation of the Beer-Lambert law:

$$I_{\text{abs}} = I_0(1 - \exp(-\sigma cl)) \quad (\text{E12})$$

which for low optical densities is closely approximated by:

$$I_{\text{abs}} \approx I_0 \sigma cl \quad (\text{E13})$$

The excimer laser power was measured regularly, and was typically $\sim 60 \text{ mJ cm}^{-2} \text{ pulse}^{-1}$ or lower. The energy per photon of 248 nm excimer laser light, ε , can be calculated as follows:

$$\varepsilon = \frac{(6.626 \times 10^{-34} \text{ Js}^{-1}) \times (2.998 \times 10^8 \text{ ms}^{-1})}{(2.48 \times 10^{-7} \text{ m})} = 8.01 \times 10^{-19} \text{ J photon}^{-1} \quad (\text{E22})$$

If the incident excimer laser light intensity, I_0 , is expressed as fluence:

$$I_0 = \frac{6.0 \times 10^{-2} \text{ J cm}^{-2} \text{ pulse}^{-1}}{8.01 \times 10^{-19} \text{ J photon}^{-1}} = 7.49 \times 10^{16} \text{ photon cm}^{-2} \text{ pulse}^{-1} \quad (\text{E23})$$

If the optical path length is assumed to be 1 cm, then $[OH]_0$ can be estimated using the following expression:

$$[OH]_0 = \sigma_{(248 \text{ nm})} \Phi_{(248 \text{ nm})} [C_4H_9OOH] I_0 \quad (\text{E24})$$

where $\sigma_{(248 \text{ nm})}$ and $\Phi_{(248 \text{ nm})}$ represent the absorption cross section and OH quantum yield for C_4H_9OOH at 248 nm, and $[C_4H_9OOH]$ is the experimental concentration of *t-butyl* hydroperoxide inside the reaction cell. A recent photochemical study reported an OH quantum yield close to unity for *t-butyl* hydroperoxide at 248 nm, and an absorption cross section of $2.20 \times 10^{-20} \text{ cm}^2 \text{ molecule}^{-1}$ at 296 K.²⁴ Typical experimental concentrations of

t-butyl hydroperoxide inside the reaction cell were 2.0×10^{14} molecule cm^{-3} , giving an initial OH concentration, $[\text{OH}]_0$, of:

$$\begin{aligned} [\text{OH}]_0 &= (2.20 \times 10^{-20} \text{ cm}^2 \text{ molecule}^{-1}) \times (2.0 \times 10^{14} \text{ molecule cm}^{-3}) \times (7.49 \times 10^{16} \text{ molecule cm}^{-3}) \\ &= 3.30 \times 10^{11} \text{ molecule cm}^{-3} \end{aligned}$$

Experimental co-reagent concentrations inside the cell typically ranged from $10^{13} - 10^{16}$ molecule cm^{-3} , and ensured *pseudo-first-order* conditions in OH were maintained.

2.8.2 Data Collection and Analysis

It has been mentioned that the LFP-LIF technique build an experimental decay trace by varying the time delay between the photolysis and probe laser pulses. The laser timing for all experimental results reported in this thesis were controlled using either in-house software written in Delphi by Peter Halford-Maw (School of Chemistry, University of Leeds), or by a custom-written LabVIEW programme. The time delay between the photolysis and probe laser pulses was varied such that a typical OH decay profile consisted of 250 time points, each averaged between 2 and 10 excimer laser shots, depending on the signal-to-noise ratio.

The fluorescence signal was collected by a PMT (EMI 9813) mounted above the reaction cell, perpendicular to both laser beams. The PMT signal was amplified using a fast pre-amplifier (Stanford Research Systems DC – 300MHz) and then transferred to a digital oscilloscope (Lecroy LT262), and a boxcar (SR250) which integrated the relevant portion of the signal. The power of the probe laser light was measured using a photodiode placed behind the exit window of the reaction cell, the signal from which was also transferred to the boxcar. Outputs from the digitised boxcar were plotted on a personal computer using the commercial software package Origin 7.5. A temporary barrier placed between the probe laser beam and the cell window, allowed both the laser power and the fluorescence signal to be corrected for a zero baseline using the mean measurement recorded before the probe light first enters the cell. The OH fluorescence could then be normalised for perturbations in laser power, and plotted as a function of time. *Pseudo-first-order* decay coefficients are then

derived from non-linear least squares analysis of the experimental data fit in Origin using equation E19. Typical raw experimental OH decay data measured in the presence of glyoxal, $(\text{HCO})_2$, and corresponding laser power measurements are included in Figure 19, together with the normalised decay trace and residuals to the exponential fit through the data.

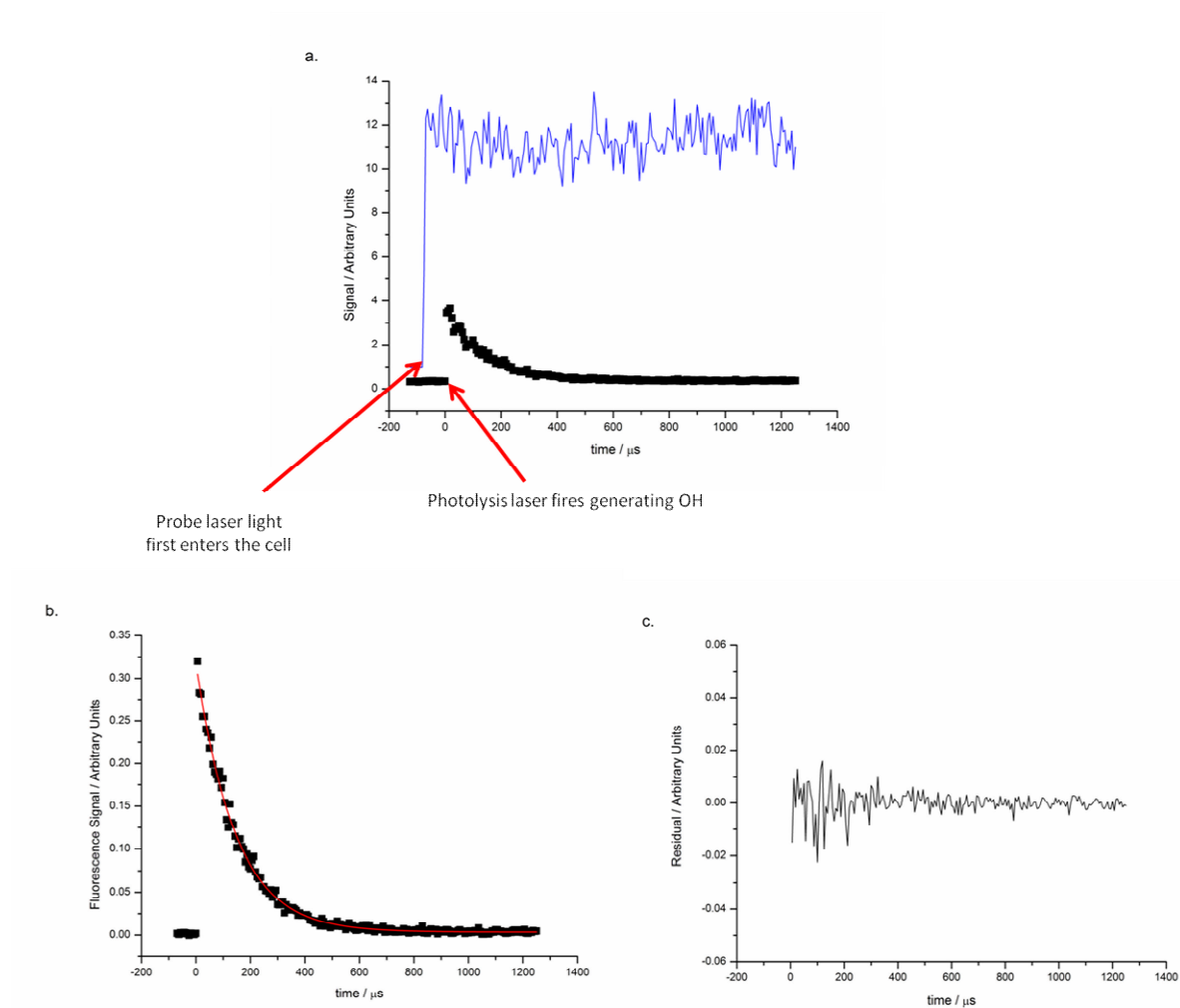


Figure 19: Typical raw experimental signal of both OH fluorescence and laser power (a); *pseudo-first-order* OH decay measured in the presence of excess $(\text{HCO})_2$ (6.66×10^{14} molecule cm^{-3}) at 295 K under 40 Torr of nitrogen, normalised for laser power, the fit using equation E19 corresponds to a pseudo-first-order decay coefficient of $(7000 \pm 75) \text{ s}^{-1}$ (b); the corresponding residuals to the exponential fit (c).

By varying the experimental concentration of the excess co-reagent, several *pseudo-first-order* decay coefficients can be measured, which when plotted as a function of the co-reagent concentration, yield a straight line bimolecular plot with a gradient equal to the bimolecular rate coefficient of interest. An example bimolecular plot for the reaction of OH with $(\text{HCO})_2$ is presented in Figure 20.

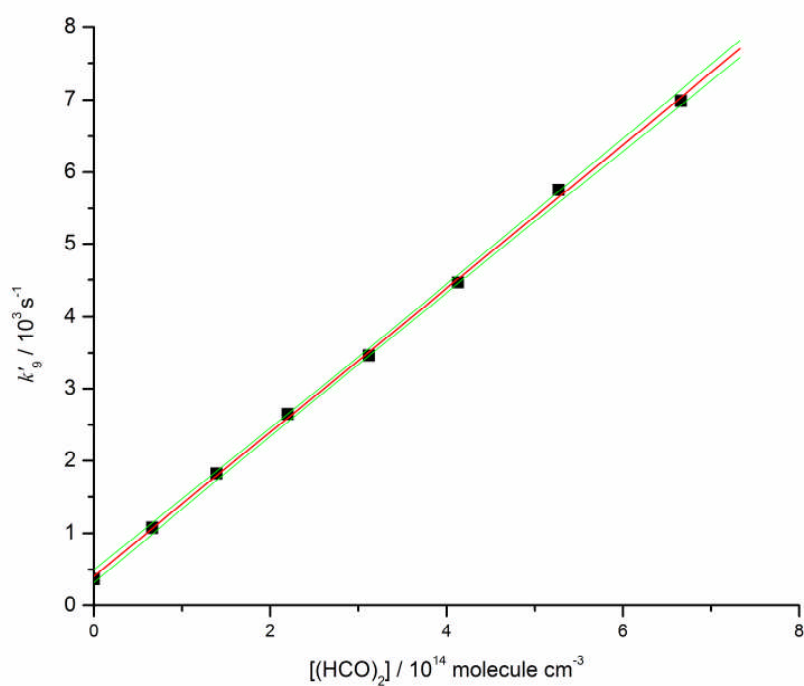


Figure 20: Bimolecular plot for the $\text{OH} + (\text{HCO})_2 \rightarrow \text{HC(O)CO} + \text{H}_2\text{O}$ reaction at room temperature in 40 Torr of nitrogen, for which a bimolecular rate coefficient of $(9.95 \pm 0.10) \times 10^{-12} \text{ cm}^3 \text{ molecule}^{-1} \text{ s}^{-1}$ was observed (where the error bar is purely statistical at the 2σ level).

2.9 References

1. Andrews, D. L., *Lasers in chemistry*. 2nd ed. ed.; Springer-Verlag: 1990; p xii,188p.
2. Norrish, R.; Porter, G., Chemical reactions produced by very high light intensities. *Nature* 1949, 164, 658.
3. Onel, L.; Thonger, L.; Blitz, M. A.; Seakins, P. W.; Bunkan, A. J. C.; Solimannejad, M.; Nielsen, C. J., Gas-Phase Reactions of OH with Methyl Amines in the Presence or Absence of Molecular Oxygen. An Experimental and Theoretical Study. *Journal of Physical Chemistry A* 2013, 117, 10736-10745.
4. Heaven, M.; Miller, T. A.; Freeman, R. R.; White, J.; Bokor, J., Two-photon absorption, laser-induced fluorescence detection of Cl atoms. *Chemical Physics Letters* 1982, 86, 458-462.
5. Schulz, C.; Sick, V.; Heinze, J.; Stricker, W., Laser-induced-fluorescence detection of nitric oxide in high-pressure flames with A-X (0, 2) excitation. *Applied optics* 1997, 36, 3227-3232.
6. Nelson, H.; Pasternack, L.; McDonald, J., Laser-induced excitation and emission spectra of nitrate radical (NO₃). *The Journal of Physical Chemistry* 1983, 87, 1286-1288.
7. Talukdar, R. K.; Gilles, M. K.; Battin-Leclerc, F.; Ravishankara, A.; Fracheboud, J. M.; Orlando, J. J.; Tyndall, G. S., Photolysis of ozone at 308 and 248 nm: Quantum yield of O (¹D) as a function of temperature. *Geophysical research letters* 1997, 24, 1091-1094.
8. DeSain, J. D.; Jusinski, L. E.; Taatjes, C. A., Temperature dependence and deuterium kinetic isotope effects in the HCO plus NO reaction. *Journal of Photochemistry and Photobiology a-Chemistry* 2005, 176, 149-154.
9. Glowacki, D. R.; Lockhart, J.; Blitz, M. A.; Klippenstein, S. J.; Pilling, M. J.; Robertson, S. H.; Seakins, P. W., Interception of Excited Vibrational Quantum States by O₂ in Atmospheric Association Reactions. *Science* 2012, 337, 1066-1069.
10. Lockhart, J.; Blitz, M. A.; Heard, D. E.; Seakins, P. W.; Shannon, R. J., Mechanism of the Reaction of OH with Alkynes in the Presence of Oxygen. *Journal of Physical Chemistry A* 2013, 117, 5407-5418.
11. Lockhart, J.; Blitz, M.; Heard, D.; Seakins, P.; Shannon, R., Kinetic Study of the OH + Glyoxal Reaction: Experimental Evidence and Quantification of Direct OH Recycling. *Journal of Physical Chemistry A* 2013, 117, 11027-11037.
12. Dawson, P. H., Quadrupole mass spectrometry and its applications. 1976.
13. Blitz, M. A.; Goddard, A.; Ingham, T.; Pilling, M. J., Time-of-flight mass spectrometry for time-resolved measurements. *Review of scientific instruments* 2007, 78, 034103.
14. Burrows, J. P.; Wallington, T. J.; Wayne, R. P., Kinetics of the gas-phase reactions of OH with NO₂ and with NO. *Journal of the Chemical Society, Faraday Transactions 2: Molecular and Chemical Physics* 1983, 79, 111-122.
15. Boodaghians, R. B.; Hall, I. W.; Toby, F. S.; Wayne, R. P., Absolute determinations of the kinetics and temperature dependences of the reactions of OH with a series of alkynes *Journal of the Chemical Society-Faraday Transactions II* 1987, 83, 2073-2080.
16. Bourmada, N.; Lafage, C.; Devolder, P., Absolute rate constants of the reactions of OH with cyclohexane and ethane at 296±2 K by the discharge flow method. *Chemical physics letters* 1987, 136, 209-214.
17. Seeley, J. V.; Jayne, J. T.; Molina, M. J., High pressure fast-flow technique for gas phase kinetics studies. *International journal of chemical kinetics* 1993, 25, 571-594.
18. Percival, C. J.; Shallcross, D. E.; Canosa-Mas, C. E.; Dyke, J. M., Recent advances in the application of discharge-flow to the determination of gas-phase rate coefficients at pressures and temperatures of relevance to the Earth's atmosphere. *Journal of Photochemistry and Photobiology a-Chemistry* 2005, 176, 250-259.
19. Tranter, R. S.; Lynch, P. T.; Yang, X., Dissociation of dimethyl ether at high temperatures. *Proceedings of the Combustion Institute* 2013, 34, 591-598.

20. Tranter, R. S.; Giri, B. R., A diaphragmless shock tube for high temperature kinetic studies. *Review of Scientific Instruments* 2008, 79.
21. Tranter, R. S.; Lynch, P. T., A miniature high repetition rate shock tube. *Review of Scientific Instruments* 2013, 84.
22. Sorensen, M.; Kaiser, E. W.; Hurley, M. D.; Wallington, T. J.; Nielsen, O. J., Kinetics of the reaction of OH radicals with acetylene in 25-8000 Torr of air at 296 K. *International Journal of Chemical Kinetics* 2003, 35, 191-197.
23. Stewart, D.; Almabrok, S.; Lockhart, J.; Mohamed, O.; Nutt, D.; Pfrang, C.; Marston, G., The kinetics of the gas-phase reactions of selected monoterpenes and cyclo-alkenes with ozone and the NO₃ radical. *Atmospheric Environment* 2013, 70, 227-235.
24. Baasandorj, M.; Papanastasiou, D. K.; Talukdar, R. K.; Hasson, A. S.; Burkholder, J. B., (CH₃)₃COOH (tert-butyl hydroperoxide): OH reaction rate coefficients between 206 and 375 K and the OH photolysis quantum yield at 248 nm. *Physical Chemistry Chemical Physics* 2010, 12, 12101-12111.

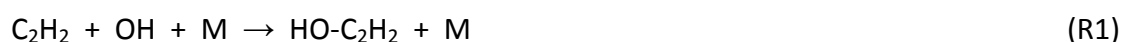
Chapter 3 Kinetic Study of the OH + Acetylene Reaction in the Presence and Absence of O₂

3.1 Abstract

This chapter provides a detailed kinetic study of the OH (OD) + acetylene, C₂H₂, reaction using N₂, and various O₂/N₂ mixture bath gas, over a range of pressures (5 – 300 Torr) and temperatures (212 – 498 K), by monitoring OH (OD) via laser induced fluorescence in excess C₂H₂. The OH (OD) + C₂H₂ reaction results in the formation of an association adduct, and rate coefficients measured for this reaction depend on the efficiency of bath gas collisions at quenching the excited vibrational quantum-states of the adduct. The pressure dependence of the OH + C₂H₂ rate coefficients measured here lie in excellent agreement with the falloff behaviour reported by other studies. Full master equation (ME) analysis of the room temperature OH + C₂H₂ rate coefficients measured here predicts a limiting high-pressure rate coefficient of $(9.10 \pm 0.45) \times 10^{-13} \text{ cm}^3 \text{ molecule}^{-1} \text{ s}^{-1}$, in good agreement with values published by other groups. The adduct formed following reaction between OH (OD) and C₂H₂ react rapidly with O₂ to give either glyoxal + OH (OD), or formic acid + HCO as first generation oxidation products. The branching ratios associated with this reaction have been quantified experimentally as a function of pressure, temperature and oxygen fraction, $f\text{-O}_2$. The experimental measurements have been analysed using a detailed model which combines ME simulations with variable reaction coordinate transition state theory (VRC-TST). This concerted approach has shown that the product branching observed following reaction between the adduct and O₂ depends critically on the vibrational quantum-state excitation of the adduct at the point of O₂ addition. Significantly, under atmospheric conditions approximately 25% of the total adduct + O₂ reactive flux occurs before the quantum-states of the adduct have fully relaxed. An extensive isotope study has also been carried out in order to clarify the mechanism responsible for glyoxal + OH formation.

3.2 Background and Previous Work

Acetylene, C₂H₂, is an important species in both combustion and atmospheric chemistry, and produced primarily through automobile combustion and biomass burning.¹⁻⁴ Alkynes are neither readily soluble or photolabile in the atmosphere, so the only significant loss process is through reaction with OH radicals.⁵ The slow rate of reaction with OH gives C₂H₂ an atmospheric lifetime of approximately 15 days (using a mean [OH] of 1 × 10⁶ molecule cm⁻³ and a *k*₁ value of 7.8 × 10⁻¹³ cm³ molecule⁻¹ s⁻¹ at 760 Torr and 295 K)⁶; explaining its detection in both remote regions and at high altitudes,⁷⁻⁹ and its use as a marker for anthropogenic emissions.¹⁰ At temperatures relevant to the atmosphere, the first step of OH initiated oxidation of C₂H₂ is pressure dependent OH-addition across the triple bond (reaction R1):



The resulting adducts react rapidly with oxygen. However, unlike many RO₂ species, the resulting peroxy radicals are unstable with respect to formation of two product channels leading to glyoxal, (HCO)₂, + OH (reaction R2a) or formic acid + HCO (reaction R2b):



Acetylene oxidation contributes significantly to the global (HCO)₂ budget, the second most important after isoprene oxidation at 20%.¹¹ (HCO)₂ has been implicated as a likely precursor of secondary organic aerosol (SOA),¹²⁻¹⁴ which can potentially influence atmospheric chemistry, air quality and climate. The HCO radicals produced through reaction R2b will react rapidly with O₂ to give HO₂ + CO (reaction R3):¹⁵



Therefore the branching ratio associated with reaction R2 will affect the partitioning of HOx (OH + HO₂) radicals, both through direct OH formation (reaction R2a) and through secondary chemistry of the HCO radicals, produced both directly (reaction R2b) and following photooxidation of (HCO)₂.¹⁶ The formic acid, HCOOH, produced following C₂H₂ oxidation is also of atmospheric importance. Carboxylic acids are ubiquitous in all phases

within the troposphere,¹⁷ where they contribute to rain acidity in both urban and remote regions,^{18, 19} affect atmospheric chemistry sensitive to pH, and modify the hygroscopic properties of particulates.²⁰ There is currently significant uncertainty in the atmospheric budgets of organic acids, particularly in regions affected by biomass burning.²¹

The pressure dependence of reaction R1 has been investigated by several groups at room temperature, and shown reasonable agreement in falloff behaviour and values for the high pressure limiting rate coefficient of $\sim 1 \times 10^{-12} \text{ cm}^3 \text{ molecule}^{-1} \text{ s}^{-1}$.²²⁻²⁸ Schmidt et al. conducted a kinetic flash photolysis study of the OH + C₂H₂ reaction monitoring OH directly by LIF; biexponential decays were observed in the presence of O₂ and attributed to fast reaction of the adduct with O₂ that generate glyoxal and recycle OH.²² Zetzsch and co-workers have carried out several studies of the OH + C₂H₂/O₂ system, using flash photolysis with either resonance fluorescence or long path absorption detection techniques.²⁸⁻³⁰ Siese and Zetzsch confirmed biexponential OH decays in the presence of trace amounts of oxygen, and derived rate coefficients for both reactions R1 and R2 from the decay profiles; k_2 was found independent of pressure with an approximate value of $(4.2 \pm 0.5) \times 10^{-12} \text{ cm}^3 \text{ molecule}^{-1} \text{ s}^{-1}$ at 295 K.²⁹ Bohn et al. then quantified room temperature OH yields, Φ_{OH} , for reaction R2 in excess O₂ as a function of total pressure, $f\text{-O}_2$, and bath gas.²⁸ These authors reported Φ_{OH} independent of total pressure, with an Φ_{OH} of (0.70 ± 0.04) under atmospheric conditions ($f\text{-O}_2 = 0.21$), but strongly dependent on $f\text{-O}_2$; decreasing from (0.83 ± 0.02) to (0.57 ± 0.04) as $f\text{-O}_2$ increase from 0.01 to 1, respectively. These authors argued that because the nascent adduct forms following reaction R2 with excess internal energy, the negative dependence of Φ_{OH} with $f\text{-O}_2$ results from less OH generated through reaction of O₂ with the chemically activated adduct. Bohn et al. conducted experiments using either N₂ or He bath gas, and observed a more marked dependence of Φ_{OH} with $f\text{-O}_2$ during experiments in He. N₂ is a more efficient third body than He; therefore this observation is consistent with product yields dependent on the degree of thermalization of the nascent adduct.²⁸ The results of Bohn et al. are in good agreement with an earlier atmospheric chamber study with FTIR stable product detection by Hatakeyama et al., which reported glyoxal (0.7 ± 0.3) and formic acid (0.4 ± 0.1) as primary products of the NO_x free OH initiated oxidation of acetylene.³¹ Hatakeyama et al. also performed isotopic studies; in the

OD + C₂H₂/O₂ system both HCOOH and HCOOD were observed, although the authors noted that isotopic exchange at the labile OH group could be responsible for this observation. Schmidt et al. also performed isotope experiments during which they observed OD formation in the OH + C₂D₂/O₂ system, which suggests the mechanism involves isotopic exchange.²² At a similar time, Liu et al. attempted to observe either OD formation in the reaction of OH + C₂D₂/O₂, or OH formation in the OD + C₂H₂/O₂ reaction at 323 and 653 K in 1 atm of argon, using resonance absorption detection.³² No evidence of isotope exchange was reported by Liu and co-workers, in contrast to the results of Schmidt et al., although evidence of OH recycling in the OH + C₂H₂/O₂ system was provided by a systematic slowing of the rate of OH decay following the introduction of O₂ to their flow system. Sorenson et al. have studied reaction R1 from 25 – 8000 Torr at 298 K in N₂, O₂ and synthetic air using the relative rate technique, which is insensitive to OH recycling.²⁴ The high-pressure limiting rate coefficient, k_1^∞ , was determined as $(9.69 \pm 0.30) \times 10^{-13} \text{ cm}^3 \text{ molecule}^{-1} \text{ s}^{-1}$, and k_1 at atmospheric pressure was measured as $8.5 \times 10^{-13} \text{ cm}^3 \text{ molecule}^{-1} \text{ s}^{-1}$; most relevant for the work presented here is that they showed the efficiencies of N₂ and O₂ as third bodies to be identical.

Theoretical treatment of reaction R1 by Yeung et al., Glowacki and Pilling, and Barker and co-workers, have all reported that the HO-C₂H₂ adduct exists in two energetically distinct conformations, with the OH group either *cis*- or *trans*- to the radical orbital (herein referred to as *cis*-adduct and *trans*-adduct isomers, respectively), and the *cis*-adduct approximately 5 kJ mol⁻¹ more stable than the *trans*.³³⁻³⁵ Theory suggests reaction of the *cis*-adduct with O₂ proceeds on an energetically downhill path to (HCO)₂ + OH products. The initial step is a 1, 5-hydrogen shift of the peroxy radical to give a QOOH intermediate species, which dissociates promptly over a small barrier to give (HCO)₂ + OH. The peroxy radical is stabilised through hydrogen bonding between its OH and peroxy substituents, yet still lies higher in energy than the transition state leading to QOOH formation (Figure 1); consequently this is the most facile product channel available to the HO-C₂H₂ adduct in the presence of O₂. Significantly, the mechanism proposed by theory suggests the proton of the OH that initiates oxidation is identical to that of the OH regenerated. The theory is therefore at odds with experimental evidence by Schmidt et al., which reported isotope exchange in

the OH + C₂D₂/O₂ system.²² The pathway to HCOOH + HCO products is more mechanistically tortuous than the bicarbonyl forming channel, and associated with reaction of the *trans*-adduct with O₂. The initial step is isomerisation of the peroxy radical to give a three-membered cyclic intermediate, which following concerted C-C and O-O bond cleavage and β-fragmentation yields HCOOH + HCO products.

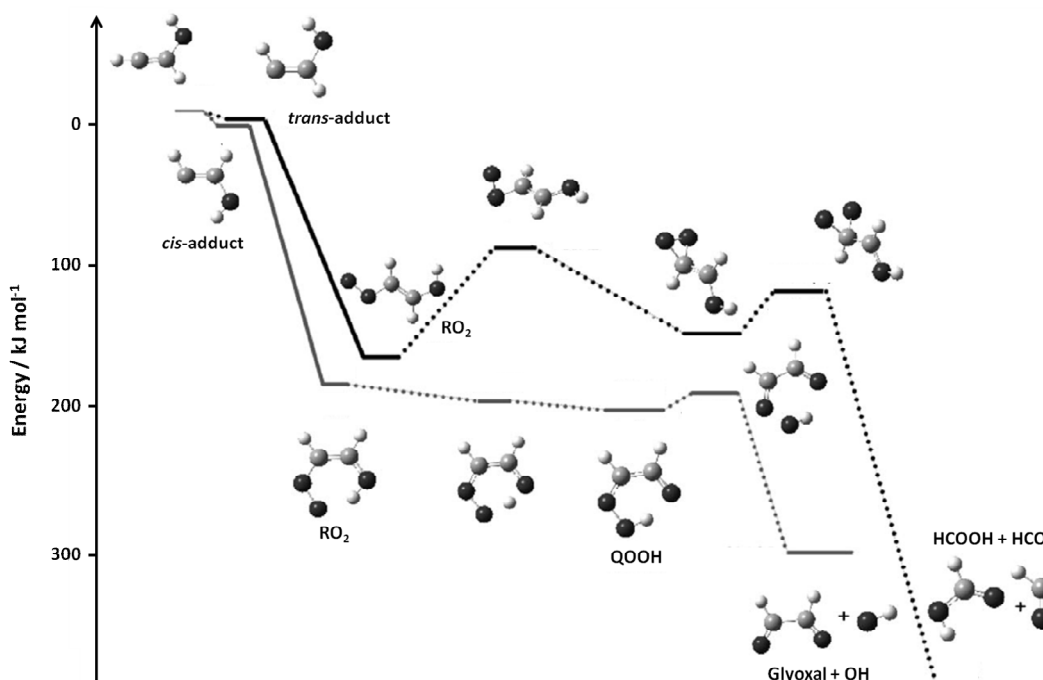


Figure 1: Main stationary points on the potential energy surface for the HO-C₂H₂ + O₂ reaction.³⁵

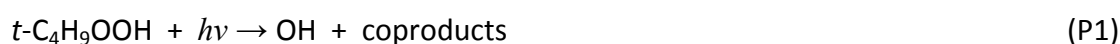
This chapter reports an extensive kinetic study of the OH + C₂H₂ reaction which aims to build on previous work by Zetzsch and co-workers by quantifying Φ_{OH} for the OH + C₂H₂/O₂ reaction as a function of total pressure, temperature, and oxygen concentration. The observed Φ_{OH} are examined using a theoretical model that combines *ab initio* quantum chemistry with stochastic master equation (ME) simulations and variable reaction coordinate transition-state theory (VRC-TST).²⁷ The kinetics of reaction R2 are investigated by analysing the biexponential OH decay traces observed in the presence of trace amounts

of O₂. Finally, isotope studies are used to elucidate the reaction mechanism associated with acetylene oxidation, and resolve the conflicting observations reported in the literature.³⁶

3.3 Experimental

This work has been carried out using conventional slow flow, laser flash photolysis, laser induced fluorescence (LIF) apparatus. The flows of radical precursor, acetylene, and bath gas (N₂ and/or O₂), were regulated via calibrated mass flow controllers, and introduced into a stainless steel, 6-way cross reactor through a mixing manifold. The total pressure in the reactor (5 – 300 Torr) was regulated via a needle valve in the exhaust line to the pump and measured using a capacitance manometer. Temperatures above 298 K were obtained using cartridge resistance heaters inserted in the walls of the central region of the reactor, and temperatures close to the reaction zone were measured using K-type thermocouples. Subambient temperatures were obtained using a different 6-way cross stainless steel reactor, which had been welded into a metal bath such that just the end flanges of the cell arms protrude through the walls of the bath. The bath was filled with iced water, salted ice water, and chloroform/dry ice to achieve temperatures of 273, 253, and 212 K, respectively.

OH radicals were generated from the excimer laser pulsed photolysis of *t*-butyl hydroperoxide at 248 nm (Lambda Physik Compex).



Photolysis energies were typically 30 – 100 mJ pulse⁻¹; the laser beam had an area of ~ 1 cm² and was introduced through one of the arms of the reactor. The laser was typically operated at 10 Hz although some studies were carried out at lower pulse repetition rates to ensure that fresh gas was present for each photolysis pulse.

Materials used: Acetylene (BOC, > 99.5%), nitrogen (BOC oxygen free), and oxygen (Air Products, high purity, 99.999%) were all used direct from the cylinder, *t*-C₄H₉OOH (Sigma Aldrich, 70% v/v aqueous), deuterated nitric acid (Sigma Aldrich, 65 wt.% in D₂O, 99 atom % D), acetone-*d*₆ (Sigma Aldrich, 99.9%), hydrogen, (BOC, 99.999%), deuterium, (Air Products, 99.999%).

OH (OD) radicals were detected by off-resonance LIF with excitation taking place at ~ 282 (287) nm ($A^2\Sigma(v=1) \leftarrow X^2\Pi(v=0)$, $Q_1(1)$) with the fluorescence being observed at ~ 308 (313) nm through an interference filter (Corion, 310 ± 10 nm) by a photomultiplier tube mounted perpendicular to the plane of the probe and photolysis lasers. Probe radiation was generated from a YAG pumped (Spectra Physics GCR-150) dye laser (Spectra Physics PDL-3) operating either with Rhodamine6G for OH detection or with a mixture of Rhodamine6G and Pyrromethene 597, which allowed access to both OH and OD probe radiation. The photomultiplier signal was integrated using a boxcar averager (SRS) and digitised before being sent to a personal computer for data analysis. The time delay between the photolysis and probe laser pulses was controlled by homemade software and was varied to build up a time profile of the OH signal following photolysis. Kinetic traces were typically 200 – 400 data points each averaged 2 – 10 times depending on the signal-to-noise ratio.

The reactions were carried out under *pseudo-first-order* conditions such that the concentration of acetylene was always in great excess over the OH. Under these conditions, with nitrogen as bath gas, OH removal is determined by reactions R1 and R4:



where reaction R4 accounts for the reaction of OH with the precursor or diffusion out of the observation region of the reactor. The time dependence of the OH signal I_f is given by

$$I_f(t) = I_f(0)\exp^{-k't} \quad (\text{E1})$$

where $I_f(0)$ and $I_f(t)$ are the OH signals at times zero and t , respectively, and k' is the observed *pseudo-first-order* rate coefficient ($k' = k_1[\text{Acetylene}] + k_4$). It follows that a plot of k' against [Acetylene] should be linear with a gradient equal to k_1 ; a typical experimental OH decay trace and bimolecular plot for the OH + C₂H₂ reaction in N₂ bath gas are shown in Figure 2.

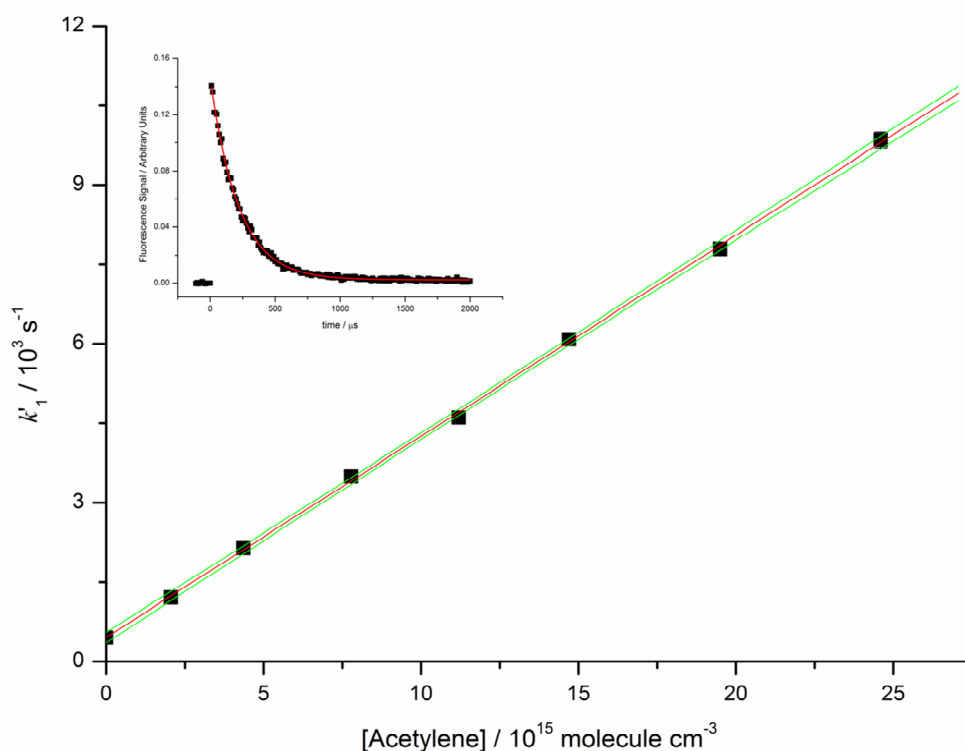


Figure 2: Typical bimolecular plot for the $\text{OH} + \text{C}_2\text{H}_2 \rightarrow \text{HO-C}_2\text{H}_2$ reaction at 295 K and 10 Torr total pressure in pure nitrogen; corresponding to an experimental k_1 value of $(3.79 \pm 0.03) \times 10^{-13} \text{ cm}^3 \text{ molecule}^{-1} \text{ s}^{-1}$. The inset shows a typical experimental OH decay trace measured in the presence of C_2H_2 ($1.11 \times 10^{16} \text{ molecule cm}^{-3}$) using pure N_2 bath gas; the fit to equation E1 corresponds to a *pseudo-first-order* decay coefficient of $(4610 \pm 30) \text{ s}^{-1}$.

3.4 OH + C₂H₂ Pressure Dependence in Nitrogen Bath Gas

A detailed investigation of the pressure dependence of reaction R1 has been carried out at room temperature, with rate coefficients measured between 5 and 300 Torr in pure N_2 . A plot of the experimental rate coefficients as a function of bath gas pressure is provided in Figure 3, with values reported by other studies included for comparison. The k_1 measurements presented here demonstrate similar falloff behaviour to those reported by Bohn et al.,²⁸ and Wahner and Zetzsch,²³ both of whom used laser flash photolysis with laser resonance absorption detection, and to measurements by Sorenson et al. who studied the kinetics of reaction R1 using the relative rates technique.²⁴ McKee et al. investigated

hole of the cavity is minimised. However, if O₂ was present in the cavity during experiments by McKee et al., then it would likely be made apparent by either biexponential OH decays, or a more marked decrease in k_1 values, neither of which were observed during their study. Therefore the reason for the discrepancy between the falloff behaviour for the OH + C₂H₂ reaction reported by McKee et al. and by other studies remains unclear.

One dimensional master equation (ME) analysis of the k_1 values measured during this work has been carried out using the freely available, open source program, MESMER.³⁷ The energy well depth of the HO-C₂H₂ adduct, relative to the reactants, was calculated by Dr David Glowacki using high-level electronic structure theory as -130.7 kJ mol⁻¹. Furthermore, rotational constants and vibrational frequencies for all stationary points across the PES were derived from *ab initio* calculations using CBS-QCI/APNO//6-311+G(3df, 2p) model chemistry. The activation energy, E_{act} , was fixed as 5 kJ mol⁻¹, in good agreement with experimental and theoretical values reported by other studies,^{25, 26, 38} while the Arrhenius A -factor and ΔE_{down} values were allowed to float during the simulation. The best fit through these experimental data was achieved using an A -factor of $(6.99 \pm 0.34) \times 10^{-12}$ cm³ molecule⁻¹ s⁻¹, and a ΔE_{down} of 433 ± 63 cm⁻¹; the energy transfer parameter lies within the expected range for N₂ bath gas. The best fit through the experimental data points following full ME analysis is shown as the solid line in Figure 3, and predicts a k_1^∞ value of $(9.10 \pm 0.45) \times 10^{-13}$ cm³ molecule⁻¹ s⁻¹, consistent with values of (8.11 ± 0.82) and $(8.30 \pm 0.80) \times 10^{-13}$ cm³ molecule⁻¹ s⁻¹, reported by Liu et al.,³² and Schmidt et al.,²² respectively, using Ar bath gas, and in excellent agreement with the values of 9.0×10^{-13} cm³ molecule⁻¹ s⁻¹ reported by Wahner and Zetzsch in N₂,²³ and $(9.69 \pm 0.30) \times 10^{-13}$ cm³ molecule⁻¹ s⁻¹ measured by Sorenson et al. during a smog chamber/ photoreactor study.²⁴ A summary of k_1^∞ values reported in the literature is presented in Table 1. Fulle et al. studied reaction R1 in He bath gas using high pressure apparatus between 1 and 130 Bar;³⁹ extrapolation of their measurements yields a k_1^∞ value of 1.8×10^{-12} cm³ molecule⁻¹ s⁻¹, significantly greater than the results from all other studies. It has been suggested that additional OH removal processes were operating during the experiments of Fulle et al., resulting in a systematic overestimation of k_1 . The proposed additional OH sinks include reaction with trace gas impurities in the acetylene, or with the HO-C₂H₂ adduct, or with radicals produced from 193 nm photolysis of acetylene.

Nevertheless, given the level of agreement between all other studies of reaction R1 (Table 1), it is reasonable to assume the error lies with the work of Fulle et al. Moreover, the consistency between the falloff behaviour reported here with that observed during other studies, support the credibility of the experimental kinetic technique employed here.

Reference	Pressure Gas	Temperature / K	Experimental Technique	$k_1^\infty / 10^{-13} \text{ cm}^3 \text{ molecule}^{-1} \text{ s}^{-1}$
This Study	Nitrogen	295	FP-LIF	(9.10 ± 0.45)
Sorenson et al., 2003	Air	296	Relative Rate	(9.69 ± 0.30)
McKee et al., 2007	Nitrogen / He / SF ₆	298	FP-CRDS	(8.56 ± 0.15)
Bohn et al., 1996	Nitrogen	296	UV-Laser long path absorption	(10.7 ± 0.7)
Wahner and Zetzsch, 1985	Nitrogen	298	CW-UV-laser absorption	9.0
Liu et al., 1989	Argon	300	Pulsed Radiolysis UV absorption	(8.11 ± 0.82)
Schmidt et al., 1985	Argon	295	FP-LIF	(8.3 ± 0.8)
Michael et al., 1980	Argon	298	FP-RF	(7.76 ± 0.73)
Fulle et al., 1997	Helium	300	FP-LIF	18.0

Table 1: Comparison of limiting high-pressure rate coefficients, k_1^∞ , for the OH + C₂H₂ reaction at room temperature with values published in the literature.

3.5 Branching Ratios from Kinetic Studies in Excess O₂

The rate of OH removal in the presence of acetylene in pure N₂ bath gas is defined as follows:

$$-\frac{d[\text{OH}]}{dt} = k_1[\text{C}_2\text{H}_2][\text{OH}] + k_4[\text{OH}] \quad (\text{E2})$$

Under *pseudo-first-order* conditions equation E2 simplifies to:

$$-\frac{d[\text{OH}]}{dt} = k_1'[\text{OH}] \quad (\text{E3})$$

where $k_1' = k_1[\text{C}_2\text{H}_2] + k_4$. As the OH concentration at time t , $[\text{OH}]_t$, is proportional to the corresponding OH signal, $I_f(t)$, integrating equation E3 with respect to time yields equation E1. Therefore the gradient of a bimolecular plot of k_1' against $[\text{C}_2\text{H}_2]$ is equal to k_1 , an example of which can be seen in the upper line in Figure 4. In the presence of molecular O_2 , the HO- C_2H_2 adduct will react with O_2 to regenerate OH via reaction R2a. For the reaction of OH with acetylene in the presence of O_2 :

$$-\frac{d[\text{OH}]}{dt} = k_1[\text{C}_2\text{H}_2][\text{OH}] - k_{2a}[\text{adduct}][\text{O}_2] + k_4[\text{OH}] \quad (\text{E4})$$

Provided the $[\text{O}_2]$ is in excess, the [adduct] can be treated in steady state, such that $k_1[\text{C}_2\text{H}_2][\text{OH}] = k_2[\text{adduct}][\text{O}_2]$. Under these conditions the biexponential solution for equation E4 reduces to the single exponential solution of:

$$\begin{aligned} -\frac{d[\text{OH}]}{dt} &= k_1[\text{C}_2\text{H}_2][\text{OH}] - \frac{k_{2a}[\text{O}_2]k_1[\text{C}_2\text{H}_2][\text{OH}]}{k_2[\text{O}_2]} + k_4[\text{OH}] \\ &= k_1[\text{C}_2\text{H}_2][\text{OH}] \left(1 - \frac{k_{2a}}{k_2} \right) + k_4[\text{OH}] \end{aligned} \quad (\text{E5})$$

The effective bimolecular rate coefficient for OH loss in the presence of O_2 will be reduced compared with its value in nitrogen (k_1) due to OH regeneration via reaction R2a, as shown by the lower lines in Figure 4. The rate coefficient for OH loss in the presence of nitrogen is $k_{\text{N}_2} = k_1$, and with O_2 present $k_{\text{O}_2} = k_1(1 - k_{2a}/k_2)$. The yield of OH, Φ_{OH} , is given by:

$$\Phi_{\text{OH}} = \frac{k_{2a}}{k_{2a} + k_{2b}} \quad (\text{E6})$$

and therefore:

$$\Phi_{\text{OH}} = 1 - \frac{k_{\text{O}_2}}{k_{\text{N}_2}} \quad (\text{E7})$$

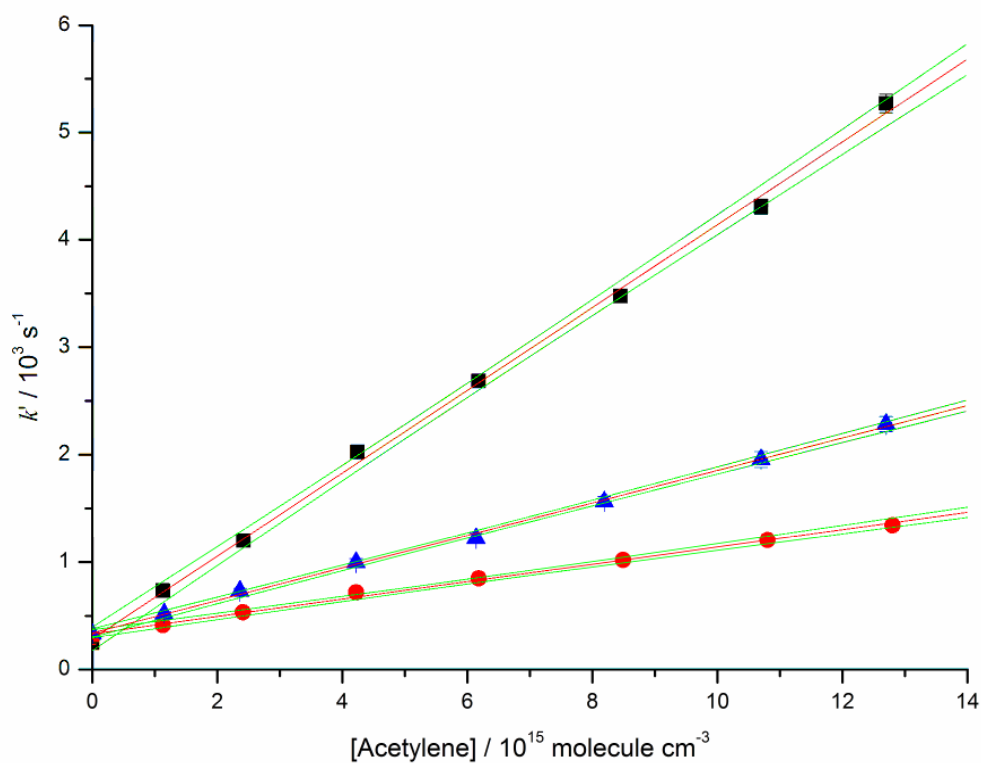


Figure 4: Bimolecular Plots for the $\text{OH} + \text{C}_2\text{H}_2 \rightarrow \text{Products}$ reaction at 10 Torr total pressure and 295 K: in pure N_2 bath gas (\blacksquare), 2% O_2 and 98% N_2 (\bullet), and in 94% O_2 and 6% N_2 (\blacktriangle). Error bars are purely statistical at the 1σ level.

3.6 Error in OH Yield Measurements

Linear-least squares analyses of the bimolecular plots provide the experimental rate coefficient uncertainty at the 1σ level. The purely statistical errors in the experimental OH yield, Φ_{OH} , were calculated by propagating the fractional errors in the nitrogen and oxygen rate coefficients as follows:

$$\text{Experimental } \Phi_{\text{OH}} \text{ Error} = \Phi_{\text{OH}} \times \sqrt{\left[\left(\frac{\text{Error in } k_{\text{N}_2}}{k_{\text{N}_2}} \right)^2 + \left(\frac{\text{Error in } k_{\text{O}_2}}{k_{\text{O}_2}} \right)^2 \right]} \quad (\text{E8})$$

3.7 Experimental OH yields for the OH + C₂H₂/O₂ Reaction

Room temperature Φ_{OH} have been measured for the OH + C₂H₂/O₂ reaction using the ratio of rate coefficients measured in the presence and absence of O₂ (equation E7), as a function of total pressure (10 – 75 Torr), and O₂ concentration. The slopes of the least squares linear fits through the bimolecular plots shown in Figure 4 give experimental rate coefficients of $(3.92 \pm 0.05) \times 10^{-13} \text{ cm}^3 \text{ molecule}^{-1} \text{ s}^{-1}$ in pure N₂ bath gas, and effective rate coefficients of (8.08 ± 0.21) and $(15.11 \pm 0.23) \times 10^{-14} \text{ cm}^3 \text{ molecule}^{-1} \text{ s}^{-1}$ using oxygen fractions, $f\text{-O}_2$, of 0.02 and 0.94, respectively; measurements made in the presence of O₂ correspond to respective experimental Φ_{OH} of (0.79 ± 0.02) and (0.61 ± 0.01) . The dependence of the observed Φ_{OH} on total pressure and O₂ concentration are presented in Figure 5.

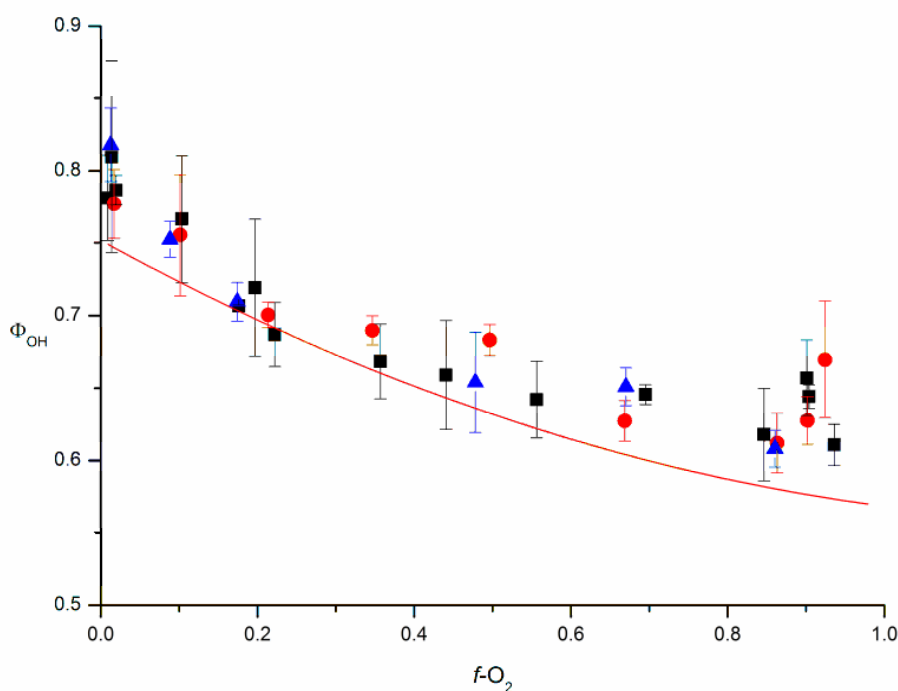


Figure 5: Dependence of the OH Yield, Φ_{OH} , for the OH + C₂H₂/O₂ reaction at 295 K as a function of oxygen fraction, $f\text{-O}_2$, at total pressures of 10 (■), 25 (●), and 75 Torr (▲). The error bars are purely statistical at the 1 σ level. The line shows the fit obtained from the ME/VRC-TST calculations (details are included in the text).²⁷

The Φ_{OH} is independent of total pressure but strongly dependent on $f\text{-O}_2$, with greatest Φ_{OH} observed under low $f\text{-O}_2$ conditions, consistent with the results of Bohn et al.²⁸ Furthermore, the Φ_{OH} observed here are in excellent agreement with values reported by other studies (Table 2), measured at total pressures ranging between 2 and 760 Torr.

Reference	Experimental Technique	Temperature / K	Pressure / Torr	Bath Gas	$f\text{-O}_2$	Φ_{OH}
This Study	Pulsed Flash Photolysis – Laser Induced Fluorescence	295	10	N_2/O_2 mix	0.02	0.79 ± 0.02
					0.20	0.71 ± 0.05
					0.94	0.61 ± 0.01
			25	N_2/O_2 mix	0.02	0.78 ± 0.02
					0.21	0.70 ± 0.01
					0.86	0.61 ± 0.02
			75	N_2/O_2 mix	0.01	0.82 ± 0.03
					0.09	0.75 ± 0.01
					0.86	0.61 ± 0.01
Hatakeyama et al. ³¹	End Product Analysis	297 ± 2	760	Synthetic Air	0.21	0.70 ± 0.30
Bohn et al. ²⁸	Pulsed Laser Photolysis – UV long path absorption	296 ± 2	760	N_2/O_2 mix	0.01	0.82 ± 0.04
				Synthetic Air	0.21	0.70 ± 0.04
				O_2	1	0.57 ± 0.04
Zhang and Peeters ⁴⁰	Discharge Flow - MS	288	2	He/O_2 mix	0.06	0.75

Table 2: Literature values for room temperature OH yields for the OH + C_2H_2 reaction in the presence of oxygen.

The independence of the Φ_{OH} on total pressure is consistent with PES calculations for the HO-C₂H₂ + O₂ reaction which report no deep energy wells on either stable product path into which an intermediate could stabilise (Figure 1), such that following peroxy radical formation, the reactions proceed on an irreversible downhill energy path to products regardless of pressure. Bohn et al. proposed that the stable product branching ratios observed for the OH + C₂H₂/O₂ reaction depend on the degree of thermalisation of the nascent HO-C₂H₂ adduct,²⁸ here we confirm this hypothesis by complementing experimental measurements with theory.²⁷

As discussed previously, potential energy surface calculations for the OH + C₂H₂/O₂ system confirm that the glyoxal + OH product path is attributed to reaction of the *cis*-adduct conformer with O₂, while formic acid + formyl radical are formed following reaction of the *trans*-adduct isomer with O₂ (Figure 6). At 298 K the nascent HO-C₂H₂ adduct forms with approximately 146.6 kJ mol⁻¹ excess energy. At these energies the *cis*- and *trans*-adduct isomers interconvert rapidly over a relatively small barrier of approximately 17 kJ mol⁻¹, and exist in near equal populations (Figure 6, short time dashed line).

Under low $f\text{-O}_2$, this excess energy is dissipated through stabilizing collisions with bath gas molecules, and the adduct conformers can be considered in thermal equilibrium prior to reaction with O₂ (Figure 6, long time solid line). At 298 K thermal equilibrium the *cis*-to-*trans* adduct population ratio is ~0.78:0.22. As the product branching ratio is controlled by the stereochemistry of the HO-C₂H₂ adduct at the point of O₂ addition, the thermal distribution of conformers is consistent with the experimental Φ_{OH} of ~0.80 observed using low $f\text{-O}_2$ (Figure 5). Under high $f\text{-O}_2$ reactive collisions with O₂ occur under non-equilibrium conditions, with a *cis*-to-*trans* adduct population ratio closer to 1, bicyclic and acid channel branching ratios of ~0.5 are expected. In reality not all collisions with O₂ are reactive, some collisional deactivation does occur resulting in experimental Φ_{OH} closer to 0.6. Significantly, under atmospheric conditions ($f\text{-O}_2 = 0.21$) Φ_{OH} of ~0.70 are observed, indicating that quantum state relaxation is in an intermediate regime, with a substantial fraction of the HO-C₂H₂ population intercepted by O₂ before relaxation is complete.

0.20 and 0.9 $f\text{-O}_2$ are plotted in Figure 7, and present further evidence of the effect of chemical activation on the product branching ratio associated with acetylene oxidation.

OH yield measurements made at $f\text{-O}_2$ of 0.01 demonstrate the most marked dependence on temperature, with Φ_{OH} increasing from ~ 0.6 at 498 K to ~ 0.9 at 212 K. Under low O_2 conditions, the *cis*- and *trans*-adduct conformers are in thermal equilibrium prior to reaction with O_2 . As temperatures decrease the thermal distribution of conformers shifts in favour of the more stable *cis*-adduct which reacts with O_2 to give OH. Therefore the Φ_{OH} observed under these conditions correspond to the temperature-dependent fraction of *cis*-adduct present at thermal equilibrium.

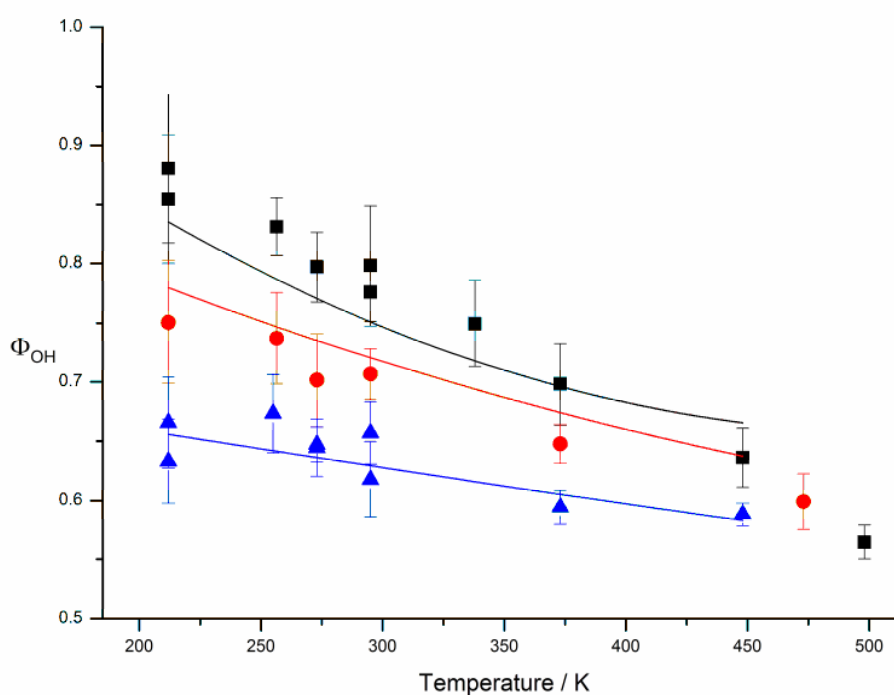


Figure 7: Variation of the OH Yield, Φ_{OH} , for the $\text{OH} + \text{C}_2\text{H}_2/\text{O}_2$ reaction with temperature at oxygen fractions, $f\text{-O}_2$, of 0.01 (■), 0.20 (●), and 0.90 (▲). The error bars are purely statistical at the 1σ level. The lines show the results obtained from the corresponding ME/VRC-TST calculations.²⁷

In contrast, OH yield measurements made at $f\text{-O}_2$ of 0.90 are relatively insensitive to temperature with respect to measurements made using $f\text{-O}_2$ of 0.01, with Φ_{OH} increasing from ~ 0.6 at 498 K to ~ 0.65 at 212 K. Under high O_2 conditions, reactive collisions between the HO-C₂H₂ adduct and O₂ occur before the internal quantum states of the nascent adduct have fully relaxed, resulting in Φ_{OH} measurements that are near independent of the thermal distribution of conformers. Under near atmospheric conditions ($f\text{-O}_2 = 0.20$) the observed Φ_{OH} are not yet at the thermal limit, and a significant fraction of the HO-C₂H₂ adduct ensemble are intercepted by O₂ before the internal quantum states are in thermal equilibrium (Figure 7).

3.9 Theoretical Treatment of the OH + C₂H₂/O₂ Reaction

A theoretical description of the OH + C₂H₂/O₂ system has been provided by Drs David Glowacki and Stephen Klippenstein using a model that combines *ab initio* quantum chemistry with stochastic master equation (ME) simulations and variable reaction coordinate transition state theory (VRC-TST). In VRC-TST both the definition and value of the reaction coordinate are optimized when calculating the reactive flux from reactants to products, this approach has proven effective at calculating rate coefficients for barrierless association reactions with a strictly loose transition state, and therefore offers a suitable method for calculating rate coefficients for the HO-C₂H₂ adduct + O₂ reaction.⁴¹⁻⁴³ Within this scheme, the reactant modes are divided into internal vibrational modes that occur in both the association fragments and association complex, known as conserved modes, and transitional modes, which include rotational modes and translational motion of the fragments, and change from free rotation and translation at infinite separation of the fragments, to vibrational motion and overall rotation upon formation of the association complex. The transitional modes are treated through Monte Carlo integration of the classical phase space representation, while the conserved modes are treated as direct sums over the quantum harmonic oscillator energies. The consideration of various pivot points for the transitional mode fragment rotations yields a range of reaction coordinate definitions. Minimization of the calculated transition state partition function with respect to the

intermolecular separation and the pivot point locations yields the VRC-TST prediction for the rate coefficient.

The successful implementation of the VRC-TST approach requires accurate potential energies for the intermolecular interaction of the reactants (HO-C₂H₂ and O₂) at arbitrary orientations for separations ranging from 2 to 4 Angstroms. Second order multireference perturbation theory employing a complete active space wavefunction (CASPT2) provides an efficient and accurate means for calculating these interaction energies. Here they employed direct CASPT2(7e, 5o) samplings with a modest basis set (aug-cc-pVDZ) to obtain the orientation dependence for these interaction energies.

Higher-level calculations along the minimum energy path (MEP) yield a one-dimensional correction to these orientation dependent energies. Here, these correction are broken down into three separate terms: (i) a correction for limitations in the basis set, (ii) a correction for limitations in the CASPT2(7e,5o) method, and (iii) a correction for the effect of relaxation of the fragment geometries. The basis set corrections were obtained from basis set extrapolation of CASPT2(7e,5o) evaluations with basis the aug-cc-pVTZ and aug-cc-pVQZ basis sets of Dunning.⁴⁴ A higher order correction to the CASPT2(7e,5o) method was obtained from Davidson corrected internally-contracted multi-reference configuration interaction (CI+QC)^{45, 46} calculations with a (9e,7o) active space, where the extra orbital correlates with the OO sigma bond. The geometry relaxation correction is obtained from constrained optimizations with the CASPT2(7e,5o)aug-cc-pVDZ method. These electronic structure calculations were all performed with MOLPRO.⁴⁷

There are two possible channels available for the O₂ association reaction with each HO-C₂H₂ conformer, with O₂ adding either *cis* or *trans* to the carbon-carbon bond of each isomer. Fully corrected one-dimensional MEP energies have been calculated for each of the four possible channels as a function of C-O separation, and show *cis* O₂ addition to the *trans*-adduct to be the most energetically favoured path; the remaining three additions have similar MEP potentials. The favoured energetics result in a significantly greater addition rate at low temperatures for the *trans*-adduct conformer. As the C-O separation approaches 2 Angstroms, the MEP potential for *cis* O₂ addition to the *cis*-adduct conformer approaches that of *cis* O₂ addition to the *trans*-adduct. Consequently, the rate coefficients

for *trans*- and *cis*-adduct associations with O₂ converge at higher temperatures. Theoretical values for the rate coefficients k_{2a} and k_{2b} , calculated using VRC-TST, are shown in Figure 8 as a function of temperature.

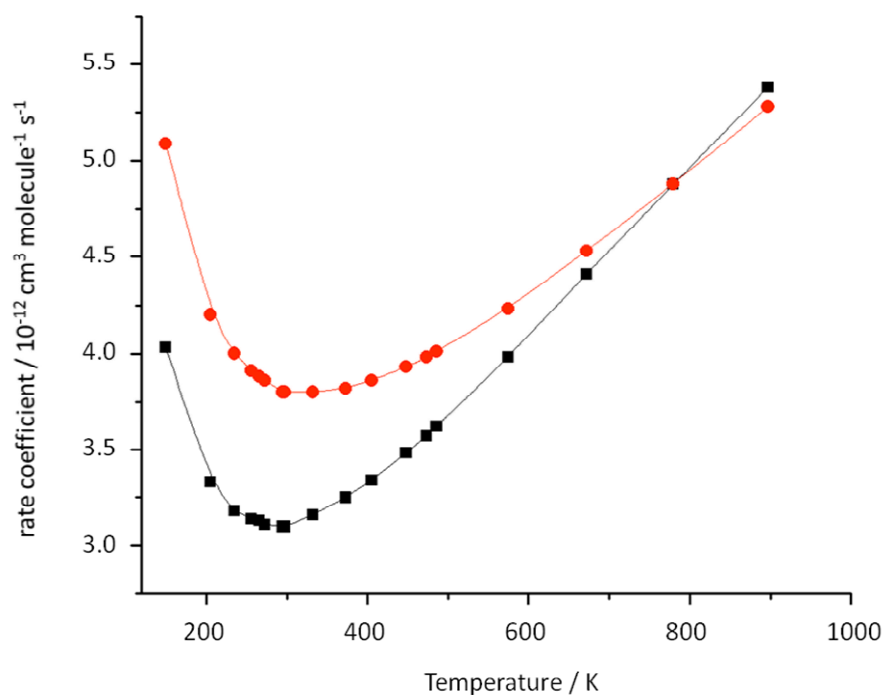


Figure 8: VRC-TST thermal rate coefficients for the O₂ association reaction with *cis*- (■) and *trans*-adduct conformers (●) based on CASPT2(7,5)/aug-cc-pVDZ orientation samplings coupled with one-dimensional corrections along the MEP based on CI+QC(9,7)CBS estimates which include geometry relaxation effects.²⁷

3.9.1 Master Equation (ME) Model

The energy grained master equation (ME) has been described previously in chapter 1. Here the model begins with the bimolecular OH + C₂H₂ reaction to give either the *cis*- or *trans*-adduct. The rotational and vibrational energy levels of each species are partitioned into grains with an energy width no larger than a few kJ mol⁻¹. Within the energy resolved state space the adduct conformers can undergo several processes, they can interconvert to the complementary isomer; transfer energy through inelastic bath gas collisions;

redissociate back to reactants; or react with O₂. A differential equation is constructed to describe the grain populations within each species, and model the rates of collisional energy transfer into and out of each grain, as well as the probability that a population will undergo reactive processes. The whole set of coupled differential equations are solved using matrix methods to define the energy resolved, microcanonical rate coefficients that describe the conversion between reactants, intermediates and products; and ultimately provide rate coefficients on the macroscopic or phenomenological level. All RRKM and ME calculations reported in this work were carried out using the MESMER programme.³⁷ Microcanonical rate coefficients for isomerisation and dissociation reactions were calculated using RRKM theory as:

$$k(E) = \frac{W(E)}{h\rho(E)} \quad (\text{E9})$$

where $W(E)$ is the sum of states at the transition state, h is Planck's constant, and $\rho(E)$ is the reactant density of states.

Collisional energy transfers were treated using an exponential down model parametrized with the temperature independent ΔE_{down} . Reaction of the *cis*- and *trans*-adduct isomers was incorporated into the model as "irreversible bimolecular sinks", as both reactions proceed rapidly to products, and effectively determine the product identity. It was assumed during the ME simulations performed here that the barrierless association kinetics of O₂ with the *cis*- and *trans*-adduct are independent of any internal vibrational excitation within the adduct radicals or O₂, and the equilibration of any rotational excitation within the radicals is very fast as a consequence of interactions with the bath gas. This allowed the *pseudo-first-order* irreversible rate coefficients, $k_{\text{loss}}^{\text{cis}}$ and $k_{\text{loss}}^{\text{trans}}$, to be calculated as follows:

$$k_{\text{loss}}^{\text{cis}} = k_{\text{O}_2+\text{cis}}^{\text{VRC-TST}}(T)[\text{O}_2] \quad (\text{E10})$$

$$k_{\text{loss}}^{\text{trans}} = k_{\text{O}_2+\text{trans}}^{\text{VRC-TST}}(T)[\text{O}_2] \quad (\text{E11})$$

where VRC-TST denotes a rate coefficient obtained from the aforementioned VRC-TST calculations, and [O₂] is calculated based on the experimental pressure and f -O₂.

Sums and densities of states for calculating the ME matrix elements were calculated using vibrational harmonic oscillator approximations and by treating all molecules and transition state structures as either 2D classical rotors or 3D asymmetric classical rotors. For OH, C₂H₂, and the *trans*-adduct, rotational constants, vibrational frequencies, and energies from B3LYP/6-311+G(3df,2p) geometry optimizations and vibrational analysis. For the OH + C₂H₂ association transition state, microcanonical rate coefficients were calculated utilising the inverse Laplace transform (ILT) method. For the *cis*- and *trans*-adduct isomers and the transition state connecting them geometry optimizations and vibrational analysis at both the B3LYP/6-31G(2df,p) and B3LYP/6-311+G(3df,2p) levels of theory were performed. Subsequently, UCCSD(T)-ROHF single point energy calculations were extrapolated to the infinite basis set limit using the cc-pVTZ and cc-pVQZ basis sets.

Full ME simulations of the OH + C₂H₂/O₂ system have been run in order to determine theoretical stable product yields and investigate the time-dependent energy distributions of the *cis*- and *trans*-adduct conformers. Initially, the irreversible bimolecular sinks were included in the model, and all population initialized in OH + C₂H₂. Steady state product yields were then determined following addition of O₂ at *f*-O₂ of 0.01, 0.10, and 0.90 at 298 K and 760 Torr, giving respective Φ_{OH} of 0.751, 0.718, and 0.630. Under these model conditions, the adduct conformers are kept in approximate steady state owing to their rate of formation being slow relative to their rates of removal; consequently their concentrations never accumulate appreciably. In order to demonstrate the time-dependent energy distributions of the adduct conformers a second simulation was ran for which all initial population was placed in the *cis*- and *trans*-adducts. The initial energy was chosen as the average nascent adducts energy after crossing the OH + C₂H₂ association barrier; at 298 K this energy is 146.6 kJ mol⁻¹ above the *cis*-adduct minimum. At *f*-O₂ of 0.01, 0.10, and 0.90 the steady state product yields determined following addition of O₂ to the adduct conformers were identical to within three decimal places to the yields obtained with all population initialized in OH + C₂H₂. Significantly, these simulations allow relaxation of the nascent *cis*- and *trans*-adduct energy distribution to be visualised, and simultaneously give the product yields. The results of ME/VRC-TST calculations at 298 K and 760 Torr are shown

in Figure 9. The three-dimensional plots show the evolution of *cis*- and *trans*-adduct rovibrational quantum states as a function of time and energy.

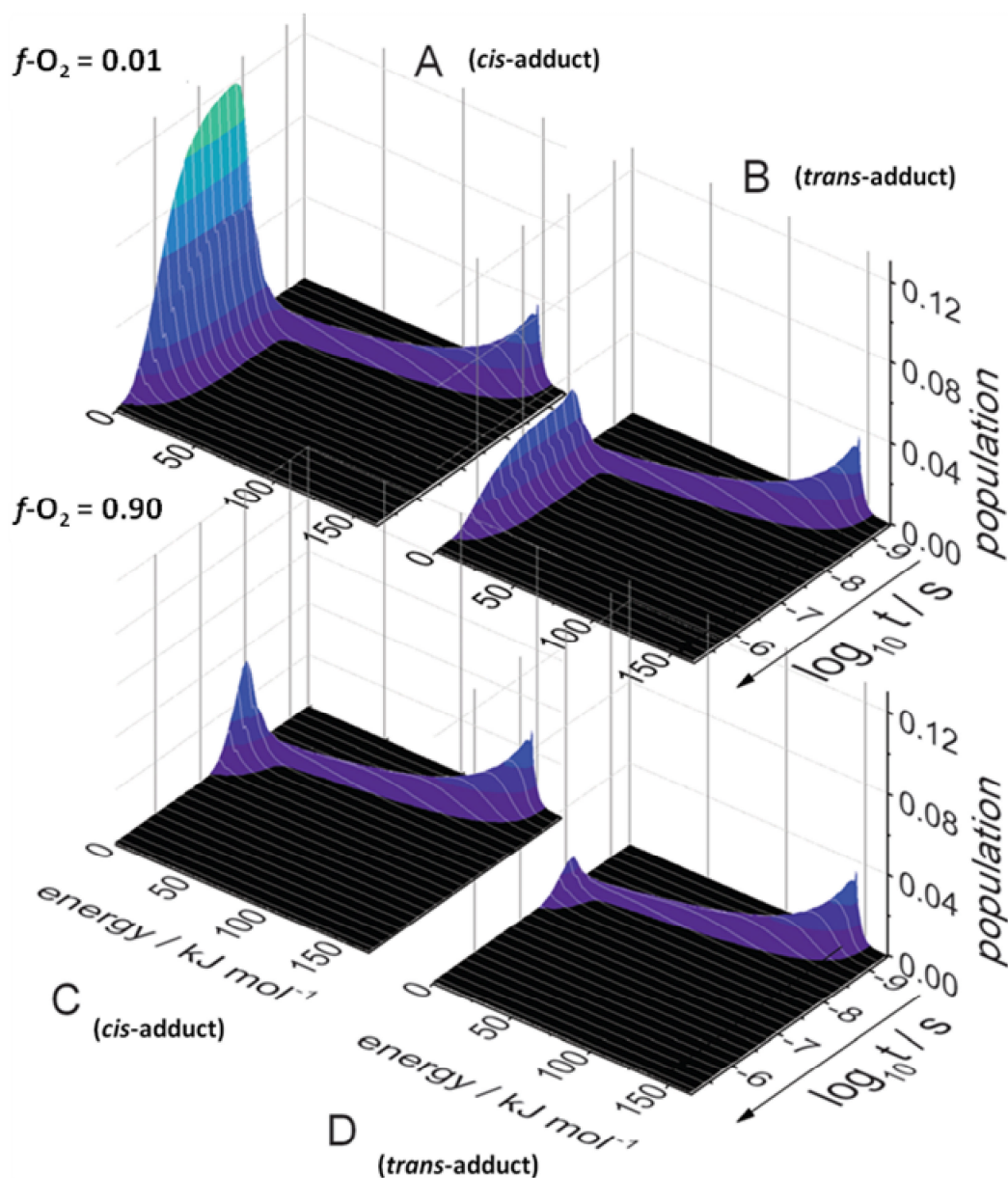


Figure 9: Results from ME-VRC/TST calculations at 298 K and 760 Torr showing evolution of the vibrational state distributions in *cis*- and *trans*-adduct isomers, as a function of both energy and time. (A and B) show results with $f\text{-O}_2 = 0.01$ for *cis*- and *trans*-adduct, respectively, (C and D) show results with $f\text{-O}_2 = 0.90$ for *cis*- and *trans*-adduct, respectively.²⁷

By definition, the nascent adduct forms at short times with a high degree of internal vibrational energy, under these conditions the populations of *cis*- and *trans*-adducts are essentially identical (Figure 9). The system reaches thermal equilibrium at ~ 17 ns, where the relative populations of the *cis*- and *trans*-adducts shifts in favour of the more stable *cis*-adduct. For $f\text{-O}_2 \sim 0.01$ (Figure 9, A and B), the majority of O_2 addition takes place under equilibrium conditions over the following $10 \mu\text{s}$ in which *cis*-adduct accounts for $\sim 79\%$ of the total adduct population. Under high O_2 conditions, using $f\text{-O}_2$ of ~ 0.90 (Figure 9, C and D), approximately 70% of the adduct population is lost through association with O_2 before vibrational deactivation is complete at ~ 17 ns; with total adduct removal complete within ~ 100 ns.

A final set of simulations was run for which all initial population was placed in the *cis*- and *trans*-adduct isomers, with $146.6 \text{ kJ mol}^{-1}$ excess energy, at 298 K and 760 Torr, but for which the irreversible bimolecular sink O_2 association reactions were turned off. This allows the average energy of the adduct isomers to be calculated as a function of time, and consequently, the time taken for the *cis*- and *trans*-adduct isomers to achieve thermal equilibrium to be determined (upper panel of Figure 10). By comparing this profile with species profiles obtained under identical conditions but with the irreversible bimolecular loss channels turned on, it is possible to determine the fraction of the *cis*- and *trans*-adduct populations that are intercepted by O_2 prior to complete vibrational deactivation under atmospheric conditions ($f\text{-O}_2 = 0.21$). At atmospheric $f\text{-O}_2 \sim 25\%$ of the total *cis*- and *trans*-adduct populations undergo reactive collisions with O_2 before their vibrational quantum states have fully relaxed (lower panel Figure 10).

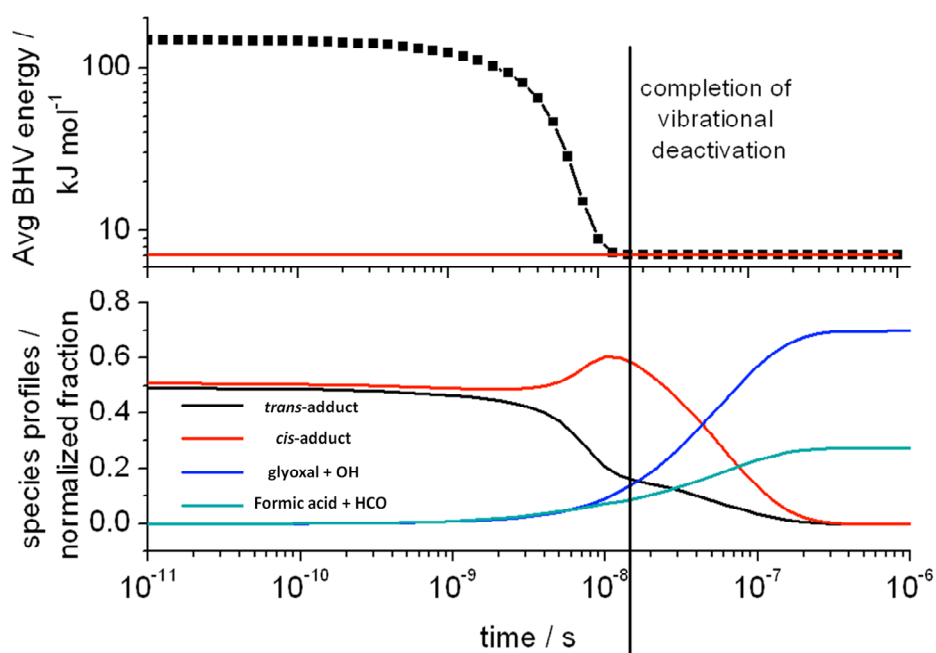


Figure 10: Schematic of the ME/VRC-TST results used to determine the fraction of each adduct conformer intercepted by O_2 before complete of vibrational deactivation at 298 K and 760 Torr. The top panel shows the average adduct energy as a function of time with the irreversible bimolecular loss channels turned off. As indicated, the system reaches thermal equilibrium at ~ 17 ns. The bottom panel shows the species profiles obtained from a separate simulation with the loss channels turned on at 298 K and 760 Torr using f_{O_2} of 0.21. The profiles shows that upon completion of vibrational deactivation $\sim 25\%$ of the total *cis*- and *trans*-adduct population has gone to O_2 addition products.²⁷

3.9.2 Master Equation Sensitivity Analysis

The model described above was used to simulate experimental Φ_{OH} measured as a function of total pressure, oxygen concentration and temperature; the ME/VRC-TST fits through these data points are shown in Figures 5 and 7. The quality of the fitting proved particularly sensitive to two of the model parameters, ΔE_{down} and the relative energy of the *trans*-adduct isomer with respect to the *cis*-adduct ($E_{trans} - E_{cis}$). Consequently, a detailed sensitivity analysis of χ^2 with respect to these model parameters was undertaken, with:

$$\chi^2 = \sum_i \left(\frac{OH_i^{obs} - OH_i^{ME}}{OH_i^{obs}} \right)^2 \quad (E12)$$

where OH_i^{obs} is the experimentally observed Φ_{OH} at some pressure, temperature, and $f-O_2$. OH_i^{ME} is the theoretical Φ_{OH} calculated using ME/VRC-TST under the same conditions, and i is an index that runs over all experimental data points. The results of the sensitivity analysis show a broad minimum in the relevant parameter space, with ΔE_{down} values ranging between 300 – 425 cm^{-1} , and using a conformer energy difference ($E_{trans} - E_{cis}$) of between 3.3 – 3.6 $kJ mol^{-1}$ (Figure 11).

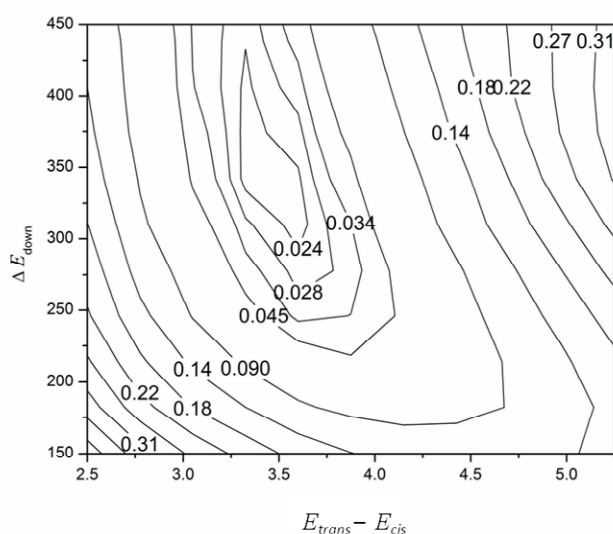


Figure 11: χ^2 surface showing the fitting produced by the ME model to the experimental data points (shown in Figures 5 and 7) as both ΔE_{down} and the $E_{trans} - E_{cis}$ adduct energy difference are varied.²⁷

The optimum ΔE_{down} value range of between 300 and 425 cm^{-1} predicted when simulating experimental Φ_{OH} is consistent with the 433 ± 63 cm^{-1} value used to model $OH + C_2H_2$ falloff kinetics (Figure 3). Furthermore, the energy difference between the *trans*- and *cis*-adduct isomers, favoured at between 3.3 and 3.6 $kJ mol^{-1}$, agrees with the values of 4.56 – 5.89 $kJ mol^{-1}$ (depending on the level of theory) determined from electronic structure calculations to well within the chemical accuracy target of 4 $kJ mol^{-1}$. The ME/VRC-TST fits through experimental data points shown in Figures 5 and 7 used a ΔE_{down} value of 310 cm^{-1} and a $E_{trans} - E_{cis}$ adduct energy difference of 3.5 $kJ mol^{-1}$.

3.10 Biexponential OH decay Traces Kinetics of the adduct + O₂

The nature of the OH decay observed in the presence of acetylene is known to be highly sensitive to trace amounts of O₂.^{22, 29, 36} Under low O₂ conditions, the reaction of the adduct with O₂ can no longer be considered fast relative to formation of the adduct, under certain concentration regimes the OH decay becomes biexponential as both the OH loss through addition, and that generated through secondary chemistry are observed on the same timescale. This kinetic behaviour has been described by previous groups and can be confirmed here by experiments conducted at room temperature and 10 Torr total pressure (Figure 12).

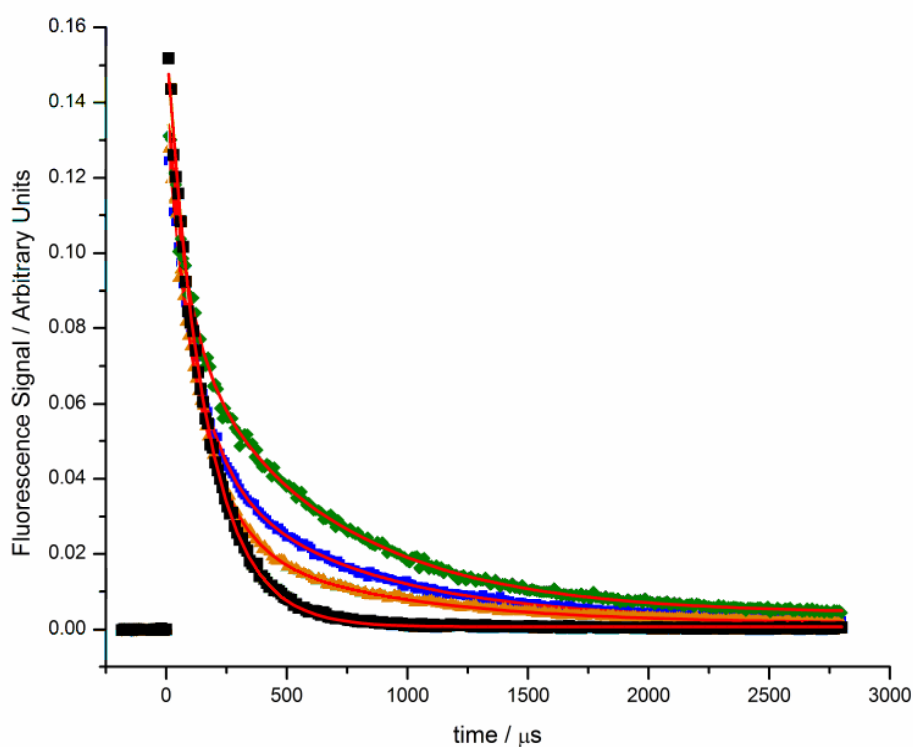


Figure 12: Experimental OH decays in the presence of acetylene with and without trace amounts of O₂ at 295 K and 10 Torr total pressure: oxygen free conditions (■), 2.30×10^{14} molecule cm⁻³ (▲), 5.1×10^{14} molecule cm⁻³ (■), and 1.02×10^{15} molecule cm⁻³ of O₂ (◆); each fit using equation E15.³⁶

In the presence of acetylene using pure N₂ bath gas, OH loss follows *pseudo-first-order* kinetics defined by single exponential decay (black squares in Figure 12); in contrast, biexponential decays are observed when trace amounts of O₂ are introduced to the reaction cell. Biexponential decay traces provide quantitative kinetic information concerning both the addition, and subsequent adduct + O₂ reaction. Under *pseudo-first-order* conditions the rate of change in the concentrations of OH and the HO-C₂H₂ adduct can be defined using the following coupled differential equations:

$$\frac{d[\text{OH}]}{dt} = - (k'_1 + k_4)[\text{OH}] + k'_{2a}[\text{adduct}] \quad (\text{E13})$$

$$\frac{d[\text{adduct}]}{dt} = k'_1[\text{OH}] - (k'_{2a} + k'_{2b} + k_5)[\text{adduct}] \quad (\text{E14})$$

where k_5 accounts for effective *pseudo-first-order* loss of the HO-C₂H₂ adduct via diffusion:

$$\text{adduct} \rightarrow \text{Loss} \quad (\text{R5})$$

The solution to equations E13 and E14 defines the time dependent [OH]_t profile by the following function:

$$[\text{OH}]_t = \frac{[\text{OH}]_0 (S - L_2)}{(L_1 - L_2)} (e^{L_1 t} - e^{L_2 t}) + [\text{OH}]_0 e^{L_2 t} \quad (\text{E15})$$

where

$$S = -(k'_1 + k_4)$$

$$M_1 = (k'_1 + k'_{2a} + k'_{2b} + k_4 + k_5)$$

$$M_2 = (k'_1 + k_4) \times (k'_{2a} + k'_{2b} + k_5) - k'_1 k'_{2a}$$

$$L_1 = \frac{-M_1 + \sqrt{(M_1)^2 - 4M_2}}{2}$$

$$L_2 = \frac{-M_1 - \sqrt{(M_1)^2 - 4M_2}}{2}$$

OH decay traces were monitored at room temperature and 10 Torr total pressure, with experimental conditions controlled such that the acetylene concentration was fixed at $\sim 1.34 \times 10^{16}$ molecule cm^{-3} for all decay traces with and without O_2 . This allowed k_1' for all biexponential decay traces to be fixed as the *pseudo-first-order* decay coefficient obtained from single exponential analysis of the OH decay observed in the absence of O_2 (black squares Figure 12). The gradient of a straight line plot of the total *pseudo-first-order* rate coefficient for the HO-C₂H₂ adduct + O_2 reaction, $k_2' (k_{2a}' + k_{2b}' + k_5)$ against O_2 concentration gives the bimolecular rate coefficient for the HO-C₂H₂ adduct + O_2 reaction, k_2 . The bimolecular plots derived from biexponential analysis of the OH decay traces observed for the OH + C₂H₂/O₂ reaction at 10 Torr total pressure and temperatures of 295 and 212 K are presented in Figure 13, and correspond to respective k_2 values of (6.15 ± 0.27) and $(19.29 \pm 0.12) \times 10^{-12}$ cm^3 molecule⁻¹ s⁻¹. Siese and Zetsch quantified k_2 directly by monitoring biexponential OH decays at room temperature and pressures ranging from 12 – 200 Torr of argon, and found k_2 to be pressure independent with a value of $(4.2 \pm 0.5) \times 10^{-12}$ cm^3 molecule⁻¹ s⁻¹;²⁹ but did not investigate the temperature dependence.

The room temperature k_2 value measured here is in reasonable agreement with the result reported by Siese and Zetsch, and with the value calculated by Dr Klippenstein using VRC/TST of $3 - 4 \times 10^{-12}$ cm^3 molecule⁻¹ s⁻¹ (Figure 8).²⁷ The VRC/TST calculations predict k_2 to increase with decreasing temperature, in qualitative agreement with the measurements presented here. However, the theory predicts k_2 to increase only fractionally as temperatures decrease from 295 to 212 K, whereas the experimental measurements suggest k_2 is far more sensitive to temperature, increasing by a factor of 3 over the same temperature range (Figure 13). The aforementioned ME/VRC-TST calculations suggest that under atmospheric conditions ~25% of the vibrationally hot adduct population are intercepted by O_2 before the internal quantum states are quenched through bath gas interactions; the experimental k_2 measurements presented here suggest this likely represents a lower limit.

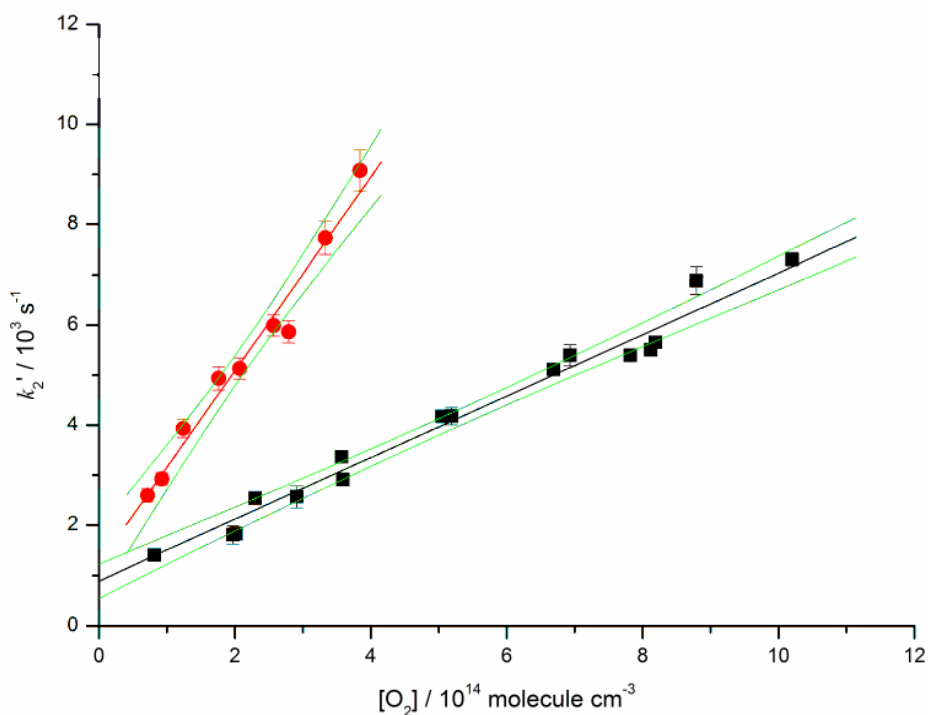


Figure 13: Temperature dependence of the bimolecular rate coefficient, k_2 , for the $\text{HO-C}_2\text{H}_2 + \text{O}_2 \rightarrow$ products reaction, measured at 10 Torr total pressure and 295 (■) and 212 K (●), corresponding to k_2 values (6.15 ± 0.27) and $(19.29 \pm 0.12) \times 10^{-12} \text{ cm}^3 \text{ molecule}^{-1} \text{ s}^{-1}$, respectively. The error bars are purely statistical at the 2σ level.

3.11 Isotopic Studies on the $\text{OH} + \text{C}_2\text{H}_2/\text{O}_2$ System

As mentioned previously, there is currently conflicting evidence in the scientific literature concerning the mechanism by which OH is regenerated in the $\text{OH} + \text{C}_2\text{H}_2/\text{O}_2$ reaction. The mechanism proposed by Maranzana and Barker,³⁴ and the experimental and theoretical work presented in this chapter, suggest that hydrogen atom exchange should not occur in the OH regeneration channel; a schematic of this reaction path is provided in Figure 14. However, the experimental evidence of Schmidt et al.²² and Hatakeyama et al.,³¹ suggest isotope exchange does occur. The OD formation reported by Schmidt et al. during the $\text{OH} + \text{C}_2\text{D}_2/\text{O}_2$ reaction suggest either conversion of the $\text{HO-C}_2\text{H}_2$ adduct to a vinoxy intermediate prior to O_2 association, a path shown by Maranzana et al. to have a barrier

height some 20 kJ mol⁻¹ higher than the entrance channel of the OH + C₂H₂ reactants,³⁴ or significant proton scrambling in one of the intermediates. Here we conduct an extensive isotopic study of the OH + C₂H₂/O₂ system which aims to elucidate the mechanism responsible for OH generation and resolve the conflicting results reported in the literature.

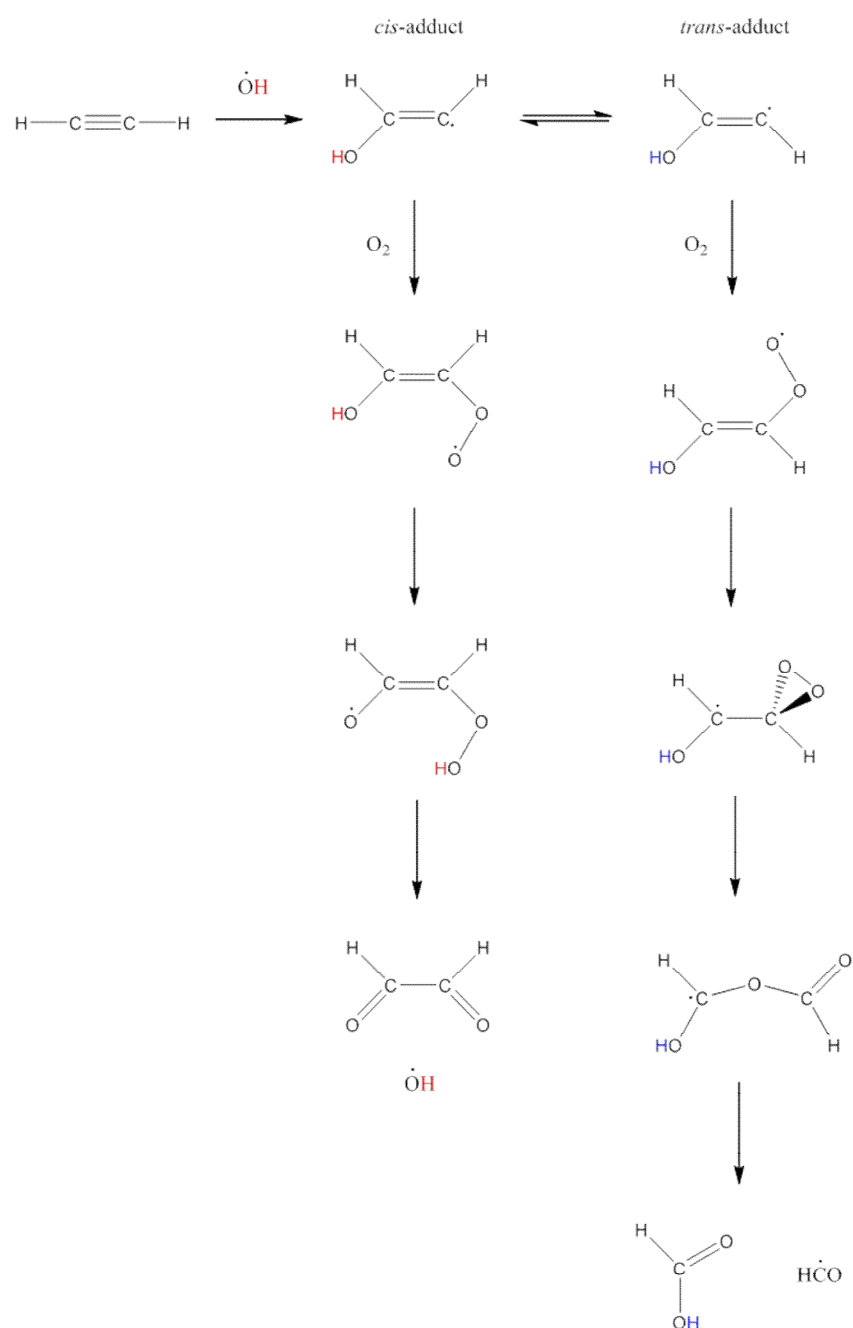


Figure 14: Theoretical pathways leading to glyoxal and formic acid production through the OH initiated oxidation of acetylene.

3.11.1 Pressure Dependence in the OD + C₂H₂ Reaction

At ambient temperatures OD reacts with acetylene via pressure dependent OD-addition across the triple bond (reaction R6).



The room temperature kinetics of reaction R6 has been studied by monitoring OD decay in the presence of excess acetylene using pure N₂ bath gas, with OD generated via 248 nm photolysis of deuterated nitric acid (P2):



A typical room temperature experimental OD decay trace and bimolecular plot for the OD + C₂H₂ reaction in N₂ bath gas is shown in Figure 15; corresponding to a k_6 value of $(5.39 \pm 0.08) \times 10^{-13} \text{ cm}^3 \text{ molecule}^{-1} \text{ s}^{-1}$ at 10 Torr total pressure.

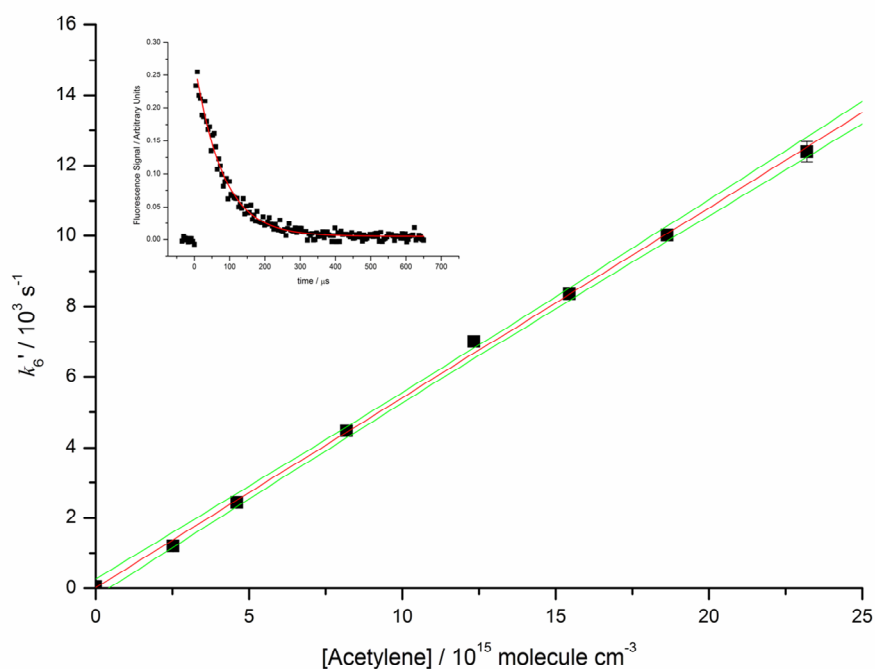


Figure 15: Typical bimolecular plot for the OD + C₂H₂ → DO-C₂H₂ reaction at 295 K and 10 Torr total pressure in pure nitrogen; corresponding to an experimental k_6 value of $(5.39 \pm 0.08) \times 10^{-13} \text{ cm}^3 \text{ molecule}^{-1} \text{ s}^{-1}$. A typical experimental OD decay trace and fit to equation E1 and corresponding to a *pseudo-first-order* decay coefficient of $(1239 \pm 285) \text{ s}^{-1}$ is included in the insert.

The pressure dependence of reaction R6 has been studied at total pressures ranging between 5 and 240 Torr of N₂. Experimental falloff data for the reaction of both OH and OD with acetylene are presented in Figure 16, together with literature values for the OH + C₂H₂ reaction.

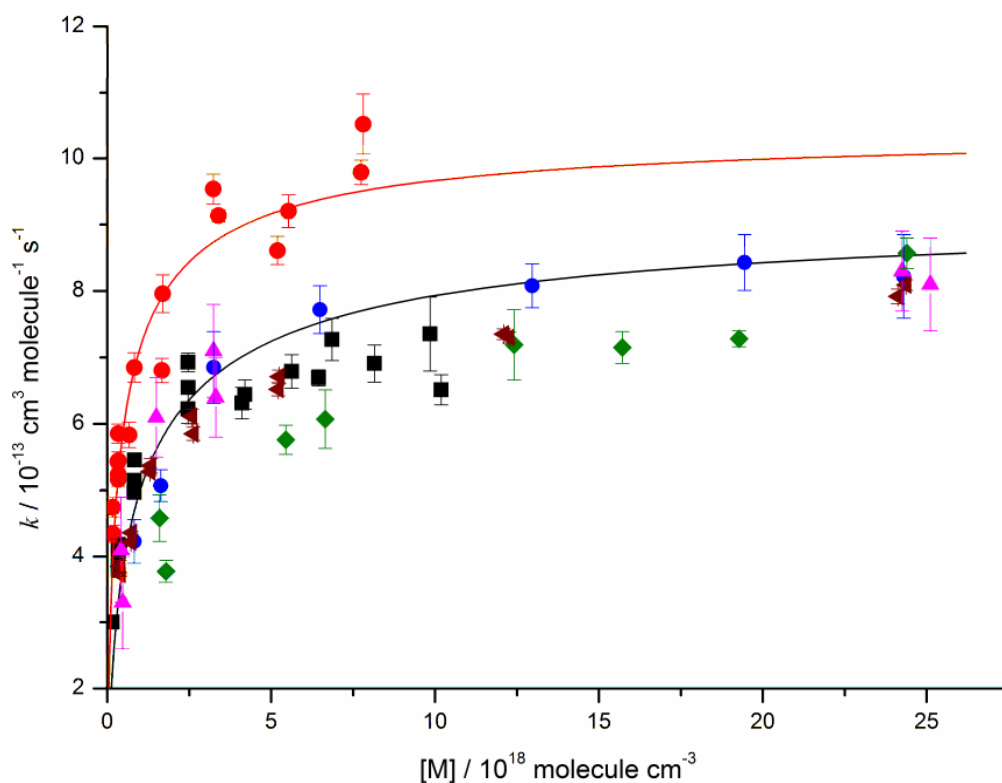


Figure 16: Pressure dependence of the bimolecular rate coefficients k_1 (■) and k_6 (●) for the respective addition of OH and OD radicals to acetylene in pure N₂ bath gas at 295 K, measured during this work; included are the pressure dependent bimolecular rate coefficients, k_1 , for the OH + C₂H₂ reaction measured by Sorensen et al. in air (●); Wahner and Zetzsch in N₂ (▲), McKee et al. in N₂ (◆), and Bohn et al. in N₂ (▲). The solid lines show the best fit through the experimental k_1 (black) and k_6 (red) values measured here using MESMER at 295 K using N₂ bath gas.

These results clearly demonstrate that in the falloff region, acetylene reacts faster with OD than OH at any given pressure. In order to explain this difference in reactivity, consideration must be given to the isotopic effect on the internal energy of the adducts, and in particular

to their vibrational energies. To a first approximation, molecular vibrations can be described as simple harmonic oscillations; with equally spaced, non-degenerate quantum states, and energy levels defined by:

$$E(v) = \left(v + \frac{1}{2} \right) \nu_q \text{ cm}^{-1} \quad (v = 0, 1, 2 \dots) \quad (\text{E16})$$

where v is the vibrational quantum number, and ν_q is the vibrational frequency of mode q defined by:

$$\nu_q = \frac{1}{2\pi c} \sqrt{\left(\frac{k_q}{M_q} \right)} \quad (\text{E17})$$

where k_q is the force constant for the mode, and M_q is the effective mass of the mode. The effective mass depends on both the nature of the vibration (eg. a symmetric or asymmetric stretch) and the atoms involved. This approximation states that the normal vibrational modes of the DO-C₂H₂ adduct that involve the deuterium atom, should oscillate at lower energies than the equivalent vibrations of the HO-C₂H₂ adduct, consequently, the successive vibrational states of the deuterated isotopologue lie closer in energy; or alternatively, the density of vibrational states (number of vibrational quantum states per unit energy) is greater for the DO-C₂H₂ adduct than the HO-C₂H₂ adduct. The Lindemann-Hinshelwood mechanism for association reactions in the falloff region defines two channels available to the nascent adduct, either collisional stabilization through interaction with bath gas molecules, or dissociation back to reactants; formally, this mechanism can be described as a competition between bimolecular quenching, and unimolecular dissociation. RRKM theory states unimolecular rate coefficients are inversely proportional to the density of states (equation E9). As both reactions R1 and R6 involve cleavage of a C-C bond and formation of a C-O bond, the net energy released following addition of OH and OD to acetylene is expected to be near identical. However, the greater density of states associated with the DO-C₂H₂ adduct means there are more quanta available to distribute this energy, therefore it is less likely that sufficient energy will be partitioned in the C-O mode in order to dissociate back to reactants. Consequently, the DO-C₂H₂ dissociates back to reactants at a

slower rate than the HO-C₂H₂ adduct, and therefore a greater proportion of the DO-C₂H₂ adduct population become stabilized through collisions with bath gas molecules.

At limiting high pressure k_1 and k_6 are dependent on the respective rates at which OH and OD associate with acetylene, and independent of the dissociation rates of the resulting adducts. It therefore follows that at infinite pressure k_1 and k_6 should converge on the same high pressure limiting rate coefficient. One dimensional master equation (ME) analysis of the k_6 values measured here has been carried out using MESMER.³⁷ The energy well depth of the DO-C₂H₂ adduct relative to the reactants, and the activation energy were estimated to be -130.7 kJ mol⁻¹ and 5 kJ mol⁻¹, respectively, identical to the values used to fit the observed pressure dependence in the rate coefficient, k_1 , for the OH + C₂H₂ reaction. The Arrhenius A -factor and ΔE_{down} values were allowed to float during the simulation. The vibrational frequencies for the DO-C₂H₂ adduct were calculated by Dr R Shannon from *ab initio* calculations using the b3lyp/6-311+G(3df, 2p) level of theory. Vibrational frequencies and rotational constants for OD were obtained from experimental values published in the literature.⁴⁸ The best fit through these experimental data was achieved using an A -factor of $(7.91 \pm 0.44) \times 10^{-12}$ cm³ molecule⁻¹ s⁻¹, and a ΔE_{down} of 449 ± 83 cm⁻¹; the energy transfer parameter lies within the expected range for N₂ bath gas, and agrees well with the value of 433 ± 63 cm⁻¹ used to fit the pressure dependence in k_1 . The best fit through the experimental data points following full ME analysis is shown as the solid red line in Figure 16, and predicts a k_6^∞ value of $(10.30 \pm 0.57) \times 10^{-13}$ cm³ molecule⁻¹ s⁻¹. This value is in reasonable agreement with the k_1^∞ value of $(9.10 \pm 0.45) \times 10^{-13}$ cm³ molecule⁻¹ s⁻¹ predicted using MESMER, although it does not agree within the combined statistical uncertainties, but is in excellent agreement with the k_1^∞ values of (9.69 ± 0.30) and $(10.7 \pm 0.7) \times 10^{-13}$ cm³ molecule⁻¹ s⁻¹ reported by Sorenson et al.²⁴ and Bohn et al.,²⁸ respectively, where experimental measurements extended to higher pressures.

3.11.2 Kinetic OD Yields

Room temperature OD yields, Φ_{OD} , have been measured for the OD + C₂H₂/O₂ reaction using the ratio of rate coefficients measured with and without O₂ present at 10 Torr total pressure as a function of $f\text{-O}_2$; using the same approach used previously to quantify

Φ_{OH} for the $\text{OH} + \text{C}_2\text{H}_2/\text{O}_2$ system (Equation E7), with OD generated by the photolysis of deuterated nitric acid at 248 nm. The principle being that if no isotope exchange occurs on route out to glyoxal + OD products and all the OD reacting with acetylene is recycled as OD, then we would expect Φ_{OD} measurements to demonstrate a similar dependence on $f\text{-O}_2$ as Φ_{OH} measured for the $\text{OH} + \text{C}_2\text{H}_2/\text{O}_2$ system. However, if isotope exchange does occur and a significant fraction of the OD reacting with acetylene is recycled as OH then Φ_{OD} measurements derived from OD decays with and without O_2 should underestimate the glyoxal branching ratio as they are blind to the fraction of OD regenerated as OH. Bimolecular plots for the $\text{OD} + \text{C}_2\text{H}_2$ reaction in pure N_2 (black squares) and using 0.01 (red circles) and 0.90 $f\text{-O}_2$ (blue triangles) are presented in Figure 17.

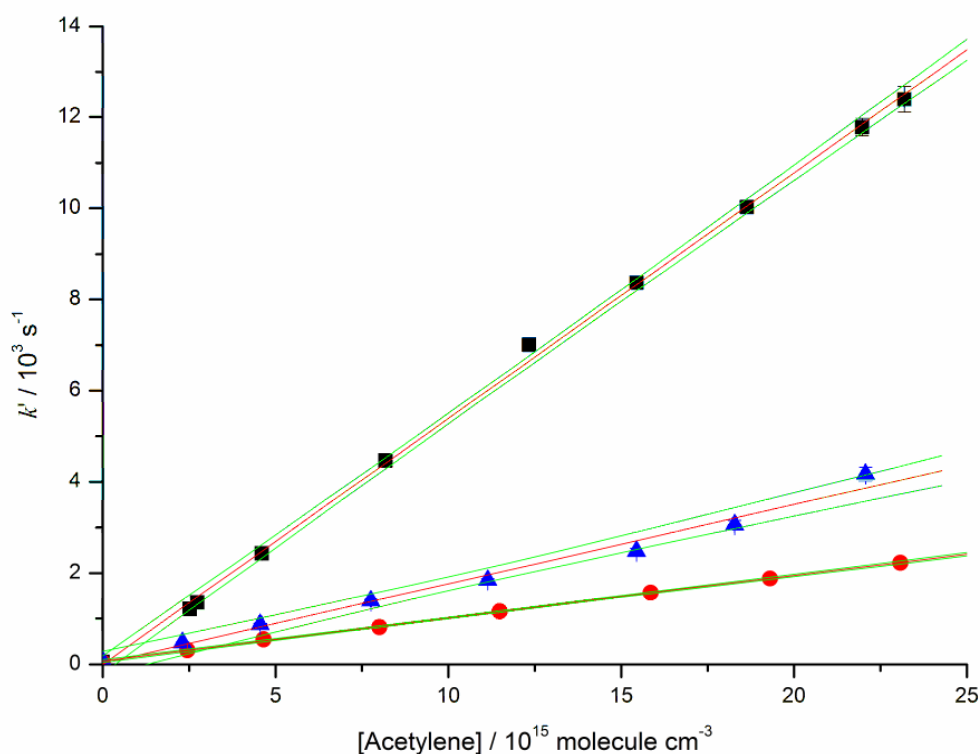


Figure 17: Bimolecular Plots for the $\text{OD} + \text{C}_2\text{H}_2 \rightarrow \text{Products}$ reaction at 10 Torr total pressure and 295 K: in pure N_2 bath gas (■), 1% O_2 and 99% N_2 (●), and in 90% O_2 and 10% N_2 (▲). Error bars are purely statistical at the 1σ level.

The slopes of the least squares linear fits through the bimolecular plots shown in Figure 17 give experimental rate coefficients of $(5.24 \pm 0.11) \times 10^{-13} \text{ cm}^3 \text{ molecule}^{-1} \text{ s}^{-1}$ in pure N_2 bath gas, and effective rate coefficients of (9.88 ± 0.23) and $(16.58 \pm 0.04) \times 10^{-14} \text{ cm}^3 \text{ molecule}^{-1} \text{ s}^{-1}$ using oxygen fractions, $f\text{-O}_2$, of 0.01 and 0.90, respectively; with measurements made in the presence of O_2 corresponding to respective experimental Φ_{OD} of 0.81 ± 0.03 and 0.68 ± 0.02 . Room temperature Φ_{OD} measured for the $\text{OD} + \text{C}_2\text{H}_2/\text{O}_2$ reaction as a function of $f\text{-O}_2$ at 10 Torr, together with Φ_{OD} measured for the $\text{OH} + \text{C}_2\text{H}_2/\text{O}_2$ reaction under the same conditions are presented in Figure 18. The good agreement between the two measurements for the $\text{OH} + \text{C}_2\text{H}_2/\text{O}_2$ and $\text{OD} + \text{C}_2\text{H}_2/\text{O}_2$ shown in Figure 18, with, if anything, Φ_{OD} measurements slightly higher than the corresponding Φ_{OH} value, suggest that no significant isotope exchange is occurring.

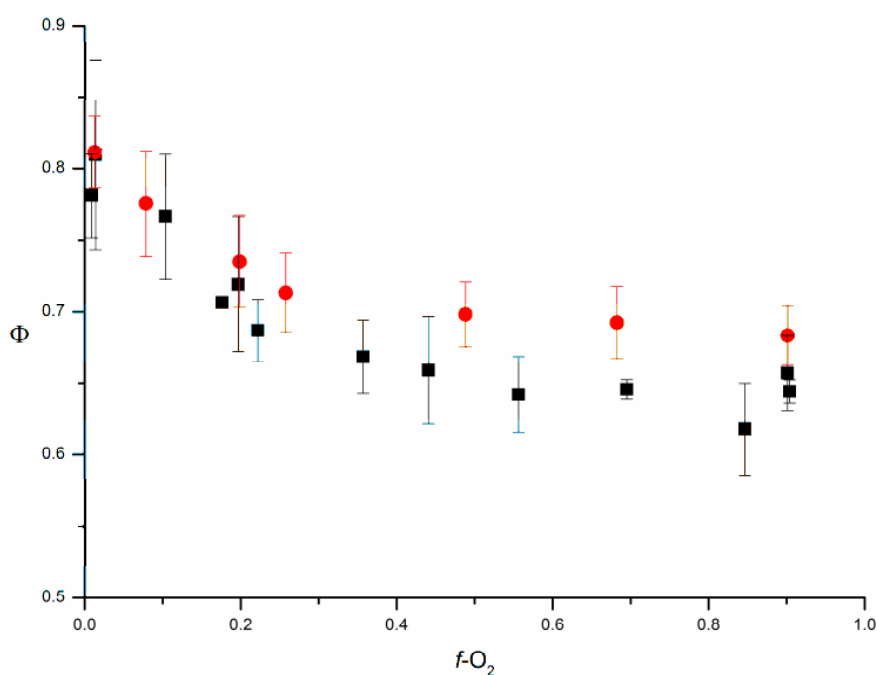


Figure 18: Room temperature Φ_{OH} for the $\text{OH} + \text{C}_2\text{H}_2/\text{O}_2$ reaction (■) and Φ_{OD} for the $\text{OD} + \text{C}_2\text{H}_2/\text{O}_2$ reaction (●) at 10 Torr total pressure as a function of $f\text{-O}_2$.³⁶

More qualitative experiments were then carried out during which OH was probed for directly following photolytic generation of OD in excess C₂H₂ and O₂. Intriguingly, OH was detected under a range of conditions, using various OD precursors, with 248 nm photolysis used in each case; specifically, deuterated nitric acid (P2), ozone photolysis in the presence of deuterium (P3, R7), and acetone-*d*6 in the presence of O₂ (P4, R8):



The sensitivity of the apparatus to OH and OD fluorescent detection will likely differ as they will depend on several factors specific to each radical; the off resonance fluorescence passes through an interference filter before detection via PMT, this filter could bias passage of one radical's fluorescence over the other; furthermore, the bath gas may physically quench the fluorescence of one radical more efficiently than the other, making the relative detection sensitive to the boxcar integration gate settings. Therefore in order to quantify Φ_{OH} for the OD + C₂H₂/O₂ reaction, the relative response factor of the experimental setup for OH and OD detection must first be quantified. Ozone photolysis in combination with reaction with either D₂ or H₂ was used to calibrate the relative sensitivity of the apparatus to OD and OH. Initial room temperature experiments were undertaken using deuterated nitric acid, DNO₃, as the photolytic OD source, in *f*-O₂ of 0.01 at 10 Torr total pressure. In order to minimise acidic hydrogen atom exchange before the precursor reaches the photolysis cell, D₂O was bubbled through the cell overnight to condition the walls of the gas lines. Figure 19 shows a typical radical profile observed during the OD + C₂H₂/O₂ reaction, with OH formation occurring on a similar timescale to OD decay; significantly, no OH growth was observed in the absence of O₂. OH growth profiles were fitted using the following biexponential function:

$$[\text{OH}]_t = \left(\left([\text{OH}]_g \times \left(\frac{k'_g}{k'_g - k'_1} \right) \right) \times \left(e^{-k'_1 t} - e^{-k'_g t} \right) \right) + \left([\text{OH}]_{\text{phot}} \times e^{-k'_1 t} \right) \quad (\text{E18})$$

where the terms $[\text{OH}]_g$ and $[\text{OH}]_{phot}$ represent respective OH signal heights due to growth and photolysis of isotopic impurities in the precursor, and the *pseudo-first-order* rates of OH growth and loss are defined by the coefficients k_g' and k_l' , respectively. All OH growth profiles were fit using the k_g' values derived from single exponential analysis of the OD decay trace.

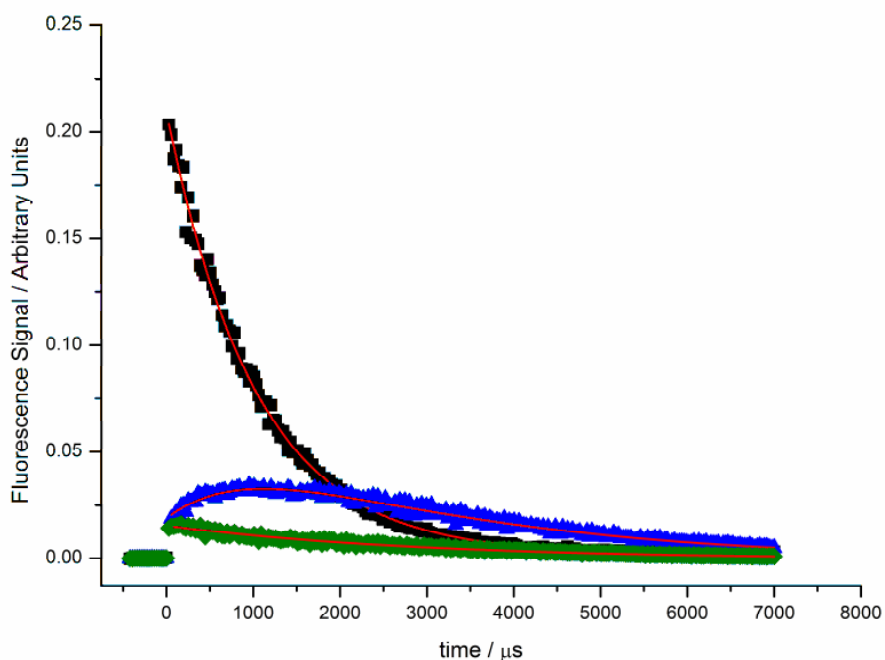


Figure 19: Experimental radical profiles during the OD + C₂H₂/O₂ reaction showing OD decay (■) and OH growth (▲) occurring on the same timescale at 10 Torr and 295 K; included is the OH profile in the absence of O₂ (◆).³⁶

Experimental $[\text{OH}]_g$ values were corrected for the difference in radical sensitivity at 10 Torr allowing isotope exchange yields to be calculated from the ratio of OH-to-OD signal heights. However, Φ_{OH} measured during these experiments varied considerably from 0.1 to 0.6, and are neither consistent with each other or with the kinetic Φ_{OD} measured under similar conditions (Figure 18).

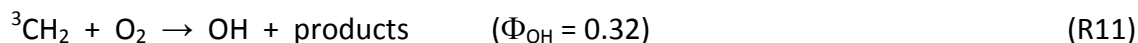
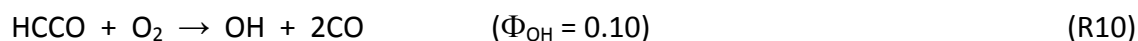
A second set of room temperature experiments were conducting using acetone-*d6* as the OD source, using $f\text{-O}_2$ of 0.06 at 5 Torr total pressure. Radical signal heights were again corrected for the difference in sensitivity under these conditions, and suggest Φ_{OH} between 0.4 and 0.5. While repeat experiments using acetone-*d6* as the OD precursor are more precise than those using DNO_3 , they remain inconsistent with the kinetic Φ_{OD} measured at 10 Torr. Furthermore, the OH growth observed during these experiments occurs on a significantly shorter timescale than OD removal; inconsistent with the proposed chemistry.

A final set of isotope experiments was conducted using ozone photolysis in excess deuterium as OD source at 295 K and 50 Torr total pressure, with the $f\text{-O}_2$ varied between 0.01 and 0.1. OH growth was observed on the timescale of OD removal during these experiments, with an Φ_{OH} of between 0.4 and 0.5. These results are again inconsistent with the kinetic Φ_{OD} measured at 10 Torr.

During this extensive investigation of isotope exchange during the $\text{OD} + \text{C}_2\text{H}_2/\text{O}_2$ reaction, OH production was observed, but with widely differing yields (0.1 – 0.6), and for some precursors (acetone-*d6*) with poor temporal correlation between OD loss and OH production, suggesting that the OH source is secondary chemistry. OH production using acetone-*d6* as OD precursor shows a strong dependence on the excimer laser pulse repetition rate, suggesting OH formation occurs through product photolysis. Figure 20 shows an example of the OD and OH profiles observed when the excimer laser pulse repetition rate was reduced to 1 Hz. In this case, the small OH production is all prompt, and there is no evidence of OH growth on the timescale of OD removal, consistent with the kinetic results presented above, the experimental results of Liu et al.,³² and the potential energy surface calculations by Maranzana et al.,³⁴ and Glowacki and Pilling.³⁵

The production of OH on timescales comparable with OD loss for experiments using either DNO_3 or O_3 in excess deuterium as OD precursor can be explained by the production of $\text{O}(^3\text{P})$ in the reaction cell, produced from the photolysis of NO_2 impurities in the DNO_3 , or following collisional relaxation of the $\text{O}(^1\text{D})$ produced following O_3 photolysis. $\text{O}(^3\text{P})$ reacts with acetylene on a timescale comparable to $\text{OD} + \text{C}_2\text{H}_2$ at low pressures to give HCCO and

$^3\text{CH}_2$ (reaction R9);^{49, 50} both products reacts rapidly in excess O_2 to give OH (Reactions R10 And R11):^{51, 52}



Experimental details in the paper by Schmidt and co-workers are limited, but HNO_3 was used as a photolytic OH precursor in at least some of their experiments. The secondary chemistry described above could explain their detection of OD in the $\text{OH} + \text{C}_2\text{D}_2/\text{O}_2$ system.²²

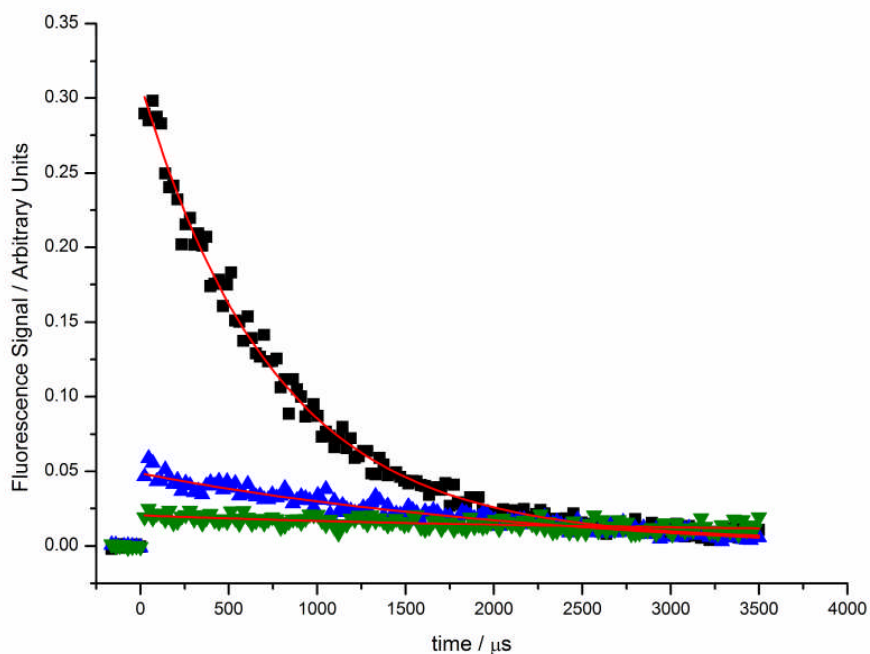


Figure 20: Radical profiles of OD (■) and OH (▲) observed during the $\text{OD} + \text{C}_2\text{H}_2/\text{O}_2$ reaction using acetone-*d*6 as OD precursor at 295 K and 10 Torr total pressure, using an $f\text{-O}_2$ of 0.07, with the excimer laser operating at a pulse repetition rate of 1Hz. Included is the OH profile observed in the absence of acetylene (▼).³⁶

3.12 Conclusions

The radical chemistry responsible for the degradation of atmospheric trace gases is predominantly initiated by OH via either addition or H-atom abstraction, depending on the nature of the radical co-reagent. These bimolecular processes are known to yield nascent products with excited vibrational quantum-states.^{25, 53} Exciting reagent vibrational modes has been shown to influence bimolecular reaction products under single collision conditions.⁵⁴⁻⁵⁷ However, it is widely accepted that at pressures relevant to the troposphere, reactions between radicals and molecules take place in the ground energetic state only. Acetylene, C₂H₂, is the dominant alkyne in the atmosphere, and removed primarily through reaction with OH radicals. The reaction proceeds by preliminary adduct formation between OH and C₂H₂, with subsequent O₂ addition. The first generation oxidation products are glyoxal + OH, or formic acid + HCO. The work presented in this chapter provides a complete description of the OH + C₂H₂ reaction in the presence of varying amounts of O₂ and N₂. A combination of experiment and theory has been used to demonstrate that the stable product branching ratios depend critically on the excited vibrational quantum-state distribution of the adduct at the point of O₂ addition. Significantly, this work has also shown that under atmospheric conditions more than 25% of the total adduct + O₂ reactive flux occurs under non-thermal conditions. Finally, an extensive isotopic study of the OD + C₂H₂/O₂ has been carried out in order to clarify the mechanism responsible for the glyoxal + OH product channel, and resolve conflicting reports in the literature.

3.13 References

1. Blake, N. J.; Blake, D. R.; Sive, B. C.; Chen, T. Y.; Rowland, F. S.; Collins, J. E.; Sachse, G. W.; Anderson, B. E., Biomass burning emissions and vertical distribution of atmospheric methyl halides and other reduced carbon gases in the South Atlantic region. *Journal of Geophysical Research-Atmospheres* 1996, 101, 24151-24164.
2. Greenberg, J. P.; Zimmerman, P. R.; Heidt, L.; Pollock, W., Hydrocarbon and Carbon-Monoxide Emissions from Biomass Burning in Brazil. *Journal of Geophysical Research-Atmospheres* 1984, 89, 1350-1354.
3. Hegg, D. A.; Radke, L. F.; Hobbs, P. V.; Rasmussen, R. A.; Riggan, P. J., Emissions of Some Trace Gases from Biomass Fires. *Journal of Geophysical Research-Atmospheres* 1990, 95, 5669-5675.
4. Fraser, M. P.; Cass, G. R.; Simoneit, B. R. T., Gas-phase and particle-phase organic compounds emitted from motor vehicle traffic in a Los Angeles roadway tunnel. *Environmental Science & Technology* 1998, 32, 2051-2060.
5. Finlayson-Pitts, B. J.; Pitts, J. N. J., *Chemistry of the Upper and Lower Atmosphere. Theory, Experiments and Applications*. Academic Press: San Diego, 2000.
6. Atkinson, R.; Baulch, D.; Cox, R.; Crowley, J.; Hampson, R.; Hynes, R.; Jenkin, M.; Rossi, M.; Troe, J.; Subcommittee, I., Evaluated kinetic and photochemical data for atmospheric chemistry: Volume II—gas phase reactions of organic species. *Atmospheric Chemistry and Physics* 2006, 6, 3625-4055.
7. Greenberg, J. P.; Zimmerman, P. R., Nonmethane Hydrocarbons in Remote Tropical, Continental, and Marine Atmospheres. *Journal of Geophysical Research-Atmospheres* 1984, 89, 4767-4778.
8. Fischer, H.; Brunner, D.; Harris, G. W.; Hoor, P.; Lelieveld, J.; McKenna, D. S.; Rudolph, J.; Scheeren, H. A.; Siegmund, P.; Wernli, H.; Williams, J.; Wong, S., Synoptic tracer gradients in the upper troposphere over central Canada during the Stratosphere-Troposphere Experiments by Aircraft Measurements 1998 summer campaign. *Journal of Geophysical Research-Atmospheres* 2002, 107.
9. Whalley, L. K.; Lewis, A. C.; McQuaid, J. B.; Purvis, R. M.; Lee, J. D.; Stemmler, K.; Zellweger, C.; Ridgeon, P., Two high-speed, portable GC systems designed for the measurement of non-methane hydrocarbons and PAN: Results from the Jungfraujoch High Altitude Observatory. *Journal of Environmental Monitoring* 2004, 6, 234-241.
10. Schmidt, F. M.; Vaittinen, O.; Metsälä, M.; Kraus, P.; Halonen, L., Direct detection of acetylene in air by continuous wave cavity ring-down spectroscopy. *Applied Physics B* 2010, 101, 671-682.
11. Fu, T. M.; Jacob, D. J.; Wittrock, F.; Burrows, J. P.; Vrekoussis, M.; Henze, D. K., Global budgets of atmospheric glyoxal and methylglyoxal, and implications for formation of secondary organic aerosols. *Journal of Geophysical Research-Atmospheres* 2008, 113.
12. Hastings, W. P.; Koehler, C. A.; Bailey, E. L.; De Haan, D. O., Secondary organic aerosol formation by glyoxal hydration and oligomer formation: Humidity effects and equilibrium shifts during analysis. *Environmental Science & Technology* 2005, 39, 8728-8735.
13. Kroll, J. H.; Ng, N. L.; Murphy, S. M.; Varutbangkul, V.; Flagan, R. C.; Seinfeld, J. H., Chamber studies of secondary organic aerosol growth by reactive uptake of simple carbonyl compounds. *Journal of Geophysical Research-Atmospheres* 2005, 110.
14. Liggio, J.; Li, S. M.; McLaren, R., Reactive uptake of glyoxal by particulate matter. *Journal of Geophysical Research-Atmospheres* 2005, 110.

15. DeSain, J. D.; Jusinski, L. E.; Ho, A. D.; Taatjes, C. A., Temperature dependence and deuterium kinetic isotope effects in the HCO(DCO)+O₂ reaction between 296 and 673 K. *Chemical Physics Letters* 2001, 347, 79-86.
16. Lockhart, J.; Blitz, M.; Heard, D.; Seakins, P.; Shannon, R., Kinetic Study of the OH + Glyoxal Reaction: Experimental Evidence and Quantification of Direct OH Recycling. *Journal of Physical Chemistry A* 2013, 117, 11027-11037.
17. Khare, P.; Kumar, N.; Kumari, K. M.; Srivastava, S. S., Atmospheric formic and acetic acids: An overview. *Reviews of Geophysics* 1999, 37, 227-248.
18. Fornaro, A.; Gutz, I. G. R., Wet deposition and related atmospheric chemistry in the Sao Paulo metropolis, Brazil: Part 2 - contribution of formic and acetic acids. *Atmospheric Environment* 2003, 37, 117-128.
19. Galloway, J. N.; Gaudry, A., The Composition of Precipitation on Amsterdam-Island, Indian-Ocean. *Atmospheric Environment* 1984, 18, 2649-2656.
20. Yu, S. C., Role of organic acids (formic, acetic, pyruvic and oxalic) in the formation of cloud condensation nuclei (CCN): a review. *Atmospheric Research* 2000, 53, 185-217.
21. Paulot, F.; Wunch, D.; Crouse, J. D.; Toon, G. C.; Millet, D. B.; DeCarlo, P. F.; Vigouroux, C.; Deutscher, N. M.; Abad, G. G.; Notholt, J.; Warneke, T.; Hannigan, J. W.; Warneke, C.; de Gouw, J. A.; Dunlea, E. J.; De Maziere, M.; Griffith, D. W. T.; Bernath, P.; Jimenez, J. L.; Wennberg, P. O., Importance of secondary sources in the atmospheric budgets of formic and acetic acids. *Atmospheric Chemistry and Physics* 2011, 11, 1989-2013.
22. Schmidt, V.; Zhu, G. Y.; Becker, K. H.; Fink, E. H., Study of OH reactions at high-pressures by excimer laser photolysis - dye laser fluorescence *Berichte Der Bunsen-Gesellschaft-Physical Chemistry Chemical Physics* 1985, 89, 321-322.
23. Wahner, A.; Zetzsch, C., The Reaction of OH with C₂H₂ at Atmospheric Conditions Investigated by CW-UV-Laser-Longpath-Absorption of OH. *Berichte Der Bunsen-Gesellschaft-Physical Chemistry Chemical Physics* 1985, 89, 323-325.
24. Sorensen, M.; Kaiser, E. W.; Hurley, M. D.; Wallington, T. J.; Nielsen, O. J., Kinetics of the reaction of OH radicals with acetylene in 25-8000 Torr of air at 296 K. *International Journal of Chemical Kinetics* 2003, 35, 191-197.
25. McKee, K. W.; Blitz, M. A.; Cleary, P. A.; Glowacki, D. R.; Pilling, M. J.; Seakins, P. W.; Wang, L. M., Experimental and master equation study of the kinetics of OH+C₂H₂: Temperature dependence of the limiting high pressure and pressure dependent rate coefficients. *Journal of Physical Chemistry A* 2007, 111, 4043-4055.
26. Michael, J. V.; Nava, D. F.; Borkowski, R. P.; Payne, W. A.; Stief, L. J., Pressure-Dependence of the Absolute Rate-Constant for the Reaction OH+C₂H₂ from 228 to 413 K *Journal of Chemical Physics* 1980, 73, 6108-6116.
27. Glowacki, D. R.; Lockhart, J.; Blitz, M. A.; Klippenstein, S. J.; Pilling, M. J.; Robertson, S. H.; Seakins, P. W., Interception of Excited Vibrational Quantum States by O₂ in Atmospheric Association Reactions. *Science* 2012, 337, 1066-1069.
28. Bohn, B.; Siese, M.; Zetzsch, C., Kinetics of the OH+C₂H₂ reaction in the presence of O₂. *Journal of the Chemical Society-Faraday Transactions* 1996, 92, 1459-1466.
29. Siese, M.; Zetzsch, C. Addition of OH to Acetylene and Consecutive Reactions of the Adduct with O₂. Part 1-2, 1995.
30. Bohn, B.; Zetzsch, C., Formation of HO₂ from OH and C₂H₂ in the presence of O₂. *Journal of the Chemical Society-Faraday Transactions* 1998, 94, 1203-1210.
31. Hatakeyama, S.; Washida, N.; Akimoto, H., Rate constants and mechanisms for the reaction of OH (OD) radicals with acetylene, propyne, and 2-butyne in air at 297 +/- 2K. *Journal of Physical Chemistry* 1986, 90, 173-178.

32. Liu, A. D.; Mulac, W. A.; Jonah, C. D., Temperature-dependence of the rate constants of the reactions of OH with C₂H₂ and C₂D₂ at 1-atm in Ar and from 333 K to 1273 K. *Journal of Physical Chemistry* 1988, 92, 5942-5945.
33. Yeung, L. Y.; Pennino, M. J.; Miller, A. M.; Elrod, M. J., Kinetics and mechanistic studies of the atmospheric oxidation of alkynes. *Journal of Physical Chemistry A* 2005, 109, 1879-1889.
34. Maranzana, A.; Ghigo, G.; Tonachini, G.; Barkert, J. R., Tropospheric oxidation of ethyne and but-2-yne. 1. Theoretical mechanistic study. *Journal of Physical Chemistry A* 2008, 112, 3656-3665.
35. Glowacki, D. R.; Pilling, M. J., Unimolecular Reactions of Peroxy Radicals in Atmospheric Chemistry and Combustion. *Chemphyschem* 2010, 11, 3836-3843.
36. Lockhart, J.; Blitz, M. A.; Heard, D. E.; Seakins, P. W.; Shannon, R. J., Mechanism of the Reaction of OH with Alkynes in the Presence of Oxygen. *Journal of Physical Chemistry A* 2013, 117, 5407-5418.
37. Glowacki, D. R.; Liang, C. H.; Morley, C.; Pilling, M. J.; Robertson, S. H., MESMER: An Open-Source Master Equation Solver for Multi-Energy Well Reactions. *Journal of Physical Chemistry A* 2012, 116, 9545-9560.
38. Miller, J. A.; Melius, C. F. In *A theoretical analysis of the reaction between hydroxyl and acetylene*, Symposium (International) on Combustion, Elsevier: 1989; pp 1031-1039.
39. Fulle, D.; Hamann, H. F.; Hippler, H.; Jansch, C. P., The high pressure range of the addition of OH to C₂H₂ and C₂H₄. *Berichte Der Bunsen-Gesellschaft-Physical Chemistry Chemical Physics* 1997, 101, 1433-1442.
40. Zhang, Z. Y.; Peeters, J., The Reaction of OH with C₂H₂ and the Subsequent Reaction of Hydroxyvinyl with O₂. In *Physico-Chemical Behaviour of Atmospheric Pollutants*, 1990; Vol. 23, pp 377-382.
41. Klippenstein, S. J., Variational optimizations in the Rice-Ramsberger-Kassel-Marcus theory calculations for unimolecular dissociations with no reverse barrier. *Journal of Chemical Physics* 1992, 96, 367-371.
42. Georgievskii, Y.; Klippenstein, S. J., Transition state theory for multichannel addition reactions: Multifaceted dividing surfaces. *Journal of Physical Chemistry A* 2003, 107, 9776-9781.
43. Klippenstein, S. J.; Georgievskii, Y.; Harding, L. B., Predictive theory for the combination kinetics of two alkyl radicals. *Physical Chemistry Chemical Physics* 2006, 8, 1133-1147.
44. Kendall, R. A.; Dunning, T. H.; Harrison, R. J., Electron-affinities of the 1st-row atoms revisited - Systematic basis-sets and wave-functions. *Journal of Chemical Physics* 1992, 96, 6796-6806.
45. Knowles, P. J.; Werner, H. J., An efficient method for the evaluation of coupling-coefficients in configuration-interaction calculations. *Chemical Physics Letters* 1988, 145, 514-522.
46. Werner, H. J.; Knowles, P. J., An efficient internally contracted multiconfiguration reference configuration-interaction method *Journal of Chemical Physics* 1988, 89, 5803-5814.
47. Werner, H.-J.; Knowles, P. J.; Knizia, G.; Manby, F. R.; Schuetz, M., Molpro: a general-purpose quantum chemistry program package. *Wiley Interdisciplinary Reviews-Computational Molecular Science* 2012, 2, 242-253.
48. Huber, K.-P.; Herzberg, G., *Constants of diatomic molecules*. Springer: 1979.
49. Mahmud, K.; Fontijn, A., A high-temperature photochemistry kinetics study of the reaction of O(³P) atoms with acetylene from 290 K to 1510 K. *Journal of Physical Chemistry* 1987, 91, 1918-1921.
50. Peeters, J.; Boullart, W.; Langhans, I., Branching ratio of the C₂H₂ + O reaction at 290 K from kinetic modeling of relative methylene concentrations versus time profiles in C₂H₂/O/H systems. *International Journal of Chemical Kinetics* 1994, 26, 869-886.
51. Blitz, M. A.; Kappler, C.; Pilling, M. J.; Seakins, P. W., ³CH₂ + O₂: Kinetics and Product Channel Branching Ratios. *Zeitschrift Fur Physikalische Chemie-International Journal of Research in Physical Chemistry & Chemical Physics* 2011, 225, 957-967.

52. Hancock, G.; Haverd, V., A time-resolved FTIR emission study of the gas phase removal processes of $\text{CH}_2((X)^3B_1$ and $\text{CH}_2((a)^1A_1$ in collisions with O_2 . *Chemical Physics Letters* 2003, 372, 288-294.
53. Baeza-Romero, M. T.; Glowacki, D. R.; Blitz, M. A.; Heard, D. E.; Pilling, M. J.; Rickard, A. R.; Seakins, P. W., A combined experimental and theoretical study of the reaction between methylglyoxal and OH/OD radical: OH regeneration. *Physical Chemistry Chemical Physics* 2007, 9, 4114-4128.
54. Sinha, A.; Hsiao, M. C.; Crim, F. F., Bond-Selected Bimolecular Chemistry - $\text{H}+\text{HOD}(4\nu_{\text{OH}})-\text{OD}+\text{H}_2$. *Journal of Chemical Physics* 1990, 92, 6333-6335.
55. Zare, R. N., Laser control of chemical reactions. *Science* 1998, 279, 1875-1879.
56. Yan, S.; Wu, Y.-T.; Zhang, B.; Yue, X.-F.; Liu, K., Do vibrational excitations of CHD_3 preferentially promote reactivity toward the chlorine atom? *Science* 2007, 316, 1723-1726.
57. Crim, F. F., Chemical dynamics of vibrationally excited molecules: Controlling reactions in gases and on surfaces. *Proceedings of the National Academy of Sciences of the United States of America* 2008, 105, 12654-12661.

Chapter 4 Experimental OH Yields following OH initiated Oxidation of Higher Alkynes

4.1 Abstract

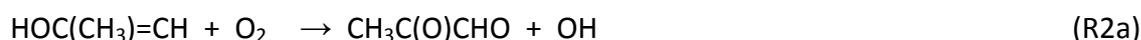
This chapter builds on the work presented previously for the OH + C₂H₂/O₂ system by investigating the OH initiated oxidation of the higher alkynes propyne, C₃H₄, and 2-butyne, C₄H₆. A kinetic study of the OH + C₃H₄ (R1) and OH + C₄H₆ (R4) reactions has been carried out using N₂, or various N₂/O₂ mixture bath gas, over a range of pressures (2 – 75 Torr) and temperatures (212 – 498 K), by monitoring OH via laser induced fluorescence in excess alkyne co-reagent. The reactions of OH with both C₃H₄ and C₄H₆ result in the formation of an association adduct. The room temperature rate coefficient for the OH + C₃H₄ reaction is close to the high pressure limit above 25 Torr with k_1^∞ (295 K) = $(4.20 \pm 0.48) \times 10^{-12}$ cm³ molecule⁻¹ s⁻¹. The room temperature rate coefficient for the OH + C₄H₆ reaction is independent of pressure over this experimental pressure range with k_4^∞ (295 K) = $(1.85 \pm 0.21) \times 10^{-11}$ cm³ molecule⁻¹ s⁻¹; a negative temperature dependence in k_4 was observed over the experimental temperature range of this study. The alkyne-OH adducts formed following reactions R1 and R4 react rapidly with O₂ to generate a bicarbonyl species and recycle OH, or an organic acid and acyl radical as first generation products. The product branching ratios of these reactions have been quantified experimentally for the first time as a function of pressure, temperature and oxygen concentration. The OH yields, Φ_{OH} , for the higher alkyne systems show qualitatively similar behaviour to that observed for the OH + C₂H₂/O₂ system; with Φ_{OH} independent of pressure but critically dependent on the experimental temperature and oxygen fraction, f -O₂. These results are consistent with alkyne oxidation product yields governed by the stereochemistry of the alkyne-OH adduct at the point of reaction with O₂, and suggest that under atmospheric conditions a significant fraction of the total product yield is formed through reaction of the vibrationally excited alkyne-OH adduct with O₂. The atmospheric implications of this study are briefly discussed.

4.2 Background and Previous Work

While acetylene is the dominant alkyne released through automobile exhaust and biomass burning¹, higher chain alkynes such as propyne, C₃H₄, and 2-butyne, C₄H₆, are also produced during these processes.^{2, 3} Both propyne and 2-butyne have been detected in remote and polluted regions in sub ppb concentrations.⁴⁻¹¹ Alkynes are primarily removed from the troposphere through reaction with OH. The asymmetry across the propyne triple bond means OH addition can occur at two sites:



Reaction R1 is at limiting high pressure at pressures and temperature relevant to the troposphere and proceeds with a rate coefficient, k_1 , $\sim 5.71 \times 10^{-12} \text{ cm}^3 \text{ molecule}^{-1} \text{ s}^{-1}$,^{12, 13} giving an atmospheric lifetime of approximately two days (using a mean OH concentration of $10^6 \text{ molecule cm}^{-3}$). The resulting adducts react rapidly with oxygen to give methylglyoxal and OH (R2a, R3a) or an organic acid and acyl radical (R2b, R3b):¹³⁻¹⁵

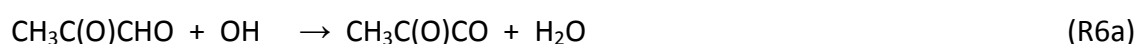


Methylglyoxal has been suggested as a likely precursor of secondary organic aerosol (SOA), with implications for atmospheric air quality and climate.¹⁶ For 2-butyne, a similar reaction sequence has been reported to result in formation of biacetyl and OH (R5a), or acetic acid and acetyl (R5b):¹³⁻¹⁵

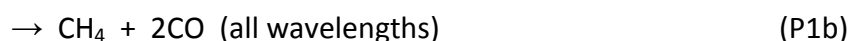


Organic acids are ubiquitous in all phases within the troposphere,¹⁷ where they contribute to rain acidity, in both urban and remote regions,^{18, 19} influence chemistry sensitive to pH, and modify the hygroscopic properties of particulates.²⁰ There is currently significant uncertainty in the atmospheric budgets of organic acids, particularly in regions affected by biomass burning;²¹ alkyne oxidation could be a significant source.

The branching between bicarbonyl and organic acid products in reactions R2, R3 and R5 will clearly affect the HOx budget through primary production of OH. However, secondary chemistry associated with the co-products will also influence the atmospheric HOx budget. The methylglyoxal produced through reactions R2a and R3a is removed primarily through reaction with OH (R6):²²



or by UV photolysis (P1):²³

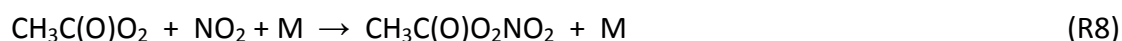


Reaction channel R2b and photolysis channels P1a and P1d are HOx generating as the formyl radical and hydrogen atom produced are rapidly converted to HO₂ in the atmosphere.²⁴

Under atmospheric conditions the CH₃C(O)CO radical produced in reactions R6a and P1d rapidly dissociates to CH₃CO and CO (R7).²⁵ Furthermore, reaction R6 is sufficiently exothermic (~120 kJ mol⁻¹) that near 40% of the nascent acetyl produced in reaction R6a dissociate further to CH₃ and CO. At atmospheric pressure acetyl reacts with O₂ to form a peroxy radical (R7a):²⁶



The acetylperoxy radical can react with NO₂ to form peroxyacetylnitrate (PAN),²⁷ a secondary pollutant and constituent of photochemical smog (R8).



PAN is thermally unstable and dissociates back to the acetylperoxy and NO₂ within a few hours at room temperature, but has a moderate to long lifetime at lower temperatures (~50 hours at 273 K).²⁸ This means PAN can transport and release NO₂ far from its source and potentially influence ozone formation and air quality in remote unpolluted regions.

Clearly the products of alkyne oxidation have significant ramifications for both the oxidising capacity of the troposphere and air quality. Accurately quantifying the branching ratios for reactions of the adducts with oxygen (R2, R3 and R5) is fundamental in understanding these consequences. Despite the atmospheric implications, there have been only two kinetic product studies on the OH-initiated oxidation of propyne and 2-butyne in the presence of oxygen.

Hatakeyama et al. studied the kinetics and products of the reactions of OH with acetylene, propyne and 2-butyne in an atmosphere of synthetic air at room temperature in a chamber study.¹³ These authors observed glyoxal (0.7 ± 0.3) and formic acid (0.4 ± 0.1) as primary products of the OH-initiated oxidation of acetylene, with a bicarbonyl yield consistent with that reported by other groups. For 2-butyne the corresponding products of biacetyl (0.87 ± 0.07) and acetic acid (0.12 ± 0.01) were detected. The carbon balance reported by Hatakeyama and co-workers suggests the bicarbonyl and acid forming channels are the only primary products of the OH-initiated oxidation of 2-butyne. For propyne only formic acid was detected (R3b), but the carbon balance associated with propyne oxidation dropped below unity with a methylglyoxal yield of (0.53 ± 0.03) reported.¹³

More recently, Yeung et al. studied the kinetics of the reactions of OH with acetylene, propyne and 2-butyne in 100 Torr of nitrogen with added oxygen at 298 K using turbulent flow chemical ionization mass spectrometry, with quantitative studies focusing on 2-butyne.¹⁴ This investigation reported biacetyl (0.86 ± 0.11) and acetic acid (0.14 ± 0.11) as major products of the OH + 2-butyne reaction in the presence of oxygen, consistent with Hatakeyama et al.¹³ In addition, Yeung and co-workers reported evidence of formic acid

production in the OH + C₃H₄/O₂ system (R3b) via observation of the dimer, but, unlike Hatakeyama et al., also reported evidence of acetic acid production for the propyne system (R2b).¹⁴ Yeung and co-workers determined the branching ratios for reaction R5 based on the rates of product formation following addition of oxygen to their flow tube system. The biacetyl and acetic acid yields reported by Yeung et al. are in excellent agreement with those reported by Hatakeyama et al. However, the chamber study by Hatakeyama et al. was conducted using one atmosphere of synthetic air, with an oxygen fraction, $f\text{-O}_2$, of 0.21.¹³ Conversely, the experiments by Yeung and co-workers were carried out using oxygen concentrations ranging between 3×10^{13} and 3×10^{14} molecule cm⁻³, which in 100 Torr of nitrogen correspond to sub 30 ppm oxygen levels ($f\text{-O}_2 < 3 \times 10^{-6}$).¹⁴ Experimental and theoretical evidence has shown the bicarbonyl and acid yields associated with the OH + acetylene/O₂ system are critically dependent on the $f\text{-O}_2$ present.²⁹⁻³¹ If this behaviour extends to higher chain alkynes, such as 2-butyne, then the agreement between the biacetyl and acetic acid yields observed during the experiments of Hatakeyama et al. and Yeung et al. is unexpected. Yeung and co-workers were also able to quantify the bimolecular rate coefficient for reaction of the 2-butyne-OH adduct with O₂ (R5) by modelling the time dependence of biacetyl and acetic acid formation observed as a function of oxygen concentration.¹⁴ Their analysis suggests a k_5 value of $(7.04 \pm 0.60) \times 10^{-13}$ cm³ molecule⁻¹ s⁻¹ and constrains the lifetime of the 2-butyne-OH adduct to less than 300 ns at one atmosphere of air. However, this value is an order of magnitude lower than other radical + O₂ reactions,^{24, 26, 32} including previous work on the HO-C₂H₂ + O₂ reaction.²⁹⁻³¹

The potential energy surface (PES) for the OH + C₄H₆/O₂ system was constructed following electronic structure calculations by Maranzana et al.,³³ and indicates the mechanism for the OH-initiated oxidation of 2-butyne shares many similarities with that for acetylene; with dicarbonyl and organic acid product forming channels strongly thermodynamically favoured and product branching governed by the stereochemistry of the alkyne-OH adduct at the point of reaction with O₂. The adduct formed following reaction of OH with 2-butyne exists in two energetically distinct isomeric forms; with the OH group either *cis*- or *trans*- to the carbon radical orbital. The *cis*-adduct is estimated to be between 5 and 7 kJ mol⁻¹ more stable than the *trans*-,^{15, 33} depending on the level of theory.

Association between the *cis*-adduct conformer and oxygen occurs with a concerted 1, 5-hydrogen shift from the hydroxyl group to the terminal peroxy oxygen. The resulting hydroperoxylalkeneyloxy radical is highly unstable and dissociates promptly at the energies it is formed to give biacetyl and OH products.³³ This product path proceeds down a steep free energy profile and is the dominant source of biacetyl and OH in the OH + C₄H₆/O₂ system.

Acetic acid + acetyl radical products follow association between the *trans*-adduct and oxygen,³³ where ring closure of the resulting peroxy adduct radical leads to formation of a 3-membered alkyl dioxiranyl cyclic radical species. Successive O-O bond cleavages and β-fragmentations of this cyclic intermediate result in formation of acetic acid and an acetyl radical.

The calculations by Maranzana et al. suggested two further intramolecular hydrogen shift paths were possible following association between the *trans*-adduct and oxygen,³³ although full master equation (ME) analysis by these authors suggested these represent minor channels which collectively account for less than 8% of the total OH + C₄H₆/O₂ product yield.³⁴ Both paths begin with a hydrogen transfer from one of the methyl groups to the terminal peroxy oxygen. In one path, hydrogen atom transfer occurs with concerted generation of OH and an enolic α, β-unsaturated carbonyl. In the second path, the resulting allyl radical undergoes a second hydrogen atom transfer from the OH group to the carbon radical centre, with concerted OH loss to give biacetyl. The mechanism proposed by Maranzana and co-workers is provided below in Figure 1.

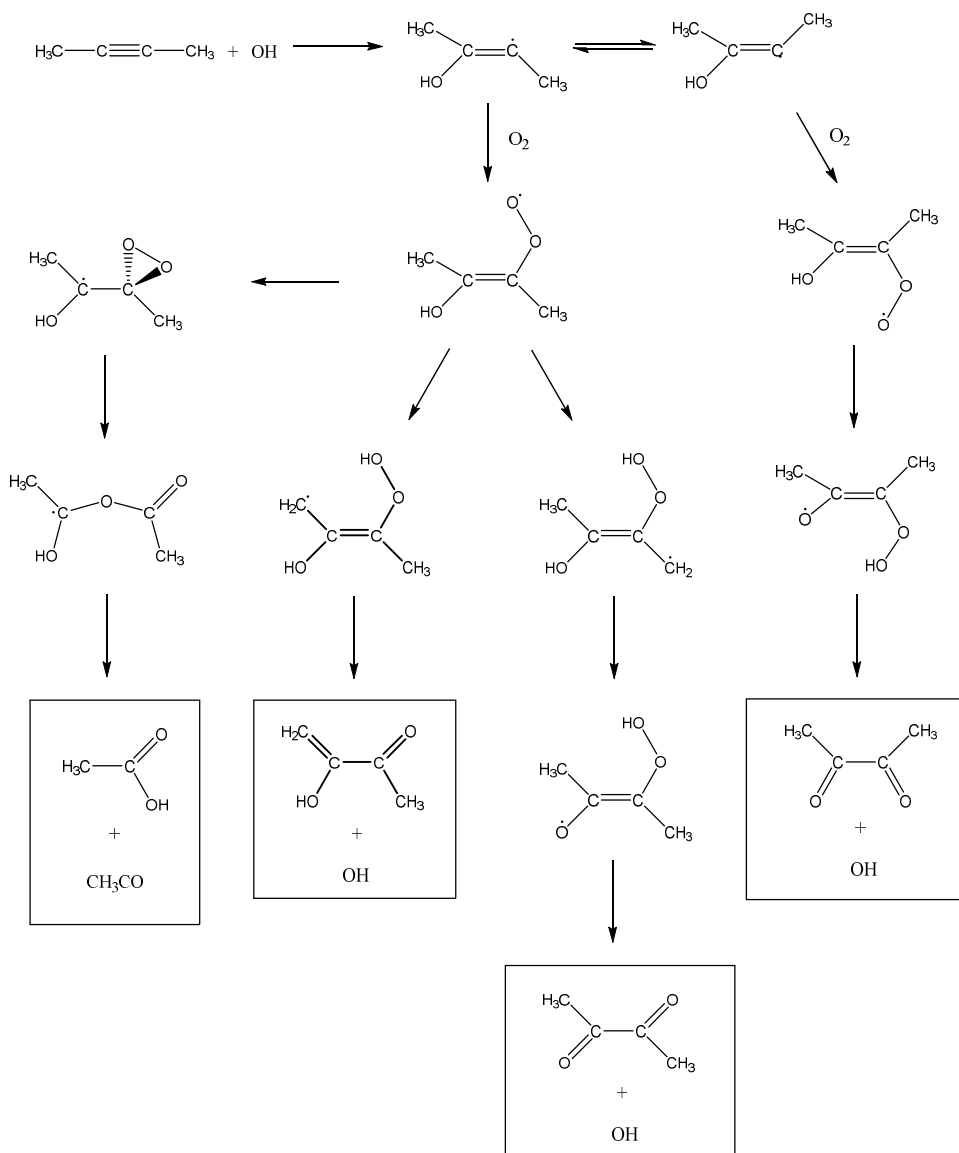


Figure 1: Schematic mechanism for the OH-initiated oxidation of 2-butyne.³³

The kinetic study of the OH + C₄H₆/O₂ system by Yeung et al.¹⁴ included a theoretical component, in which these authors derived a PES for the general OH + alkyne/O₂ system, for which the energies at various stages of oxidation depended very little on the identity of the parent alkyne (Figure 2).

The surface calculated by Yeung and co-workers for the general alkyne system lies in excellent agreement with the surface proposed by Maranzana et al.³³ for the specific 2-butyne system. However, it is worthwhile to note that neither Hatakeyama et al.¹³ or Yeung et al.¹⁴ detected the enolic α , β -unsaturated carbonyl proposed by Maranzana et al.³³ as a

potential product of OH-initiated oxidation of 2-butyne, suggesting the biacetyl + OH, and acetic acid + CH₃CO paths described above are likely exclusive product channels for the OH + C₄H₆/O₂ system.

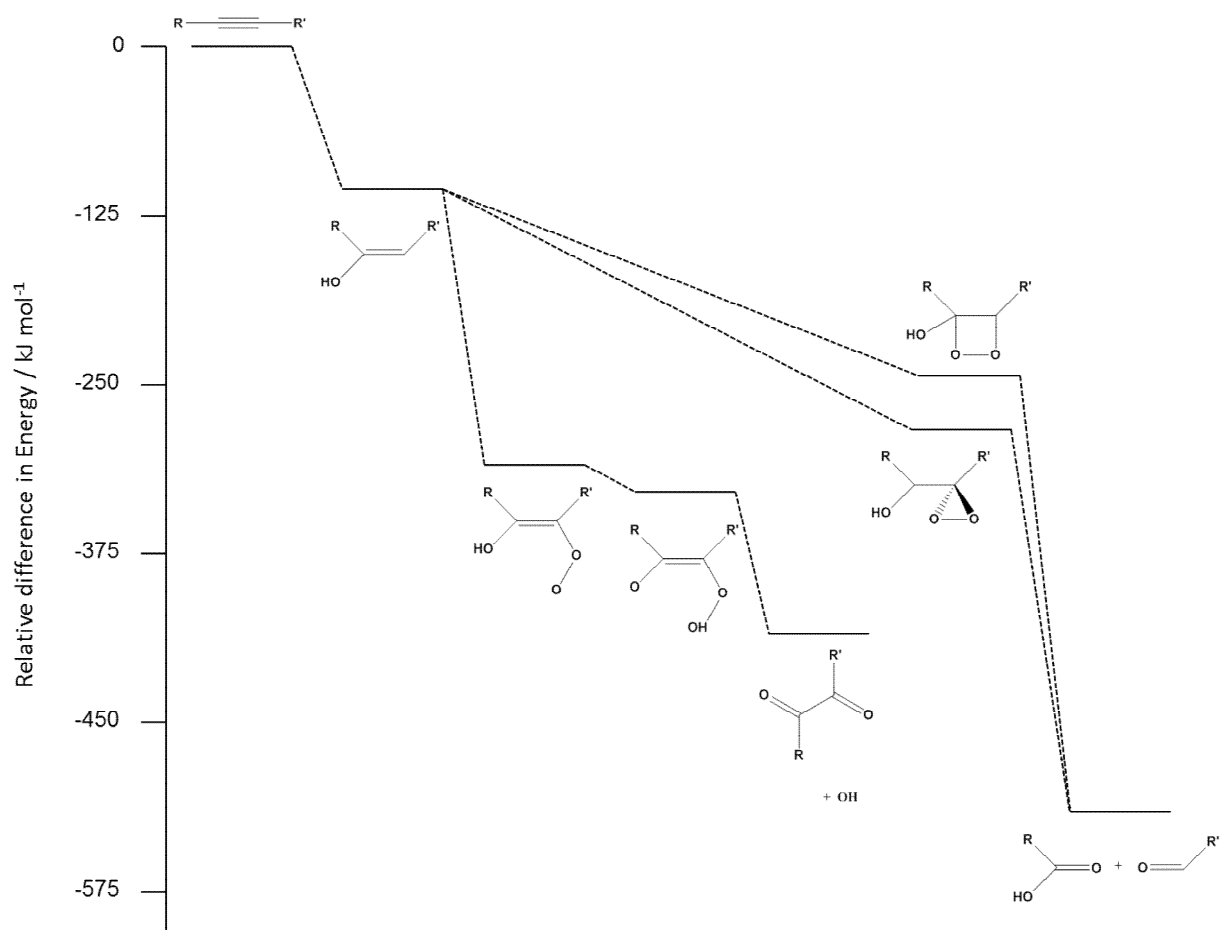


Figure 2: Diagram of the relative energies of the reactants, intermediates and products associated with the OH initiated oxidation of alkynes (redrawn from Yeung et al.)

Full ME analysis of the OH + C₄H₆/O₂ reaction was carried out by Maranzana et al.,³⁴ using their PES for this system, in order to simulate the experimental product yields reported by Hatakeyama et al.¹³ and Yeung et al.¹⁴ The quality of their fits was found to be highly sensitive to the model energy transfer parameter, ΔE_{down} , consistent with recent ME analysis of experimental glyoxal yields for the OH + C₂H₂/O₂ system by Glowacki et al.³¹ Excellent agreement with the biacetyl yield (~0.86) reported through experiment could be

achieved under atmospheric conditions,³⁴ but only when using a ΔE_{down} value of 900 cm^{-1} which exceeds the normal range for a nitrogen bath gas. However, when attempting to simulate the product yields reported by Yeung et al.,¹⁴ Maranzana and co-workers³⁴ used atmospheric oxygen fractions ($f\text{-O}_2 = 0.21$), despite the fact that the experiments by Yeung et al. were carried out using considerably lower oxygen concentrations.¹⁴

The work presented here aims to build on the detailed kinetic and mechanistic study of the OH + acetylene/O₂ system (chapter 3), by measuring product branching ratios for the reactions of OH with propyne and 2-butyne for the first time as a function of pressure, temperature and oxygen concentration, using OH recycling methods. In addition, directly observing equilibrium behaviour associated with the OH + alkyne/O₂ systems has allowed the bimolecular rate coefficients for the alkyne-OH + O₂ (R2 and R5) reactions to be determined as a function of temperature.

4.3 Experimental

All the measurements discussed in this chapter were carried out using the exact same slow-flow, pulsed laser photolysis, laser induced fluorescence apparatus described in chapter 3 and therefore the details are not repeated here. Bimolecular rate coefficients for the reactions of OH with propyne (R1) and 2-butyne (R4) were determined by monitoring OH decay under *pseudo-first-order* conditions such that the experimental alkyne concentration (typically ranging between 10^{14} and $10^{15} \text{ molecule cm}^{-3}$) were always in great excess over OH ($\sim 10^{11} \text{ molecule cm}^{-3}$) using pure nitrogen bath gas. OH radicals were generated from the excimer laser pulsed photolysis of *t-butyl* hydroperoxide at 248 nm (P2):



and detected by off-resonance fluorescence at $\sim 308 \text{ nm}$, following excitation at $\sim 282 \text{ nm}$. Under these conditions OH removal is governed by reaction with the respective alkyne (R9) and a relatively small loss through reaction with the precursor and diffusion out of the probed region of the reactor (R10):





Under these conditions the observed OH signal decays exponentially, and the time dependent OH signal, $I_f(t)$, is defined by the following equation:

$$I_f(t) = I_f(0) \exp^{-k't} \quad (\text{E1})$$

where $I_f(0)$ is the initial OH signal intensity, and k' is the observed *pseudo-first-order* decay constant equal to $k[\text{alkyne}] + k_9$. It follows that a bimolecular plot of k' against [alkyne] yields a straight line with a gradient equal to the bimolecular rate coefficient for the OH + alkyne reaction. An example bimolecular plot associated with the OH + C₃H₄ reaction in pure N₂ bath gas is provided in Figure 3, with a typical OH decay trace included in the inset.

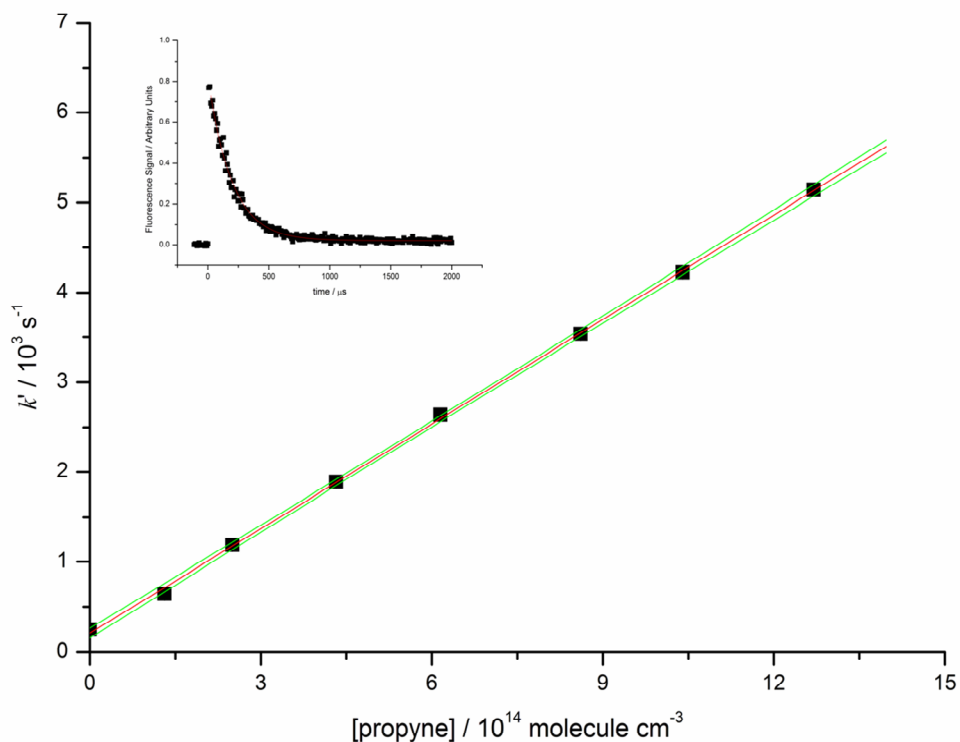


Figure 3: Typical bimolecular plot for the OH + C₃H₄ reaction at 295 K under 10 Torr of nitrogen; corresponding to a k_1 value of $(3.88 \pm 0.03) \times 10^{-12} \text{ cm}^3 \text{ molecule}^{-1} \text{ s}^{-1}$ (where the error is purely statistical at the 2σ level). The inset shows a typical experimental OH decay trace in the presence of propyne ($1.27 \times 10^{15} \text{ molecule cm}^{-3}$) using pure N₂ bath gas that corresponds to a *pseudo-first-order* decay constant of $(5140 \pm 50) \text{ s}^{-1}$.

4.4 Kinetics of the Reactions of OH with propyne and 2-butyne

Room temperature rate coefficients have been measured for the OH + C₃H₄ reaction at total pressures ranging between 2 and 75 Torr using pure nitrogen bath gas; a plot of the rate coefficients as a function of nitrogen pressure for propyne is presented in Figure 4. Reaction R1 demonstrates a typical pressure dependence for an association reaction. Above 25 Torr ($\sim 8 \times 10^{17}$ molecule cm⁻³) the reaction would appear to be at or close to the high pressure limit with a $k_1^\infty = (4.20 \pm 0.48) \times 10^{-12}$ cm³ molecule⁻¹ s⁻¹ obtained from averaging all of the ten independent measurements at 25 and 75 Torr (the error is statistical (2 σ) combined with an estimated 10% systematic error).

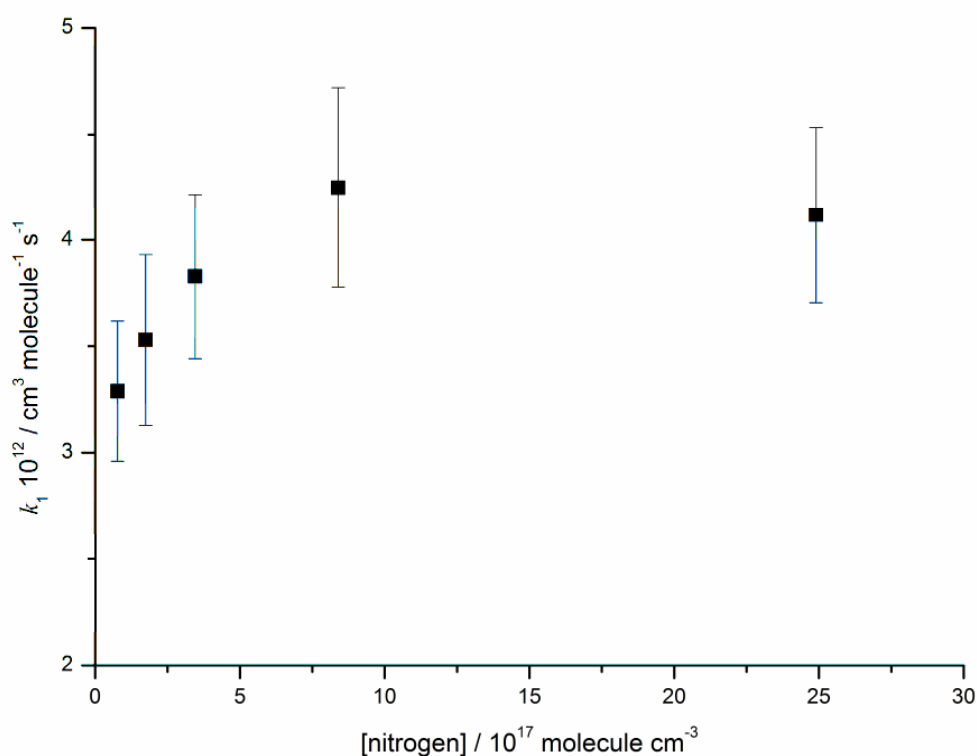


Figure 4: Pressure dependence of the bimolecular rate coefficients, k_1 , for the OH + C₃H₄ reaction using pure nitrogen bath gas at 295 K. The error bars include both the statistical (2 σ) and estimated systematic errors (10%).

Few experimental studies have reported rate coefficients for reaction R1; therefore comparison with literature values is limited. Boodaghians et al.¹² measured rate coefficients for the OH + C₃H₄ reaction using helium diluent at 298 K and total pressures ranging from 2 to 6 Torr using discharge-flow coupled with resonance fluorescence OH detection and reported a k_1 value of $(3.05 \pm 0.07) \times 10^{-12} \text{ cm}^3 \text{ molecule}^{-1} \text{ s}^{-1}$. This result is in good agreement with low pressure measurements undertaken in this laboratory by Taylor et al.,³⁵ who measured a rate coefficient of $(3.11 \pm 0.09) \times 10^{-12} \text{ cm}^3 \text{ molecule}^{-1} \text{ s}^{-1}$ at 299 K under approximately 1 Torr of nitrogen using the pulsed laser photolysis, laser induced fluorescence technique. The values of k_1 reported here are consistent with the low pressure direct measurements by Boodaghians et al.¹² and Taylor et al.³⁵ While the rate coefficient reported by Boodaghians and co-workers¹² is lower than the values obtained at comparable total pressures in this work, their experiments were conducted in helium bath gas, a less efficient third body than nitrogen. No pressure dependence was observed by Boodaghians et al.,¹² but the expected variation in the rate coefficient in this region would only be 10 - 20%.

Hatakeyama et al.¹³ and Atkinson and Aschmann³⁶ have carried out relative rate studies of the OH + C₃H₄ reaction at room temperature in one atmosphere of synthetic air and reported values of (5.71 ± 0.18) and $(6.21 \pm 0.31) \times 10^{-12} \text{ cm}^3 \text{ molecule}^{-1} \text{ s}^{-1}$, respectively. These indirect measurements are both slightly higher than the estimate for the high-pressure limiting rate coefficient for reaction R1 presented here. Both Hatakeyama et al.¹³ and Atkinson and Aschmann³⁶ used the reaction of OH with cyclohexane as the reference reaction; using the latest recommendation of Atkinson³⁷ for this rate coefficient slightly reduces their rate coefficients for reaction R1 to 5.25 and $5.74 \times 10^{-12} \text{ cm}^3 \text{ molecule}^{-1} \text{ s}^{-1}$, respectively.

For the reaction of OH with 2-butyne, bimolecular rate coefficients were measured using pure nitrogen bath gas at total pressures ranging between 5 and 25 Torr and temperatures ranging between 212 and 498 K. The observed rate coefficients, k_4 , were found independent of pressure over this range, with a room temperature k_4^∞ (295 K) value of $(1.85 \pm 0.21) \times 10^{-11} \text{ cm}^3 \text{ molecule}^{-1} \text{ s}^{-1}$ obtained by averaging all nine room temperature measurements (the error includes both the statistical error (2σ) and an estimated 10%

systematic error). The rate coefficients measured for reaction R4 exhibit a negative temperature dependence with k_4 increasing from (1.34 ± 0.33) to $(2.81 \pm 0.65) \times 10^{-11} \text{ cm}^3 \text{ molecule}^{-1} \text{ s}^{-1}$ as temperatures decrease from 498 to 212 K, respectively.

Only two previous studies have reported rate coefficient measurements for the OH + C₄H₆ reaction. Boodaghians et al.¹² measured rate coefficients for the OH + C₄H₆ reaction directly at temperatures ranging from 253 to 343 K in 5 Torr of helium using the discharge-flow coupled with resonance fluorescence technique. These authors reported a k_4 value of $(2.46 \pm 0.19) \times 10^{-11} \text{ cm}^3 \text{ molecule}^{-1} \text{ s}^{-1}$ at 298 K, and also observed a negative temperature dependence over their experimental temperature range, consistent with the measurements presented here. The relative rate study by Hatakeyama et al.¹³ was conducted at room temperature under one atmosphere of synthetic air, and reported a rate coefficient, k_4 , of $(3.01 \pm 0.28) \times 10^{-11} \text{ cm}^3 \text{ molecule}^{-1} \text{ s}^{-1}$. Hatakeyama and co-workers used the reaction of OH with cyclohexane as reference and again using the latest recommendation of Atkinson³⁷ for this rate coefficient slightly reduces their room temperature rate coefficient for reaction R4 to $(2.77 \pm 0.24) \times 10^{-11} \text{ cm}^3 \text{ molecule}^{-1} \text{ s}^{-1}$. The rate coefficients reported by these groups are in reasonable agreement and suggest the OH + C₄H₆ reaction to be at the high pressure limit by 5 Torr, consistent with the measurements presented here. An Arrhenius plot of the k_4 values reported here is provided in Figure 5 with values published by other groups included for comparison.

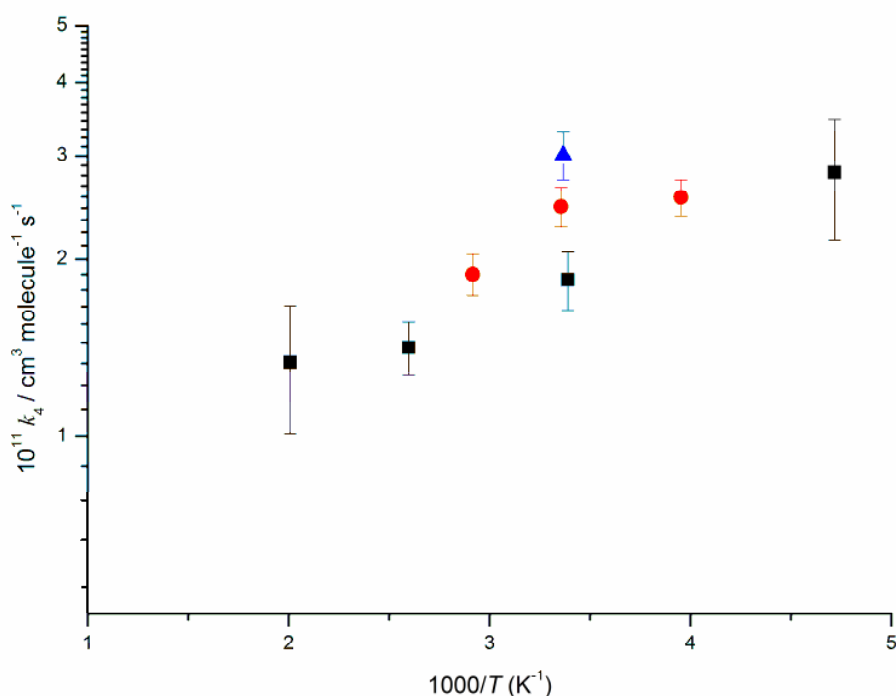


Figure 5: Temperature dependence of the bimolecular rate coefficients, k_4 , measured during this work for the OH + C₄H₆ reaction using pure nitrogen bath gas over a range of temperatures from 212 to 498 K (■). Included for comparison are the direct measurements of k_4 by Boodaghians et al.¹² (●) at temperatures ranging between 253 and 343 K using helium bath gas, and the room temperature measurement by Hatakeyama et al.¹³ (▲) using synthetic air bath gas.

4.5 Product Yields for the OH initiated oxidation of Propyne and 2-Butyne

The principal focus of this study is to quantify the experimental OH yield, Φ_{OH} , following the reactions of OH with propyne and 2-butyne in the presence of oxygen, as a function of pressure and temperature. In the presence of molecular oxygen, OH is rapidly regenerated through reaction of the alkyne-OH adduct with O₂ (R2 and R5). If the concentration of oxygen is such that reactions R2 and R5 are fast compared to formation of the respective OH + alkyne reaction, then, under these conditions, the rate of OH removal is determined by the fraction of the alkyne-OH adduct + O₂ reaction that does not recycle OH. The bimolecular rate coefficient for OH loss in the presence of oxygen, k_{O_2} , will be reduced compared to that measured in pure nitrogen, k_{N_2} (see lower traces in Figure 6).

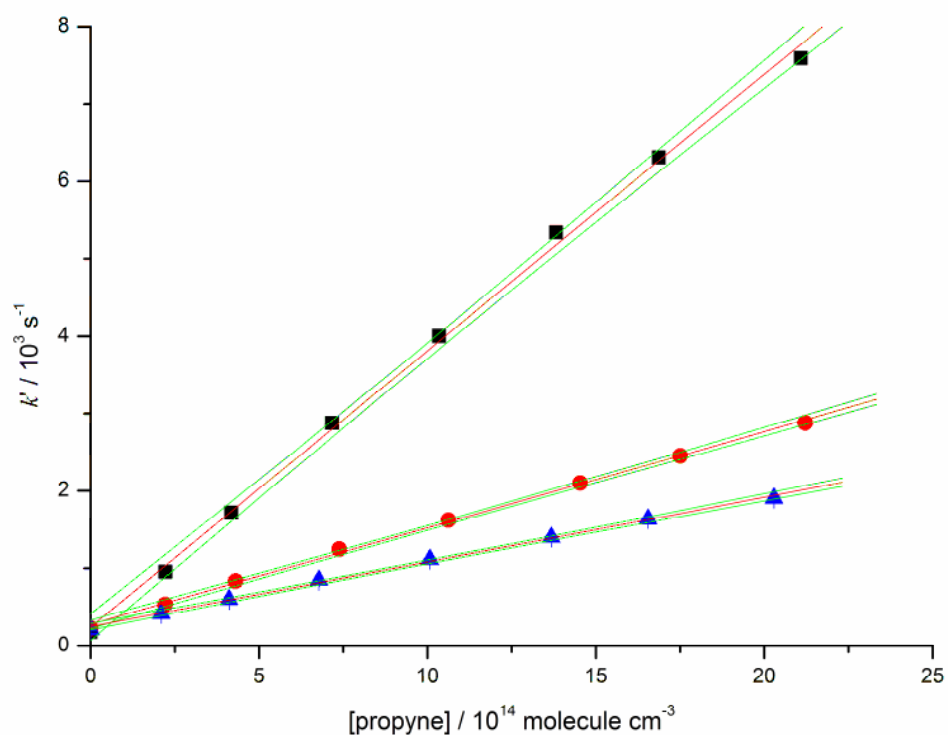
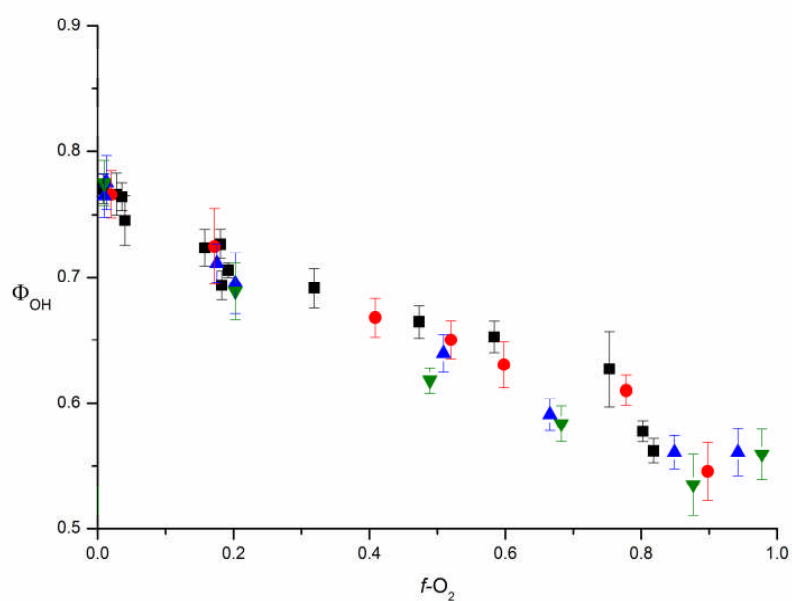


Figure 6: Bimolecular plots for the $\text{OH} + \text{C}_3\text{H}_4 \rightarrow \text{Products}$ reaction at 295 K and 10 Torr total pressure: using pure nitrogen bath gas (■), 48% nitrogen and 52% oxygen (●), and 2% oxygen and 98% nitrogen (▲). Error bars are purely statistical at the 2σ level.

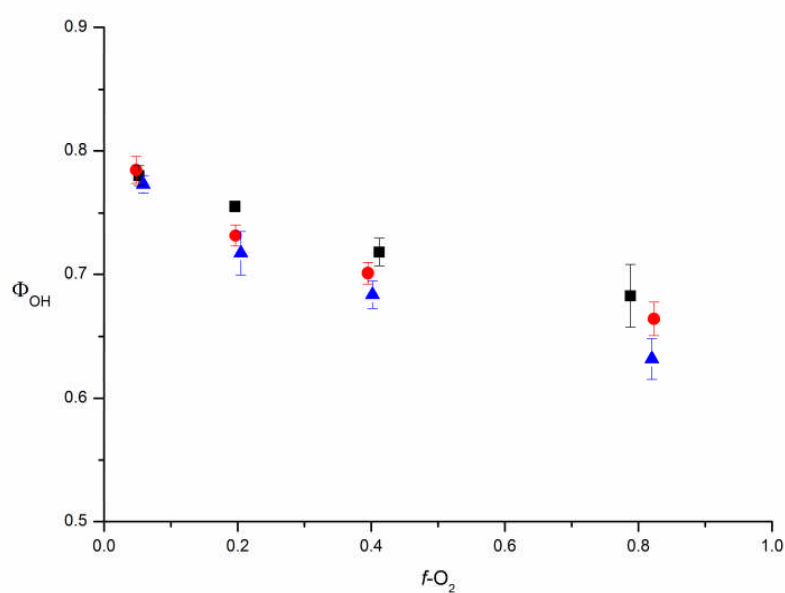
Assuming that both oxygen and nitrogen remove excess energy from the nascent alkyne-OH adduct with similar efficiencies following a collision, then the OH yield (branching ratio for the bicarbonyl channel) can be calculated from the ratio of rate coefficients measured in the presence and absence of O_2 , as follows:

$$\frac{k_{\text{O}_2}}{k_{\text{N}_2}} = 1 - \Phi_{\text{OH}} \quad (\text{E2})$$

Experimental OH yields, Φ_{OH} , have been measured following the reactions of OH with propyne and 2-butyne as a function of oxygen fraction, $f\text{-O}_2$, and total pressure; the results are presented in Figure 7.



a.



b.

Figure 7: (a) Dependence of the OH yield for the OH + C₃H₄/O₂ reaction as a function of oxygen fraction, $f\text{-O}_2$, and total pressure at 295 K and 5 (■), 10 (●), 25 (▲) and 75 Torr (▼). (b) Dependence of the OH yield for the OH + C₄H₆/O₂ reaction as a function of oxygen fraction, $f\text{-O}_2$, and total pressure at 295 K at 5 (■), 10 (●) and 25 Torr (▲).

The room temperature Φ_{OH} are independent of total pressure over the 5 to 75 Torr of N_2/O_2 range, but demonstrate a similar qualitative dependence on $f\text{-O}_2$ as was observed for the OH + acetylene system (Chapter 3); with the Φ_{OH} decreasing from ~ 0.76 (propyne) and ~ 0.80 (2-butyne), to ~ 0.56 (propyne) and ~ 0.62 (2-butyne) as $f\text{-O}_2$ increases from ~ 0.01 to 1. The pressure independent Φ_{OH} observed for the OH + 2-butyne/ O_2 system during this work are consistent with the biacetyl and acetic acid yields reported by Hatakeyama et al.¹³ and Yeung et al.¹⁴ Furthermore, the dominance of the OH + bicarbonyl yield for both alkyne systems at $f\text{-O}_2$ lower than 0.21 is also consistent with the results of Hatakeyama et al.¹³ and Yeung et al.¹⁴

The dependence of the Φ_{OH} on the $f\text{-O}_2$ observed during the OH initiated oxidation of both propyne and 2-butyne are consistent with theoretical treatment of these systems by Yeung et al.¹⁴ and Maranzana et al.³³ The theory suggests that both initial alkyne-OH adducts exist in two energetically distinct conformations, separated by a barrier of less than 10 kJ mol^{-1} , and that regardless of the initial OH addition site (ie. Markovnikov or anti-Markovnikov OH addition for propyne) the conformer characterised by the carbon radical orbital arranged *cis* to the OH group is always more stable ($5 - 7 \text{ kJ mol}^{-1}$) than the corresponding *trans* isomer. Reactions R1 and R4 are exothermic by approximately 120 and 96 kJ mol^{-1} ,^{14, 33} respectively. Consequently, the nascent adducts formed following reactions of OH with propyne and 2-butyne with sufficient energy to rapidly interconvert. Under low oxygen conditions, non-reactive interactions between the alkyne-OH adduct and bath gas molecules remove this excess energy and the adduct conformers can be considered in thermal equilibrium before a reactive collision with oxygen occurs. The thermal distribution favours the more stable *cis*-adduct stereoisomer which reacts with oxygen to give biacetyl and regenerate OH, hence higher Φ_{OH} are observed under low oxygen (thermal) conditions (Figure 7).

Conversely, under high oxygen conditions, reactive collisions between the alkyne-OH adduct and oxygen occur before the adduct has been collisionally deactivated. This serves to reduce the experimental Φ_{OH} as an increasing fraction of the total alkyne-OH adduct population is removed through reaction of the less stable *trans*-adduct isomer with O_2 , which yields an organic acid and acyl radical. Significantly, this work has shown that under

atmospheric conditions ($f\text{-O}_2 = 0.21$) oxygen intercepts a significant fraction of the total alkyne-OH adduct population before these systems are in thermal equilibrium.

The experimental investigation of the OH + 2-butyne/ O_2 system by Yeung et al.¹⁴ was carried out using extremely low oxygen concentrations ($f\text{-O}_2 < 3 \times 10^{-6}$) in 100 Torr of N_2 . The biacetyl + OH yield (0.86 ± 0.11) reported by these authors is in excellent agreement with the Φ_{OH} of ~ 0.8 measured under low $f\text{-O}_2$ conditions during this study (Figure 5b). The indirect measurements of Hatakeyama et al.¹³ were carried out using one atmosphere of synthetic air and reported a biacetyl + OH yield of (0.87 ± 0.07). This value is slightly higher than the yield of (0.74 ± 0.03) measured here using an $f\text{-O}_2$ of 0.2 (Figure 7). The methylglyoxal + OH yield reported by Hatakeyama and co-workers¹³ for the OH + propyne/ O_2 system of (0.53 ± 0.03) is inconsistent with the (0.70 ± 0.03) value measured here using similar $f\text{-O}_2$ (Figure 7a). Hatakeyama et al.¹³ reported formic acid as the only stable co-product to methylglyoxal, although the reported carbon balance for this reaction is less than unity; the normalized methylglyoxal yield would be 0.79.

The acetyl co-product of reactions R3b and R5b could influence these measurements via secondary chemistry and potentially provide some insight into the product yields. At low pressures, acetyl is known to react with oxygen and generate OH (R7b).³⁸



The OH yield following the reaction of acetyl with oxygen (R7b) is pressure dependent,³⁹ in contrast to the OH yield for the OH + alkyne/ O_2 system, and so any pressure dependence of the OH yield could quantify the acetyl yield.

Experimentally, no significant pressure dependence was observed in the OH yield from either alkyne system (Figure 7), although previous work on the acetyl + O_2 reaction suggests a pressure dependent OH yield should be observed for reaction R7b at pressures below 75 Torr.³⁹ In order to rationalize the present observation of no secondary OH formation through reaction R7b, Dr Robin Shannon investigated the energy distribution in the acetyl radical assuming a statistical energy distribution following reaction R5b, using MESMER.⁴⁰ The energy distribution of the nascent acetyl radicals formed from the OH + 2-butyne/ O_2 system was calculated using a prior distribution model implemented in

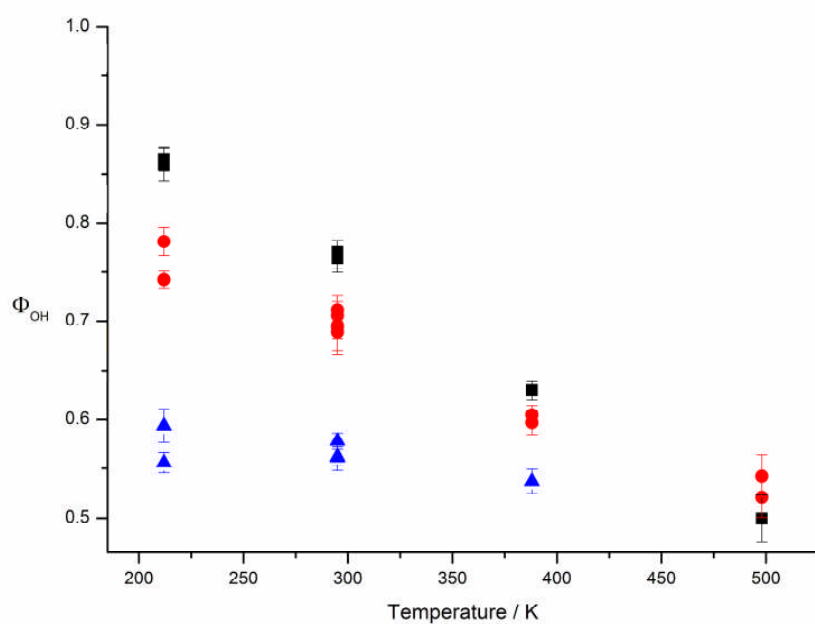
MESMER,²⁵ and the total available excess energy from the OH + 2-butyne reaction was taken from the PES of Maranzana et al.³³ The nascent acetyl radical energy distribution calculated via a prior analysis was then allowed to either react with oxygen (R7) or dissociate (R11):



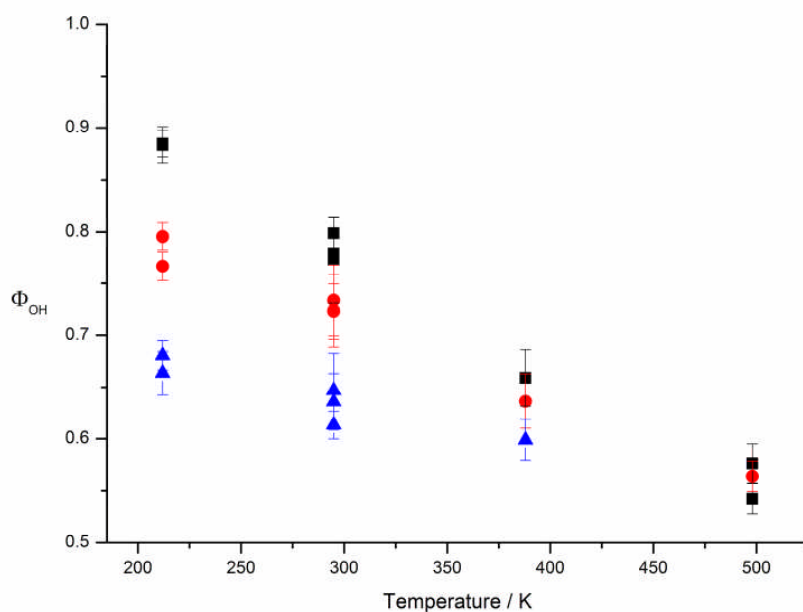
The PES and molecular parameters presented in Carr et al.³⁹ were used for most species involved in these calculation, but the transition state corresponding to acetyl decomposition (R11) was taken from Lee and Bozzelli⁴¹ and Huynh and Violi.⁴² For the barrierless association between the acetyl radical and O₂ a rate coefficient of $6.2 \times 10^{-12} \text{ cm}^3 \text{ molecule}^{-1} \text{ s}^{-1}$ was assumed, consistent with the calculations of Carr et al.,³⁹ but it was found that increasing this rate coefficient to $6.2 \times 10^{-11} \text{ cm}^3 \text{ molecule}^{-1} \text{ s}^{-1}$ affected the calculated OH yield by less than 0.1%.

The calculations show that under the experimental conditions of this study (5 – 75 Torr of oxygen) over 99.9% of the acetyl formed from reaction R5b dissociates, accounting for the lack of any pressure dependence in the observed OH yield in the OH + 2-butyne/O₂ system. Repeating the calculations for a pressure of 760 Torr of air showed that 99% of the acetyl dissociates; at such pressures any reaction of acetyl with oxygen would lead exclusively to the stabilized acetylperoxy radical (R7a). Given that the overall exothermicity of the OH + propyne/O₂ system is similar to the corresponding 2-butyne system, the prior distribution would predict that an even greater fraction of the acetyl formed in reaction R3b would dissociate, again consistent with the observations of no pressure dependence in the OH yield (Figure 7a). Due to the prompt acetyl dissociation, this study provided no information on the organic acid branching for either alkyne system.

The OH yields, Φ_{OH} , associated with the reactions of OH with propyne and 2-butyne in the presence of oxygen have been measured as a function of temperature (212 – 498 K). The temperature dependent Φ_{OH} measured under 10 Torr total pressure using fixed $f\text{-O}_2$ (0.04, 0.20 and 0.80) are plotted in Figure 8.



a.



b.

Figure 8: (a) Temperature dependence of the OH yield for the OH + C₃H₄/O₂ reaction measured at 10 Torr total pressure using 0.04 (■), 0.20 (●), and 0.80 oxygen fractions, f_{O_2} (▲). (b) Temperature dependence of the OH yield for the OH + C₄H₆/O₂ reaction measured at 10 Torr total pressure using 0.04 (■), 0.20 (●) and 0.80 oxygen fractions, f_{O_2} (▲).

Both alkyne systems show a marked increase in the Φ_{OH} as temperatures decrease with yields of ~ 0.5 at 498 K increasing to ~ 0.9 at 212 K (Figure 8). As the $f\text{-O}_2$ increase, the temperature dependence of the Φ_{OH} decreases until the yield becomes effectively independent of temperature under high oxygen conditions. The results are qualitatively similar to that of the corresponding OH + acetylene/ O_2 system with the Φ_{OH} at low and atmospheric $f\text{-O}_2$ decreasing with increasing temperature.

These observations are again consistent with OH-initiated alkyne oxidation product yields dependent on the stereochemistry of the alkyne-OH adduct at the point of reaction with oxygen. As experimental temperatures decrease, the thermal distribution of the *cis*- and *trans*-adduct conformers shifts in favour of the more stable *cis*-isomer; consequently greater Φ_{OH} are observed under low $f\text{-O}_2$ (thermal), low temperature conditions. As temperatures increase, so does the thermal distribution of the less stable *trans*-adduct conformer; resulting in a reduced Φ_{OH} . Significantly, the temperature dependent Φ_{OH} measured here show that under atmospheric conditions ($f\text{-O}_2 = 0.21$) the Φ_{OH} observed are not yet at the thermal limit, and provide further evidence that under conditions relevant to the troposphere, oxygen intercepts a significant fraction of the total alkyne-OH adduct population before the internal quantum states have fully relaxed.

4.6 Kinetics of the Alkyne-OH Adduct + O_2 Reaction

Under low oxygen concentrations ($[\text{O}_2] < 4 \times 10^{15}$ molecule cm^{-3}) the reaction of the alkyne-OH adduct with O_2 can no longer be considered fast compared to the rate of adduct formation, and under these conditions, as was demonstrated for the OH + $\text{C}_2\text{H}_2/\text{O}_2$ system in chapter 3, biexponential OH decay traces are observed (see inset of Figure 9). This biexponential behaviour allows the kinetics of the alkyne-OH adduct + O_2 reaction (R2 + R3 and R5), which is lost in excess oxygen, to be quantified. For the general OH + alkyne/ O_2 system the following reaction scheme can be applied:





where reactions R14 and R15 represent respective loss of the alkyne-OH adduct and OH through reaction with the precursor and diffusion out of the probed region of the reactor. Under low oxygen conditions, the time dependent OH profile is defined by equation E3:

$$[\text{OH}]_t = \frac{[\text{OH}]_0 (S - L_2)}{(L_1 - L_2)} (e^{L_1 t} - e^{L_2 t}) + [\text{OH}]_0 e^{L_2 t} \quad (\text{E3})$$

where

$$S = -(k'_{12} + k_{10})$$

$$M_1 = (k_{12}' + k'_{13a} + k'_{13b} + k_{14} + k_{10})$$

$$M_2 = (k'_{12} + k_{10}) \times (k'_{13a} + k'_{13b} + k_{14}) - k'_{12}k'_{13a}$$

$$L_1 = \frac{-M_1 + \sqrt{(M_1^2 - 4M_2)}}{2}$$

$$L_2 = \frac{-M_1 - \sqrt{(M_1^2 - 4M_2)}}{2}$$

OH decay traces were recorded at total pressures of 10 Torr and temperatures of 295 and 212 K, with experimental conditions controlled such that the concentration of either propyne or 2-butyne inside the reactor was maintained at (~ 1.35) and (~ 1.41) $\times 10^{15}$ molecule cm^{-3} , respectively, for all decay traces, both with and without oxygen. This allowed k'_{12} to be fixed as the *pseudo-first-order* decay coefficient obtained from single exponential analysis of the OH decay profile in the absence of oxygen when fitting the biexponential OH decays observed in the presence of trace amounts of oxygen using equation E3. The gradient of a straight line plot of the total *pseudo-first-order* rate coefficient, k' ($k_{13} + k_{14}$), against oxygen concentration gives the bimolecular rate coefficient for the alkyne-OH adduct + O_2 reaction. A typical bimolecular plot for the $\text{HO-C}_4\text{H}_6 + \text{O}_2 \rightarrow \text{Products}$ reaction is

provided in Figure 9. Bimolecular rate coefficients for the reactions of oxygen with the alkyne-OH adducts of acetylene, propyne, and 2-butyne, measured at 295 and 212 K under 10 Torr of nitrogen bath gas are listed in Table 1.

The alkyne-OH adducts of acetylene and 2-butyne both react with oxygen at similar rates at room temperature with rate coefficients of (6.15 ± 0.27) and $(6.45 \pm 0.22) \times 10^{-12} \text{ cm}^3 \text{ molecule}^{-1} \text{ s}^{-1}$, respectively. As mentioned previously in chapter 3, the acetylene-OH + O₂ rate coefficient measured at room temperature is reasonably consistent with theoretical and experimental values that range from $(3 - 5) \times 10^{-12} \text{ cm}^3 \text{ molecule}^{-1} \text{ s}^{-1}$.^{29, 31} However, the room temperature k_5 value of $(7.04 \pm 0.60) \times 10^{-13} \text{ cm}^3 \text{ molecule}^{-1} \text{ s}^{-1}$ measured by Yeung et al.¹⁴ is significantly lower than the $(6.45 \pm 0.22) \times 10^{-12} \text{ cm}^3 \text{ molecule}^{-1} \text{ s}^{-1}$ value measured here (Table 1).

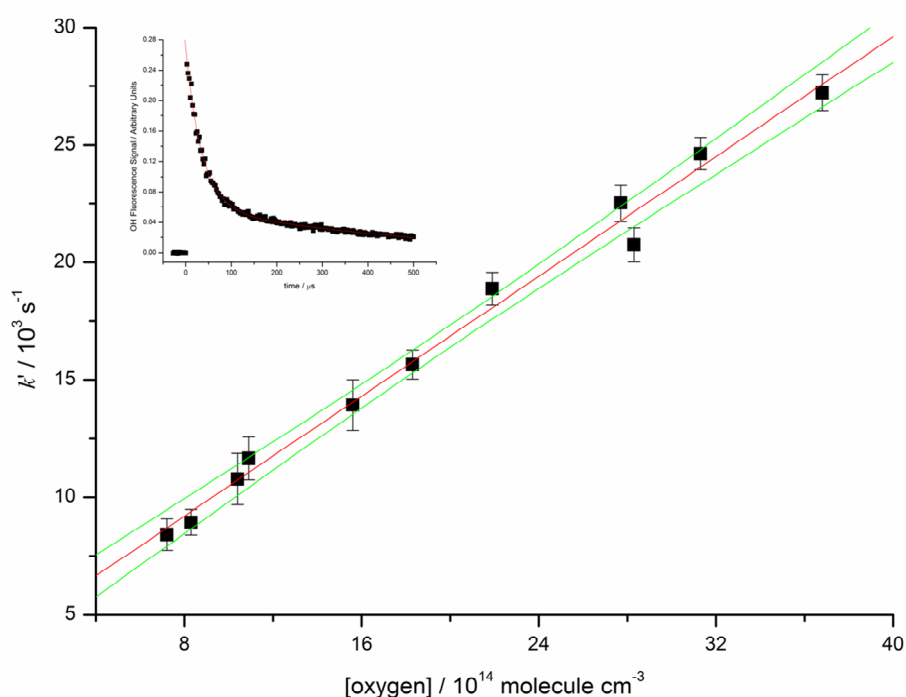


Figure 9: Bimolecular plot for the HO-C₄H₆ + O₂ → Products reaction at 10 Torr pressure and 295 K, corresponding to a k_5 value of $(6.45 \pm 0.22) \times 10^{-12} \text{ cm}^3 \text{ molecule}^{-1} \text{ s}^{-1}$. A typical biexponential OH decay trace is included in the inset, with OH monitored in the presence of $\sim 1.41 \times 10^{15} \text{ molecule cm}^{-3}$ of 2-butyne and $\sim 8.3 \times 10^{14} \text{ molecule cm}^{-3}$ of oxygen; under these conditions a *pseudo-first-order* rate coefficient of $(8940 \pm 540) \text{ s}^{-1}$ was observed.

Reaction	Temperature / K	$k \ 10^{12} / \text{cm}^3 \text{ molecule}^{-1} \text{ s}^{-1}$
HO-C ₂ H ₂ + O ₂ → Products	295	(6.15 ± 0.27)
	212	(19.29 ± 0.12)
HO-C ₃ H ₄ + O ₂ → Products	295	(8.01 ± 0.17)
	212	(10.41 ± 0.32)
HO-C ₄ H ₆ + O ₂ → Products	295	(6.45 ± 0.22)
	212	(15.08 ± 0.53)

Table 1: Temperature dependence of the rate coefficients measured for alkyne-OH + O₂ reaction.

Biexponential behaviour is observed when OH loss through reaction with the alkyne occurs on a similar timescale to OH production through reaction of the alkyne-OH adduct with oxygen. In order to ascertain the credibility of the k_5 rate coefficient reported by Yeung and co-workers,¹⁴ the numerical programme KINTECUS⁴³ was used to generate an OH profile for the OH + 2-butyne/O₂ system under the exact experimental conditions used when recording the biexponential OH decay trace shown in the inset of Figure 9, but using the k_5 rate coefficient reported by Yeung et al.¹⁴ The corresponding simulated OH decay profile is presented in Figure 10 (blue line), included is a second OH decay profile simulated using the k_5 rate coefficient reported here (red line); all fitting parameters are listed in table 2. Figure 10 shows clearly that the biexponential behaviour observed during this study (inset of Figure 9) is inconsistent with the 2-butyne-OH + O₂ rate coefficient reported by Yeung et al.¹⁴

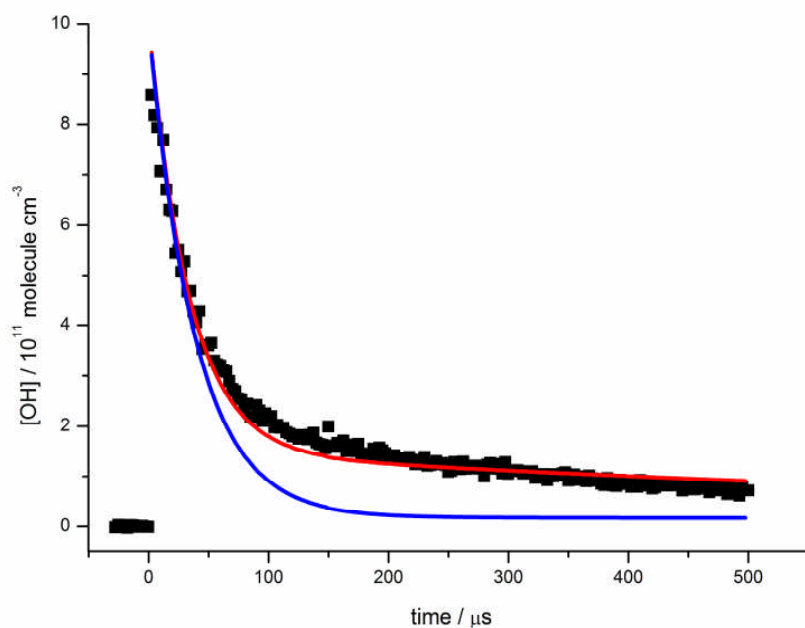


Figure 10: Experimental OH decay profile associated with the reaction of OH with 2-butyne (1.41×10^{15} molecule cm^{-3}) in the presence of trace oxygen (8.3×10^{14} molecule cm^{-3}). Simulated OH decay profiles under identical conditions are included using a k_5 rate coefficient value of either 7.03×10^{-13} cm^3 molecule $^{-1}$ s $^{-1}$ (blue line), determined by Yeung et al.,¹⁴ or 6.45×10^{-12} cm^3 molecule $^{-1}$ s $^{-1}$ (red line), measured here.

Reaction	Fitting Routine	
	Red Line	Blue Line
$\text{OH} + \text{C}_4\text{H}_6 \rightarrow \text{HO-C}_4\text{H}_6$	$1.64 \times 10^{-11} \text{ cm}^3 \text{ molecule}^{-1} \text{ s}^{-1}$	$1.64 \times 10^{-11} \text{ cm}^3 \text{ molecule}^{-1} \text{ s}^{-1}$
$\text{HO-C}_4\text{H}_6 + \text{O}_2 \rightarrow$ $\text{OH} + \text{CH}_3\text{C(O)C(O)CH}_3$	$5.55 \times 10^{-12} \text{ cm}^3 \text{ molecule}^{-1} \text{ s}^{-1}$	$6.05 \times 10^{-13} \text{ cm}^3 \text{ molecule}^{-1} \text{ s}^{-1}$
$\text{HO-C}_4\text{H}_6 + \text{O}_2 \rightarrow$ $\text{CH}_3\text{COOH} + \text{CH}_3\text{CO}$	$9.03 \times 10^{-13} \text{ cm}^3 \text{ molecule}^{-1} \text{ s}^{-1}$	$9.84 \times 10^{-14} \text{ cm}^3 \text{ molecule}^{-1} \text{ s}^{-1}$
$\text{OH} \rightarrow \text{Loss}$	2400 s^{-1}	2400 s^{-1}

Table 2: Model parameters used to fit biexponential OH decay trace presented in Figure 10.

The rate coefficients for the reactions of oxygen with all the alkyne-OH adducts considered in this study increase as temperatures decrease from 295 to 212 K (Table 1). The room temperature propyne-OH adduct + O₂ rate coefficient increases by approximately 25% as the temperature decreases to 212 K. However, rate coefficients for the reactions of the acetylene-OH and 2-butyne-OH adducts with oxygen increase by more than a factor of two over the same temperature range. The trend in reaction rate sensitivity to temperature observed for the propyne-OH adduct and the symmetric alkyne-OH adducts is difficult to explain in terms of steric or inductive effects of the methyl group substituents of the carbon radical centre. It is possible that subtle differences in the PES for the OH + propyne/O₂ system result in this reaction being less sensitive to temperature than either of the corresponding acetylene and 2-butyne systems.

4.7 Conclusions

Experimental OH yields, Φ_{OH} , have been measured for the OH + propyne/O₂ and OH + 2-butyne/O₂ systems for the first time as a function of pressure, temperature and oxygen concentration. Φ_{OH} for both systems were found to be independent of pressure between 5 and 75 Torr, but strongly dependent on the fraction of oxygen, $f\text{-O}_2$, present. These results are qualitatively similar to analogous studies of the OH + C₂H₂/O₂ system, and consistent with previous theoretical studies of alkyne oxidation which suggest that product branching is governed by the stereochemistry of the alkyne-OH adduct at the point of reaction with oxygen. Under thermal conditions, Φ_{OH} for both the propyne and 2-butyne systems depend critically on temperature, with the highest yields (~0.90) observed at low temperatures (212 K). Significantly, this work has shown that under atmospheric conditions a fraction of the total product yield of OH initiated oxidation of alkynes results from the reaction of chemically activated alkyne-OH adduct radicals with oxygen.

The room temperature Φ_{OH} measured here for the OH + 2-butyne/O₂ system are in reasonable agreement with the biacetyl (OH co-product) yields reported by other groups for this reaction.^{13, 14} However, the results from this study suggest the OH + methylglyoxal yield for the OH + propyne/O₂ system is more dominant under atmospheric conditions than

previous work by Hatakeyama et al.¹³ suggested. ME calculations have shown that under atmospheric conditions, the acetyl co-fragment of organic acid production in reactions R3b and R5b will promptly dissociate. Propyne and 2-butyne are not currently included in atmospheric models such as the Maser Chemical Mechanism,⁴⁴ but this study suggests that any chemical model of the OH initiated oxidation of propyne or 2-butyne under atmospheric conditions should include the chemically activated dissociation of acetyl; consequently the OH initiated oxidation of propyne and 2-butyne will not be an additional source of PAN.

4.8 References

1. Whitby, R. A.; Altwicker, E. R., Acetylene in atmosphere - sources, representative ambient concentrations and ratios to other hydrocarbons. *Atmospheric Environment* 1978, 12, 1289-1296.
2. Barrefors, G.; Petersson, G., Assessment by gas-chromatography and gas-chromatography mass-spectrometry of volatile hydrocarbons from biomass burning. *Journal of Chromatography A* 1995, 710, 71-77.
3. Schuetzle, D.; Siegl, W. O.; Jensen, T. E.; Dearth, M. A.; Kaiser, E. W.; Gorse, R.; Kreucher, W.; Kulik, E., The relationship between gasoline composition and vehicle hydrocarbon emissions - A review of current studies and future-research needs *Environmental Health Perspectives* 1994, 102, 3-12.
4. Gentner, D. R.; Worton, D. R.; Isaacman, G.; Davis, L. C.; Dallmann, T. R.; Wood, E. C.; Herndon, S. C.; Goldstein, A. H.; Harley, R. A., Chemical Composition of Gas-Phase Organic Carbon Emissions from Motor Vehicles and Implications for Ozone Production. *Environmental Science & Technology* 2013, 47, 11837-11848.
5. Sauvage, S.; Plaisance, H.; Locoge, N.; Wroblewski, A.; Coddeville, P.; Galloo, J. C., Long term measurement and source apportionment of non-methane hydrocarbons in three French rural areas. *Atmospheric Environment* 2009, 43, 2430-2441.
6. Greenberg, J. P.; Zimmerman, P. R., Nonmethane Hydrocarbons in Remote Tropical, Continental, and Marine Atmospheres. *Journal of Geophysical Research-Atmospheres* 1984, 89, 4767-4778.
7. Barletta, B.; Meinardi, S.; Simpson, I. J.; Khwaja, H. A.; Blake, D. R.; Rowland, F. S., Mixing ratios of volatile organic compounds (VOCs) in the atmosphere of Karachi, Pakistan. *Atmospheric Environment* 2002, 36, 3429-3443.
8. Ding, W. H.; Wang, J. L., Spatial concentration profiles of C₂-C₆ hydrocarbons in the atmosphere of Taipei metropolitan area. *Chemosphere* 1998, 37, 1187-1195.
9. George, L. A.; Hard, T. M.; O'Brien, R. J., Measurement of free radicals OH and HO₂ in Los Angeles smog. *Journal of Geophysical Research-Atmospheres* 1999, 104, 11643-11655.
10. Velasco, E.; Lamb, B.; Westberg, H.; Allwine, E.; Sosa, G.; Arriaga-Colina, J. L.; Jobson, B. T.; Alexander, M. L.; Prazeller, P.; Knighton, W. B.; Rogers, T. M.; Grutter, M.; Herndon, S. C.; Kolb, C. E.; Zavala, M.; de Foy, B.; Volkamer, R.; Molina, L. T.; Molina, M. J., Distribution, magnitudes, reactivities, ratios and diurnal patterns of volatile organic compounds in the Valley of Mexico during the MCMA 2002 & 2003 field campaigns. *Atmospheric Chemistry and Physics* 2007, 7, 329-353.
11. Akagi, S. K.; Yokelson, R. J.; Burling, I. R.; Meinardi, S.; Simpson, I.; Blake, D. R.; McMeeking, G. R.; Sullivan, A.; Lee, T.; Kreidenweis, S.; Urbanski, S.; Reardon, J.; Griffith, D. W. T.; Johnson, T. J.; Weise, D. R., Measurements of reactive trace gases and variable O₃ formation rates in some South Carolina biomass burning plumes. *Atmospheric Chemistry and Physics* 2013, 13, 1141-1165.
12. Boodaghians, R. B.; Hall, I. W.; Toby, F. S.; Wayne, R. P., Absolute determinations of the kinetics and temperature dependences of the reactions of OH with a series of alkynes *Journal of the Chemical Society-Faraday Transactions II* 1987, 83, 2073-2080.
13. Hatakeyama, S.; Washida, N.; Akimoto, H., Rate constants and mechanisms for the reaction of OH (OD) radicals with acetylene, propyne, and 2-butyne in air at 297 +/- 2K. *Journal of Physical Chemistry* 1986, 90, 173-178.
14. Yeung, L. Y.; Pennino, M. J.; Miller, A. M.; Elrod, M. J., Kinetics and mechanistic studies of the atmospheric oxidation of alkynes. *Journal of Physical Chemistry A* 2005, 109, 1879-1889.
15. Lockhart, J.; Blitz, M. A.; Heard, D. E.; Seakins, P. W.; Shannon, R. J., Mechanism of the Reaction of OH with Alkynes in the Presence of Oxygen. *Journal of Physical Chemistry A* 2013, 117, 5407-5418.

16. Fu, T. M.; Jacob, D. J.; Wittrock, F.; Burrows, J. P.; Vrekoussis, M.; Henze, D. K., Global budgets of atmospheric glyoxal and methylglyoxal, and implications for formation of secondary organic aerosols. *Journal of Geophysical Research-Atmospheres* 2008, 113.
17. Khare, P.; Kumar, N.; Kumari, K. M.; Srivastava, S. S., Atmospheric formic and acetic acids: An overview. *Reviews of Geophysics* 1999, 37, 227-248.
18. Fornaro, A.; Gutz, I. G. R., Wet deposition and related atmospheric chemistry in the Sao Paulo metropolis, Brazil: Part 2 - contribution of formic and acetic acids. *Atmospheric Environment* 2003, 37, 117-128.
19. Galloway, J. N.; Gaudry, A., The Composition of Precipitation on Amsterdam-Island, Indian-Ocean. *Atmospheric Environment* 1984, 18, 2649-2656.
20. Yu, S. C., Role of organic acids (formic, acetic, pyruvic and oxalic) in the formation of cloud condensation nuclei (CCN): a review. *Atmospheric Research* 2000, 53, 185-217.
21. Paulot, F.; Wunch, D.; Crouse, J. D.; Toon, G. C.; Millet, D. B.; DeCarlo, P. F.; Vigouroux, C.; Deutscher, N. M.; Abad, G. G.; Notholt, J.; Warneke, T.; Hannigan, J. W.; Warneke, C.; de Gouw, J. A.; Dunlea, E. J.; De Maziere, M.; Griffith, D. W. T.; Bernath, P.; Jimenez, J. L.; Wennberg, P. O., Importance of secondary sources in the atmospheric budgets of formic and acetic acids. *Atmospheric Chemistry and Physics* 2011, 11, 1989-2013.
22. Talukdar, R. K.; Zhu, L.; Feierabend, K. J.; Burkholder, J. B., Rate coefficients for the reaction of methylglyoxal (CH₃COCHO) with OH and NO₃ and glyoxal (HCO)₂ with NO₃. *Atmospheric Chemistry and Physics* 2011, 11, 10837-10851.
23. Atkinson, R.; Baulch, D.; Cox, R.; Crowley, J.; Hampson, R.; Hynes, R.; Jenkin, M.; Rossi, M.; Troe, J.; Subcommittee, I., Evaluated kinetic and photochemical data for atmospheric chemistry: Volume II—gas phase reactions of organic species. *Atmospheric Chemistry and Physics* 2006, 6, 3625-4055.
24. DeSain, J. D.; Jusinski, L. E.; Ho, A. D.; Taatjes, C. A., Temperature dependence and deuterium kinetic isotope effects in the HCO(DCO)+O₂ reaction between 296 and 673 K. *Chemical Physics Letters* 2001, 347, 79-86.
25. Baeza-Romero, M. T.; Glowacki, D. R.; Blitz, M. A.; Heard, D. E.; Pilling, M. J.; Rickard, A. R.; Seakins, P. W., A combined experimental and theoretical study of the reaction between methylglyoxal and OH/OD radical: OH regeneration. *Physical Chemistry Chemical Physics* 2007, 9, 4114-4128.
26. Tyndall, G. S.; Orlando, J. J.; Wallington, T. J.; Hurley, M. D., Pressure dependence of the rate coefficients and product yields for the reaction of CH₃CO radicals with O₂. *International Journal of Chemical Kinetics* 1997, 29, 655-663.
27. Bridier, I.; Caralp, F.; Loirat, H.; Lesclaux, R.; Veyret, B.; Becker, K.; Reimer, A.; Zabel, F., Kinetic and theoretical studies of the reactions CH₃C(O)O₂+NO₂+M→CH₃C(O)O₂NO₂+M between 248 and 393 K and between 30 and 760 Torr. *Journal of Physical Chemistry* 1991, 95, 3594-3600.
28. Seefeld, S.; Kinnison, D. J.; Kerr, J. A., Relative rate study of the reactions of acetylperoxy radicals with NO and NO₂: Peroxyacetyl nitrate formation under laboratory conditions related to the troposphere. *Journal of Physical Chemistry A* 1997, 101, 55-59.
29. Siese, M.; Zetzsch, C. Addition of OH to Acetylene and Consecutive Reactions of the Adduct with O₂. Part 1-2, 1995.
30. Bohn, B.; Siese, M.; Zetzsch, C., Kinetics of the OH+C₂H₂ reaction in the presence of O₂. *Journal of the Chemical Society-Faraday Transactions* 1996, 92, 1459-1466.
31. Glowacki, D. R.; Lockhart, J.; Blitz, M. A.; Klippenstein, S. J.; Pilling, M. J.; Robertson, S. H.; Seakins, P. W., Interception of Excited Vibrational Quantum States by O₂ in Atmospheric Association Reactions. *Science* 2012, 337, 1066-1069.
32. Eskola, A. J.; Carr, S. A.; Blitz, M. A.; Pilling, M. J.; Seakins, P. W., Kinetics and yields of OH radical from the CH₃OCH₂ + O₂ reaction using a new photolytic source. *Chemical Physics Letters* 2010, 487, 45-50.

33. Maranzana, A.; Ghigo, G.; Tonachini, G.; Barkert, J. R., Tropospheric oxidation of ethyne and but-2-yne. 1. Theoretical mechanistic study. *Journal of Physical Chemistry A* 2008, 112, 3656-3665.
34. Maranzana, A.; Barker, J. R.; Tonachini, G., Oxidation of ethyne and but-2-yne. 2. Master equation simulations. *Journal of Physical Chemistry A* 2008, 112, 3666-3675.
35. Taylor, S. E.; Goddard, A.; Blitz, M. A.; Cleary, P. A.; Heard, D. E., Pulsed Laval nozzle study of the kinetics of OH with unsaturated hydrocarbons at very low temperatures. *Physical Chemistry Chemical Physics* 2008, 10, 422-437.
36. Atkinson, R.; Aschmann, S. M., Rate Constants for the Reactions of O₃ and OH Radicals with a Series of Alkynes. *International Journal of Chemical Kinetics* 1984, 16, 259-268.
37. Atkinson, R., Kinetics of the gas-phase reactions of OH radicals with alkanes and cycloalkanes. *Atmospheric Chemistry and Physics* 2003, 3, 2233-2307.
38. Michael, J. V.; Keil, D. G.; Klemm, R. B., Rate Constants for the Reaction of Hydroxyl Radicals with Acetaldehyde from 244-528 K. *Journal of Chemical Physics* 1985, 83, 1630-1636.
39. Carr, S. A.; Glowacki, D. R.; Liang, C. H.; Baeza-Romero, M. T.; Blitz, M. A.; Pilling, M. J.; Seakins, P. W., Experimental and Modeling Studies of the Pressure and Temperature Dependences of the Kinetics and the OH Yields in the Acetyl + O₂ Reaction. *Journal of Physical Chemistry A* 2011, 115, 1069-1085.
40. Glowacki, D. R.; Liang, C. H.; Morley, C.; Pilling, M. J.; Robertson, S. H., MESMER: An Open-Source Master Equation Solver for Multi-Energy Well Reactions. *Journal of Physical Chemistry A* 2012, 116, 9545-9560.
41. Lee, J.; Bozzelli, J. W., Reaction of H plus ketene to formyl methyl and acetyl radicals and reverse dissociations. *International Journal of Chemical Kinetics* 2003, 35, 20-44.
42. Huynh, L. K.; Violi, A., Thermal decomposition of methyl butanoate: Ab initio study of a biodiesel fuel surrogate. *Journal of Organic Chemistry* 2008, 73, 94-101.
43. Ianni, J. C., Kintecus, Windows Version 2.80, 2002, www.kintecus.com.
44. Saunders, S. M.; Jenkin, M. E.; Derwent, R. G.; Pilling, M. J., Protocol for the development of the Master Chemical Mechanism, MCM v3 (Part A): tropospheric degradation of non-aromatic volatile organic compounds. *Atmospheric Chemistry and Physics* 2003, 3, 161-180.

Chapter 5 Products of the OH + Acetaldehyde Reaction

5.1 Abstract

A kinetic study of the reaction of OH with acetaldehyde, CH₃CHO, has been carried out using either pure N₂ or O₂/N₂ mixture bath gas over a range of pressures (1 – 60 Torr) and temperatures (212 – 468 K), using pulsed laser flash photolysis with laser induced fluorescence OH detection. The title reaction proceeds predominantly via abstraction of the aldehydic hydrogen resulting in formation of an acetyl radical, CH₃CO, and H₂O. At low pressures the CH₃CO radical reacts with oxygen to generate OH with near unity yield. OH recycling in the OH/CH₃CHO/O₂ system has been investigated as a function of pressure and temperature, with OH yields measured from the ratio of rate coefficients measured with and without oxygen present. Stern-Volmer analyses of the OH yields measured between 212 and 385 K are linear with an intercept greater than 1, indicating that ~16% of the total product yield for the title reaction generate products which do not react with O₂ and recycle OH at low pressures. These kinetic measurements have been complemented by a direct investigation of the products of the OH + CH₃CHO reaction using laser flash photolysis coupled to photo-ionization time-of-flight mass spectrometry (PIMS), which detect methyl radicals (CH₃) as primary products with a yield of ~15% at 295 K in 1 – 2 Torr of helium bath gas. Strong experimental evidence indicates that the source of methyl radicals is from prompt dissociation of chemically activated acetyl products and hence is consistent with previous studies which have shown that abstraction is the sole route for the OH + CH₃CHO reaction. However, the observation of a significant methyl product suggests that energy partitioning in this reaction is different from the typical energy barrier mechanism where reaction exothermicity is channelled preferentially into the newly formed bond. The implications of the observations in atmospheric and combustion chemistry are briefly discussed.

5.2 Background and Previous Work

Acetaldehyde, CH₃CHO, is one of the most abundant carbonyl compounds in the troposphere, where it has significant roles in both atmospheric photochemistry and air quality. Acetaldehyde is a recognised hazardous air pollutant,¹ and produced extensively during the atmospheric photochemical degradation of a great many volatile organic compounds (VOCs).²⁻⁷ The dominant anthropogenic source of acetaldehyde is direct emission following incomplete combustion of fossil and oxygenated fuels, while primary biogenic sources include biomass burning, live and decaying plants, and seawater.⁸ The concentration of acetaldehyde in the troposphere ranges from sub ppb in remote regions,⁹ to tens of ppb in polluted cities.¹⁰⁻¹³ During daylight hours, acetaldehyde is removed primarily through reaction with OH,¹⁴ via hydrogen atom abstraction at either the aldehydic (R1a) or methyl group (R1b):



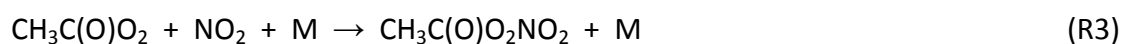
but also by UV photolysis (P1):¹⁵



Acetaldehyde has an atmospheric lifetime of ~18.5 hours at 298 K with respect to reaction R1 (using a k_1 value of $1.5 \times 10^{-11} \text{ cm}^3 \text{ molecule}^{-1} \text{ s}^{-1}$, as recommended recently by IUPAC,¹⁴ and an average OH radical concentration of $1 \times 10^6 \text{ molecule cm}^{-3}$). Under atmospheric conditions, the acetyl radical, CH₃CO, produced following reaction R1a rapidly reacts with O₂ to produce an acetylperoxy radical (R2a):



In polluted regions, the acetylperoxy radical can temporarily sequester NO₂ in the form of peroxyacetylnitrate (PAN):



a secondary pollutant present in photochemical smog,¹⁶ and a known irritant.¹⁷ The only significant loss process for PAN is thermal decomposition that regenerates NO₂ (R4):



Reaction R4 is strongly temperature dependent such that PAN decomposes within an hour at 298 K, but has a lifetime of several months at 250 K.¹⁸ Consequently, in the middle and upper troposphere, PAN can be transported over long distances before decomposing, and release NO₂ far from its source. The subsequent photolysis of NO₂ drives ground level ozone production, and therefore potentially affects air quality in remote unpolluted regions.¹⁹

Several groups have investigated the temperature dependence of reaction R1, and collectively reported non-Arrhenius behaviour over the 200 – 900 K temperature range. All studies report k_1 to increase as temperatures decrease below ~350 K. However, as temperatures increase above ~550 K, a positive temperature dependence is observed. It is widely accepted that the positive temperature dependence observed in the high temperature range, reflects a switch in the dominant hydrogen atom abstraction site; with the acetyl group (R1a) favoured at low and medium temperatures, and the methyl group (R1b) favoured at higher temperatures. Taylor et al. interpreted the negative temperature dependence below ~350 K as evidence of a mechanism involving OH addition to the carbonyl group, followed by dissociation of the adduct complex by elimination of either a methyl radical (R1c) or H-atom (R1d).²⁰



Taylor and co-workers investigated the OH + CH₃CHO reaction mechanism using a quantum RRK model, and suggested the addition-elimination paths dominated reaction R1 at room temperature; although there is no experimental evidence to support this conclusion. Cameron et al. used pulsed laser photolysis with either UV transient absorption spectroscopy or resonance fluorescence techniques to quantify the primary radical products of reaction R1.²¹ At room temperature the dominant product path leads to CH₃CO + H₂O

formation with a yield of (0.93 ± 0.18) . Cameron et al. were unable to detect CH_3 or H-atoms as primary products of reaction R1, and placed upper limits of 0.03 and 0.02 for respective yields of reactions R1c and R1d, based on the detection limits of their apparatus. However, the acetyl UV spectrum is broad, featureless and overlaps with the sharper CH_3 spectrum; therefore there is potential for incorrect assignment of absorptions, especially if vibrational excitation is present in the radical species. Vandenberg and Peeters quantified product branching ratios for the $\text{OH} + \text{CH}_3\text{CHO}$ reaction at 298 K using a fast-flow reactor coupled with molecular beam sampling mass spectrometry (MBMS).²² These authors quantified the contribution of H-atom abstraction to reaction R1 as (0.89 ± 0.06) based on their experimental H_2O yield. Furthermore, they were unable to detect HCOOH as a primary product of reaction R1, and placed an upper limit branching ratio of 0.03 for channel R1c. Tyndall et al. studied the $\text{OH} + \text{CH}_3\text{CHO}$ reaction in 1 atm of synthetic air at 298 and 251 K, using a photoreactor equipped with FTIR stable product analysis.²³ They found no evidence of carboxylic acid formation following reaction R1, in agreement with the results of Cameron et al.²¹ and Vandenberg and Peeters,²² and reported a total carboxylic acid yield (R1c and R1d) of less than 10%, based on experimental detection limits. Butkovskaya et al. studied the $\text{OH} + \text{CH}_3\text{CHO}$ reaction in 200 Torr of N_2 at 298 and 248 K, using a high pressure turbulent flow reactor (HPTFR) coupled with chemical ionisation mass spectrometry (CIMS).²⁴ These authors reported hydrogen atom abstraction as the dominant path for reaction R1 with an experimental H_2O yield of (0.98 ± 0.05) ; with approximately 5% of total abstraction yielding the vinoxy radical, CH_2CHO (R1b). Wang et al. studied the kinetics and product yields of reaction R1 at room temperature using pulsed laser photolysis with IR transient absorption spectroscopy, and reported H_2O yields of approximately 100% in close agreement with previous studies.²⁵ In addition, these authors reported evidence of modest CH_3 production, but failed to detect H-atoms using indirect methods, placing upper limit yields of 5% for each of the addition-elimination pathways. These experimental findings are consistent with theoretical treatment of the $\text{OH} + \text{CH}_3\text{CHO}$ reaction by D'Anna et al., where high level *ab initio* calculations suggest a significant barrier height of 30.9 kJ mol^{-1} for OH addition to the carbonyl double bond.²⁶ Furthermore, the calculations by D'Anna et al. predict the abstraction channels proceed via a hydrogen bonded pre-reactive complex. The rate of reactions of OH with other carbonyl compounds involving a pre-reactive complex

have been shown recently to demonstrate strong negative temperature dependences at low temperatures.²⁷ It is now generally accepted that the major, if not exclusive, reaction channel for OH + CH₃CHO proceeds via hydrogen atom abstraction (R1a and R1b). The study by D'Anna et al. included an experimental investigation of the OH + CH₃CHO reaction under atmospheric conditions using a smog chamber equipped with FTIR detection.²⁶ OH radicals were generated from the photolysis of deuterated 2-propyl nitrite:



These authors observed PAN as the major product of the OH + CH₃CHO reaction, consistent with reactions R1a, R2a and R3, together with HCHO and CO in relatively small yields of approximately 10%, as the only products. D'Anna and co-workers interpreted these observations as evidence of a third product channel following abstraction, where a fraction of the acetyl produced following reaction R1 fragments (R1e):



as HCHO is formed following methyl radical oxidation in the presence of NO:



The enthalpy of reaction R1a is approximately -123 kJ mol^{-1} ,²⁸ while the activation energy for acetyl decomposition is near 71 kJ mol^{-1} .²⁹ Therefore reaction R1a occurs with sufficient exothermicity for the nascent CH₃CO radical to dissociate to CH₃ + CO in a chemically activated process; although this channel requires a significant fraction of the total reaction exothermicity to be partitioned into the CH₃CO fragment. Classically, hydrogen atom abstraction reactions are thought to partition the majority of the available energy into the newly formed bond,³⁰ and in the case of OH initiated hydrogen abstraction

channels, into the H-O bond of the H₂O molecule. However, the pre-reactive complex associated with the OH + CH₃CHO reaction could facilitate a more statistical energy distribution between the CH₃CO and H₂O products. Experimental evidence of H-atom abstraction reactions partitioning reaction exothermicity into spectator bonds has been provided by recent studies conducted at the University of Leeds; namely the reactions of OH with glyoxal and methylglyoxal.^{29, 31} The OH + glyoxal system is discussed in detail in chapter 6 of this thesis. Briefly, the OH + glyoxal reaction proceeds via hydrogen atom abstraction, the resulting HC(O)CO radical forms with sufficient energy that a significant fraction of the population promptly dissociates to HCO + CO. Similar behaviour was observed by Baeza-Romero et al. when studying the OH + methylglyoxal reaction, which also proceeds via aldehydic hydrogen abstraction.²⁹ The resulting CH₃C(O)CO radical forms with sufficient energy not only to dissociate to CH₃CO + CO, but for a fraction of the acetyl radical formed to dissociate further to CH₃ + CO.

This chapter aims to investigate the significance of chemical activation in the acetyl produced following the reaction of OH with acetaldehyde. At low total pressures acetyl reacts with O₂ to generate OH (R2b):³²



Kinetic OH yields, Φ_{OH} , for reaction R2b have been measured as a function of total pressure (1 – 60 Torr) and temperature (212 – 385 K). Stern-Volmer analysis of the Φ_{OH} measured allows the fraction of the total product yield for reaction R1 that does not recycle OH in the presence of oxygen at low pressure be quantified. This work was carried out in concert with a separate study of the OH + CH₃CHO reaction using laser flash photolysis coupled with photo-ionization time-of-flight mass spectrometry (PIMS), conducted at the University of Leeds by Neil Howes and Dr Mark Blitz, which identified CH₃CO and CH₃ as primary products of reaction R1.

5.3 Experimental

The slow-flow laser flash photolysis, laser induced fluorescence (LFP-LIF) apparatus used to study the kinetics of the OH + CH₃CHO reaction at 212 and 295 K is identical to that described in chapter 3. The same kinetic technique was used for experiments carried out at 385 K, but using a different high temperature LFP-LIF apparatus that has been used in two recent publications,^{33, 34} the details of this apparatus are provided here. The flows of *t*-butyl hydroperoxide, acetaldehyde, and bath gas (N₂ and/or O₂) were regulated via calibrated mass flow controllers, mixed, and flowed into a stainless steel, 10-way cross reactor. The total pressure inside the reactor was monitored using a baratron pressure gauge, and controlled via a needle valve between the reactor and rotary pump. The temperature of the reactor was controlled using cartridge heaters inserted into the body of the reactor, and measured using thermocouples located above and below the reaction zone.

OH radicals were generated by pulsed excimer laser photolysis (Lambda Physik 2101, at 248 nm) of *t*-butyl hydroperoxide:



The photolysis laser pulse was introduced through one of the arms of the reactor, and typically operated at 5 Hz. Tests were carried out at lower excimer laser pulse repetition rates to ensure that a fresh sample of gas was present inside the reactor for each photolysis laser pulse. OH radicals were detected by off-resonance LIF, with ~282 nm probe radiation generated using a NdYAG pumped (Powerlite Precision II 8010) dye laser (Sirah PRSC-DA-24) operating with Rhodamine6G. The off-resonance fluorescence at ~308 nm was observed through a filter using a PMT mounted mutually perpendicular to both the photolysis and probe laser beams. The time delay between the photolysis and probe laser pulses was controlled using LabVIEW software, and was varied to build up a time profile of the OH signal following photolysis. Kinetic traces were typically 250 data points each averaged 2 – 10 times depending on the signal-to-noise ratio. Acetaldehyde was degassed thoroughly by several freeze-pump-thaw cycles, and diluted into a blackened glass sample bulb in N₂. The concentration of acetaldehyde in the sample bulbs was determined barometrically.

Materials used: nitrogen (BOC oxygen free), oxygen (Air Products, high purity, 99.999%), *t*-butyl hydroperoxide (Sigma Aldrich, 70% v/v aqueous), acetaldehyde (Sigma Aldrich, > 99.5%).

The reactions were carried out under *pseudo-first-order* conditions with acetaldehyde concentrations ($> 1 \times 10^{13}$ molecule cm^{-3}) in great excess over OH ($\sim 1 \times 10^{11}$ molecule cm^{-3}). In N_2 bath gas the OH decay is governed by reactions R1 and R11:



where reaction R10 accounts for reaction with *t*-butyl hydroperoxide and diffusion from the probed region of the reactor. Under these conditions the observed OH signal decays exponentially, and the time dependent OH signal, $I_{\text{f}}(t)$, is defined by the following equation:

$$I_{\text{f}}(t) = I_{\text{f}}(0) \exp^{-k't} \quad (\text{E1})$$

where $I_{\text{f}}(0)$ is the initial OH signal intensity, and k' is the observed *pseudo-first-order* decay constant equal to $k_1[\text{CH}_3\text{CHO}] + k_{10}$. It follows that a plot of k' against $[\text{CH}_3\text{CHO}]$ yields a straight line with a gradient equal to the bimolecular rate coefficient k_1 ; an example of such a plot is provided in Figure 1, with a typical experimental decay trace included in the inset.

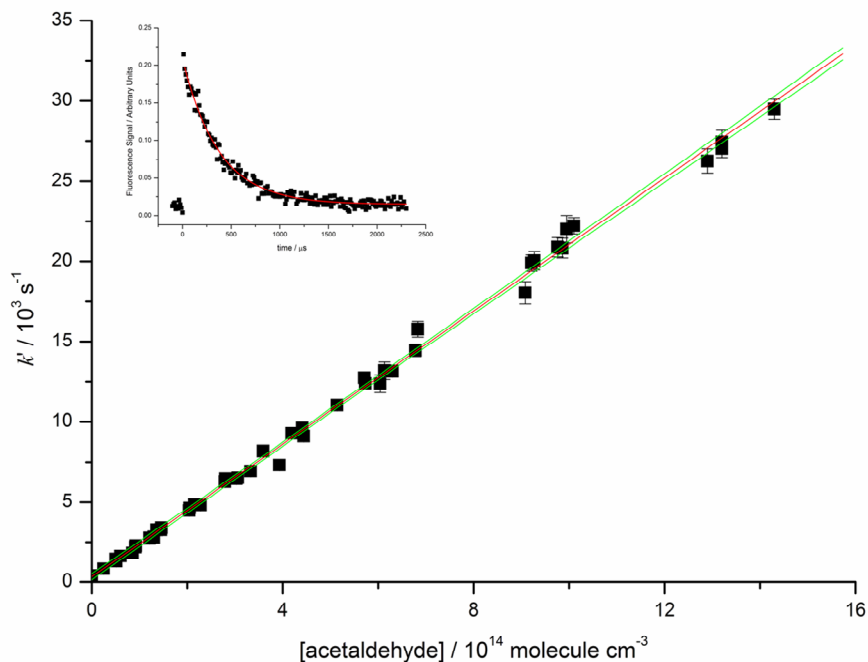


Figure 1: Bimolecular plot for the OH + CH₃CHO reaction at 212 K at pressures ranging from between 1 and 10 Torr; least squares linear analysis through all data points yields a bimolecular rate coefficient of $(2.07 \pm 0.02) \times 10^{-11} \text{ cm}^3 \text{ molecule}^{-1} \text{ s}^{-1}$; a typical experimental OH decay trace at 212 K fit using equation E1 is included in the inset.

5.4 OH + CH₃CHO Temperature Dependence in Nitrogen Bath Gas

The temperature dependence of the OH + CH₃CHO reaction has been investigated using the pulsed laser photolysis, laser induced fluorescence technique, at 212, 295, 385, and 468 K, using pure N₂ bath gas at total pressures ranging from 1 – 60 Torr. The observed rate coefficient, k_1 , was found to be independent of total pressure at all temperatures (Figure 1), consistent with a reaction proceeding exclusively via hydrogen atom abstraction, and not via OH addition to the carbonyl group, as proposed by Taylor et al.²⁰ The experimental $k_1(T)$ measurements were highly reproducible with values of (2.07 ± 0.21) , (1.36 ± 0.14) , (1.29 ± 0.13) , and $(1.16 \pm 0.12) \times 10^{-11} \text{ cm}^3 \text{ molecule}^{-1} \text{ s}^{-1}$ at temperatures of 212, 295, 385, and 468 K, respectively, obtained by fitting least squares linear regression through all pressure data at each temperature; the uncertainty in $k_1(T)$ was estimated at 10% and includes both statistical and systematic errors. A comparison between the present results and literature data is presented in Arrhenius form in Figure 2.

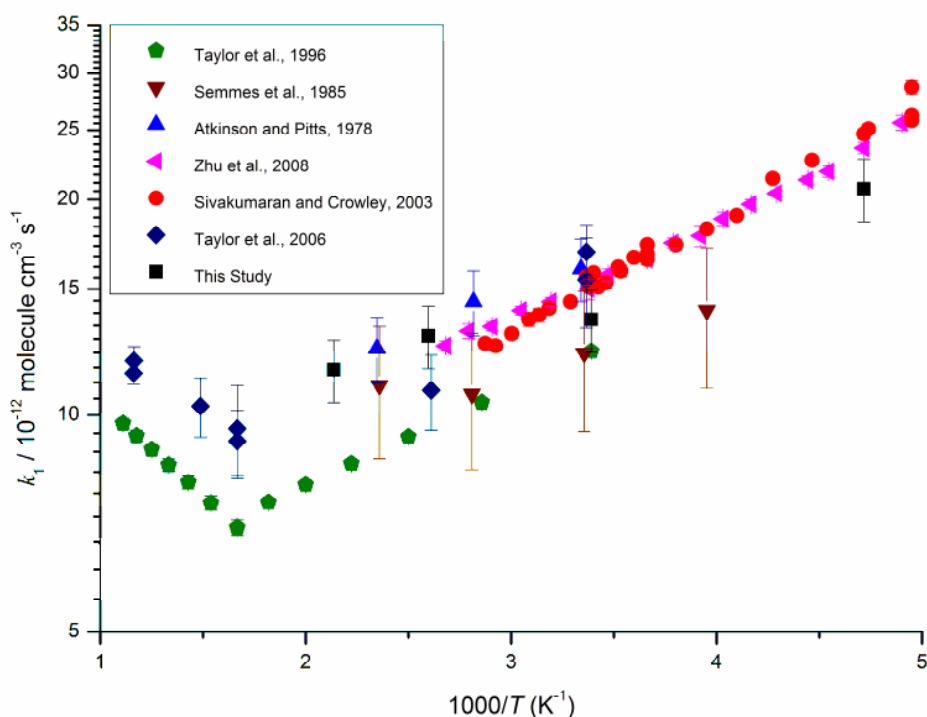


Figure 2: Arrhenius plot of the experimental rate coefficients, $k_1(T)$, for the $\text{OH} + \text{CH}_3\text{CHO} \rightarrow \text{Products}$ reaction, measured during this work. $k_1(T)$ measurements reported by other studies are included for comparison. The data of Taylor et al. 1996 were not tabulated in their publication and were therefore taken from their Arrhenius plot.²⁰ The error bars quoted by Sivakumaran and Crowley,³⁵ Zhu et al.,³⁶ and Taylor et al., 2006³⁷ are purely statistical (2σ). The error bars quoted by Atkinson and Pitts,³⁸ and Semmes et al.³⁹ combine both the statistical (2σ) and estimated systematic errors.

The room temperature k_1 value of $(1.36 \pm 0.14) \times 10^{-11} \text{ cm}^3 \text{ molecule}^{-1} \text{ s}^{-1}$ measured during this study is in excellent agreement with previous determinations of this rate coefficient which fall in the range $(1.2 - 1.7) \times 10^{-11} \text{ cm}^3 \text{ molecule}^{-1} \text{ s}^{-1}$,^{20, 35-39} and also agrees well within the combined uncertainty limits with the $(1.5 \pm 0.1) \times 10^{-11} \text{ cm}^3 \text{ molecule}^{-1} \text{ s}^{-1}$ value recently recommended by IUPAC.¹⁴ Furthermore, the negative temperature dependence reported by other studies of reaction R1 at temperatures ranging from 200 – 550 K is consistent with the results presented here. As discussed previously, the experimental measurements made at 212 and 295 K were carried out using the same

In the presence of acetaldehyde, using pure nitrogen bath gas and ignoring the relatively minor contribution from diffusion and reaction with the precursor to total OH removal (which does not scale with the acetaldehyde concentration and therefore does not influence the kinetics), OH loss is defined by the following differential rate law:

$$-\frac{d[\text{OH}]}{dt} = k_1[\text{CH}_3\text{CHO}][\text{OH}] \quad (\text{E3})$$

In the presence of molecular oxygen, a fraction of the acetyl formed through reaction R1a will react with O₂ and generate OH. If the O₂ concentration is sufficient to make the acetyl + O₂ reaction fast compared with reaction of OH with acetaldehyde (R1), OH loss is determined by the fraction of reaction R1 that does not go on to recycle OH:

$$-\frac{d[\text{OH}]}{dt} = k_1[\text{CH}_3\text{CHO}][\text{OH}] - k_{1a}[\text{CH}_3\text{CHO}][\text{OH}] \times \left(\frac{k_{2b}}{k_{2a}[\text{M}] + k_{2b}} \right) \quad (\text{E4})$$

Consequently, the bimolecular rate coefficient measured using pure nitrogen bath gas, k_{N_2} (see upper black line in Figure 3), will be faster than rate coefficients measured in excess O₂, k_{O_2} (see lower lines in Figure 3), which are subject to rapid OH regeneration. The pressure dependent OH yield, Φ_{OH} , attributed to secondary acetyl chemistry following the OH + CH₃CHO reaction can be expressed as:

$$\Phi_{\text{OH}} = \frac{k_{1a}}{k_1} \left(\frac{k_{2b}}{k_{2a}[\text{M}] + k_{2b}} \right) \quad (\text{E5})$$

It follows from equations E3 – 5, that the ratio of rate coefficients measured in the presence and absence of oxygen is:

$$\frac{k_{\text{O}_2}}{k_{\text{N}_2}} = 1 - \Phi_{\text{OH}} \quad (\text{E6})$$

Therefore the experimental Φ_{OH} can be calculated by:

$$\Phi_{\text{OH}} = 1 - \left(\frac{k_{\text{O}_2}}{k_{\text{N}_2}} \right) \quad (\text{E7})$$

As total pressures increase a greater fraction of the nascent acetylperoxy radical population undergo collisional deactivation, at the expense of the formally direct decomposition channel, resulting in less OH regeneration; consequently k_{O_2} and k_{N_2} converge at elevated pressures (Figure 3).

Stern-Volmer (S-V) analysis is often used to parameterize the effect of collisional deactivation on the branching ratios of chemically activated or formally direct product paths. Whereby a plot of the reciprocal activated product yield against total pressure yields a straight line with a gradient equal to the bath gas quenching efficiency and an intercept equal to the inverse formally direct product yield at zero pressure. For the acetyl + O₂ system (Scheme 1), a plot of the inverse Φ_{OH} against total pressure, [M], should be linear with a gradient equal to the k_{2a}/k_{2b} ratio, and an intercept of 1 (E2).

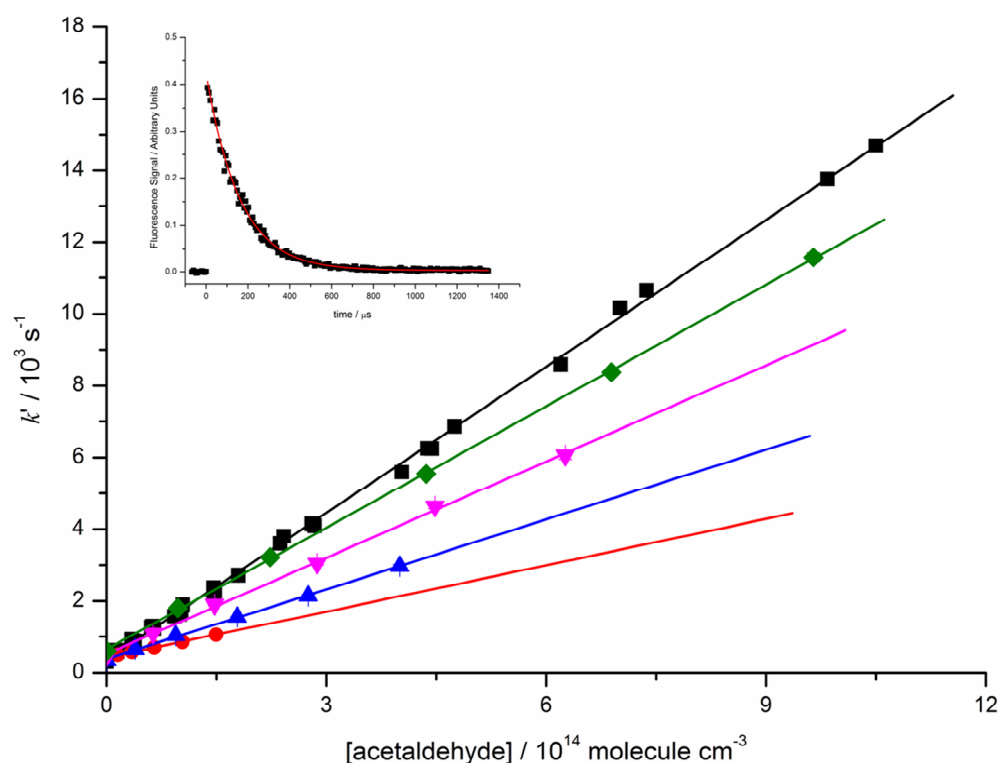


Figure 3: Bimolecular plots for the OH + CH₃CHO → Products reaction at 295 K using both pure nitrogen bath gas (■), and in the presence of excess O₂ at total pressures of 10 (◆), 5 (▼), 2 (▲) and 1 Torr (●). A typical OH decay trace at this temperature is included in the inset.

Blitz and co-workers at the University of Leeds have studied the kinetics and Φ_{OH} associated with the acetyl + O₂ reaction extensively.^{40, 41, 44} In a recent elegant study, Carr et al. used 248 nm photolysis of acetic acid, CH₃COOH, in helium or nitrogen bath gas to generate CH₃CO and OH in equal yields (P4):⁴⁰



The OH signal was then monitored directly via off-resonance LIF. Following addition of O₂ to the system, the OH profile comprised of both an instant photolytic signal and a slow growth due to reaction of acetyl with O₂ (R2b). The absolute Φ_{OH} was then quantified as a function of total pressure from the observed OH growth by using the photolytic signal as an internal standard. S-V analysis of the Φ_{OH} measured by Carr and co-workers reported k_{2a}/k_{2b} ratios of (1.31 ± 0.51) and $(3.59 \pm 0.60) \times 10^{-18} \text{ molecule}^{-1} \text{ cm}^3$ using helium and nitrogen bath gas, respectively, at room temperature. These results are consistent with nitrogen being a more effective third body collision partner for the nascent acetylperoxy radical than helium. Importantly for the work presented in this chapter, the S-V plots by Carr et al. also reported unity intercepts, signifying that at zero pressure reaction R2 proceeds exclusively to OH.⁴⁰

As previously mentioned, the analysis described above requires that the CH₃CO + O₂ reaction (k_2) is fast compared with the reaction between OH and acetaldehyde (k_1). During the work presented here, all the experiments undertaken at 212 K were carried out at pressures ranging between 1 and 10 Torr. Under these conditions, all *pseudo-first-order* rate coefficients, k' , measured in pure nitrogen bath gas were less than $3 \times 10^4 \text{ s}^{-1}$ (Figure 1). ME analysis of experimental measurements of the pressure- and temperature dependent rate coefficients for the CH₃CO + O₂ reaction by Carr et al. suggests a k_2 value of $3.18 \times 10^{-12} \text{ cm}^3 \text{ molecule}^{-1} \text{ s}^{-1}$ at 1 Torr and 212 K using nitrogen bath gas.⁴¹ The minimum O₂ concentration used during all the OH + CH₃CHO/O₂ experiments at 212 K was $\sim 2 \times 10^{16} \text{ molecules cm}^{-3}$, corresponding to an acetyl + O₂ *pseudo-first-order* rate coefficient, k'_2 , of $6.4 \times 10^4 \text{ s}^{-1}$. Therefore the rate of the CH₃CO + O₂ reaction, k_2 , is expected to be at least a factor of two faster than the OH + CH₃CHO reaction; with the k_2/k_1 ratio increasing further at higher total pressures as both k_2 and the absolute O₂ concentration increase. Similar calculations at 295 and 385 K confirm that k_2 was at least a factor of two faster than k_1 under all experimental conditions.

For the OH yields associated with secondary chemistry following the OH + CH₃CHO/O₂ reaction (E5), S-V analysis yields the following linear expression:

$$\frac{1}{\Phi_{\text{OH}}} = \left(\frac{k_1 k_{2a}}{k_{1a} k_{2b}} \right) [M] + \frac{k_1}{k_{1a}} \quad (\text{E8})$$

With an intercept defined by the reciprocal acetyl yield at zero pressure, and a gradient equal to $\frac{k_1 k_{2a}}{k_{1a} k_{2b}}$.

Experimental Φ_{OH} have been measured for the OH + CH₃CHO/O₂ system at 212, 295, and 385 K, from the ratio of rate coefficients measured in the presence and absence of O₂ at pressures ranging from 1 – 60 Torr using N₂ bath gas (E7). S-V plots at each temperature are presented in Figure 4, with each data set fit using a linear weighted least squares regression confidence interval (1 σ); the results of this linear analysis are tabulated in Table 1. The error in the reciprocal Φ_{OH} is purely statistical (2 σ) and calculated by multiplying the reciprocal Φ_{OH} by the fractional error of the experimental Φ_{OH} .

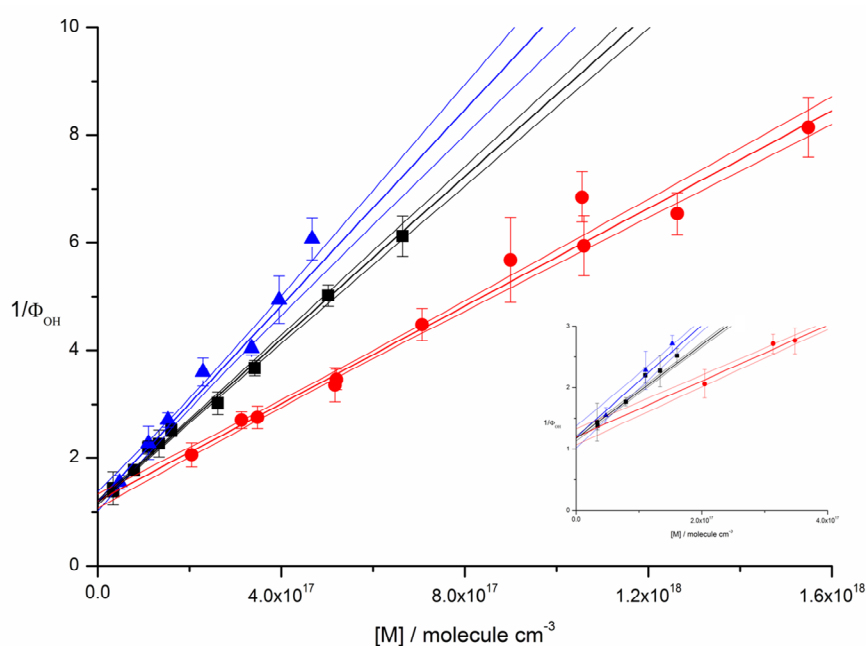


Figure 4: Stern-Volmer Plots of reciprocal OH yield against total pressure for the OH + CH₃CHO → Products reaction at 212 (▲), 295 (■) and 385 K (●); error bars a purely statistical (2 σ). Weighted least squares linear regression fits through the data with 1 σ confidence intervals are included. The magnified intercept is included in the inset.

Temperature / K	$k_1 / 10^{-11} \text{ cm}^3 \text{ molecule}^{-1} \text{ s}^{-1}$	Intercept of SV plot	Maximum and minimum values of SV intercept	Gradient / $10^{-18} \text{ cm}^3 \text{ molecule}^{-1}$
212	(2.07 ± 0.02)	1.20	1.34	(9.09 ± 0.54)
			1.06	
295	(1.36 ± 0.01)	1.18	1.23	(7.57 ± 0.30)
			1.12	
385	(1.29 ± 0.02)	1.20	1.36	(4.53 ± 0.27)
			1.04	

Table 1: Results of linear Stern-Volmer analysis of the experimental OH yields associated with the $\text{OH} + \text{CH}_3\text{CHO}/\text{O}_2 \rightarrow \text{Products}$ reaction; error bars are purely statistical (1σ).

Across all experimental temperatures the 1σ confidence interval for the intercept do not include, and are greater than unity (1.05 – 1.36). An intercept greater than 1 is consistent with a fraction of reaction R1 generating products which do not recycle OH in the presence of O_2 at low pressures. All temperatures converge on an intercept of 1.18 – 1.20, suggesting that between 15 and 17% of the total $\text{OH} + \text{CH}_3\text{CHO}$ product yield does not recycle OH at low pressure. The vinoxy radical yield of $(5.1^{+2.4}_{-1.7})\%$ reported by Butkovskaya et al.,²⁴ cannot account for the S-V intercepts reported here; particularly given that reaction of the vinoxy radical with O_2 is also likely to generate OH (R11).⁴⁵⁻⁴⁸



The results presented here are consistent with a fraction of the acetyl formed following reaction R1a, promptly decomposing to $\text{CH}_3 + \text{CO}$ (R1e). Furthermore, these results show S-V intercepts independent of temperature, suggesting that acetyl fragments as a result of chemical activation, and does not dissociate thermally over this temperature

range. In contrast to the intercepts, the S-V gradients reported here do depend on temperature, decreasing from (9.09 ± 0.54) to $(4.53 \pm 0.27) \times 10^{-18} \text{ cm}^3 \text{ molecule}^{-1}$ as temperatures increase from 212 to 385 K, respectively (Table 1). It follows from equation E8, and the S-V plot intercepts, that the k_1/k_{1a} ratio is independent of temperature between 212 and 385 K. Therefore the temperature dependent S-V plot gradients can only be attributed to the k_{2a}/k_{2b} ratio. As temperatures decrease the nascent activated $\text{CH}_3\text{C}(\text{O})\text{O}_2$ radical forms with less energy and consequently is less likely to dissociate prior to collisional stabilisation, resulting in an increased k_{2a}/k_{2b} ratio.

Groß et al. have very recently studied OH formation following the $\text{CH}_3\text{CO} + \text{O}_2$ reaction in helium or nitrogen with added O_2 , or synthetic air bath gas, at 296 K and pressures ranging between 20 and 300 Torr, using pulsed laser photolysis-laser induced fluorescence (PLP-LIF) apparatus.⁴⁹ These authors generated CH_3CO by 248 nm photolysis of COCl_2 in the presence of acetaldehyde (P5, R12).



The OH formed following subsequent reaction of acetyl with O_2 (R2) was monitored directly by off resonance LIF. The LIF-system was then calibrated in back-to-back experiments by the 248 nm photolysis of H_2O_2 as OH precursor (P6).



Comparison of the OH signals observed following COCl_2 and H_2O_2 photolysis allowed the experimental OH yield associated with the $\text{CH}_3\text{CO} + \text{O}_2$ reaction to be quantified directly as a function of pressure. S-V analysis of the Φ_{OH} measurements by Groß and co-workers yields a straight line with unity intercept and a quenching efficiency of $(9.4 \pm 1.7) \times 10^{-18} \text{ cm}^3 \text{ molecule}^{-1}$ using nitrogen bath gas.⁴⁹ This value agrees within the combined uncertainty limits with the $(7.57 \pm 0.30) \times 10^{-18} \text{ cm}^3 \text{ molecule}^{-1}$ value reported here. It is worthwhile to note the unity S-V intercept reported by Groß et al. is to be expected, given that the $\text{Cl} + \text{CH}_3\text{CHO}$ reaction enthalpy is $\sim -58 \text{ kJ mol}^{-1}$,⁵⁰ and therefore acetyl radicals produced following reaction R12 do not possess enough energy to dissociate to $\text{CH}_3 + \text{CO}$.

Tyndall et al. studied the Cl + CH₃CHO reaction at room temperature using N₂ and/or O₂ bath gas at pressures ranging between 1 and 700 Torr, using an environmental photoreactor equipped with FTIR absorption spectroscopy.⁵¹ They measured the kinetics of reaction R12 relative to the pressure independent Cl + CH₃OH reaction (R13).



These authors reported k_{13}/k_{14} ratios independent of pressure using N₂ bath gas, but observed a significant increase in the k_{13}/k_{14} ratio with decreasing pressure in the presence of O₂. Tyndall and co-workers suggested these findings provide indirect evidence of OH formation through reaction R2b, which then reacts with acetaldehyde significantly faster than it does with methanol. Tyndall et al. quantified Φ_{OH} for reaction R2 as a function of pressure, but did not perform S-V analysis of their results. However, subsequent linear analysis of the results of Tyndall et al. by Carr and co-workers,⁴¹ assuming a zero pressure intercept of 1, derived a quenching efficiency of $5.9 \times 10^{-18} \text{ cm}^3 \text{ molecule}^{-1}$, in good agreement with the results presented here.

Talukdar et al. investigated the OH formation associated with reaction R2 in helium, nitrogen and oxygen diluents at room temperature and total pressures ranging between 20 and 600 Torr.⁵² These authors used 248 nm photolysis of acetone (P6) and OH and Cl-atom initiated oxidation of acetaldehyde (R1a, R12) to generate acetyl radicals.



OH radicals were monitored directly by LIF in the presence of oxygen, allowing the pressure dependent Φ_{OH} for reaction R2 to be determined from either the observed OH profiles or the modified OH kinetics. S-V analysis of the OH yields measured by Talukdar and co-workers report a quenching efficiency of $(11 \pm 2.5) \times 10^{-18} \text{ cm}^3 \text{ molecule}^{-1}$ using nitrogen bath gas.⁵² This value is broadly consistent with the result presented here, although these results have yet to be published in a peer reviewed journal.

Carr and co-workers have published work investigating the kinetics and Φ_{OH} of the CH₃CO + O₂ reaction twice in recent years,^{40, 41} using a suitable photolytic acetyl precursor with LIF OH detection on both occasions. Their first study generated CH₃CO using 248 nm

photolysis of acetic acid (P4) in nitrogen with added oxygen at room temperature.⁴⁰ This method was self-calibrating and has been described previously, yielding a quenching efficiency of $(3.59 \pm 0.60) \times 10^{-18} \text{ cm}^3 \text{ molecule}^{-1}$. More recently, Carr and co-workers generated acetyl by 248 nm photolysis of acetone (P7), in nitrogen with added oxygen, and fitted the resulting OH profile using a bi-exponential function.⁴¹ As the LIF signal does not provide absolute OH concentrations, back-to-back experiments were carried out using nitrogen diluents, at pressures ranging between 5 and 300 Torr at 298 and 378 K, with OH yields expressed relative to a reference yield at a fixed pressure close to zero. Plots of the reciprocal relative OH yield against total pressure were in linear S-V form, allowing the bath gas quenching efficiency to be determined from the S-V gradient/intercept ratio. Data were corrected for the effect of pressure on the yield of acetyl following acetone photolysis and for quenching of the LIF OH signal. This novel approach by Carr and co-workers reported quenching efficiency of (2.67 ± 1.40) and $(2.20 \pm 0.81) \times 10^{-18} \text{ cm}^3 \text{ molecule}^{-1}$ in nitrogen at 298 and 378 K, respectively.⁴¹ In addition to this published work, Carr also measured the pressure-dependent OH yield associated with reaction R2 by generating acetyl chemically as part of his doctoral research at the University of Leeds.⁵³ Linear S-V analysis of the room temperature OH yields measured following reaction of OH with acetaldehyde (R1) in excess oxygen using helium bath gas, yields a straight line with an intercept of 1.41 ± 0.30 and a quenching efficiency of $(2.9 \pm 2.0) \times 10^{-18} \text{ cm}^3 \text{ molecule}^{-1}$, where the errors represent the 2σ confidence interval. This intercept suggests 29% of the total product yield following reaction R1, do not recycle OH in the presence of oxygen at low pressures, and is consistent with the results presented here. Kovacs et al. measured OH yields for the same system in helium bath gas at 298 K under low total pressures (1 – 8 Torr) using a discharge flow reactor coupled with OH LIF detection.⁵⁴ OH was generated from $\text{H} + \text{NO}_2$ or $\text{F} + \text{H}_2\text{O}$. S-V analysis of the OH yields reported by Kovacs and co-workers gives a helium quenching efficiency of $(3.97 \pm 0.56) \times 10^{-18} \text{ cm}^3 \text{ molecule}^{-1}$ with an intercept fixed at unity. The acetyl quenching efficiency of helium measured by Carr is in excellent agreement with the value determined using the data of Kovacs, particularly when you consider fixing the S-V plot by Carr with an intercept of 1 increases the gradient to $(5.4 \pm 1.6) \times 10^{-18} \text{ cm}^3 \text{ molecule}^{-1}$.⁵³ These results suggest that the gradients of S-V plots associated with the OH yield of the acetyl + O₂ reaction are dependent on the method used to generate acetyl, with photolytic acetyl

sources (acetic acid and acetone) showing significantly less quenching than chemical acetyl sources (OH or Cl-atom + acetaldehyde). The 248 nm photolysis wavelength used by Carr and co-workers corresponds to a total energy of 428 kJ mol^{-1} , while the energy released following reaction R1 is only $\sim 123 \text{ kJ mol}^{-1}$.²⁸ If the acetyl radicals produced through photolysis are more vibrationally excited at the point of association with O_2 than the acetyl formed chemically, then this may enhance the reactive flux which bypasses the reactive intermediate, termed 'well-skipping' reactions, and favour direct OH formation (R2b). This could explain the reduced quenching efficiency reported by studies in which acetyl was generated photolytically.

5.6 Photoionisation Mass Spectrometry (PIMS) Measurements

The kinetic study described previously provides indirect evidence of the non-acetyl yield associated with the OH + CH_3CHO reaction at zero pressure, but does not formally identify the reaction products. Direct evidence of the products of the OH + CH_3CHO reaction has been provided by photoionisation mass spectrometry (PIMS) measurements carried out by Dr Mark Blitz and Neil Howes. The PIMS instrument allows the time-resolved products of the title reaction to be monitored, with methyl and acetyl radicals assigned by the m/z 15 and 43 ion signals, respectively. Differences in the ionisation potentials of acetyl and vinoxy radicals allowed Blitz and Howes to definitively assign acetyl with the m/z 43 signal. Figure 5 shows an example of the acetyl and methyl signals recorded during the same experiment, the time signatures confirm both species originate from the same source.

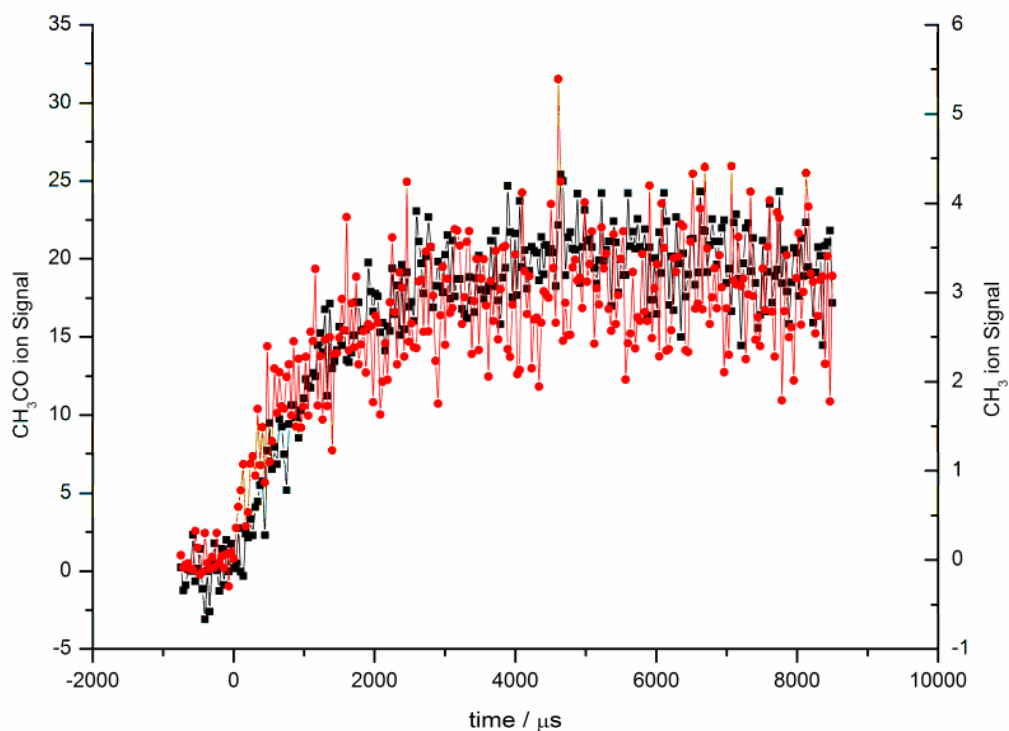


Figure 5: Overlaid plots of acetyl (-■-) and methyl radical (-●-) signals from the same experiments demonstrating they are produced on identical timescales.

Figure 5 in itself does not confirm methyl radicals are primary products of reaction R1, as methyl radicals are also produced during the acetyl photoionization process. In order to distinguish the sources of methyl radicals during the PIMS study, the ratio of signal at m/z 15 (methyl): m/z 43 (acetyl) were quantified by generating acetyl both through reaction of OH (R1) and Cl-atoms (R13) with acetaldehyde. Reaction 12 is insufficiently exothermic to cause subsequent acetyl fragmentation, therefore the 15: 43 ratio observed following this reaction is solely due to acetyl fragmentation during the photoionization process. However, the 15: 43 ratio observed following reaction R1 is higher than that following reaction R12, as the methyl signal (m/z 15) is produced both by fragmentation and direct methyl production through reaction R1e (Figure 6).

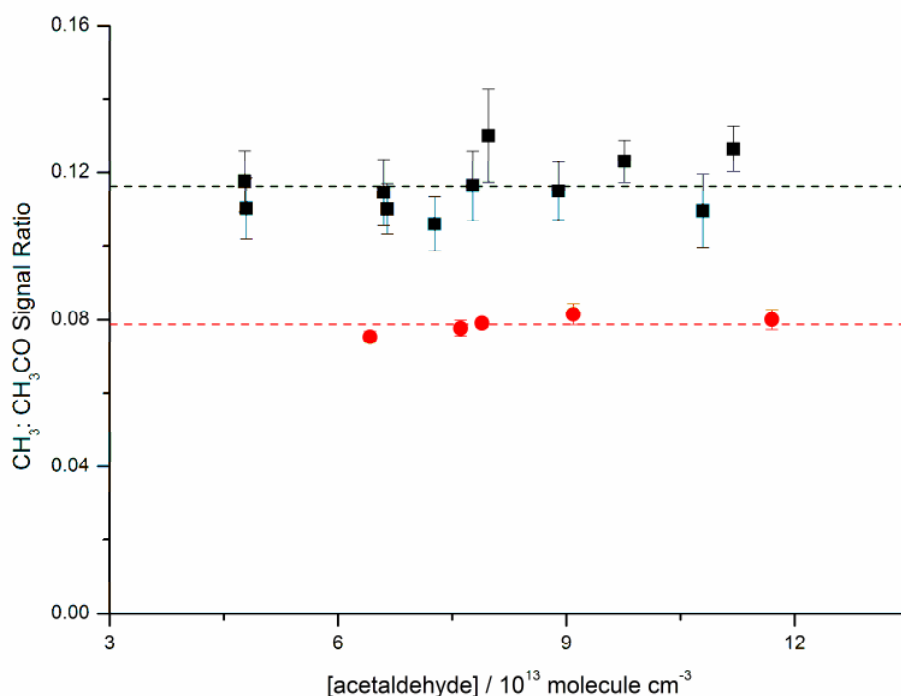


Figure 6: Methyl-to-acetyl signal ratios observed following reaction of OH (■) and Cl-atoms (●) with acetaldehyde at 295 K.

In a final set of experiments, a small amount of oxygen (~10 mTorr) was added to the system. The fraction of acetyl that survive reaction 1 (R1a) react with oxygen to form energised acetylperoxy radicals, which, under the low pressure (~ 4 Torr) conditions of the PIMS flow tube, subsequently dissociate to give OH and a lactone in near 100% yield (R2b); the lactone is identified using the PIMS instrument by the m/z 42 signal. The OH produced through reaction R2b then reacts with acetaldehyde, resulting in a chain reaction sequence which maintains radicals in the system for several milliseconds. Each time the chain is propagated both acetyl (R1a) and methyl radicals are generated (R1e). Both radical species are removed through reaction with oxygen, but under the low experimental pressures the acetyl radicals are lost much faster than methyl radicals, which consequently accumulate in the system. Figure 7 shows the methyl and acetyl radical concentrations which clearly behave very differently as a function of time. The solid lines in Figure 7 are fits to these data using the numerical programme Kintecus.⁵⁵

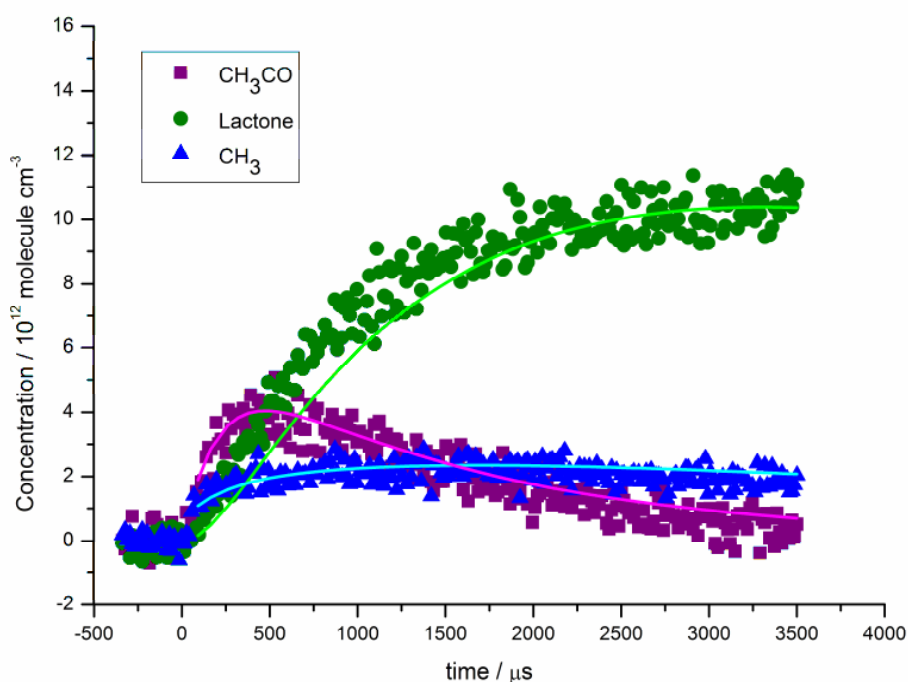


Figure 7: Behaviour of acetyl, methyl and lactone signals in an OH/CH₃CHO/O₂ system. The solid points are the experimental data and the lines are a numerical simulation using Kintecus.⁵⁵

The 15: 43 m/z ratios observed following the reaction of Cl-atoms with acetaldehyde clearly shows that a fraction of the acetyl ion formed following reaction R12 fragments to 15 (Figure 6). The 15 ion signal is solely from acetyl fragmentation as thermodynamically there is not sufficient energy to form CH₃. If the 15: 43 m/z ratios observed following the reaction of OH (R1) and Cl-atoms with acetaldehyde (R12) were the same, then there is no acetyl fragmentation associated with the title reaction (R1e). However, from Figure 6 it can be clearly seen that the 15: 43 m/z ratio is enhanced in reaction R1 which implies that CH₃ is being formed. To assign the CH₃ yield from reaction R1 we need to calibrate the ion signals from CH₃CO and CH₃, where we need to assign the relative ionisation cross-sections and the amount of fragmentation of CH₃CO to 15 ion. The latter is simply the observed ratio from reaction R12. The relative ionisation cross-sections are determined in the following procedure.

Acetylchloride photolyses to give either acetyl (P8a) or methyl radicals (P8b) or a closed-shell stable ketene (P8c) at 248 nm:



In the presence of enough acetaldehyde, the Cl-atoms produced following acetylchloride photolysis (P8a, P8b) titrate completely to $\text{CH}_3\text{CO} + \text{HCl}$ (R12). Under these conditions the 43 m/z signal profile consists of an instant signal due to acetylchloride photolysis (P8a), and a growth on top due to reaction R12. The ratio of instant-to-growth signal heights provide the relative quantum yields of photolysis to channel P8a with respect to P8b. Using this approach Blitz and Howes were able to determine that acetylchloride photolyses to give acetyl and methyl in approximately a 5: 4 ratio at 248 nm. In the absence of acetaldehyde, the prompt 15 m/z signal is attributed to the methyl radicals produced through photolysis (P8b) and a small contribution from acetyl fragmentation (P8a). By observing the 15 and 43 m/z signals from reaction R12, Blitz and Howes concluded that ~5% of the 43 m/z acetyl signal fragments to 15 m/z. The absolute CH_3 yield from acetylchloride photolysis (P8b) was determined by comparison to the 15 m/z signal observed using the PIMS instrument via the photolysis of methyl iodide (P9), known to have a methyl quantum yield of unity.^{14, 56}



By knowing the relative concentrations of CH_3 and CH_3CO from P8, the amount of CH_3CO fragmentation to m/z 15 and the absolute CH_3 by comparison to CH_3I , the observed ion signals from 43 and 15 could be used to determine the relative CH_3CO and CH_3 ionisation cross-sections. In reaction R1, if the ratio of the 15: 43 m/z signals were equal to 0.05 the CH_3 yield (R1e) is zero and if this ratio is equal to ~0.27 the CH_3 yield is 1. In reaction R1 the observed 15: 43 m/z ratio is ~0.12 (Figure 6) and implies the CH_3 yield is 0.15 – 0.20. The PIMS experiments were carried out using a variety of OH precursors, with coated and uncoated flowtube walls, using different detectors and a wide range of acetaldehyde

concentrations to ensure the results were not subject to systematic errors. The PIMS and kinetic experimental results are presented in Table 2.

Experiment	Methyl Yield
248 nm photolysis of O ₃ /H ₂ O as OH source	0.18 ± 0.05
193 nm photolysis of N ₂ O/H ₂ O as OH source	0.18 ± 0.06
193 nm photolysis of N ₂ O/H ₂ O as OH source (Using a different detector)	0.14 ± 0.02
Kinetic experiments based on the zero pressure S-V intercept	0.15 ± 0.04

Table 2: Experimental methyl Yields following reaction of OH with acetaldehyde at room temperature. The kinetic methyl yield assumes that the vinoxyl radical reacts with oxygen to generate OH at zero pressure.

5.7 Discussion

The direct methyl yields measured following the OH + CH₃CHO reaction using the PIMS instrument are consistent with the less direct kinetic study results (Table 2), and with studies that show reaction R1 proceeds exclusively via hydrogen atom abstraction,^{21, 25, 26} but disagree with the methyl yields determined by other groups.^{21, 25, 26} While the OH + CH₃CHO reaction has been investigated extensively by other workers, there are comparatively few studies that focus on methyl production from the title reaction.

Wang et al. used tuneable diode IR absorption to monitor the production of ground state methyl radicals from reaction R1 at 296 K in ~14 Torr of helium.²⁵ OH was generated through reaction of O(¹D) with excess water (R14):



A prompt methyl signal was observed that Wang and co-workers attributed to reaction of O(¹D) with acetaldehyde (R15), with a slower growth on the 100's of μs timescale through reaction R1.



These authors reported a methyl yield of less than 5% by calibrating with the known methyl yield following the reaction of O(¹D) with methane (R16):



However, the methyl profile reported by Wang et al. shows methyl loss occurring on a similar timescale to its formation. It is not clear from their paper how the significant loss of methyl radicals, through radical-radical processes or the production of vibrationally excited methyl radicals, was accounted for and therefore it is possible that Wang and co-workers underestimate the methyl yield in their analysis.

Cameron et al. used UV absorption (200 – 240 nm) to observe acetyl and methyl radicals produced in reaction R1.²¹ The acetyl absorption spectrum is quite broad a featureless in this region, whereas in contrast the ground state methyl absorption peaks sharply at ~216 nm. The high concentrations of acetaldehyde (~10¹⁶ molecule cm⁻³) used by Cameron et al. meant time resolution on the production of acetyl and methyl radicals was lost in their experiments. Methyl radicals were observed, but Cameron and co-workers proposed this was due to acetaldehyde photolysis and the maximum yield of methyl radicals was set at 3% for their 60 Torr experiments using nitrogen bath gas. Uncertainties in the methyl quantum yield or possible contributions from vibrationally excited species may result in a low bias in the methyl yield reported in this study.

D'Anna et al. studied the title reaction in synthetic air at 298 K and 760 Torr using a smog chamber equipped with long path FTIR detection.²⁶ OH radicals were generated by photolysis of various alkylnitrate isotopologues (P2) which in the presence of O₂ generate OH and NO₂ (R5, R6). These authors observed HCHO and CO in 10% yield. At atmospheric pressure the vinoxy radical produced through reaction R1b reacts with oxygen to form a stable peroxy radical (R11c) rather than dissociating to radical fragments (R11a, R11b):⁴⁵⁻⁴⁸



In the presence of NO and O₂ the following reaction sequence might explain formation of formaldehyde and CO reported by D'Anna and co-workers:



However, the vinoxy radical yield (R1b) of $(5.1_{1.7}^{+2.4})\%$ reported by Butkovskaya et al.²⁴ is inconsistent with the 10% yield of HCHO and CO observed in the chamber by study D'Anna et al.²⁶ Consequently, D'Anna and colleagues proposed that CH₃ and CO form directly from the reaction of OH with acetaldehyde (R1e),²⁶ with HCHO produced following oxidation of the primary methyl radical; consistent with the radical profiles of Blitz and Howes which show methyl and acetyl are produced following reaction R1 on identical timescales (Figure 5). The work presented in this chapter, and the results of D'Anna et al., provides compelling evidence that methyl radical production is a minor channel in reaction R1.

Conventional understanding states the exothermicity of an abstraction reaction is preferentially partitioned into the newly formed bond.³⁰ Acetyl fragmentation requires more than 50% of the total exothermicity of the OH + acetaldehyde reaction to be channelled into the acetyl. The observation of more than 15% fragmentation of the acetyl radical formed from reaction R1 suggests that the energy is partitioned more statistically between the CH₃CO and H₂O products. A completely statistical distribution of energy would preferentially excite the acetyl fragment (12 modes vs 3 modes) and result in near complete acetyl fragmentation. The experimental observations presented here suggest that neither the classical 'dynamic' or 'statistical' models adequately describe the partitioning of energy following the OH + acetaldehyde reaction. Butkovskaya and Setser determined the nascent vibrational distribution in the H₂O produced following the title reaction by observing the IR chemiluminescent spectra.⁵⁷ Based on their observations they calculate that 52% of the reaction exothermicity is partitioned into vibrational excitation of the water. These authors also highlighted a significant difference in the disposal of energy following the reactions of OH with carbonyls and hydrocarbons; in the latter a greater fraction of the reaction exothermicity is distributed in the vibrational modes of the water molecule. The reactions of

OH with glyoxal and methylglyoxal have also recently been shown to contest the classical 'dynamic' model with a significant fraction of the reaction exothermicity deposited in the HC(O)CO and CH₃C(O)CO fragments, respectively.^{29, 31}

The methyl radicals formed from the OH + acetaldehyde reaction are only a minor product channel and therefore unlikely to have significant atmospheric implications, although a yield of more than 15% could potentially influence PAN and HCHO budgets in polluted regions. Conversely, the implications of this study for low temperature combustion could be significant, particularly under the pure oxygen conditions used during oxyfuel combustion. Aldehydes are known to be important intermediates in the combustion of alcohols and Kaiser et al. have modelled the chemistry of acetaldehyde oxidation under low temperature combustion conditions.⁵⁸ At temperatures below 750 K chain branching can occur via reactions R2a, R17 and R18.



Reaction R2a will be in competition with the chain propagation reaction R2b:



with the likely decomposition products of the lactone being HCHO and CO. MESMER calculations emphasize the importance of 'well-skipping' reactions in such R + O₂ systems and well-skipping will be enhanced with vibrational excitation of the R radical. The results presented in this chapter indicate significant vibrational excitation of the acetyl fragment following reaction R1 and, particularly under oxyfuel combustion where there will be less vibrational relaxation, the fraction of chain branching (R2a, R17-18) versus chain propagation (R2b) will change, and could potentially influence modelled ignition delays for ethanol combustion.

5.8 References

1. Ris, C., US EPA health assessment for diesel engine exhaust: a review. *Inhalation toxicology* 2007, 19, 229-239.
2. Luecken, D. J.; Hutzell, W. T.; Strum, M. L.; Pouliot, G. A., Regional sources of atmospheric formaldehyde and acetaldehyde, and implications for atmospheric modeling. *Atmospheric Environment* 2012, 47, 477-490.
3. Karavalakis, G.; Durbin, T. D.; Shrivastava, M.; Zheng, Z.; Villela, M.; Jung, H., Impacts of ethanol fuel level on emissions of regulated and unregulated pollutants from a fleet of gasoline light-duty vehicles. *Fuel* 2012, 93, 549-558.
4. Millet, D. B.; Apel, E.; Henze, D. K.; Hill, J.; Marshall, J. D.; Singh, H. B.; Tessum, C. W., Natural and Anthropogenic Ethanol Sources in North America and Potential Atmospheric Impacts of Ethanol Fuel Use. *Environmental Science & Technology* 2012, 46, 8484-8492.
5. Carr, S. A.; Blitz, M. A.; Seakins, P. W., Site-Specific Rate Coefficients for Reaction of OH with Ethanol from 298 to 900 K. *Journal of Physical Chemistry A* 2011, 115, 3335-3345.
6. Dagaut, P.; Togbe, C., Oxidation kinetics of butanol-gasoline surrogate mixtures in a jet-stirred reactor: Experimental and modeling study. *Fuel* 2008, 87, 3313-3321.
7. He, B.-Q.; Liu, M.-B.; Yuan, J.; Zhao, H., Combustion and emission characteristics of a HCCI engine fuelled with n-butanol-gasoline blends. *Fuel* 2013, 108, 668-674.
8. Millet, D. B.; Guenther, A.; Siegel, D. A.; Nelson, N. B.; Singh, H. B.; de Gouw, J. A.; Warneke, C.; Williams, J.; Eerdekens, G.; Sinha, V.; Karl, T.; Flocke, F.; Apel, E.; Riemer, D. D.; Palmer, P. I.; Barkley, M., Global atmospheric budget of acetaldehyde: 3-D model analysis and constraints from in-situ and satellite observations. *Atmospheric Chemistry and Physics* 2010, 10, 3405-3425.
9. Read, K. A.; Carpenter, L. J.; Arnold, S. R.; Beale, R.; Nightingale, P. D.; Hopkins, J. R.; Lewis, A. C.; Lee, J. D.; Mendes, L.; Pickering, S. J., Multiannual Observations of Acetone, Methanol, and Acetaldehyde in Remote Tropical Atlantic Air: Implications for Atmospheric OVOC Budgets and Oxidative Capacity. *Environmental Science & Technology* 2012, 46, 11028-11039.
10. Zhang, Y.; Mu, Y.; Liang, P.; Xu, Z.; Liu, J.; Zhang, H.; Wang, X.; Gao, J.; Wang, S.; Chai, F.; Mellouki, A., Atmospheric BTEX and carbonyls during summer seasons of 2008-2010 in Beijing. *Atmospheric Environment* 2012, 59, 186-191.
11. Wang, H.-K.; Huang, C.-H.; Chen, K.-S.; Peng, Y.-P., Seasonal Variation and Source Apportionment of Atmospheric Carbonyl Compounds in Urban Kaohsiung, Taiwan. *Aerosol and Air Quality Research* 2010, 10, 559-570.
12. Correa, S. M.; Arbilla, G.; Martins, E. M.; Quiterio, S. L.; Guimaraes, C. d. S.; Gatti, L. V., Five years of formaldehyde and acetaldehyde monitoring in the Rio de Janeiro downtown area - Brazil. *Atmospheric Environment* 2010, 44, 2302-2308.
13. Fortner, E. C.; Zheng, J.; Zhang, R.; Knighton, W. B.; Volkamer, R. M.; Sheehy, P.; Molina, L.; Andre, M., Measurements of Volatile Organic Compounds Using Proton Transfer Reaction - Mass Spectrometry during the MILAGRO 2006 Campaign. *Atmospheric Chemistry and Physics* 2009, 9, 467-481.
14. Atkinson, R.; Baulch, D.; Cox, R.; Crowley, J.; Hampson, R.; Hynes, R.; Jenkin, M.; Rossi, M.; Troe, J.; Subcommittee, I., Evaluated kinetic and photochemical data for atmospheric chemistry: Volume II—gas phase reactions of organic species. *Atmospheric Chemistry and Physics* 2006, 6, 3625-4055.
15. Moortgat, G. K.; Meyrahn, H.; Warneck, P., Photolysis of Acetaldehyde in Air: CH₄, CO and CO₂ Quantum Yields. *Chemphyschem* 2010, 11, 3896-3908.
16. Taylor, O., Importance of peroxyacetyl nitrate (PAN) as a phytotoxic air pollutant. *Journal of the Air Pollution Control Association* 1969, 19, 347-351.
17. Vyskocil, A.; Viau, C.; Lamy, S., Peroxyacetyl nitrate: review of toxicity. *Human & Experimental Toxicology* 1998, 17, 212-220.

18. Bridier, I.; Caralp, F.; Loirat, H.; Lesclaux, R.; Veyret, B.; Becker, K.; Reimer, A.; Zabel, F., Kinetic and theoretical studies of the reactions $\text{CH}_3\text{C}(\text{O})\text{O}_2 + \text{NO}_2 + \text{M} \rightarrow \text{CH}_3\text{C}(\text{O})\text{O}_2\text{NO}_2 + \text{M}$ between 248 and 393 K and between 30 and 760 Torr. *Journal of Physical Chemistry* 1991, 95, 3594-3600.
19. Finlayson-Pitts, B. J.; Pitts, J. N. J., *Chemistry of the Upper and Lower Atmosphere. Theory, Experiments and Applications*. Academic Press: San Diego, 2000.
20. Taylor, P. H.; Rahman, M. S.; Arif, M.; Dellinger, B.; Marshall, P. In *Kinetic and mechanistic studies of the reaction of hydroxyl radicals with acetaldehyde over an extended temperature range*, Symposium (international) on Combustion, Elsevier: 1996; pp 497-504.
21. Cameron, M.; Sivakumaran, V.; Dillon, T. J.; Crowley, J. N., Reaction between OH and CH_3CHO Part 1. Primary product yields of CH_3 (296 K), CH_3CO (296 K), and H (237–296 K). *Physical Chemistry Chemical Physics* 2002, 4, 3628-3638.
22. Vandenberg, S.; Peeters, J., The reaction of acetaldehyde and propionaldehyde with hydroxyl radicals: experimental determination of the primary H_2O yield at room temperature. *Journal of Photochemistry and Photobiology A: Chemistry* 2003, 157, 269-274.
23. Tyndall, G. S.; Orlando, J. J.; Wallington, T. J.; Hurley, M. D.; Goto, M.; Kawasaki, M., Mechanism of the reaction of OH radicals with acetone and acetaldehyde at 251 and 296 K. *Phys. Chem. Chem. Phys.* 2002, 4, 2189-2193.
24. Butkovskaya, N. I.; Kukui, A.; Le Bras, G., Branching fractions for H_2O forming channels of the reaction of OH radicals with acetaldehyde. *Journal of Physical Chemistry A* 2004, 108, 1160-1168.
25. Wang, J.; Chen, H.; Glass, G. P.; Curl, R., Kinetic study of the reaction of acetaldehyde with OH. *The Journal of Physical Chemistry A* 2003, 107, 10834-10844.
26. D'Anna, B.; Bakken, V.; Beukes, J. A.; Nielsen, C. J.; Brudnik, K.; Jodkowski, J. T., Experimental and theoretical studies of gas phase NO_3 and OH radical reactions with formaldehyde, acetaldehyde and their isotopomers. *Physical Chemistry Chemical Physics* 2003, 5, 1790-1805.
27. Shannon, R. J.; Taylor, S.; Goddard, A.; Blitz, M. A.; Heard, D. E., Observation of a large negative temperature dependence for rate coefficients of reactions of OH with oxygenated volatile organic compounds studied at 86-112 K. *Physical Chemistry Chemical Physics* 2010, 12, 13511-13514.
28. Sander, S.; Friedl, R.; Barker, J.; Golden, D.; Kurylo, M.; Wine, P.; Abbatt, J.; Burkholder, J.; Kolb, C.; Moortgat, G., Chemical Kinetics and Photochemical Data for use in Atmospheric Studies—Evaluation Number 17, JPL Publication 10–6, June 10, 2011.
29. Baeza-Romero, M. T.; Glowacki, D. R.; Blitz, M. A.; Heard, D. E.; Pilling, M. J.; Rickard, A. R.; Seakins, P. W., A combined experimental and theoretical study of the reaction between methylglyoxal and OH/OD radical: OH regeneration. *Physical Chemistry Chemical Physics* 2007, 9, 4114-4128.
30. Polanyi, J. C., Some concepts in reaction dynamics *Science* 1987, 236, 680-690.
31. Lockhart, J.; Blitz, M.; Heard, D.; Seakins, P.; Shannon, R., Kinetic Study of the OH + Glyoxal Reaction: Experimental Evidence and Quantification of Direct OH Recycling. *Journal of Physical Chemistry A* 2013, 117, 11027-11037.
32. Michael, J. V.; Keil, D. G.; Klemm, R. B., Rate Constants for the Reaction of Hydroxyl Radicals with Acetaldehyde from 244-528 K. *Journal of Chemical Physics* 1985, 83, 1630-1636.
33. Onel, L.; Blitz, M. A.; Seakins, P. W., Direct Determination of the Rate Coefficient for the Reaction of OH Radicals with Monoethanol Amine (MEA) from 296 to 510 K. *Journal of Physical Chemistry Letters* 2012, 3, 853-856.
34. Onel, L.; Thonger, L.; Blitz, M. A.; Seakins, P. W.; Bunkan, A. J. C.; Solimannejad, M.; Nielsen, C. J., Gas-Phase Reactions of OH with Methyl Amines in the Presence or Absence of Molecular Oxygen. An Experimental and Theoretical Study. *Journal of Physical Chemistry A* 2013, 117, 10736-10745.
35. Sivakumaran, V.; Crowley, J. N., Reaction between OH and CH_3CHO Part 2. Temperature dependent rate coefficients (201–348 K). *Physical Chemistry Chemical Physics* 2003, 5, 106-111.

36. Zhu, L.; Talukdar, R. K.; Burkholder, J. B.; Ravishankara, A. R., Rate coefficients for the OH plus acetaldehyde (CH₃CHO) reaction between 204 and 373 K. *International Journal of Chemical Kinetics* 2008, 40, 635-646.
37. Taylor, P. H.; Yamada, T.; Marshall, P., The reaction of OH with acetaldehyde and deuterated acetaldehyde: Further insight into the reaction mechanism at both low and elevated temperatures. *International journal of chemical kinetics* 2006, 38, 489-495.
38. Atkinson, R.; Pitts, J. N., Kinetics of reactions of OH radical with HCHO and CH₃CHO over temperature range 299 degrees K 426 degrees K. *Journal of Chemical Physics* 1978, 68, 3581-3584.
39. Semmes, D.; Ravishankara, A.; Gump-Perkins, C.; Wine, P., Kinetics of the reactions of hydroxyl radical with aliphatic aldehydes. *International journal of chemical kinetics* 1985, 17, 303-313.
40. Carr, S. A.; Baeza-Romero, M. T.; Blitz, M. A.; Pilling, M. J.; Heard, D. E.; Seakins, P. W., OH yields from the CH₃CO+O₂ reaction using an internal standard. *Chemical Physics Letters* 2007, 445, 108-112.
41. Carr, S. A.; Glowacki, D. R.; Liang, C. H.; Baeza-Romero, M. T.; Blitz, M. A.; Pilling, M. J.; Seakins, P. W., Experimental and Modeling Studies of the Pressure and Temperature Dependences of the Kinetics and the OH Yields in the Acetyl + O₂ Reaction. *Journal of Physical Chemistry A* 2011, 115, 1069-1085.
42. Chen, S.-Y.; Lee, Y.-P., Transient infrared absorption of t-CH₃C(O)OO, c-CH₃C(O)OO, and alpha-lactone recorded in gaseous reactions of CH₃CO and O₂. *Journal of Chemical Physics* 2010, 132.
43. Hou, H.; Li, A.; Hu, H. Y.; Li, Y.; Li, H.; Wang, B. S., Mechanistic and kinetic study of the CH₃CO+O₂ reaction. *Journal of Chemical Physics* 2005, 122.
44. Blitz, M. A.; Heard, D. E.; Pilling, M. J., OH formation from CH₃CO+O₂: a convenient experimental marker for the acetyl radical. *Chemical Physics Letters* 2002, 365, 374-379.
45. Gutman, D.; Nelson, H. H., Gas-phase reactions of the vinoxy radical with O₂ and NO. *Journal of Physical Chemistry* 1983, 87, 3902-3905.
46. Lorenz, K.; Rhasa, D.; Zellner, R.; Fritz, B., Laser photolysis-LIF kinetic-studies of the reactions of CH₃O and CH₂CHO with O₂ between 300 K and 500 K. *Berichte Der Bunsen-Gesellschaft-Physical Chemistry Chemical Physics* 1985, 89, 341-342.
47. Zhu, L.; Johnston, G., Kinetics and products of the reaction of the vinoxy radical with O₂. *Journal of Physical Chemistry* 1995, 99, 15114-15119.
48. Delbos, E.; Fittschen, C.; Hippler, H.; Krasteva, N.; Olzmann, M.; Viskolcz, B., Rate coefficients and equilibrium constant for the CH₂CHO+O₂ reaction system. *Journal of Physical Chemistry A* 2006, 110, 3238-3245.
49. GroSs, C. B. M.; Dillon, T. J.; Crowley, J. N., Pressure dependent OH yields in the reactions of CH₃CO and HOCH₂CO with O₂. *Physical chemistry chemical physics : PCCP* 2014, 16, 10990-8.
50. Ammann, M.; Cox, R.; Crowley, J.; Jenkin, M.; Mellouki, A.; Rossi, M.; Troe, J.; Wallington, T., IUPAC Task Group on Atmospheric Chemical Kinetic Data Evaluation. *Report on the 34th Session of the Joint Scientific Committee of the World Climate Research Programme 2* 2014, 20.
51. Tyndall, G. S.; Orlando, J. J.; Wallington, T. J.; Hurley, M. D., Pressure dependence of the rate coefficients and product yields for the reaction of CH₃CO radicals with O₂. *International Journal of Chemical Kinetics* 1997, 29, 655-663.
52. Talukdar, R. K. D., M. E.; Zhu, L.; Ravishankara, A. R.; Burkholder, J. B. , 19th International Symposium on Gas Kinetics. *Orleans* 2006, France.
53. Carr, S. A. Mechanisms and kinetics of some reactions relevant to biofuel combustion and atmospheric oxidation. University of Leeds, 2009.
54. Kovacs, G.; Zador, J.; Farkas, E.; Nadasdi, R.; Szilagyi, I.; Dobe, S.; Berces, T.; Marta, F.; Lendvay, G., Kinetics and mechanism of the reactions of CH₃CO and CH₃C(O)CH₂ radicals with O₂. Low-pressure discharge flow experiments and quantum chemical computations. *Physical Chemistry Chemical Physics* 2007, 9, 4142-4154.

55. Ianni, J. C., Kintecus, Windows Version 2.80, 2002, www.kintecus.com.
56. Xing, J. H.; Nagai, Y.; Kusuha, M.; Miyoshi, A., Reactions of methyl- and ethylperoxy radicals with NO studied by time-resolved negative ionization mass spectrometry. *Journal of Physical Chemistry A* 2004, 108, 10458-10463.
57. Butkovskaya, N. I.; Setser, D. W., Infrared chemiluminescence study of the reaction of hydroxyl radical with acetaldehyde and the secondary reactions of acetyl radical with NO₂, OH, and H. *Journal of Physical Chemistry A* 2000, 104, 9428-9435.
58. Kaiser, E. W.; Westbrook, C. K.; Pitz, W. J., Acetaldehyde oxidation in the negative temperature-coefficient regime-Experimental and modeling results. *International Journal of Chemical Kinetics* 1986, 18, 655-688.

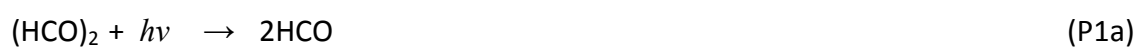
Chapter 6 Kinetic Study of the OH + Glyoxal Reaction

6.1 Abstract

This chapter centres on a detailed experimental kinetic study of the OH + glyoxal, (HCO)₂, reaction using N₂, and various O₂/N₂ bath gas mixtures over a range of total pressures (5 – 80 Torr) and temperatures (212 – 295 K), by monitoring OH decay via laser induced fluorescence (LIF) in excess (HCO)₂. The following rate coefficients, $k_{\text{OH} + (\text{HCO})_2} = (9.7 \pm 1.2)$, (12.2 ± 1.6) and $(15.4 \pm 2.0) \times 10^{-12} \text{ cm}^3 \text{ molecule}^{-1} \text{ s}^{-1}$ (where errors represent a combination of both the statistical error at the 2 σ level and estimates of systematic errors) were measured in pure N₂ at temperatures of 295, 250 and 212 K, respectively. Rate coefficients were observed to be independent of total pressure but decreased following the addition of O₂ to the reaction cell, consistent with direct regeneration of OH. OH yields, Φ_{OH} , were quantified experimentally for the first time as a function of total pressure, temperature, and O₂ concentration. The experimental results have been parameterized using a chemical scheme where a fraction of the nascent HC(O)CO population promptly dissociates to HCO + CO, the remaining HC(O)CO either dissociates thermally or reacts with O₂ to give CO₂, CO, and regenerate OH. A maximum Φ_{OH} of (0.38 ± 0.03) was observed at 212 K, independent of total pressure, suggesting that ~60% of the HC(O)CO population promptly dissociates upon formation. Qualitatively similar behaviour is observed at 250 K, with a maximum Φ_{OH} of (0.31 ± 0.04) ; at 295 K, the maximum Φ_{OH} decreases further to (0.29 ± 0.03) . From the parameterization, an Φ_{OH} of 0.19 is calculated at 295 K and 1 atmosphere of air. It is shown that the proposed mechanism is consistent with previous chamber studies. While the fits are robust, experimental evidence suggests that the system is influenced by chemical activation and cannot be fully described by thermal rate coefficients. The atmospheric implications of the measurements are briefly discussed.

6.2 Background and Previous work

Glyoxal, (HCO)₂, is an important atmospheric trace gas, and produced in high yields following the oxidation of both biogenic VOCs, such as isoprene,¹ and anthropogenic hydrocarbons, such as benzene²⁻⁴ and acetylene.⁵⁻⁷ (HCO)₂ is the simplest and most abundant α -dicarbonyl in the troposphere and its atmospheric significance stems from its roles in the formation of secondary organic aerosol (SOA)⁸⁻¹⁰, as a source of HOx (OH + HO₂) radicals in the troposphere,¹¹⁻¹³ and its use as a marker for biogenic emissions.^{14, 15} (HCO)₂ is removed from the atmosphere within a few hours; during daylight its atmospheric lifetime is largely determined by the rates of photolysis and reaction with OH:^{11, 16-18}



Several experimental and theoretical studies have been conducted that focus on (HCO)₂ oxidation. Niki et al.¹⁹ studied the Cl initiated oxidation of (HCO)₂ in chamber experiments using various N₂/O₂ bath gas mixtures at 700 Torr and 298 K, with FTIR product detection. These authors were the first to consider the subsequent fate of the HC(O)CO radical and concluded that under atmospheric conditions HC(O)CO chemistry is governed by a competition between unimolecular decomposition (R2) and bimolecular reaction with O₂, the latter including both a direct abstraction pathway (R3a) and an association channel (R3b):



Stable product analysis confirmed formation of both CO and CO₂ in the presence of O₂. While CO formation is consistent with reactions 2 and 3, CO₂ formation is not; Niki et al. suggested reaction between the HC(O)C(O)O₂ radical and HO₂ was potentially responsible (R4), with co-production of radical species HCO and OH:



Orlando and Tyndall²⁰ generated the HC(O)CO radical via both Cl and OH initiated oxidation of (HCO)₂ in an environmental chamber/FTIR system at 700 Torr between 224 and 314 K. Their study reported CO and CO₂ production associated with HC(O)CO chemistry in the presence of O₂, in agreement with Niki et al., and adopting the same mechanism showed the [CO]/[CO₂] product ratio scales linearly with the inverse O₂ partial pressure, with a gradient equal to k_2/k_{3b} . The analysis by Orlando and Tyndall provides evidence of a significant barrier to unimolecular decomposition of the HC(O)CO radical (~32 kJ mol⁻¹); consequently, k_3 exhibits a significant temperature dependence. Conversely, k_{3b} is relatively insensitive to temperature, such that unimolecular decomposition fails to compete with bimolecular reaction with O₂ at 224 K.

More recently, Feierabend et al.¹⁷ studied the kinetics of the OH + (HCO)₂ reaction, monitoring OH directly via LIF, and reported the rate of OH decay to slow following addition of O₂ to the reaction cell, but did not quantify the effect. The Feierabend et al. study confirms that OH production occurs via a primary reaction and not through secondary chemistry as proposed by chamber studies and is consistent with recent calculations by da Silva,²¹ which identified a chemically activated HC(O)CO + O₂ channel that proceeds directly to CO₂, CO and OH (reaction R5, Figure 1), and suggested this channel is competitive with unimolecular dissociation.



Setokuchi²² extended the analysis in a theoretical study that considered the energy partitioned in the nascent HC(O)CO radical and concluded that under atmospheric conditions 91% of the HC(O)CO promptly decomposes on formation.

Both proposed mechanisms for the fate of HC(O)CO following reaction with O₂ are effectively HO_x neutral, although the Niki et al. mechanism requires a radical-radical reaction to regenerate OH, whereas the mechanism proposed by da Silva directly regenerates OH and therefore occurs on a faster timescale, which is independent of the initial radical (Cl/OH) concentration.

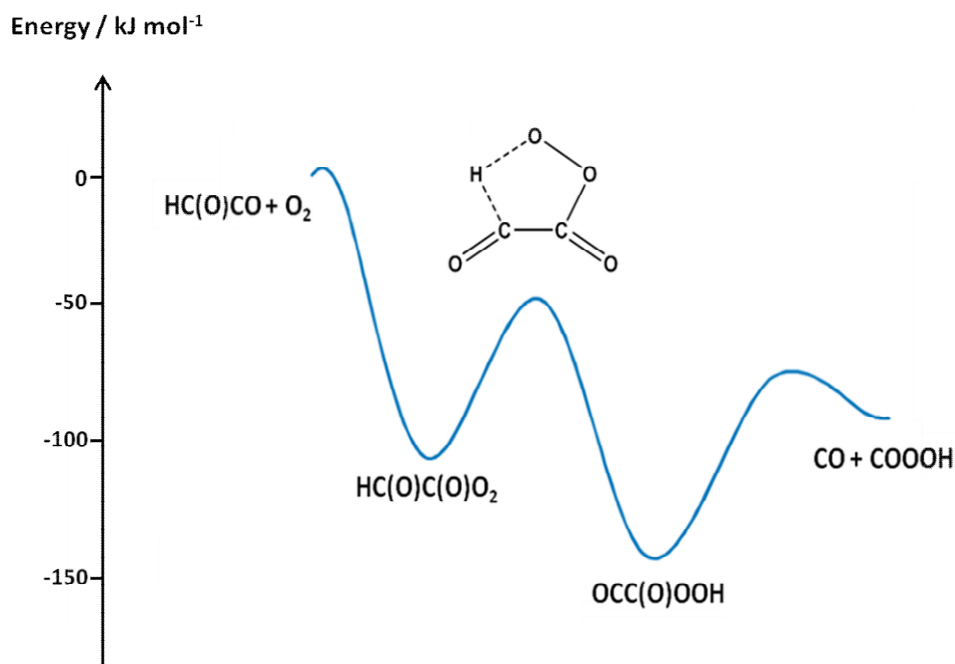


Figure 1: Schematic of the potential energy surface showing the initial addition of O_2 followed by an internal H transfer and then elimination of CO. The COOH rapidly dissociates to OH and CO_2 . Adapted with permission from da Silva.²¹

In recent decades, field measurements of OH and HO_2 radicals in unpolluted atmospheres have highlighted a major failure of the current scientific understanding of HOx chemistry in regions characterized by both low concentrations of nitrogen oxides and high concentrations of isoprene and other biogenic volatile organics.²³⁻²⁶ Measured OH concentrations in pristine environments are consistently higher than those predicted by atmospheric chemical models, and the discrepancy between the observed and modeled OH concentration correlates with the presence of isoprene. Recent field measurements of $(HCO)_2$ made over the rainforest canopy in Borneo have reported peak concentrations of ~ 1.6 ppb, significantly higher than measurements made during other field campaigns in remote forested regions.²⁷ Furthermore, model analysis has shown that $(HCO)_2$ concentrations ($(HCO)_2$ is a known isoprene oxidation product) of this magnitude are consistent with the higher than expected OH concentrations reported in the same regions.²⁷ Given the current uncertainty in isoprene oxidation mechanisms²⁸⁻³⁰ and HOx

measurements^{31, 32} and the link between glyoxal and biogenic emissions, there is a clear need to fully understand OH + (HCO)₂/O₂ chemistry.

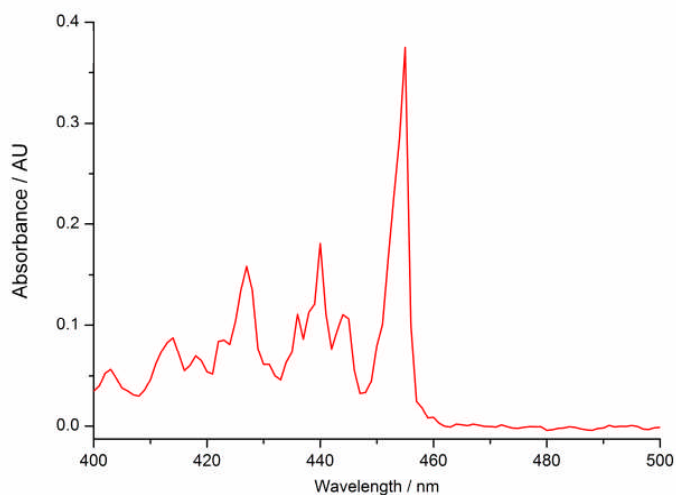
The aims of this work are to conduct a detailed kinetic study of the OH + (HCO)₂/O₂ system and to confirm OH is produced directly following the HC(O)CO + O₂ association reaction and not through secondary radical-radical chemistry; experimental Φ_{OH} can then be quantified for the first time as a function of temperature, pressure and O₂ concentration.

6.3 Experimental

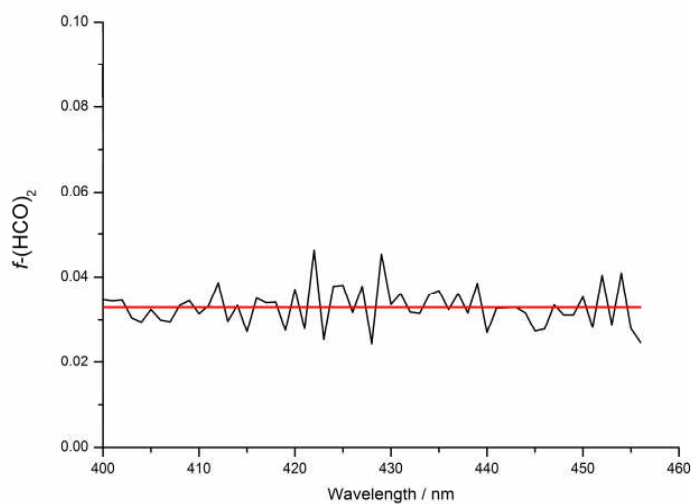
The apparatus used to study the OH kinetics of the OH + (HCO)₂/O₂ system are identical to the setup described previously to investigate the OH yields associated with OH + alkyne/O₂ and OH + CH₃CHO/O₂ chemistry at subambient temperatures; therefore only a brief description is provided here. The flows of radical precursor, (HCO)₂, and bath gas (N₂ and/or O₂) were regulated via calibrated mass flow controllers, allowed to mix, and flowed into a stainless steel 6-way cross reactor. The total pressure inside the (5 – 80 Torr) was controlled by adjusting a needle valve on the exhaust line to the pump and measured using a capacitance manometer. The bath of the low temperature cell was filled with acetone/dry ice, chloroform/ dry ice or *ortho*-xylene/dry ice to achieve subambient temperatures of 195, 212 and 250 K, respectively. Temperatures close to the reaction region were measured using K-type thermocouples.

Glyoxal was prepared by heating approximately equal masses (~15 g) of glyoxal trimer dihydrate crystals and P₂O₅ to 423 K. A small flow of N₂ was passed over the heated sample and through a collection trap submerged in liquid N₂. The glyoxal was trapped as yellow crystals, distilled into a blackened glass sample bulb, and diluted in N₂. The concentration of (HCO)₂ in each sample bulb was determined via UV-vis spectroscopy (Perkin Elmer Lambda 900). Absorption by (HCO)₂ was measured between 400 and 500 nm for each sample prepared using a homemade 10 cm glass cell with 1 nm spectral resolution; a typical absorption spectra is shown in Figure 2a. The measured absorbance were converted to base e, then combined with recently recommended absorption cross sections³³ to give the (HCO)₂ number density in accordance with the Beer-Lambert law. The

total gas number density was determined by measuring the total pressure inside the absorption cell using capacitance manometers. A typical plot of $(\text{HCO})_2$ fraction, $f\text{-}(\text{HCO})_2$, against wavelength is shown in Figure 2b.



(a)



(b)

Figure 2: Typical UV-vis absorption spectra for an $(\text{HCO})_2$ sample (a) and corresponding glyoxal fraction, $f\text{-}(\text{HCO})_2$, as a function of wavelength (b); analysis of this spectra results in an $f\text{-}(\text{HCO})_2$ of 0.033 ± 0.005 , the error is statistical at the 1σ level.

Materials used: nitrogen (BOC oxygen free), oxygen (Air Products, high purity, 99.999%), *t*-butyl hydroperoxide (Sigma Aldrich, 70% v/v aqueous), oxalyl chloride (Sigma Aldrich, $\geq 99\%$), chloroform (Sigma Aldrich, $\geq 99.8\%$), *o*-xylene (Sigma Aldrich, $\geq 98\%$), acetone (Sigma Aldrich, $> 99.9\%$), glyoxal trimer dehydrate (Sigma Aldrich, $\geq 95\%$) and phosphorus pentoxide (Sigma Aldrich, $\geq 98.5\%$).

OH radicals and Cl atoms were generated by pulsed excimer photolysis (Lambda Physik Compex, at 248 nm) of *t*-butyl hydroperoxide and oxalyl chloride, respectively:



The laser beam was introduced through one of the arms of the reactor. The laser was typically operated at 10 Hz, although tests were performed to ensure fresh gas samples were present in the reactor for each photolysis pulse. OH radicals were detected by off-resonance LIF.

The reactions were carried out under *pseudo-first-order* conditions with glyoxal concentrations ($> 9 \times 10^{13}$ molecule cm^{-3}) in great excess over OH ($\sim 1 \times 10^{11}$ molecule cm^{-3}). In N_2 bath gas the OH decay is governed by reactions R1 and R6:



where reaction R6 accounts for reaction with *t*-butyl hydroperoxide and diffusion from the probed region of the reactor. Under these conditions the OH decay, an example of which is shown in the inset of Figure 3, is defined using the following expression:

$$I_f(t) = I_f(0) \exp^{-k't} \quad (\text{E1})$$

where $I_f(0)$ and $I_f(t)$ are OH signal intensities at time 0 and time t , respectively; and k' is the observed pseudo-first-order rate coefficient ($k' = k_1[(\text{HCO})_2] + k_6$). Accordingly, the gradient of a linear plot of k' against $[(\text{HCO})_2]$ provides the bimolecular rate coefficient k_1 ; an example of which can be seen in Figure 3.

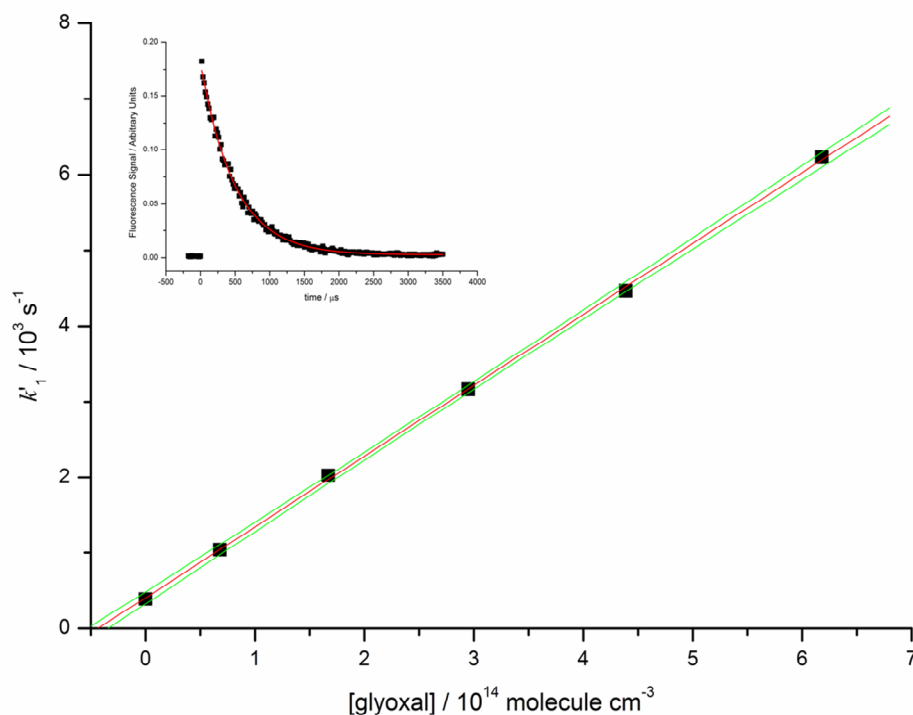


Figure 3: Typical bimolecular plot for the $\text{OH} + (\text{HCO})_2 \rightarrow \text{HC(O)CO} + \text{H}_2\text{O}$ reaction measured at 295 K under 20 Torr total pressure of pure N_2 ; corresponding to an experimental k_1 value of $(9.37 \pm 0.08) \times 10^{-12} \text{ molecule cm}^{-3} \text{ s}^{-1}$. The outer lines show the confidence intervals at the 2σ level. A typical experimental OH decay trace measured in the presence of $1.67 \times 10^{14} \text{ molecule cm}^{-3}$ of glyoxal is included in the inset, the fit to equation E1 corresponds to a *pseudo-first-order* rate coefficient of $(2030 \pm 20) \text{ s}^{-1}$.

6.4 $\text{OH} + (\text{HCO})_2$ Temperature Dependence in Nitrogen Bath Gas

Rate coefficients, $k_1(T)$, were determined under pseudo-first-order conditions in OH over the temperature range 212 – 295 K at total pressures ranging from 5 to 80 Torr in N_2 bath gas. $k_1(T)$ was found to be independent of total pressure, consistent with a reaction proceeding via H-atom abstraction at either aldehydic group. The experimental $k_1(T)$ measurements are highly reproducible, with values of (9.7 ± 1.2) , (12.2 ± 1.6) and $(15.4 \pm 2.0) \times 10^{-12} \text{ molecule cm}^{-3} \text{ s}^{-1}$ at temperatures of 295, 250 and 212 K, respectively, obtained by averaging all independent measurements (> 11) at each temperature. The errors represent the statistical error at the 2σ level combined in quadrature with an estimated 10%

systematic error. The only previous experimental investigation of the temperature dependence of k_1 reported in the literature is that by Feierabend et al.¹⁷ These authors measured $k_1(T)$ over a range of total pressures (45 – 300 Torr) and temperatures (210 – 390 K) in both N₂ and He bath gas and found experimental rate coefficients independent of bath gas or total pressure. The work by Feierabend et al. yields a $k_1(296\text{ K})$ of $(9.15 \pm 0.80) \times 10^{-12}$ molecule cm⁻³ s⁻¹; furthermore, $k_1(T)$, was found to demonstrate a negative temperature dependence with slightly non-Arrhenius behaviour over their experimental temperature range. Plum et al.³⁴ measured $k_1(296\text{ K})$ by a relative rate method in air, using OH + cyclohexane reaction as reference, and reported a value of $(11.5 \pm 0.4) \times 10^{-12}$ molecule cm⁻³ s⁻¹, assuming the reference reaction occurs at a rate of 7.57×10^{-12} molecule cm⁻³ s⁻¹. Figure 4 shows the temperature dependent $k_1(T)$ values measured during this work, alongside the other $k_1(T)$ values reported in the literature.

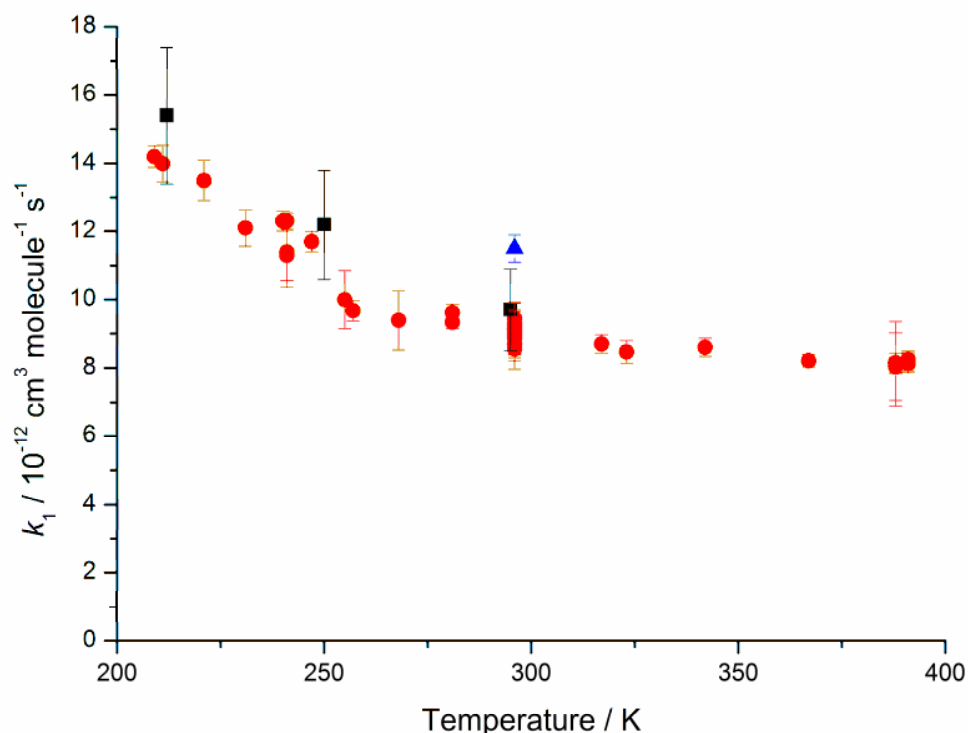


Figure 4: Temperature dependence of the OH + (HCO)₂ rate coefficient, $k_1(T)$, measured between 5 and 80 Torr total pressure using N₂ bath gas (■); the error bars include both statistical (2 σ level) and estimated systematic error. The $k_1(T)$ values measured by Feierabend et al.¹⁷ (●) and the room temperature $k_1(296\text{ K})$ relative rate value reported by Plum et al.³⁴ (▲) are included for comparison.

Feierabend and co-workers pointed out that using the recently recommended room temperature rate coefficient for the OH + cyclohexane reaction of 7.17×10^{-12} molecule $\text{cm}^{-3} \text{s}^{-1}$ reduces the Plum et al. $k_1(296 \text{ K})$ value to $(10.9 \pm 0.4) \times 10^{-12}$ molecule $\text{cm}^{-3} \text{s}^{-1}$. The experimental $k_1(T)$ values reported here are in reasonable agreement with values reported following other studies and gives confidence in our understanding of the OH + (HCO)₂ system using an inert bath gas.

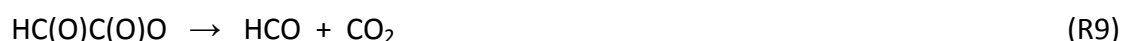
6.5 Generation of OH from the HC(O)CO + O₂ Reaction

Preliminary experiments to demonstrate primary OH production were conducted generating the HC(O)CO radical via Cl-atom initiated oxidation of (HCO)₂ in the presence of O₂ over a range of total pressures (5 – 20 Torr) and temperatures (195 and 295 K); OH production could then be monitored directly by LIF.



OH growth was observed under all experimental conditions, a typical OH profile is presented in Figure 5. Tests were carried out that confirmed OH growth was not observed in the absence of Cl-atom precursor or O₂.

While these experiments do not allow the rate or yield of OH to be quantified, they do provide insight as to which of the two proposed pathways is likely responsible for OH formation. Niki et al.¹⁹ proposed that reaction of HC(O)C(O)O₂ radicals with HO₂ could potentially result in OH formation (reaction R4) in a reaction scheme that also involved self reaction of the HC(O)C(O)O₂ peroxy radicals (R8) and unimolecular decomposition of the resulting HC(O)C(O)O alkoxy radical (R9):



Conversely, da Silva²¹ proposed OH radicals form directly following reaction of HC(O)CO radicals with O₂ in a chemically activated pathway (reaction R5); in excess O₂ this channel is consistent with observed OH formation on the microsecond timescale.

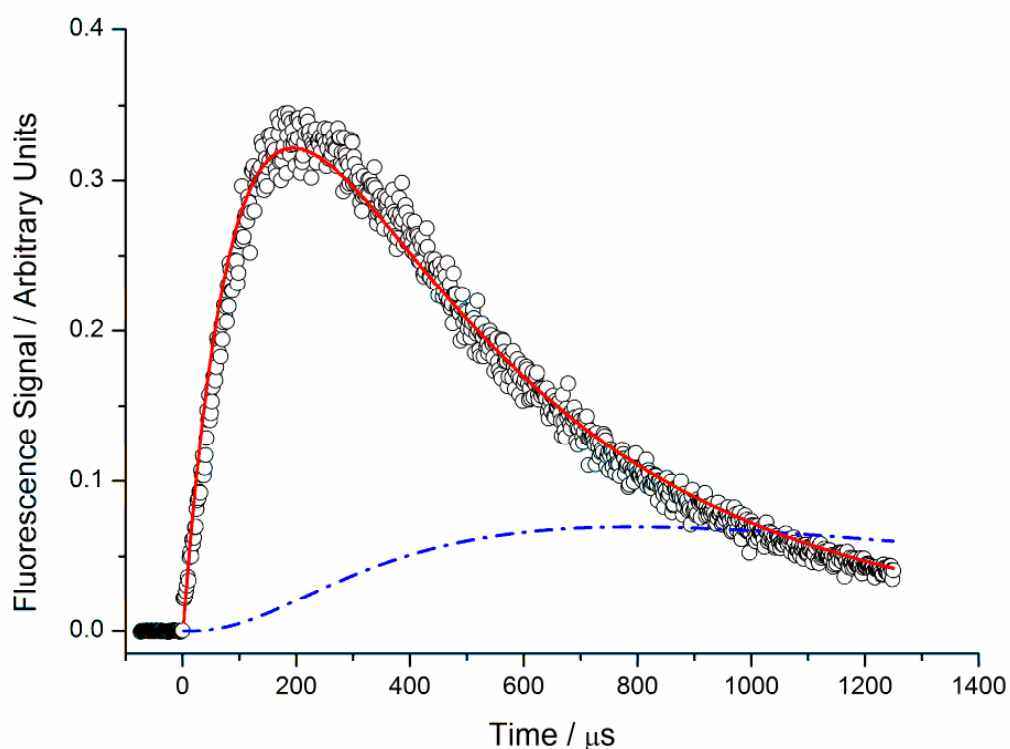


Figure 5: Experimental OH profile (open circles) following the Cl + (HCO)₂ reaction in the presence of 1.04×10^{17} molecules cm⁻³ O₂ at 295 K and 10 Torr total pressure, using initial Cl-atom and (HCO)₂ concentrations of 0.1 and 2.7×10^{14} molecules cm⁻³, respectively. Two model simulations are included. The red solid line using the OH pathways proposed by da Silva²¹ and the Cl + (HCO)₂ rate coefficient reported by Niki et al.,¹⁹ the blue dashed-dot line shows a simulation based on the Niki et al. mechanism for OH formation.

The numerical program KINTECUS³⁵ was used to simulate the observed OH profile for the Cl + (HCO)₂/O₂ reaction at 295 K and 10 Torr total pressure, as defined by either the Niki et al.¹⁹ or da Silva²¹ mechanism as shown in Figure 5. It is worthwhile to note that calculations by da Silva could not locate a transition state corresponding to the direct H-atom abstraction channel associated with the HC(O)CO + O₂ reaction (R3a).

The initial Cl-atom concentration, [Cl]₀, generated inside the reactor was estimated using:

$$[\text{Cl}]_0 = \sigma_{248 \text{ nm}} \Phi_{\text{Cl}, 248 \text{ nm}} F[(\text{COCl})_2]$$

to be of the order of $\sim 1 \times 10^{13}$ molecule cm^{-3} under our experimental conditions, where $\sigma_{248 \text{ nm}}$ and $\Phi_{\text{Cl}, 248 \text{ nm}}$ are the absorption cross section and Cl-atom quantum yield for oxalyl chloride photolysis at 248 nm,³⁶ F is the photolysis laser fluence, and $[(\text{COCl})_2]$ is the concentration of precursor in the reactor.

Radical-radical reactions are too slow to contribute to the observed OH profile given the magnitude of the estimated initial Cl-atom concentration in the reactor, and hence the Niki et al. reaction scheme fails to reproduce the experimental time-dependent OH profile, even when rate coefficients used for reactions R4 and R8 are allowed to achieve the gas-kinetic collision rate (Table 1). The blue dashed-dot line in Figure 5 shows the simulation based on the Niki et al. mechanism for OH formation where there is a clear induction period prior to OH generation and peak OH concentrations that occur much later than the experimental observation. The red line in Figure 5 shows the fit through the experimental data using the da Silva mechanism, with k_5 fixed at 5×10^{-12} molecule $\text{cm}^{-3} \text{ s}^{-1}$, typical of many radical + O_2 rate coefficients at limiting high pressure.³⁷⁻⁴⁰ The rate coefficients used in each fitting routine are listed in Table 1. Direct observation of OH following the Cl + $(\text{HCO})_2/\text{O}_2$ reaction provides strong evidence that reaction of HC(O)CO with O_2 proceeds directly to $\text{OH} + \text{CO} + \text{CO}_2$, as proposed by recent theoretical calculations by da Silva.²¹

Mechanism	Reaction	Rate coefficient, $k / \text{cm}^3 \text{ molecule}^{-1} \text{ s}^{-1}$	Reference
da Silva	$\text{Cl} + (\text{HCO})_2 \rightarrow \text{HC(O)CO} + \text{HCl}$	3.8×10^{-11}	Niki et al.
	$\text{HC(O)CO} + \text{O}_2 \rightarrow \text{CO}_2 + \text{CO} + \text{OH}$	5.0×10^{-12}	N/A
	$\text{OH} + (\text{HCO})_2 \rightarrow \text{HC(O)CO} + \text{H}_2\text{O}$	9.15×10^{-12}	Feierabend et al.
	$\text{HC(O)CO} \rightarrow \text{HCO} + \text{CO}$	$1.9 \times 10^6 \text{ cm}^3 \text{ molecule}^{-1} \text{ s}^{-2}$	N/A
	$\text{HCO} + \text{O}_2 \rightarrow \text{HO}_2 + \text{CO}$	5.5×10^{-12}	Atkinson et al.
	$\text{OH} \rightarrow \text{Loss}$	$295 \text{ cm}^3 \text{ molecule}^{-1} \text{ s}^{-2}$	N/A
Niki et al.	$\text{Cl} + (\text{HCO})_2 \rightarrow \text{HC(O)CO} + \text{HCl}$	3.8×10^{-11}	Niki et al.
	$\text{HC(O)CO} \rightarrow \text{HCO} + \text{CO}$	$1.9 \times 10^6 \text{ cm}^3 \text{ molecule}^{-1} \text{ s}^{-2}$	N/A
	$\text{HC(O)CO} + \text{O}_2 \rightarrow 2\text{CO} + \text{HO}_2$	5.0×10^{-12}	Orlando and Tyndall
	$\text{HC(O)CO} + \text{O}_2 \rightarrow \text{HC(O)C(O)O}_2$	5.0×10^{-12}	Orlando and Tyndall
	$\text{HC(O)C(O)O}_2 + \text{HO}_2 \rightarrow \text{HCO} + \text{CO}_2 + \text{O}_2 + \text{OH}$	1×10^{-10}	N/A
	$\text{OH} + (\text{HCO})_2 \rightarrow \text{HC(O)CO} + \text{H}_2\text{O}$	9.15×10^{-12}	Feierabend et al.
	$2\text{HC(O)C(O)O}_2 \rightarrow 2\text{HC(O)C(O)O} + \text{O}_2$	1.0×10^{-10}	N/A
	$\text{HC(O)C(O)O} \rightarrow \text{HCO} + \text{CO}_2$	$3.8 \times 10^8 \text{ cm}^3 \text{ molecule}^{-1} \text{ s}^{-2}$	N/A
	$\text{HCO} + \text{O}_2 \rightarrow \text{HO}_2 + \text{CO}$	5.5×10^{-12}	Atkinson et al.
	$\text{OH} \rightarrow \text{Loss}$	$295 \text{ cm}^3 \text{ molecule}^{-1} \text{ s}^{-2}$	N/A

Table 1: Rate coefficients used to fit the experimental OH profile observed following the Cl + (HCO)₂/O₂ reaction at 295 K and 10 Torr total pressure (Figure 5); using an initial (HCO)₂ concentration of $2.7 \times 10^{14} \text{ molecule cm}^{-3}$ in the presence of $1 \times 10^{17} \text{ molecules cm}^{-3} \text{ O}_2$.

6.6 Experimental OH Yields for the OH + (HCO)₂/O₂ Reaction

In excess O₂ the rate of OH decay slows relative to that measured in pure N₂ due to rapid OH regeneration through reaction R5; example bimolecular plots measured in N₂ (upper line) and in the presence of O₂ (lower line) are presented in Figure 6. Provided the

rates of reactions R2 and R5 are fast compared to the OH + (HCO)₂ reaction, then HC(O)CO can be considered in a steady state; OH loss is determined by the fraction of total HC(O)CO removal that does not recycle OH and is defined by the following rate law:

$$-\frac{d[\text{OH}]}{dt} = k'_1[\text{OH}] - k'_5[\text{HC(O)CO}] + k_6[\text{OH}] \quad (\text{E2})$$

where $k'_1 = k_1[(\text{HCO})_2]$ and $k'_5 = k_5[\text{O}_2]$. As HC(O)CO is in steady state:

$$k'_1[\text{OH}] = (k'_5 + k_2)[\text{HC(O)CO}] \quad \text{and}$$

$$-\frac{d[\text{OH}]}{dt} = k'_2[\text{OH}] \left(1 - \frac{k'_5}{k'_5 + k_2} \right) + k_6[\text{OH}] \quad (\text{E3})$$

The bimolecular rate coefficient measured in the presence of O₂, k_{O_2} , is slower than the bimolecular rate coefficient measured in pure N₂, k_{N_2} , where ($k_{\text{N}_2} = k_1$), by a factor:

$$1 - \frac{k'_5}{k'_5 + k_2} = \frac{k_{\text{O}_2}}{k_{\text{N}_2}}$$

The OH yield, Φ_{OH} , is given by:

$$\Phi_{\text{OH}} = \frac{k_5[\text{O}_2]}{k_5[\text{O}_2] + k_2} \quad (\text{E4})$$

Therefore, the experimental Φ_{OH} can be determined by the ratio of rate coefficients measured in the presence and absence of O₂:

$$\Phi_{\text{OH}} = 1 - \frac{k_{\text{O}_2}}{k_{\text{N}_2}} \quad (\text{E5})$$

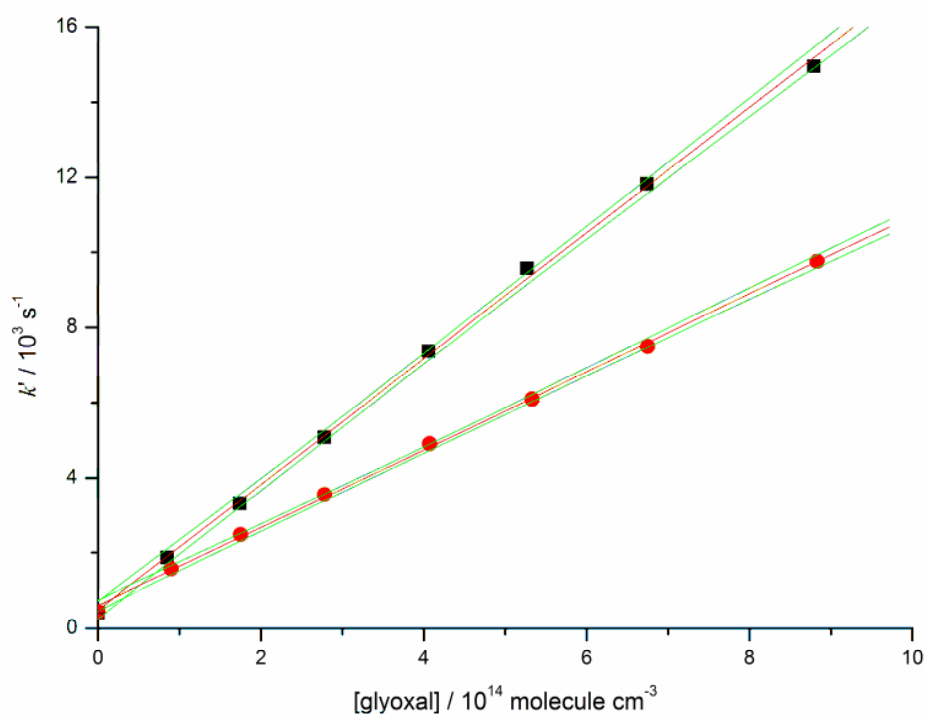


Figure 6: Bimolecular plots for the $\text{OH} + (\text{HCO})_2 \rightarrow \text{products}$ reaction at 212 K and 40 Torr; in pure N_2 (■) and in the presence of 869 mTorr of O_2 (●), corresponding to rate coefficients (16.68 ± 0.07) and $(11.45 \pm 0.12) \times 10^{-12} \text{ molecule cm}^{-3} \text{ s}^{-1}$; giving an experimental Φ_{OH} of 0.31. The outer lines show the confidence intervals at the 2σ level.

OH yields, Φ_{OH} , for the $\text{OH} + (\text{HCO})_2/\text{O}_2$ system have been quantified over a range of experimental temperatures (212 – 295 K) and pressures (5 – 80 Torr) using equation E5. Figure 7 shows the experimental Φ_{OH} data plotted as a function of total pressure and O_2 fraction, $f\text{-O}_2$, at 295 K. As mentioned previously, the statistical error (2σ level) of rate coefficients measured in pure N_2 , k_1 , was combined with an estimated 10% systematic error, reflecting the precision in the $(\text{HCO})_2$ concentration, the pressure gauges and the mass flow controllers. The scatter observed in $k_1(T)$ measurements (Figure 4) does not influence the experimental Φ_{OH} measurements, as these are based on the relative change in k_1 following addition of O_2 to the reactor (equation E5) and not on absolute k_1 values. Furthermore, OH decay traces using pure N_2 bath gas were recorded at the beginning and end of each day of experiments to ensure that the $k_1(T)$ measurement had remained constant. The purely statistical error (2σ level) in experimental Φ_{OH} measurements was considered to be low bias;

therefore an additional 2% error was assigned to each Φ_{OH} value to account for the observed experimental scatter.

The experimental Φ_{OH} are observed to increase with $f\text{-O}_2$ at a given pressure as reaction R5 becomes increasingly competitive with thermal dissociation (reaction R2). However, the Φ_{OH} tends to a limiting value. This observation is consistent with a fraction of the HC(O)CO population forming following reaction R1 with sufficient energy to promptly dissociate, in contrast to the mechanism proposed by da Silva, which treats the HC(O)CO radical at thermal equilibrium. The fate of the remaining HC(O)CO population is determined by a competition between thermal decomposition (R2) and bimolecular association with O_2 to give OH (R5).

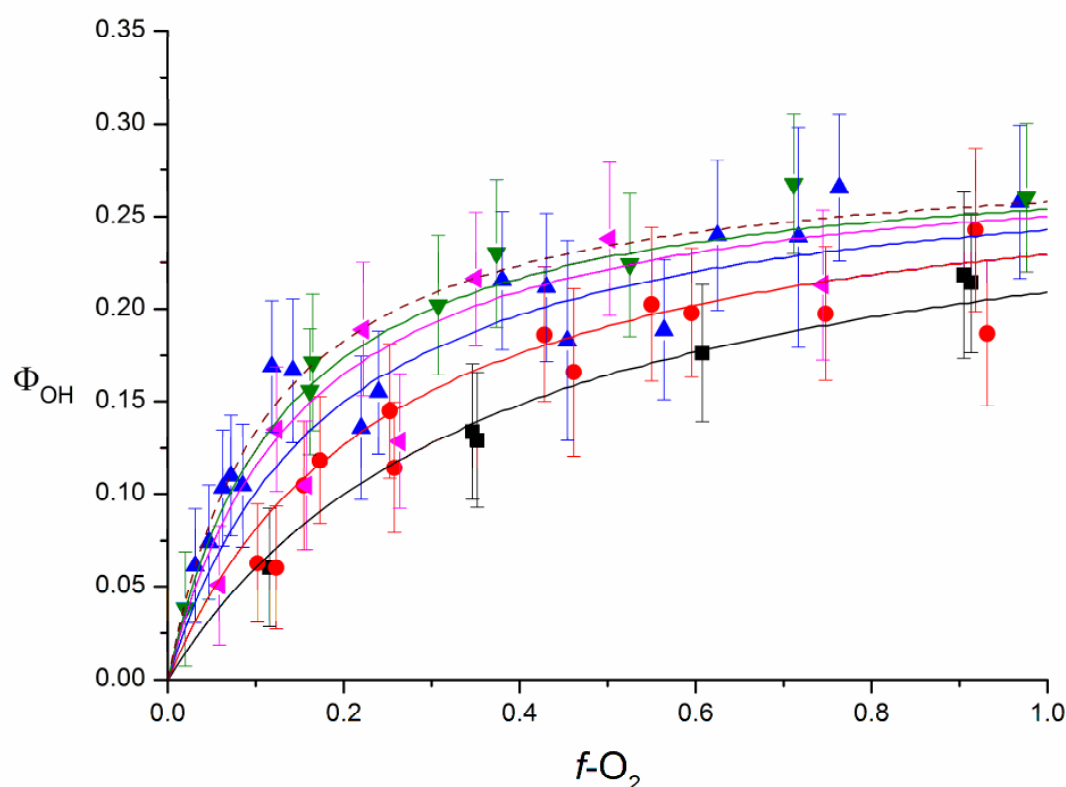
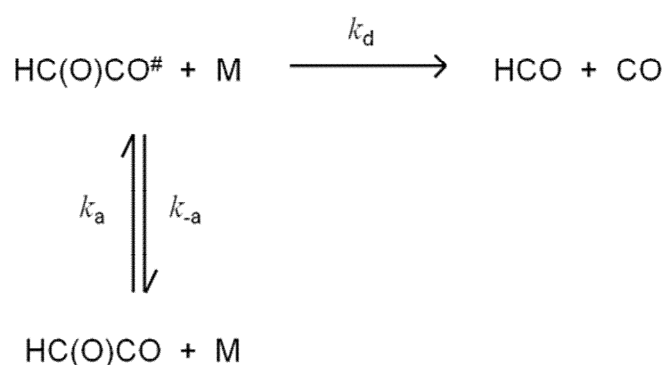


Figure 7: Experimental OH yields, Φ_{OH} , for the $\text{OH} + (\text{HCO})_2/\text{O}_2$ reaction at 295 K as a function of oxygen fraction, $f\text{-O}_2$, at total pressures of 5 (■), 10 (●), 20 (▲), 40 (◄) and 80 Torr (▼) total pressure. The dashed line shows the predicted Φ_{OH} dependence on $f\text{-O}_2$ at 760 Torr. The error bars include both the statistical (2σ level) and estimated systematic errors. Included are fits through each total pressure data set using the extended Lindemann-Hinshelwood model (See text for details).

In order to determine the limiting OH yields and to determine the Φ_{OH} as a function of pressure at atmospheric oxygen fractions ($f\text{-O}_2 = 0.21$), the data have been parametrized with a model based on a simple Lindemann-Hinshelwood (LH) mechanism that allows for prompt dissociation of a fraction of the chemically activated HC(O)CO radical. Unimolecular dissociation and bimolecular association reactions potentially have rate coefficients that show a dependence on pressure and a Lindemann-Hinshelwood mechanism can be used to provide a qualitative description of reaction R2 (Scheme 1):



Scheme 1. Reaction scheme to describe unimolecular decomposition of the HC(O)CO radical

where HC(O)CO[#] represents the chemically activated HC(O)CO radical, k_a and k_{-a} signify the rates of activation and deactivation of the HC(O)CO radical, respectively, through collisions with bath gas molecules, M, and k_d represents the rate of unimolecular dissociation of the activated HC(O)CO[#] radical. Treating the HC(O)CO[#] radical in a steady state, then it follows that:

$$k_2 = \frac{k_a k_d [\text{M}]}{k_d + k_{-a} [\text{M}]} \quad (\text{E6})$$

At limiting high pressure k_2 tends towards the unimolecular rate coefficient, k_2^∞ :

$$k_2^\infty = \frac{k_a k_d}{k_{-a}}$$

At limiting low pressure k_2 tends towards the bimolecular rate coefficient, k_2^0 :

$$k_2^0 = k_a$$

Inverting both sides of equation E6 It follows that:

$$\frac{1}{k_2} = \frac{1}{k_2^0[M]} + \frac{1}{k_2^\infty}$$

multiplying through by [M] and equating to k_2 it follows that:

$$k_2 = \frac{[M]}{\frac{1}{k_2^0} + \frac{[M]}{k_2^\infty}} \quad (E7)$$

A similar Lindemann-Hinshelwood expression can be used to describe the pressure dependence in the bimolecular HC(O)CO + O₂ association reaction R5. The Lindemann-Hinshelwood model captures the physical steps involved in reaction but inadequately accounts for the internal energy of the molecule.⁴¹ Here, Lindemann-Hinshelwood forms are assigned to the pressure dependence of both the HC(O)CO decomposition and bimolecular association with O₂ rate constants. This model is flexible enough to adequately parameterize these data, but it is concluded that system is more complex and that limited physical significance is assigned to the fitting parameters. Complications arise because the HC(O)CO radical is formed with excess energy (exothermicity of reaction R1 ~129.7 kJ mol⁻¹)²², and undergoes subsequent chemistry before this excess energy is removed. In this work a model is developed to parameterize the system based on thermal rate constants and prompt dissociation, which allows the Φ_{OH} to be predicted under atmospheric conditions; evidence suggesting the role of chemical activation in this system is also discussed.

The fraction of prompt HC(O)CO dissociation is accounted for in this analysis by the OH_{limit} parameter, which signifies the fraction of total HC(O)CO that survives the OH + (HCO)₂ reaction. How close the OH yield system is to the OH_{limit} depends on k_2 and $k_5[O_2]$, and is given by:

$$\Phi_{OH} = OH_{limit} \left(\frac{k_5[O_2]}{k_5[O_2] + k_2} \right) \quad (E8a)$$

If Lindemann-Hinshelwood forms are assigned to k_2 and k_5 , then equation E8a gives:

$$\Phi_{\text{OH}} = \text{OH}_{\text{limit}} \left(\frac{\left(\frac{[\text{M}][\text{O}_2]}{\text{A}^{-1} + \text{B}^{-1}[\text{M}]} \right)}{\left(\frac{[\text{M}][\text{O}_2]}{\text{A}^{-1} + \text{B}^{-1}[\text{M}]} \right) + \left(\frac{[\text{M}]}{\text{C}^{-1} + \text{D}^{-1}[\text{M}]} \right)} \right) \quad (\text{E8b})$$

where the A and B parameters are related to the pressure dependence in the HC(O)CO + O₂ association reaction, while the C and D parameters are related to the pressure-dependent decomposition channel.

The pressure- and oxygen-dependent experimental Φ_{OH} have been fitted at each experimental temperature independently, using equation E8b. These Φ_{OH} only identify the ratio k_2/k_5 ; hence, there is no unique solution for each temperature data set. In order to constrain the fit, the parameters B and D, which are related to the high-pressure limiting rates of HC(O)CO association with O₂ and decomposition, respectively, have been fixed. The B parameter was fixed at a value of $5 \times 10^{-12} \text{ cm}^3 \text{ molecule}^{-1} \text{ s}^{-1}$. It was also assumed that the B parameter was independent of temperature. High pressure limiting rate coefficients for HC(O)CO decomposition were calculated using an RRKM/master equation analysis with the open source MESMER computer programme⁴² by Dr Robin Shannon. The zero-point energy corrected barrier height for decomposition was obtained by performing geometry optimizations of HC(O)CO and the decomposition transition state and subsequent harmonic frequency analysis at the bb1K/aug-cc-pVDZ level of theory followed by single-point energy calculations at the CCSD(T)/aug-cc-pVTZ level of theory using the Gaussian09 suite of programs. Collisions between the nitrogen bath gas and HC(O)CO were parameterized using a Lennard-Jones model parameterized with a temperature independent ΔE_d . Molecular densities of states were obtained assuming a rigid rotor-harmonic oscillator model, and one vibration within the transition state was treated as a hindered rotation. Furthermore, the energy partitioned in the products following reaction R1 has been investigated by Dr Shannon by incorporating a prior distribution model in MESMER;⁴³ with initial calculations assuming the exothermicity was distributed statistically between the HC(O)CO and H₂O products. However, it was found that a non-statistical energy distribution is required for theoretical Φ_{OH} to match those observed experimentally, with over 90 kJ mol⁻¹ partitioned in

the H₂O. This result provides quantitative evidence that a significant fraction of the exothermicity following reaction R1 is channelled into the HC(O)CO radical fragment, inconsistent with the widely accepted rules of abstraction reaction dynamics.⁴⁴

Room temperature Φ_{OH} measurements are presented in Figure 7 as a function of total pressure and oxygen fraction, $f\text{-O}_2$; together with analysis using the extended Lindemann-Hinshelwood model (E8b). Figure 7 shows that equation E8b adequately parameterizes the data set; Figures 8 and 9 show this to also be the case at the lower experimental temperatures. Both experimental and theoretical studies have indicated that at ambient temperatures and pressures k_2 is in its pressure-dependent regime, close to the low pressure limit.^{20, 21, 45} Therefore, as the total pressure is increased, more O₂ is required for the bimolecular reaction channel (reaction R5) to effectively compete with dissociation (Figure 7). The analysis of all the ambient temperature Φ_{OH} measurements suggests an OH_{limit} of (0.29 ± 0.03) at 295 K.

In contrast to the data at 295 K, the experimental Φ_{OH} measurements at 250 K are independent of total pressure but strongly dependent on oxygen concentration; reaching an OH_{limit} of (0.31 ± 0.04) . All of the data collected at 250 K are plotted in Figure 8.

Qualitatively similar behaviour to Figure 8 is observed at 212 K (Figure 9), although less O₂ is required to titrate all available HC(O)CO to OH, consistent with an Arrhenius temperature dependence in k_2 . The OH_{limit} at 212 K increases further to (0.38 ± 0.03) , suggesting an increasing fraction of the nascent HC(O)CO population form with energy in excess of the threshold to dissociation as the temperature increases. The parameters used to fit each temperature data set are presented in Table 2.

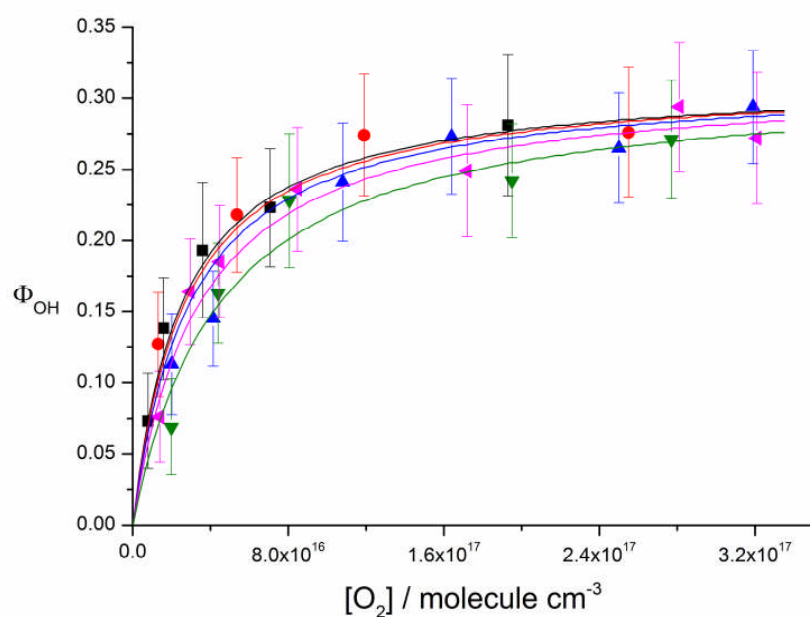


Figure 8: Experimental OH yields, Φ_{OH} , for the OH + (HCO)₂/O₂ reaction at 250 K as a function of oxygen concentration at total pressures of 5 (■), 10 (●), 20 (▲), 40 (◄) and 80 Torr (▼). The errors include both the statistical (2σ) and estimated systematic errors.

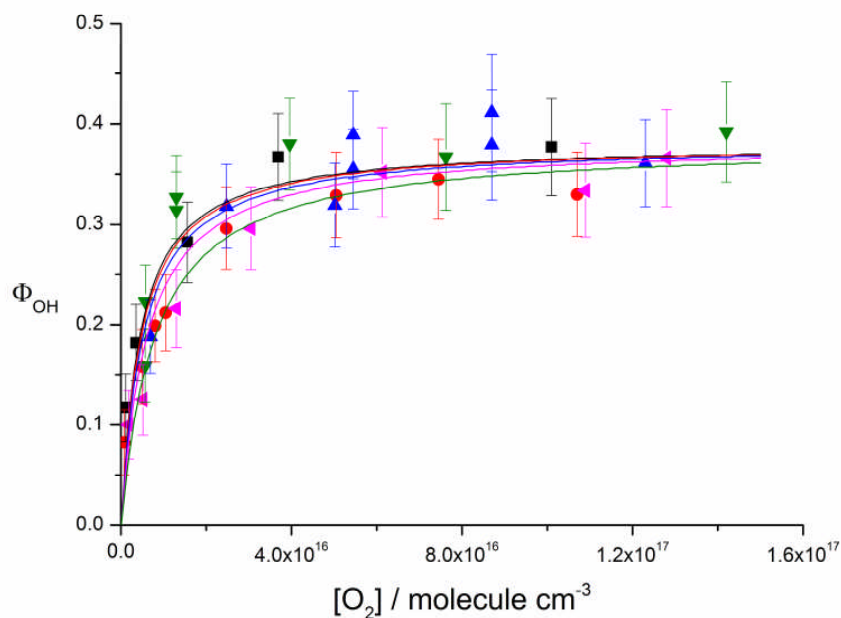


Figure 9: Experimental OH yields, Φ_{OH} , for the OH + (HCO)₂/O₂ reaction at 212 K as a function of oxygen concentration at total pressures of 5 (■), 10 (●), 20 (▲), 40 (◄) and 80 Torr (▼). The error bars include both the statistical (2σ level) and estimated systematic errors.

Parameter	Temperature (K)		
	295	250	212
OH_{limit}	0.29 ± 0.03	0.31 ± 0.04	0.38 ± 0.03
A	$(12.0 \pm 4.8) \times 10^{-30} \text{ cm}^3 \text{ molecule}^{-1} \text{ s}^{-1}$	$(14.0 \pm 9.6) \times 10^{-31} \text{ cm}^3 \text{ molecule}^{-1} \text{ s}^{-1}$	$(12.9 \pm 7.85) \times 10^{-31} \text{ cm}^3 \text{ molecule}^{-1} \text{ s}^{-1}$
B	$5 \times 10^{-12} \text{ cm}^3 \text{ molecule}^{-1} \text{ s}^{-1}$	$5 \times 10^{-12} \text{ cm}^3 \text{ molecule}^{-1} \text{ s}^{-1}$	$5 \times 10^{-12} \text{ cm}^3 \text{ molecule}^{-1} \text{ s}^{-1}$
C	$(5.6 \pm 1.2) \times 10^{-13} \text{ s}^{-1}$	$(3.4 \pm 1.2) \times 10^{-14} \text{ s}^{-1}$	$(5.4 \pm 1.6) \times 10^{-15} \text{ s}^{-1}$
D	$2.6 \times 10^9 \text{ s}^{-1}$	$3.0 \times 10^8 \text{ s}^{-1}$	$2.4 \times 10^7 \text{ s}^{-1}$

Table 2: Parameters used to model experimental OH yields, Φ_{OH} , for the OH + (HCO)₂/O₂ reaction as a function of total pressure and temperature.

6.7 Ambient OH yields

The parameters used to describe the observed Φ_{OH} for the OH + (HCO)₂/O₂ system under the experimental conditions considered here have been used to predict the Φ_{OH} dependence on temperature and total pressure using an $f\text{-O}_2$ of 0.21 and suggest that at total pressures relevant to the troposphere the Φ_{OH} predicted at 295, 250 and 212 K are 0.19, 0.30 and 0.38, respectively (Figure 10); the Φ_{OH} predicted at 295 K using an $f\text{-O}_2$ of 1 are included in Figure 9 (dashed black line) and confirm a significant contribution from both chemically activated and thermal HC(O)CO dissociation under tropospheric conditions. At 760 Torr and 295 K, the Φ_{OH} calculated here, based on experimental measurements, of ~0.19 is approximately a factor of two greater than that predicted from calculations by Setokuchi.²² da Silva²¹ calculates a significantly higher Φ_{OH} of 0.36 under tropospheric conditions, with very little stabilization to HC(O)C(O)O₂, and with decomposition accounting for the vast majority of the balance of 0.64. However, as noted before, da Silva considered only a thermal distribution of HC(O)CO radicals.

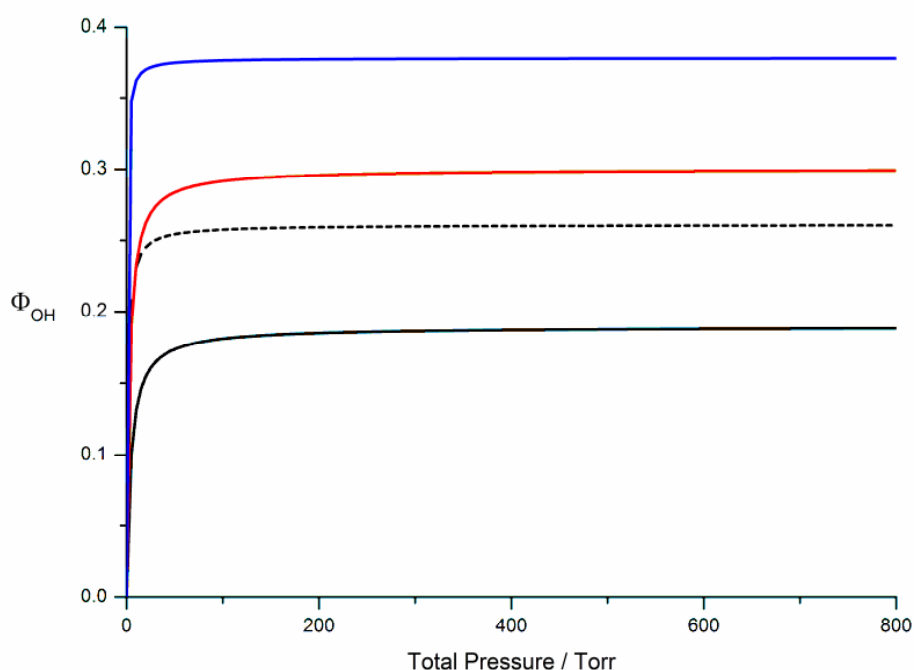


Figure 10: OH yields, Φ_{OH} , as a function of total pressure at 295 (black line), 250 (red line), and 212 K (blue line) and atmospheric oxygen fractions ($f\text{-O}_2 = 0.21$); included are Φ_{OH} predicted at 295 K in pure O_2 (dashed line).

6.8 Evidence for Nonthermal Rate Behaviour

As the experimental Φ_{OH} are essentially independent of pressure at 250 and 212 K (Figures 8 and 9), both k_2 and k_5 might be assumed to be at their high-pressure limits at these temperatures; indeed, master equation calculations performed as part of this work and by da Silva,²¹ suggest that k_5 should be pressure independent at just a few Torr total pressure. However, satisfactory fits through the 250 and 212 K data sets constraining k_2 to the high-pressure limiting values of 3×10^8 and $2.4 \times 10^7 \text{ s}^{-1}$ (Table 2), respectively, require k_5 values of 1×10^{-8} and $5 \times 10^{-9} \text{ cm}^3 \text{ molecule}^{-1} \text{ s}^{-1}$ at 250 and 212 K, respectively, which exceed the gas-kinetic collision rate by several orders of magnitude. Alternatively, given that k_5 is calculated to be pressure independent at all experimental pressures and temperatures, attempts were made to fit the complete data set by allowing only k_2 to be pressure

dependent, but poor quality fits were obtained. Our experimental results indicate that pressure dependence in both k_2 and k_5 is required to fit the data.

However, if both k_2 and k_5 are allowed to vary according to the Lindemann-Hinshelwood mechanism, then the A parameter (Table 2) shows anomalous behaviour if it is interpreted as the low-pressure limiting rate constant for k_5 . Low-pressure rate constants for association reactions increase as the temperature decreases due to the increased lifetime of the activated adduct, whereas the data presented here predicts the opposite behaviour for A. This observation suggests that the system is not described by thermal rate constants.

Further evidence for nonthermal behaviour comes from a consideration of the ratio of k_2/k_5 . It follows from equation E8a that the $\text{OH}_{\text{limit}}/\Phi_{\text{OH}}$ ratio should scale linearly with the inverse O_2 concentration, with a gradient equal to k_2/k_5 and an intercept of 1. Figure 11 shows such a plot at 295 K at selected pressures.

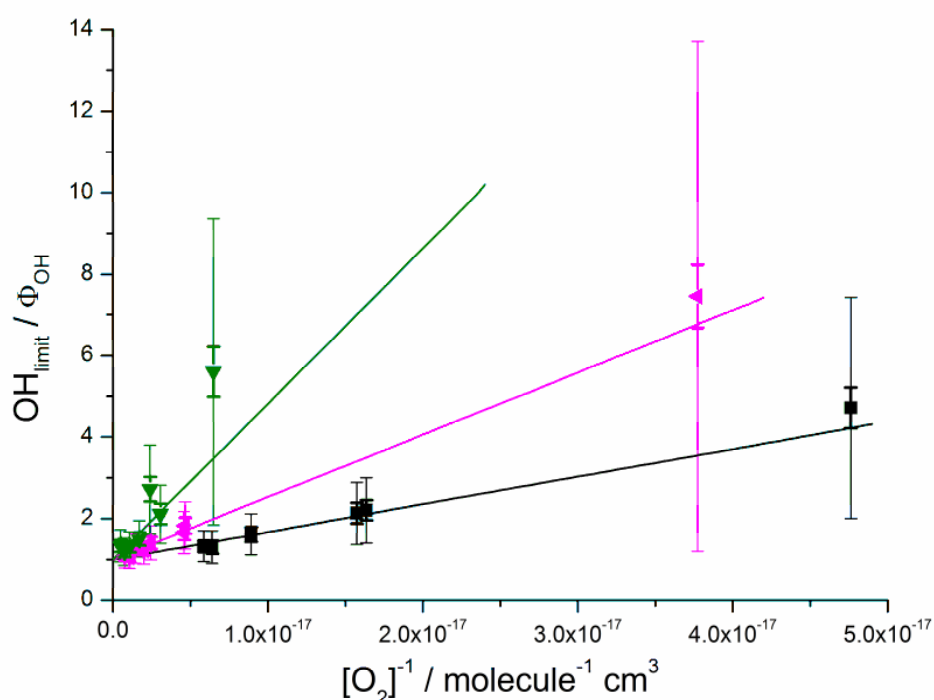


Figure 11: Ratios of the observed $\text{OH}_{\text{limit}}/\Phi_{\text{OH}}$ ratio following glyoxal oxidation as a function of the inverse O_2 concentration at total pressures of 5 (■), 40 (◀) and 80 Torr (▼) and 295 K; the small error bars are purely statistical (2σ level); the larger error bars include the estimated systematic error.

The k_2/k_5 ratios derived following linear analysis of the Φ_{OH} observed at all experimental pressures at 295 K are presented in Figure 12 as a function of total pressure. The solid line in Figure 12 is the ratio of thermal rate coefficients calculated in MESMER by Dr R. Shannon. Given that k_5 is essentially at the high-pressure limit under all experimental conditions, Figure 12 maps out the pressure dependence of k_2 . As the total pressure is increased above 20 Torr, the observed k_2/k_5 ratio increases with total pressure, indicating that k_2 increases more rapidly with total pressure than k_5 as predicted by calculations. However, below 20 Torr, the k_2/k_5 ratio appears pressure independent, suggesting that k_2 is faster than expected under these conditions due to the effect of chemical activation.

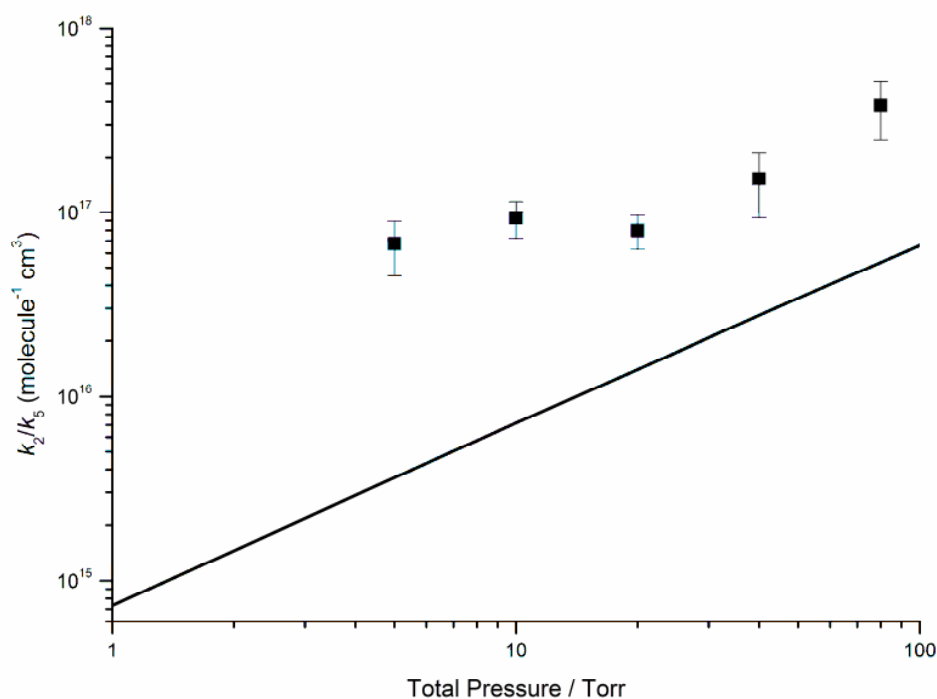


Figure 12: The observed k_2/k_5 pressure dependence on total pressure (5 – 80 Torr) at 295 K. The solid line is the k_2/k_5 calculated using MESMER based on thermal rate coefficients for k_2 and k_5 suggesting a linear dependence to pressures of ~1 Torr.

Similar linear behaviour of the $\text{OH}_{\text{limit}}/\Phi_{\text{OH}}$ ratio with inverse O_2 concentration was observed at all experimental pressures at 250 and 212 K. The k_2/k_5 ratios derived following linear analysis of all experimental Φ_{OH} measurements at 250 and 212 K are plotted in Figures 13 and 14, respectively, as a function of total pressure. The observed k_2/k_5 ratios appear independent of total pressure at both subambient temperatures considered here. The k_2/k_5 ratios calculated in MESMER based on thermal rate coefficients both underestimate the magnitude of the ratio (by up to an order of magnitude), and predict linear pressure dependence between 1 and 100 Torr; providing further evidence that this system cannot be described by thermal rate coefficients. k_2/k_5 ratios are observed to scale with temperature, as expected under the assumption that k_5 lacks significant temperature dependence and HC(O)CO dissociates over a barrier.

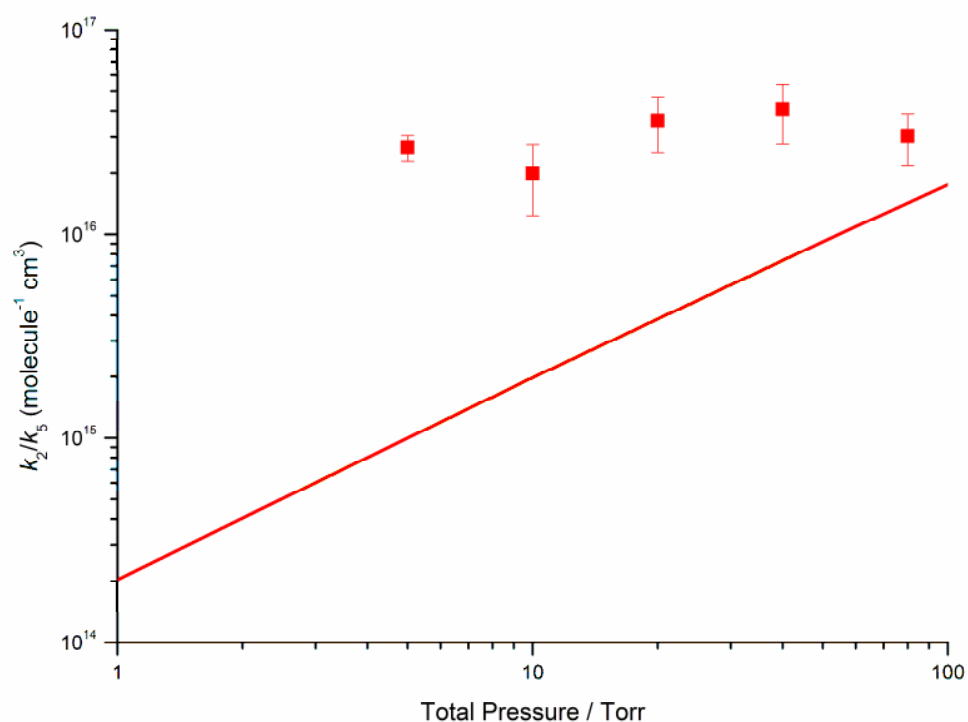


Figure 13: The observed k_2/k_5 pressure dependence on total pressure (5 – 80 Torr) at 250 K. The solid line is the k_2/k_5 calculated using MESMER based on thermal rate coefficients for k_2 and k_5 .

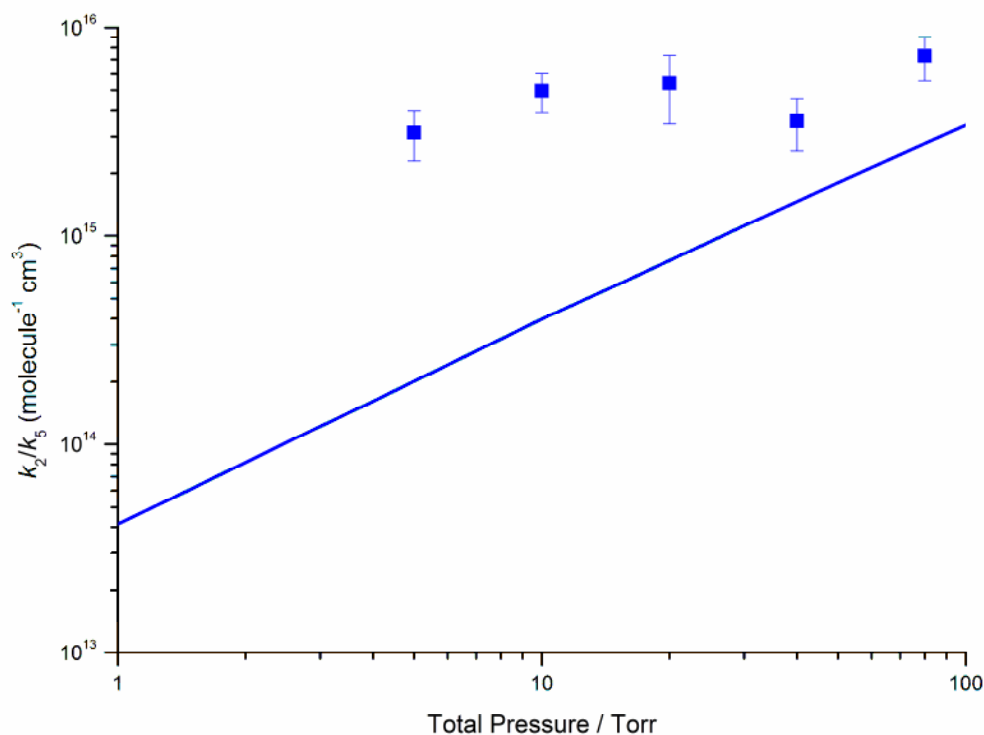


Figure 14: The observed k_2/k_5 pressure dependence on total pressure (5 – 80 Torr) at 212 K. The solid line is the k_2/k_5 calculated using MESMER based on thermal rate coefficients for k_2 and k_5 .

6.9 Linear Dependence of $[CO]/[CO_2]$ Products as a Function of $1/[O_2]$

Orlando and Tyndall²⁰ carried out an extensive investigation of HC(O)CO chemistry over a range of temperatures (224 – 317 K) at near atmospheric conditions, during chamber experiments coupled with FTIR product detection. Analysis by these authors was based on the mechanism proposed by Niki et al.¹⁹ and reported a strong linear dependence of the $[CO]/[CO_2]$ ratio on the inverse O_2 partial pressure (Figure 15). The data presented here show a similar behaviour (Figure 11), as OH_{limit}/Φ_{OH} is directly related to $[CO]/[CO_2]$; to assert the credibility of the mechanism proposed here, similar behaviour must be predicted.

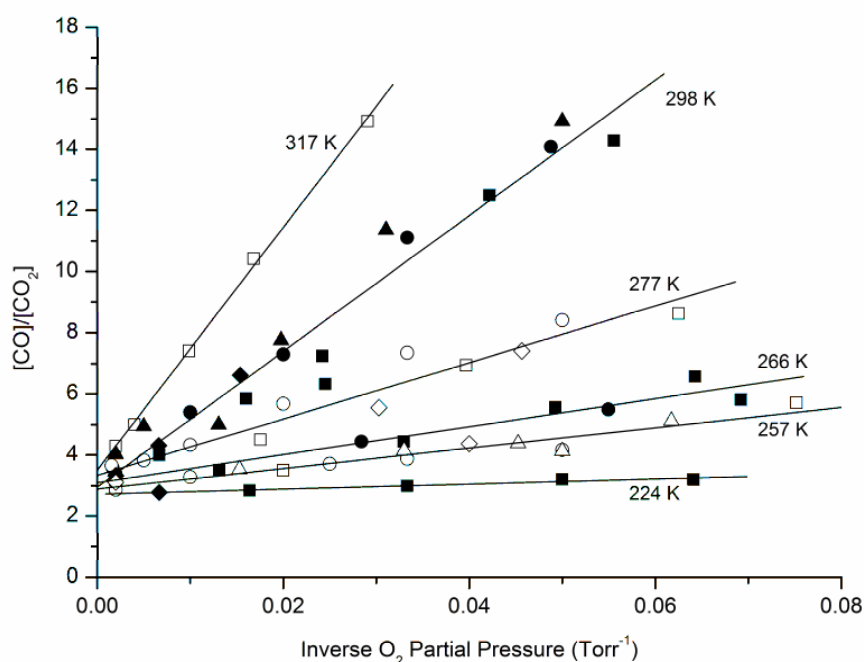


Figure 15: Observed $[\text{CO}]/[\text{CO}_2]$ ratios from glyoxal oxidation as a function of inverse O_2 partial pressure and temperature at 700 Torr total pressure; with data obtained from the photolysis of $\text{Cl}_2/\text{glyoxal}/\text{O}_2/\text{N}_2$ mixtures (squares), from the photolysis of $\text{Cl}_2/\text{glyoxal}/\text{NO}/\text{O}_2/\text{N}_2$ mixtures (circles), from the photolysis of $\text{C}_2\text{H}_5\text{ONO}/\text{glyoxal}/\text{NO}/\text{O}_2/\text{N}_2$ mixtures (triangles), from the photolysis of $\text{Cl}_2/\text{glyoxal}/\text{NO}_2/\text{O}_2/\text{N}_2$ mixtures. (Redrawn from Orlando and Tyndall²⁰).

In the mechanism suggested here, the HCO radicals that form following prompt and thermal dissociation of the $\text{HC}(\text{O})\text{CO}$ radical will be rapidly converted to HO_2 and CO in excess O_2 via reaction R10:



Defining the term α as the fraction of the $\text{HC}(\text{O})\text{CO}$ population that decomposes promptly before the possibility of reaction with O_2 , it follows that:

$$[\text{CO}]_{\text{prompt}} = 2\alpha[\text{HC}(\text{O})\text{CO}]_0 \quad (\text{E9})$$

$$[\text{CO}]_{\text{thermal}} = (1 - \alpha)[\text{HC}(\text{O})\text{CO}]_0 \left(\frac{2k_2}{k_2 + k_5[\text{O}_2]} + \frac{k_5[\text{O}_2]}{k_2 + k_5[\text{O}_2]} \right) \quad (\text{E10})$$

$$[\text{CO}_2]_{\text{thermal}} = (1 - \alpha)[\text{HC(O)CO}]_0 \left(\frac{k_5[\text{O}_2]}{k_2 + k_5[\text{O}_2]} \right) \quad (\text{E11})$$

where subscripts ‘prompt’ and ‘thermal’ refer to the mechanism for HC(O)CO chemistry. Assuming the [CO]/[CO₂] ratios observed by Orlando and Tyndall are defined by equation E12:

$$\frac{[\text{CO}]_{\text{obs}}}{[\text{CO}_2]_{\text{obs}}} = \frac{[\text{CO}]_{\text{prompt}} + [\text{CO}]_{\text{thermal}}}{[\text{CO}_2]_{\text{thermal}}} \quad (\text{E12})$$

it follows that:

$$\frac{[\text{CO}]_{\text{obs}}}{[\text{CO}_2]_{\text{obs}}} = \left(\frac{2\alpha}{1 - \alpha} \right) \frac{k_5[\text{O}_2] + k_2}{k_5[\text{O}_2]} + \left(\frac{2k_2 + k_5[\text{O}_2]}{k_5[\text{O}_2]} \right) \quad (\text{E13a})$$

$$= \frac{2\alpha}{1 - \alpha} \left(1 + \frac{k_2}{k_5[\text{O}_2]} \right) + \frac{2k_2}{k_5[\text{O}_2]} + 1 \quad (\text{E13b})$$

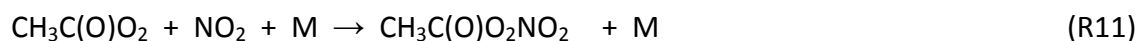
$$= \frac{2k_2}{k_5} \left(\frac{\alpha}{(1 - \alpha)} + 1 \right) \frac{1}{[\text{O}_2]} + \frac{2\alpha}{1 - \alpha} + 1 \quad (\text{E13c})$$

$$= \left(\frac{2k_2}{k_5(1 - \alpha)} \right) \frac{1}{[\text{O}_2]} + \left(\frac{1 + \alpha}{1 - \alpha} \right) \quad (\text{E13d})$$

Therefore, the mechanism proposed here does predict a linear dependence of [CO]/[CO₂] ratios with inverse O₂ partial pressures (with a gradient equal to 2k₂/(k₅(1-α)) and an intercept equal to (1+α)/(1-α), consistent with experimental measurements by Orlando and Tyndall. These authors reported the intercept to increase with temperature from (2.8 ± 0.4) to (3.1 ± 0.4) from 224 to 317 K, respectively; although these results were not deemed statistically significant. These observations suggest that α increases with temperature, as defined by equation E13d, or alternatively that OH_{limit} decreases with temperature, consistent with the results presented here. Orlando and Tyndall observed the slopes of [CO]/[CO₂] vs 1/[O₂] plots to increase with temperature (Figure 15), which they attributed to a strongly Arrhenius temperature dependence of k₂. The gradient predicted using the mechanism proposed here (equation E13d) is again consistent with the observed increased

gradient with temperature, given that both k_2 and α are shown to increase with temperature, and k_5 is presumed to lack a strong temperature dependence. Orlando and Tyndall observed $[\text{CO}]/[\text{CO}_2]$ ratios independent of inverse O_2 partial pressure at 224 K and concluded that unimolecular dissociation is unable to compete with bimolecular reaction with O_2 under these conditions. Given that the minimum O_2 concentration used during these experiments is estimated to be $\sim 6.5 \times 10^{17}$ molecule cm^{-3} , more than enough to titrate all available HC(O)CO out to CO_2 via reaction R5, these results are also in strong agreement with the results presented here.

It is worthwhile to note that during the work of Orlando and Tyndall,²⁰ experiments were conducted in the presence of NO_2 to ascertain whether or not glyoxal derived peroxy radicals, HC(O)C(O)O_2 , could react with NO_2 to give an acyl peroxy nitrate species, analogous to the peroxy acetyl nitrate (PAN) formed through reaction of acetyl peroxy radicals with NO_2 (reaction R11); no experimental evidence for formation of the PAN like species, $\text{HC(O)C(O)O}_2\text{NO}_2$, could be found even at the lowest experimental temperatures.



These observations are again consistent with $\text{HC(O)CO} + \text{O}_2$ chemistry occurring via an open channel out to OH, rather than through stabilization into the HC(O)C(O)O_2 peroxy well.

6.10 Comparison of the OH/Glyoxal/O₂ and OH/Methyl-glyoxal/O₂ Systems

It is interesting to contrast the work presented here with a previous experimental study on the reaction of OH with methylglyoxal by Baeza-Romeo et al.,⁴³ which was also conducted at the University of Leeds. The OH + methylglyoxal reaction is predicted to occur exclusively via abstraction of the aldehydic H-atom, and the resulting peroxy radical formed following the addition of O_2 , $\text{CH}_3\text{C(O)C(O)O}_2$, might be expected to undergo a similar internal abstraction to $\text{CH}_2\text{C(O)C(O)O}_2\text{H}$ with subsequent fragmentation to give OH + CO_2 + HCHO. However, while OH recycling in the presence of O_2 was observed, the pressure dependence of the observed OH yield closely matched that of acetyl + O_2 .^{46, 47}

The difference in mechanism relates to the much faster rate of decomposition of $\text{CH}_3\text{C(O)CO}$ relative to HC(O)CO . The decomposition kinetics of the R-CO carbonyl radicals have been calculated by Mereau et al.⁴⁵ The thermal decomposition of $\text{CH}_3\text{C(O)CO}$ at one atmosphere is calculated to be a factor of 40 faster than that of HC(O)CO . As the total pressure is lowered, HC(O)CO will enter the falloff regime before $\text{CH}_3\text{C(O)CO}$ further increasing this ratio. Jagiella and Zabel⁴⁸ measured a rate coefficient of $1.1 \times 10^8 \text{ s}^{-1}$ for $\text{CH}_3\text{C(O)CO}$ decomposition (measured relative to reaction with O_2 assuming $k_{\text{O}_2} = 5 \times 10^{-12} \text{ cm}^3 \text{ molecule}^{-1} \text{ s}^{-1}$) where $\text{CH}_3\text{C(O)CO}$ was formed by the endothermic reaction of Br atoms with methylglyoxal. At the typical experimental O_2 concentrations of the OH + methylglyoxal study, $\sim 10^{16} - 10^{17} \text{ molecule cm}^{-3}$, thermal decomposition will be a factor of 200 – 2000 times faster than peroxy radical formation. Additionally, as discussed by Baeza-Romero and co-workers, the $\text{CH}_3\text{C(O)CO}$ is formed from the significantly exothermic OH reaction with methylglyoxal and hence prompt dissociation dominates. OH recycling is the result of the reaction of O_2 with the acetyl, CH_3CO , radicals formed through decomposition of the $\text{CH}_3\text{C(O)CO}$ radical.⁴⁶

6.11 Atmospheric Implications

The dominant processes responsible for the atmospheric removal of $(\text{HCO})_2$ are photolysis and reaction with OH. The HC(O)CO radicals that form following reaction with OH either dissociate to $\text{HCO} + \text{CO}$ or react with O_2 to give CO_2 , CO and OH directly. The HCO radicals produced through photolysis and decomposition react rapidly with O_2 to give HO_2 and CO . The dissociation channel is net HOx neutral as OH is consumed in generating the HC(O)CO radical, and HO_2 is then generated through secondary chemistry. The bimolecular channel also consumes OH in generating the HC(O)CO radical but produces OH through reaction with O_2 . While both the unimolecular and bimolecular channels are net HOx neutral, the $\text{HC(O)CO} + \text{O}_2$ reaction recycles OH as OH without conversion to HO_2 , and therefore acts to increase the OH/ HO_2 ratio. Chemical models require reaction channels such as this to resolve the discrepancy between measured and modeled HOx concentrations in remote pristine environments. Reaction with OH typically accounts for 14 – 23% of total $(\text{HCO})_2$ removal under tropospheric conditions,¹⁸ of which only a fraction (Figure 10) directly

regenerates OH through reaction of HC(O)CO with O₂. Therefore, this chemistry only contributes marginally to increase OH concentrations in pristine forested environments, and the very large missing OH source reported in the literature remains unresolved.

The Master Chemical Mechanism (MCM)⁴⁹ used to describe the chemical degradation of tropospheric volatile organic compounds, currently defines HC(O)CO chemistry using the mechanism proposed by Niki et al.¹⁹ The MCM currently treats the HC(O)C(O)O₂ + HO₂ reaction as comprising three competing channels. In addition to the OH forming channel proposed by Niki et al. are peracid and ozone forming channels, analogous to acetylperoxy + HO₂ chemistry.^{50, 51} The work presented here suggests that the MCM should be amended to include direct OH formation following the HC(O)CO + O₂ reaction, with limited formation of HC(O)C(O)O₂ from OH initiated oxidation of glyoxal.

As mentioned previously, chemical activation is known to influence the product distributions observed following OH initiated oxidation of alkynes, through chemistry initiated via OH addition.^{5, 37} Here, it has been shown that the influence of chemical activation may be extended to the OH + (HCO)₂/O₂ reaction, with chemistry initiated by an H-abstraction channel.

6.12 References

1. Carter, W. P. L.; Atkinson, R., Development and evaluation of a detailed mechanism for the atmospheric reactions of isoprene and NOx. *International Journal of Chemical Kinetics* 1996, 28, 497-530.
2. Atkinson, R.; Aschmann, S. M.; Arey, J.; Carter, W. P. L., Formation of ring-retaining products from the OH radical-initiated reactions of benzene and toluene. *International Journal of Chemical Kinetics* 1989, 21, 801-827.
3. Tuazon, E. C.; Macleod, H.; Atkinson, R.; Carter, W. P. L., Alpha-dicarbonyl yields from the NOx-air photooxidations of a series of aromatic-hydrocarbons in air. *Environmental Science & Technology* 1986, 20, 383-387.
4. Tuazon, E. C.; Atkinson, R.; Macleod, H.; Biermann, H. W.; Winer, A. M.; Carter, W. P. L.; Pitts, J. N., Yields of glyoxal and methylglyoxal from the NOx-air photooxidations of toluene and m-xylene and p-xylene. *Environmental Science & Technology* 1984, 18, 981-984.
5. Glowacki, D. R.; Lockhart, J.; Blitz, M. A.; Klippenstein, S. J.; Pilling, M. J.; Robertson, S. H.; Seakins, P. W., Interception of Excited Vibrational Quantum States by O₂ in Atmospheric Association Reactions. *Science* 2012, 337, 1066-1069.
6. Hatakeyama, S.; Washida, N.; Akimoto, H., Rate constants and mechanisms for the reaction of OH (OD) radicals with acetylene, propyne, and 2-butyne in air at 297 +/- 2K. *Journal of Physical Chemistry* 1986, 90, 173-178.
7. Schmidt, V.; Zhu, G. Y.; Becker, K. H.; Fink, E. H., Study of OH reactions at high-pressures by excimer laser photolysis - dye laser fluorescence *Berichte Der Bunsen-Gesellschaft-Physical Chemistry Chemical Physics* 1985, 89, 321-322.
8. Hastings, W. P.; Koehler, C. A.; Bailey, E. L.; De Haan, D. O., Secondary organic aerosol formation by glyoxal hydration and oligomer formation: Humidity effects and equilibrium shifts during analysis. *Environmental Science & Technology* 2005, 39, 8728-8735.
9. Kroll, J. H.; Ng, N. L.; Murphy, S. M.; Varutbangkul, V.; Flagan, R. C.; Seinfeld, J. H., Chamber studies of secondary organic aerosol growth by reactive uptake of simple carbonyl compounds. *Journal of Geophysical Research-Atmospheres* 2005, 110.
10. Liggio, J.; Li, S. M.; McLaren, R., Reactive uptake of glyoxal by particulate matter. *Journal of Geophysical Research-Atmospheres* 2005, 110.
11. Salter, R. J.; Blitz, M. A.; Heard, D. E.; Kovacs, T.; Pilling, M. J.; Rickard, A. R.; Seakins, P. W., Quantum yields for the photolysis of glyoxal below 350 nm and parameterisations for its photolysis rate in the troposphere. *Physical Chemistry Chemical Physics* 2013, 15, 4984-4994.
12. Salter, R. J.; Blitz, M. A.; Heard, D. E.; Pilling, M. J.; Seakins, P. W., New Chemical Source of the HCO Radical Following Photoexcitation of Glyoxal, (HCO)₂. *Journal of Physical Chemistry A* 2009, 113, 8278-8285.
13. Salter, R. J.; Blitz, M. A.; Heard, D. E.; Pilling, M. J.; Seakins, P. W., Pressure and temperature dependent photolysis of glyoxal in the 355-414 nm region: evidence for dissociation from multiple states. *Physical Chemistry Chemical Physics* 2013, 15, 6516-6526.
14. Wittrock, F.; Richter, A.; Oetjen, H.; Burrows, J. P.; Kanakidou, M.; Myriokefalitakis, S.; Volkamer, R.; Beirle, S.; Platt, U.; Wagner, T., Simultaneous global observations of glyoxal and formaldehyde from space. *Geophysical Research Letters* 2006, 33.
15. Volkamer, R.; Molina, L. T.; Molina, M. J.; Shirley, T.; Brune, W. H., DOAS measurement of glyoxal as an indicator for fast VOC chemistry in urban air. *Geophysical Research Letters* 2005, 32.
16. Feierabend, K. J.; Flad, J. E.; Brown, S. S.; Burkholder, J. B., HCO Quantum Yields in the Photolysis of HC(O)C(O)H (Glyoxal) between 290 and 420 nm. *Journal of Physical Chemistry A* 2009, 113, 7784-7794.

17. Feierabend, K. J.; Zhu, L.; Talukdar, R. K.; Burkholder, J. B., Rate Coefficients for the OH+HC(O)C(O)H (glyoxal) Reaction between 210 and 390. *Journal of Physical Chemistry A* 2008, 112, 73-82.
18. Fu, T. M.; Jacob, D. J.; Wittrock, F.; Burrows, J. P.; Vrekoussis, M.; Henze, D. K., Global budgets of atmospheric glyoxal and methylglyoxal, and implications for formation of secondary organic aerosols. *Journal of Geophysical Research-Atmospheres* 2008, 113.
19. Niki, H.; Maker, P. D.; Savage, C. M.; Breitenbach, L. P., An FTIR study of the Cl-atom initiated reaction of glyoxal. *International Journal of Chemical Kinetics* 1985, 17, 547-558.
20. Orlando, J. J.; Tyndall, G. S., The atmospheric chemistry of the HC(O)CO radical. *International Journal of Chemical Kinetics* 2001, 33, 149-156.
21. da Silva, G., Hydroxyl radical regeneration in the photochemical oxidation of glyoxal: kinetics and mechanism of the HC(O)CO + O₂ reaction. *Physical Chemistry Chemical Physics* 2010, 12, 6698-6705.
22. Setokuchi, O., Trajectory calculations of OH radical- and Cl atom-initiated reaction of glyoxal: atmospheric chemistry of the HC(O)CO radical. *Physical Chemistry Chemical Physics* 2011, 13, 6296-6304.
23. Carslaw, N.; Creasey, D. J.; Harrison, D.; Heard, D. E.; Hunter, M. C.; Jacobs, P. J.; Jenkin, M. E.; Lee, J. D.; Lewis, A. C.; Pilling, M. J.; Saunders, S. M.; Seakins, P. W., OH and HO₂ radical chemistry in a forested region of north-western Greece. *Atmospheric Environment* 2001, 35, 4725-4737.
24. Ren, X. R.; Olson, J. R.; Crawford, J. H.; Brune, W. H.; Mao, J. Q.; Long, R. B.; Chen, Z.; Chen, G.; Avery, M. A.; Sachse, G. W.; Barrick, J. D.; Diskin, G. S.; Huey, L. G.; Fried, A.; Cohen, R. C.; Heikes, B.; Wennberg, P. O.; Singh, H. B.; Blake, D. R.; Shetter, R. E., HOx chemistry during INTEX-A 2004: Observation, model calculation, and comparison with previous studies. *Journal of Geophysical Research-Atmospheres* 2008, 113.
25. Pugh, T. A. M.; MacKenzie, A. R.; Hewitt, C. N.; Langford, B.; Edwards, P. M.; Furneaux, K. L.; Heard, D. E.; Hopkins, J. R.; Jones, C. E.; Karunaharan, A.; Lee, J.; Mills, G.; Misztal, P.; Moller, S.; Monks, P. S.; Whalley, L. K., Simulating atmospheric composition over a South-East Asian tropical rainforest: performance of a chemistry box model. *Atmospheric Chemistry and Physics* 2010, 10, 279-298.
26. Whalley, L. K.; Edwards, P. M.; Furneaux, K. L.; Goddard, A.; Ingham, T.; Evans, M. J.; Stone, D.; Hopkins, J. R.; Jones, C. E.; Karunaharan, A.; Lee, J. D.; Lewis, A. C.; Monks, P. S.; Moller, S. J.; Heard, D. E., Quantifying the magnitude of a missing hydroxyl radical source in a tropical rainforest. *Atmospheric Chemistry and Physics* 2011, 11, 7223-7233.
27. MacDonald, S. M.; Oetjen, H.; Mahajan, A. S.; Whalley, L. K.; Edwards, P. M.; Heard, D. E.; Jones, C. E.; Plane, J. M. C., DOAS measurements of formaldehyde and glyoxal above a south-east Asian tropical rainforest. *Atmospheric Chemistry and Physics* 2012, 12, 5949-5962.
28. Peeters, J.; Nguyen, T. L.; Vereecken, L., HOx radical regeneration in the oxidation of isoprene. *Physical Chemistry Chemical Physics* 2009, 11, 5935-5939.
29. Taraborrelli, D.; Lawrence, M. G.; Crowley, J. N.; Dillon, T. J.; Gromov, S.; Gross, C. B. M.; Vereecken, L.; Lelieveld, J., Hydroxyl radical buffered by isoprene oxidation over tropical forests. *Nature Geoscience* 2012, 5, 190-193.
30. Wolfe, G. M.; Crouse, J. D.; Parrish, J. D.; St. Clair, J. M.; Beaver, M. R.; Paulot, F.; Yoon, T. P.; Wennberg, P. O.; Keutsch, F. N., Photolysis, OH reactivity and ozone reactivity of a proxy for isoprene-derived hydroperoxyenals (HPALDs). *Physical Chemistry Chemical Physics* 2012, 14, 7276-7286.
31. Fuchs, H.; Bohn, B.; Hofzumahaus, A.; Holland, F.; Lu, K. D.; Nehr, S.; Rohrer, F.; Wahner, A., Detection of HO₂ by laser-induced fluorescence: calibration and interferences from RO₂ radicals. *Atmospheric Measurement Techniques* 2011, 4, 1209-1225.
32. Stone, D.; Whalley, L. K.; Heard, D. E., Tropospheric OH and HO₂ radicals: field measurements and model comparisons. *Chemical Society Reviews* 2012, 41, 6348-6404.

33. Volkamer, R.; Spietz, P.; Burrows, J.; Platt, U., High-resolution absorption cross-section of glyoxal in the UV-vis and IR spectral ranges. *Journal of Photochemistry and Photobiology A: Chemistry* 2005, 172, 35-46.
34. Plum, C. N.; Sanhueza, E.; Atkinson, R.; Carter, W. P. L.; Pitts, J. N., OH radical rate constants and photolysis rates of alpha-dicarbonyls *Environmental Science & Technology* 1983, 17, 479-484.
35. Ianni, J. C., Kintecus, Windows Version 2.80, 2002, www.kintecus.com.
36. Ghosh, B.; Papanastasiou, D. K.; Burkholder, J. B., Oxalyl chloride, ClC(O)C(O)Cl: UV/vis spectrum and Cl atom photolysis quantum yields at 193, 248, and 351 nm. *Journal of Chemical Physics* 2012, 137.
37. Lockhart, J.; Blitz, M. A.; Heard, D. E.; Seakins, P. W.; Shannon, R. J., Mechanism of the Reaction of OH with Alkynes in the Presence of Oxygen. *Journal of Physical Chemistry A* 2013, 117, 5407-5418.
38. Romero, M. T. B.; Blitz, M. A.; Heard, D. E.; Pilling, M. J.; Price, B.; Seakins, P. W., OH formation from the C₂H₅CO+O₂ reaction: An experimental marker for the propionyl radical. *Chemical Physics Letters* 2005, 408, 232-236.
39. Siese, M.; Zetzsch, C. Addition of OH to Acetylene and Consecutive Reactions of the Adduct with O₂. Part 1-2, 1995.
40. DeSain, J. D.; Jusinski, L. E.; Ho, A. D.; Taatjes, C. A., Temperature dependence and deuterium kinetic isotope effects in the HCO(DCO)+O₂ reaction between 296 and 673 K. *Chemical Physics Letters* 2001, 347, 79-86.
41. Pilling, M. J.; Seakins, P. W., *Reaction kinetics*. Oxford University Press: Oxford, 1995; p xiii,305p.
42. Glowacki, D. R.; Liang, C. H.; Morley, C.; Pilling, M. J.; Robertson, S. H., MESMER: An Open-Source Master Equation Solver for Multi-Energy Well Reactions. *Journal of Physical Chemistry A* 2012, 116, 9545-9560.
43. Baeza-Romero, M. T.; Glowacki, D. R.; Blitz, M. A.; Heard, D. E.; Pilling, M. J.; Rickard, A. R.; Seakins, P. W., A combined experimental and theoretical study of the reaction between methylglyoxal and OH/OD radical: OH regeneration. *Physical Chemistry Chemical Physics* 2007, 9, 4114-4128.
44. Polanyi, J. C., Some concepts in reaction dynamics *Science* 1987, 236, 680-690.
45. Mereau, R.; Rayez, M. T.; Rayez, J. C.; Caralp, F.; Lesclaux, R., Theoretical study on the atmospheric fate of carbonyl radicals: kinetics of decomposition reactions. *Physical Chemistry Chemical Physics* 2001, 3, 4712-4717.
46. Blitz, M. A.; Heard, D. E.; Pilling, M. J., OH formation from CH₃CO+O₂: a convenient experimental marker for the acetyl radical. *Chemical Physics Letters* 2002, 365, 374-379.
47. Carr, S. A.; Glowacki, D. R.; Liang, C. H.; Baeza-Romero, M. T.; Blitz, M. A.; Pilling, M. J.; Seakins, P. W., Experimental and Modeling Studies of the Pressure and Temperature Dependences of the Kinetics and the OH Yields in the Acetyl + O₂ Reaction. *Journal of Physical Chemistry A* 2011, 115, 1069-1085.
48. Jagiella, S.; Zabel, F., Thermal stability of carbonyl radicals - Part II. Reactions of methylglyoxyl and methylglyoxylperoxy radicals at 1 bar in the temperature range 275-311 K. *Physical Chemistry Chemical Physics* 2008, 10, 1799-1808.
49. Saunders, S. M.; Jenkin, M. E.; Derwent, R. G.; Pilling, M. J., Protocol for the development of the Master Chemical Mechanism, MCM v3 (Part A): tropospheric degradation of non-aromatic volatile organic compounds. *Atmospheric Chemistry and Physics* 2003, 3, 161-180.
50. Dillon, T. J.; Crowley, J. N., Direct detection of OH formation in the reactions of HO₂ with CH₃C(O)O₂ and other substituted peroxy radicals. *Atmospheric Chemistry and Physics* 2008, 8, 4877-4889.

51. Hasson, A. S.; Tyndall, G. S.; Orlando, J. J., A product yield study of the reaction of HO₂ radicals with ethyl peroxy (C₂H₅O₂), acetyl peroxy (CH₃C(O)O₂), and acetonyl peroxy (CH₃C(O)CH₂O₂) radicals. *Journal of Physical Chemistry A* 2004, 108, 5979-5989.

Chapter 7 Some Known and Novel HCO Chemistry

7.1 Abstract

In the final experimental chapter of this thesis a laser system is developed to detect the formyl, HCO, radical. The system was characterised by measuring room temperature rate coefficients for the reactions of HCO with O₂, NO and NO₂, and for the reaction of chlorine atoms with glyoxal, (HCO)₂. Bimolecular rate coefficients for the reactions of HCO with O₂ and NO were measured in 10 and 30 Torr of nitrogen, and were found independent of pressure with respective values of $(5.27 \pm 0.01) \times 10^{-12} \text{ cm}^3 \text{ molecule}^{-1} \text{ s}^{-1}$ and $(1.30 \pm 0.03) \times 10^{-11} \text{ cm}^3 \text{ molecule}^{-1} \text{ s}^{-1}$. The HCO + NO₂ reaction was studied under 10 Torr of nitrogen with a room temperature rate coefficient of $(6.99 \pm 0.16) \times 10^{-11} \text{ cm}^3 \text{ molecule}^{-1} \text{ s}^{-1}$. The kinetics of the Cl + (HCO)₂ reaction were studied directly for the first time with a rate coefficient of $(3.88 \pm 0.12) \times 10^{-11} \text{ cm}^3 \text{ molecule}^{-1} \text{ s}^{-1}$ measured at 295 K under 5 Torr of nitrogen. All the room temperature rate coefficient measurements based on HCO detection were found to be in good agreement with existing literature values.

Experimental attempts were made to quantify the rate of thermal decomposition of the HC(O)CO radical produced following the reaction of Cl atoms with (HCO)₂. However, at the low temperatures required by these experiments ($T = 220 \text{ K}$), rapid HCO removal was observed. Further experiments provided evidence that HCO reacts rapidly with a range of aldehyde species. Quantitative kinetic studies focused on the reactions of HCO with formaldehyde, HCHO, and acetaldehyde, CH₃CHO. The HCO kinetics associated with the HCO + HCHO reaction were studied at 212 K in 10 and 30 Torr of nitrogen, and were found independent of pressure with a rate coefficient of $(3.44 \pm 0.15) \times 10^{-11} \text{ cm}^3 \text{ molecule}^{-1} \text{ s}^{-1}$. The rate coefficient for the reaction of HCO with CH₃CHO was measured at 212 K in 10 Torr of nitrogen with a value of $(1.24 \pm 0.05) \times 10^{-11} \text{ cm}^3 \text{ molecule}^{-1} \text{ s}^{-1}$. Significant HCO removal rates were not observed in the presence of either aldehyde at higher temperatures suggesting that the thermally unstable HC(O)CO radical is a likely product of both reactions.

7.2 Background

The formyl radical, HCO, is an important species for atmospheric,¹ combustion,² and interstellar chemistry.³ It is produced extensively in the troposphere following the radical propagating oxidation of anthropogenic and biogenic hydrocarbons;⁴⁻⁶ and also produced directly through aldehyde photolysis.^{7, 8} The only significant loss process for HCO in the troposphere is through reaction with oxygen (R1):¹



HCO is a key intermediate in hydrocarbon combustion, and can be removed through thermal decomposition (R2) or bimolecular reactions with oxygen (R1), OH radical (R3), or hydrogen atoms (R4):⁹



The chain branching reaction of hydrogen atoms (R5) with oxygen is of central importance to combustion chemistry:



Thermal decomposition of HCO generates hydrogen atoms (R2) and is therefore chain propagating, while bimolecular reactions (R1, R3 and R4) are chain terminating. Therefore the competition between the unimolecular and bimolecular reaction channels of HCO will control the chain branching rate, and consequently influence a number of important characteristics of combustion, such as the autoignition thresholds and delays.¹⁰ Development in the scientific understanding of combustion phenomena requires complex combustion models, which in turn rely on detailed kinetic mechanisms. Improvements in the efficiency of combustion processes require detailed chemical kinetic mechanisms with well characterised elementary reactions.

The HCO radical has also been detected in the interstellar medium and dense clouds.¹¹ Recent theoretical work has suggested the chemistry of this radical may provide a

means of generating more complex organic molecules such as amino acids and simple sugars in these environments.^{12, 13}

Gas-phase spectroscopic detection techniques for the HCO radical are desirable owing to its importance in both atmospheric and combustion chemistry. Ramsay and co-workers were first to detect the HCO radical in the early 1950s, using conventional absorption in the visible spectral region.^{14, 15} Since then various laser based methods have been used to probe the A – X system, including intracavity dye laser absorption (IDLA) spectroscopy,¹⁶⁻¹⁸ resonance enhanced multiphoton ionisation (REMPI),¹⁹ cavity ring-down spectroscopy (CRDS),²⁰ and degenerate four-wave mixing techniques.²¹ Laser induced fluorescence (LIF) has also been used for this system,^{22, 23} but rapid predissociation of the A state results in a very low fluorescence quantum yield. Fortunately, the development of non-linear optic technologies (specifically beta barium borate (BBO) crystals in the 1990s), has made shorter wavelength laser radiation accessible, allowing LIF measurements of HCO in the B – X system. Several experimental studies have monitored HCO using off-resonance LIF in the B – X system, following excitation at approximately 258 nm.²⁴⁻²⁷

The Dainton Laboratory at the University of Leeds routinely use laser flash photolysis coupled with LIF detection of OH to study the kinetics and mechanisms of reactions relevant to atmospheric and combustion chemistry. In this chapter a laser system was developed in order to detect HCO directly using the laser flash photolysis, laser induced fluorescence (LFP-LIF) technique. The system was tested by measuring well established rate coefficients for the reactions of HCO with O₂, NO and NO₂. The aim of this work was to build on the work presented in Chapter 6 and use the LFP-LIF technique to monitor the HCO produced following the reaction of OH with glyoxal, (HCO)₂ (R6), and to then quantify the rate of HC(O)CO decomposition experimentally for the first time as a function of pressure (R7):



7.3 Experimental

This work has been carried using conventional slow-flow, laser flash photolysis, laser induced fluorescence apparatus. Experiments were conducted using the same stainless steel, 6-way cross reactor described in chapter 3. The flows of radical precursor, co-reagent, and nitrogen (used as bath gas), were regulated via calibrated mass flow controllers, and introduced into the reactor through a mixing manifold. HCO was generated by pulsed excimer laser (Lambda Physik Compex) 248 nm photolysis of either glyoxal (P1), or oxalyl chloride (P2) in the presence of formaldehyde (R8):



HCO was detected by off-resonant LIF in the (B – X) system following excitation at ~258 nm. The fluorescence was filtered through a Schott glass filter (250 ± 10 nm) and observed using a photomultiplier tube (PMT) mounted perpendicular to the planes of both the photolysis and probe laser beams. Probe radiation was generated using the doubled output of an excimer (Lambda Physik, LPX 100, XeCl, 308 nm) pumped dye laser (Lambda Physik, FL 2002) operating on Coumarin 307 dye. An interference filter (248 ± 10 nm) was placed between the reactor window and the PMT in order to avoid bleaching the PMT with probe radiation. The PMT output was digitized and transferred to a personal computer for analysis. The time delay between the photolysis and probe laser pulses was controlled using LabVIEW and was varied to build up a temporal profile for the HCO radical. Kinetic traces were typically 200 – 400 data points each averaged 2 – 10 times depending on the signal-to-noise ratio.

The formaldehyde, HCHO, was prepared by pyrolysis of paraformaldehyde, without further purification, passed into a glass sample bulb and diluting in pure nitrogen. Formaldehyde sample bulbs were typically used within two days of preparation. NO and NO₂ were purified prior to use by several freeze-pump-thaw cycles in liquid nitrogen, then transferred to an evacuated blackened glass sample bulb on a vacuum line, and diluted in nitrogen. The concentration of NO or NO₂ in each sample bulb was determined barometrically. Glyoxal was prepared using the method described in chapter 6, and diluted in nitrogen on a glass vacuum line. The concentration of glyoxal in each sample bulb was determined by UV-vis absorption spectroscopy.

Materials: nitrogen (BOC oxygen free), oxygen (Air Products, high purity, 99.999%), paraformaldehyde (Sigma Aldrich, 95%), acetaldehyde (Sigma Aldrich, > 99.5%), acetone (Sigma Aldrich, > 99.9%), carbon monoxide (Argo International Ltd, 99.5%), nitric oxide (BOC Special gases, 99.5%), nitrogen dioxide (Sigma Aldrich, 99.5%), oxalyl chloride (Sigma Aldrich, ≥ 99%), chloroform (Sigma Aldrich, ≥ 99.8%), glyoxal trimer dehydrate (Sigma Aldrich, ≥ 95%) and phosphorus pentoxide (Sigma Aldrich, ≥ 98.5%).

7.4 Room temperature kinetics of the Reactions of HCO with O₂, NO and NO₂

Room temperature rate coefficients were measured for the reactions of HCO with oxygen (R1), NO (R9) and NO₂ (R10) by monitoring the HCO decay by LIF under *pseudo-first-order* conditions in HCO, using nitrogen bath gas at total pressures of 10 and 30 Torr. HCO radicals were generated by the reaction of chlorine atoms with formaldehyde (R8), with chlorine atoms formed following 248 nm photolysis of oxalyl chloride (P2).





Following the near instant growth through reaction R8, HCO decays exponentially in the presence of excess O₂ and NO (see inset of Figures 1 and 2), with a decay coefficient dependent on its rate of reaction with the experimental co-reagent and its rate of diffusion from the probed region of the reactor (R11):



Pseudo-first-order HCO decay coefficients were measured by fitting the decay component of the experimental HCO profile in the presence of excess O₂ or NO using equation E1:

$$I_f(t) = I_f(0) \exp^{-k't} \quad (\text{E1})$$

where $I_f(0)$ and $I_f(t)$ are HCO signal intensities at time 0 and time t , respectively; and k' is the observed *pseudo-first-order* rate coefficient ($k' = k[\text{co-reagent}] + k_{11}$).

In the presence of excess NO₂, HCO removal is governed by its reaction with NO₂ (R2) and diffusion from the probed region of the reactor (R11). The reaction of HCO with NO₂ is known to generate OH radicals (R10d) and hydrogen atoms (R10a),²⁹ with the latter rapidly converted to OH in excess NO₂ (R12):³⁰



The OH produced will react with HCHO and provide a secondary source of HCO (R13), resulting in biexponential HCO decay traces in the presence of excess NO₂:



Consequently, *pseudo-first-order* HCO decay coefficients were measured by fitting the decay component of the experimental HCO traces in the presence of NO₂ using equation E2:

$$[\text{HCO}]_t = \frac{[\text{HCO}]_0 (S - L_2)}{(L_1 - L_2)} (e^{L_1 t} - e^{L_2 t}) + [\text{HCO}]_0 e^{L_2 t} \quad (\text{E2})$$

where:

$$S = - (k'_2 + k_{11})$$

$$M_1 = (k'_2 + k_{11} + k'_{12})$$

$$M_2 = k'_{12}(k'_2 + k_{11}) - (k'_2 k_{11})$$

$$L_1 = \frac{-M_1 + \sqrt{(M_1)^2 - 4M_2}}{2}$$

$$L_2 = \frac{-M_1 - \sqrt{(M_1)^2 - 4M_2}}{2}$$

7.4.1 Kinetics of the Reactions of HCO with O₂ and NO

Bimolecular rate coefficients measured for reactions R1 and R9 were found to be independent of pressure using nitrogen bath gas at total pressures of 10 and 30 Torr, consistent with both reactions proceeding via hydrogen atom abstraction. Bimolecular plots showing all *pseudo-first-order* decay measurements across this experimental pressure range are presented in Figures 1 and 2. Linear least squares analysis of each data set yields room temperature k_1 and k_9 values of $(5.27 \pm 0.01) \times 10^{-12} \text{ cm}^3 \text{ molecule}^{-1} \text{ s}^{-1}$ and $(1.30 \pm 0.03) \times 10^{-11} \text{ cm}^3 \text{ molecule}^{-1} \text{ s}^{-1}$, respectively, where the quoted errors are purely statistical at the 2σ level.

Reaction R1 has been studied extensively elsewhere owing to its importance to both atmospheric and combustion chemistry. The majority of direct kinetic measurements of reaction R1 report k_1 values ranging between $(4 - 6) \times 10^{-12} \text{ cm}^3 \text{ molecule}^{-1} \text{ s}^{-1}$ at room temperature. Gill et al. generated HCO by flash photolysis of acetaldehyde and monitored its decay in the presence of oxygen using IDLA spectroscopy.¹⁸ These authors reported a k_1 value of $(4.2 \pm 0.7) \times 10^{-12} \text{ cm}^3 \text{ molecule}^{-1} \text{ s}^{-1}$ at 298 K. More recently, DeSain and co-workers investigated the kinetics of reaction R1 in 8 to 30 Torr of helium using laser flash photolysis and laser induced fluorescence (LIF) HCO detection.²⁴ These authors generated HCO using a variety of sources (photolytic and chemical), and reported a k_1 value of $(5.63 \pm 0.31) \times 10^{-12} \text{ cm}^3 \text{ molecule}^{-1} \text{ s}^{-1}$ at 296 K.

Several publications in the literature include kinetic studies of both reaction R1 and R9. Shibuya et al. used flash photolysis of acetaldehyde as HCO source and measured room

temperature bimolecular rate coefficients for reactions R1 and R9 by monitoring HCO directly via vis-UV absorption spectroscopy.³¹ Their study reported k_1 and k_9 values of (5.6 ± 0.9) and $(8.5 \pm 1.0) \times 10^{-12} \text{ cm}^3 \text{ molecule}^{-1} \text{ s}^{-1}$, respectively.

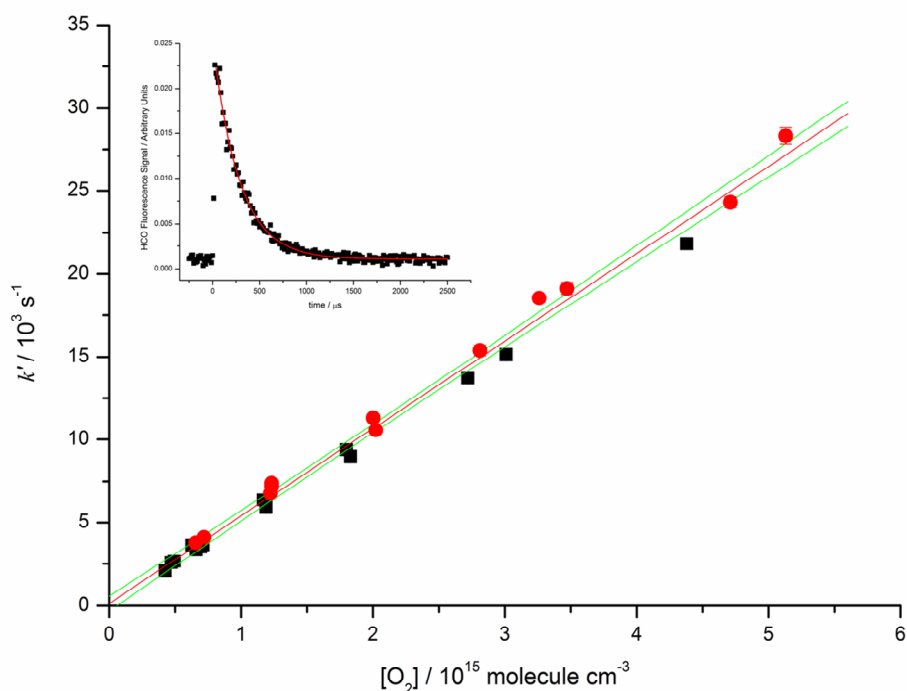


Figure 1: Bimolecular plot for the HCO + O₂ reaction at 295 K and 10 (■) and 30 Torr (●) total pressure using N₂ bath gas corresponding to a k_1 value of $(5.27 \pm 0.01) \times 10^{-12} \text{ cm}^3 \text{ molecule}^{-1} \text{ s}^{-1}$. A typical experimental HCO decay trace is included in the inset, measured in the presence of $6.95 \times 10^{14} \text{ molecule cm}^{-3}$ of O₂ and corresponding to a *pseudo-first-order* decay constant of $(3550 \pm 50) \text{ s}^{-1}$.

Reilly and co-workers investigated reactions R1 and R9 by photolysing formaldehyde to generate HCO and then monitoring the decay in the presence of O₂ and NO using the IDLA technique.³² The analysis of these authors yielded k_1 and k_9 values of $(4.0 \pm 0.8) \times 10^{-12} \text{ cm}^3 \text{ molecule}^{-1} \text{ s}^{-1}$ and $(1.4 \pm 0.2) \times 10^{-11} \text{ cm}^3 \text{ molecule}^{-1} \text{ s}^{-1}$, respectively, at room temperature in 10 Torr of pure formaldehyde. Veyret and Lesclaux measured rate coefficients for reactions R1 and R9 using flash photolysis of formaldehyde or acetaldehyde as HCO source, and monitored the radical via extracavity dye laser absorption spectroscopy (EAS).³³ These authors measured k_1 and k_9 at 298 K in 45 and 500 Torr of nitrogen and

reported values of $(5.6 \pm 0.6) \times 10^{-12} \text{ cm}^3 \text{ molecule}^{-1} \text{ s}^{-1}$ and $(1.23 \pm 0.12) \times 10^{-11} \text{ cm}^3 \text{ molecule}^{-1} \text{ s}^{-1}$, respectively, independent of total pressure.

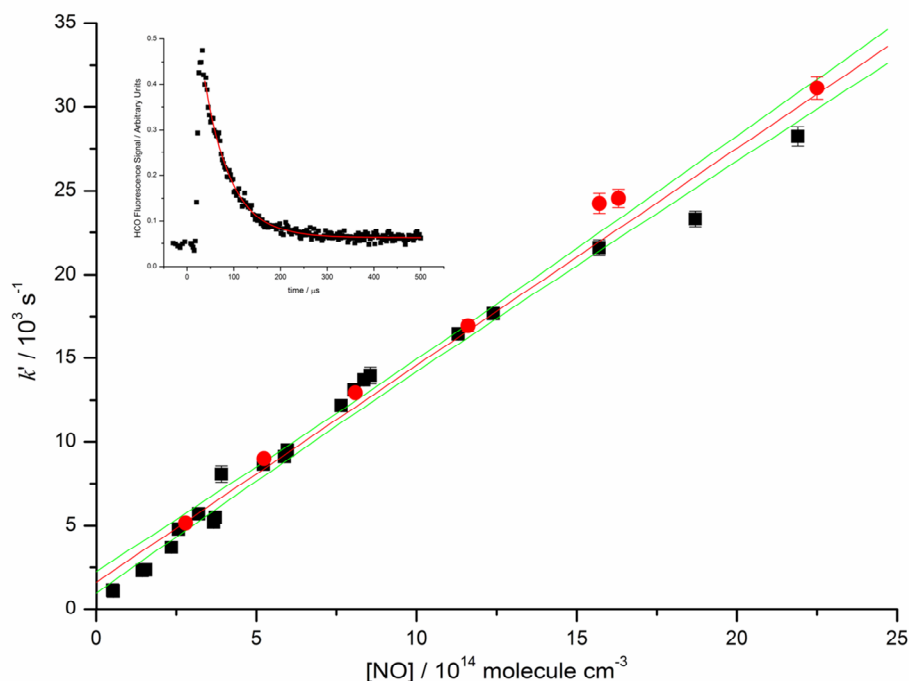


Figure 2: Bimolecular plot for the HCO + NO reaction at 295 K and 10 (■) and 30 Torr (●) total pressure using N₂ bath gas corresponding to a k_9 value of $(12.96 \pm 0.29) \times 10^{-12} \text{ cm}^3 \text{ molecule}^{-1} \text{ s}^{-1}$. A typical experimental HCO decay trace is included in the inset, measured in the presence of $1.24 \times 10^{15} \text{ molecule cm}^{-3}$ of NO and corresponding to a *pseudo-first-order* decay constant of $(17655 \pm 300) \text{ s}^{-1}$.

More recently, Nesbitt and co-workers investigated the kinetics of reactions R1 and R9 using a discharge flow system equipped with photoionization mass spectrometry (PIMS) at 298 K under 1 Torr of helium.³⁴ Their study measured k_1 and k_9 values of $(4.0 \pm 0.6) \times 10^{-12} \text{ cm}^3 \text{ molecule}^{-1} \text{ s}^{-1}$ and $(1.3 \pm 0.2) \times 10^{-11} \text{ cm}^3 \text{ molecule}^{-1} \text{ s}^{-1}$, respectively. Ninomiya et al. also studied the kinetics of reactions R1 and R9 under 4 to 10 Torr of nitrogen at 298 K using pulsed photolysis of acetaldehyde to generate HCO and cavity ring-down spectroscopy (CRDS) to monitor the radical.²⁰ These authors reported k_1 and k_9 values of $(5.9 \pm 0.5) \times 10^{-12} \text{ cm}^3 \text{ molecule}^{-1} \text{ s}^{-1}$ and $(1.9 \pm 0.2) \times 10^{-11} \text{ cm}^3 \text{ molecule}^{-1} \text{ s}^{-1}$, respectively.

Nadtochenko et al. studied reaction R9 at room temperature using flash photolysis of acetaldehyde coupled with IDLA radical detection.³⁵ The bimolecular rate coefficient, k_9 , was measured as $(1.2 \pm 0.4) \times 10^{-11} \text{ cm}^3 \text{ molecule}^{-1} \text{ s}^{-1}$ in pure acetaldehyde at total pressures ranging from 20 to 90 Torr. DeSain and co-workers investigated reaction R9 using the laser flash photolysis, CW LIF method.²⁵ These authors generated HCO both photolytically and chemically during their study, and reported a k_9 value of $(1.81 \pm 0.10) \times 10^{-11} \text{ cm}^3 \text{ molecule}^{-1} \text{ s}^{-1}$ at 296 K under 10 Torr of helium. In a kinetic study by Dammeier et al., k_9 was measured at room temperature in 40 Torr of argon using a slow flow reactor equipped with frequency modulation (FM) spectroscopy, with HCO generated by excimer laser photolysis of glyoxal at 193 nm.³⁶ These authors reported a k_9 value of $1.35 \times 10^{-11} \text{ cm}^3 \text{ molecule}^{-1} \text{ s}^{-1}$ under their experimental conditions.

With the exception of the early study by Shibuya et al.,³¹ all previous experimental investigations of the HCO + NO reaction report room temperature k_9 values ranging between $(1.2 - 1.9) \times 10^{-11} \text{ cm}^3 \text{ molecule}^{-1} \text{ s}^{-1}$, consistent with the $(1.30 \pm 0.03) \times 10^{-11} \text{ cm}^3 \text{ molecule}^{-1} \text{ s}^{-1}$ value measured here. The room temperature k_1 value of $(5.27 \pm 0.01) \times 10^{-12} \text{ cm}^3 \text{ molecule}^{-1} \text{ s}^{-1}$ reported here lies in excellent agreement with the value of $(5.1 \pm 0.15) \times 10^{-12} \text{ cm}^3 \text{ molecule}^{-1} \text{ s}^{-1}$ recently recommended by IUPAC³⁷ and with the existing literature values, and gives confidence in the experimental HCO detection system.

7.4.2 Kinetic Study of the HCO + NO₂ Reaction

The room temperature rate coefficient for the HCO + NO₂ reaction has been measured in 10 Torr of nitrogen using laser flash photolysis coupled with LIF HCO detection. HCO was again generated by the reaction of chlorine atoms with formaldehyde, with chlorine atoms generated by 248 nm excimer photolysis of oxalyl chloride (P2). The resulting biexponential HCO decay traces recorded in excess NO₂ were fit using equation E2. Linear least squares analysis of the fast *pseudo-first-order* decay coefficients measured, plotted against the NO₂ concentration yields a k_{10} value of $(6.99 \pm 0.16) \times 10^{-11} \text{ cm}^3 \text{ molecule}^{-1} \text{ s}^{-1}$ (Figure 3).

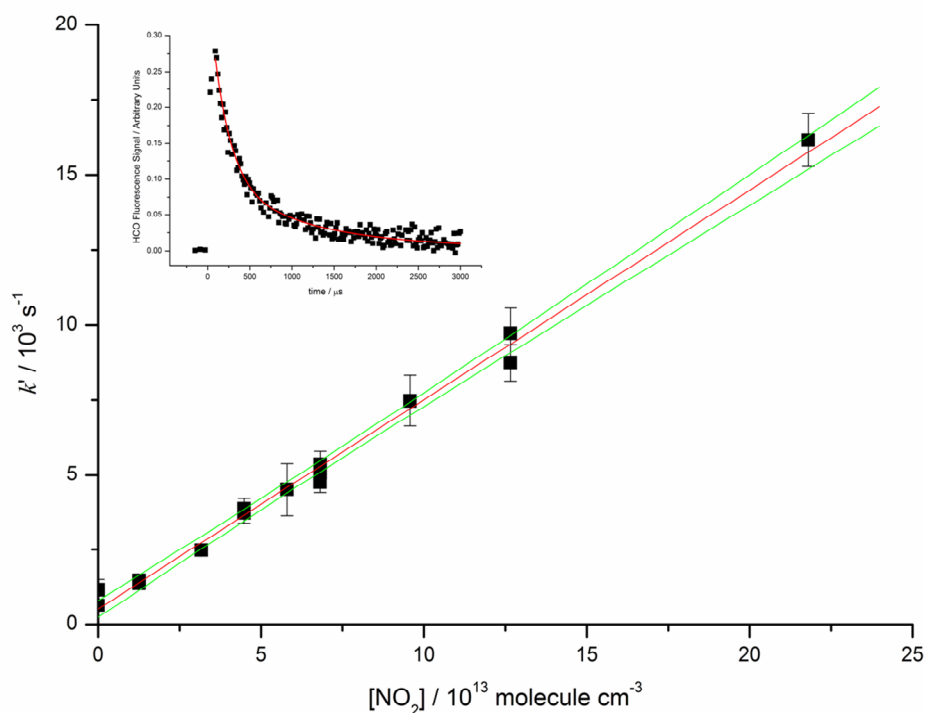


Figure 3: Bimolecular plot for the $\text{HCO} + \text{NO}_2 \rightarrow \text{Products}$ reaction at 295 K under 10 Torr of N_2 , corresponding to a k_{10} value of $(6.99 \pm 0.16) \times 10^{-11} \text{ cm}^3 \text{ molecule}^{-1} \text{ s}^{-1}$, where the error is purely statistical at the 2σ level. Included is a typical biexponential HCO decay trace measured in the presence of $4.48 \times 10^{13} \text{ molecule cm}^{-3}$ of NO_2 , corresponding to a *pseudo-first-order* HCO decay coefficient of $(3865 \pm 340) \text{ s}^{-1}$.

Several groups have studied the kinetics of reaction R10 using both direct and indirect techniques. Timonen et al. studied the kinetics of reaction R10 under *pseudo-first-order* conditions, in helium bath gas, using a flow tube equipped with a PIMS instrument, generating HCO radicals by 308 nm excimer photolysis of acetaldehyde.³⁸ These authors fit experimental HCO decay profiles using a single exponential function to obtain a room temperature k_{10} value of $5.6 \times 10^{-11} \text{ cm}^3 \text{ molecule}^{-1} \text{ s}^{-1}$. In a subsequent study, Guo and co-workers also generated HCO by excimer laser photolysis of acetaldehyde at 308 nm, and monitored HCO directly via UV-vis absorption spectroscopy under *pseudo-first-order* conditions, in up to 700 Torr of SF_6 bath gas.³⁹ These authors reported a k_{10} value of $(5.7 \pm 0.9) \times 10^{-11} \text{ cm}^3 \text{ molecule}^{-1} \text{ s}^{-1}$, where the error bar includes both statistical and estimated

systematic errors. More recently, Dammeier et al. measured k_{10} at room temperature under 40 Torr of argon in a slow flow reactor equipped with frequency modulation spectroscopy, with HCO generated by 193 nm excimer laser photolysis of glyoxal (P1).³⁶ These authors reported a k_{10} value of $(5.15 \pm 2.0) \times 10^{-11} \text{ cm}^3 \text{ molecule}^{-1} \text{ s}^{-1}$ at 295 K. The k_{10} values measured by Guo et al.³⁹ and Dammeier et al.³⁶ are both in excellent agreement with the earlier study by Timonen et al.,³⁸ and are consistent within the combined uncertainties with the $(6.99 \pm 0.16) \times 10^{-11} \text{ cm}^3 \text{ molecule}^{-1} \text{ s}^{-1}$ value reported here.

Ninomiya et al. measured k_{10} relative to their direct measurement of the rate of reaction between HCO and Cl₂ (R14) at room temperature and total pressures ranging between 4 and 10 Torr of nitrogen, using CRDS:²⁰



Their experimental k_{14} value of $(7.6 \pm 0.7) \times 10^{-12} \text{ cm}^3 \text{ molecule}^{-1} \text{ s}^{-1}$, is in good agreement with direct measurements of the same reaction by Timonen and co-workers³⁸ who reported a value of $7.2 \times 10^{-12} \text{ cm}^3 \text{ molecule}^{-1} \text{ s}^{-1}$. Ninomiya et al. measured a k_{10} value of $(6.4 \pm 0.3) \times 10^{-11} \text{ cm}^3 \text{ molecule}^{-1} \text{ s}^{-1}$, relative to their own k_{14} measurement.²⁰ The k_{10} value reported in this chapter is within 25% of both direct and indirect measurements published in the literature. The room temperature rate coefficients measured for the reactions of HCO with O₂, NO and NO₂ during this work are listed in table 1.

Reaction	Rate coefficient $k / \text{cm}^3 \text{ molecule}^{-1} \text{ s}^{-1}$
$\text{HCO} + \text{O}_2 \rightarrow \text{HO}_2 + \text{CO}$	$(5.27 \pm 0.01) \times 10^{-12}$
$\text{HCO} + \text{NO} \rightarrow \text{HNO} + \text{CO}$	$(1.30 \pm 0.03) \times 10^{-11}$
$\text{HCO} + \text{NO}_2 \rightarrow \text{Products}$	$(6.99 \pm 0.16) \times 10^{-11}$

Table 1: Room temperature rate coefficients for the reaction of HCO with O₂, NO and NO₂; the error bars are purely statistical at the 2σ level.

7.5 HC(O)CO Decomposition Kinetics

As mentioned in the introduction to this chapter, the immediate aim of developing an HCO detection system was to monitor the HCO produced from thermal dissociation of the HC(O)CO radical (R7), and to quantify the unimolecular rate coefficient k_7 from the recorded HCO growth profiles as a function of pressure and temperature. The HC(O)CO radical is produced following the reaction of glyoxal, (HCO)₂, with chlorine atoms (R15) and OH radicals (R6).^{6, 40}



Chlorine atom initiated oxidation of glyoxal is less exothermic than OH initiated oxidation, consequently less prompt fragmentation of the nascent HC(O)CO radical occurs following reaction R15 than R6. Recent trajectory calculations by Setokuchi suggested 47% of the HC(O)CO population forms following reaction R15 with sufficient energy to promptly dissociate.²⁸ In a relative rates study of the Cl + (HCO)₂ reaction, Niki et al. reported a k_{15} value of $(3.8 \pm 0.3) \times 10^{-11} \text{ cm}^3 \text{ molecule}^{-1} \text{ s}^{-1}$ at room temperature;⁴⁰ nearly a factor four faster than the OH + (HCO)₂ reaction at room temperature.⁶ The differences in the kinetics and enthalpies of reactions R15 and R6 make the anticipated prompt and slow HCO signal more easily distinguishable when generating the HC(O)CO radical through Cl-atom initiated oxidation of (HCO)₂ (R15), rather than oxidation by OH (R6).

The numerical integrator programme KINTECUS⁴¹ was used to simulate the HCO profiles following the Cl + (HCO)₂ reaction under 5 Torr of nitrogen at 295, 250 and 212 K (Figure 4); all the reactions and corresponding rate coefficients used are listed in Table 2. The model treated the Cl + (HCO)₂ reaction as independent of temperature between 295 and 212 K and used the k_{15} value of $3.8 \times 10^{-11} \text{ cm}^3 \text{ molecule}^{-1} \text{ s}^{-1}$ reported by Niki et al.⁴⁰ in each simulation. The fraction of the HC(O)CO population that promptly dissociate to HCO + CO following reaction R15 was taken from trajectory calculations by Setokuchi.²⁸ The unimolecular rate coefficients used to describe thermal dissociation of HC(O)CO were calculated using the parameters used to fit the OH yields measured as a function of temperature and pressure for the OH + (HCO)₂/O₂ system described in chapter 6.⁶

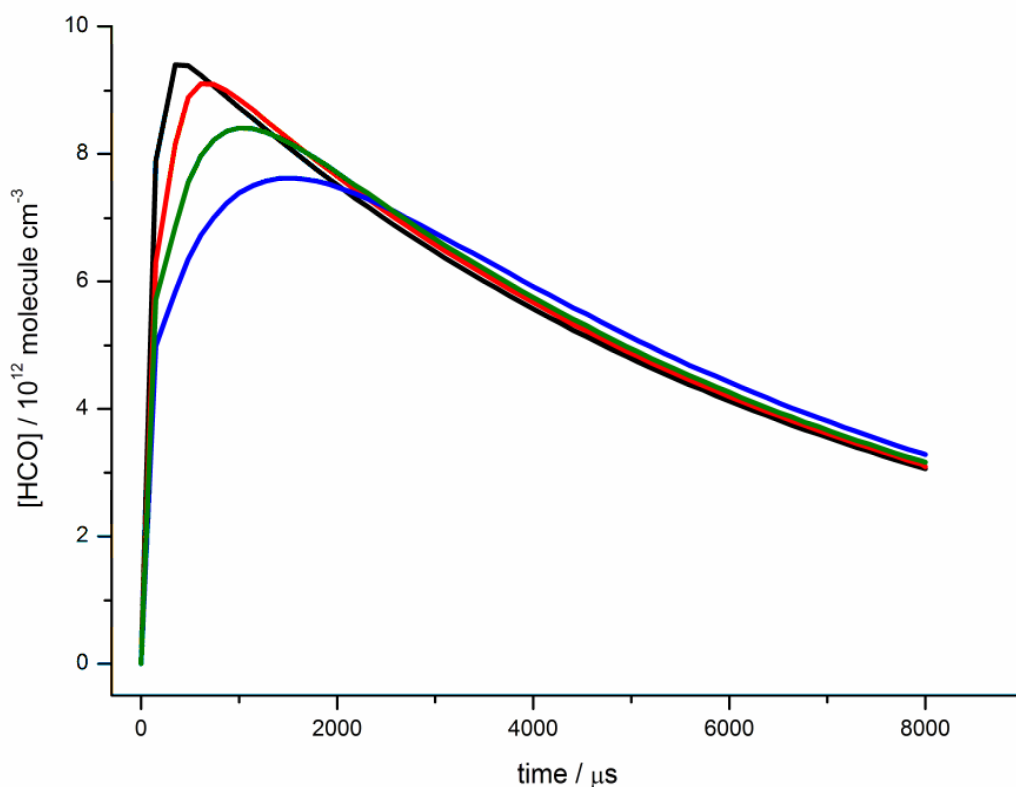


Figure 4: Simulated HCO profiles following the $\text{Cl} + (\text{HCO})_2$ reaction at 295 (black), 250 (red), and 212 K (blue) under 5 Torr of nitrogen. The green line shows the model HCO profile at 212 K under 10 Torr total pressure. These model profiles are all based on initial $(\text{HCO})_2$ and Cl-atom concentrations of 3×10^{14} molecule cm^{-3} and 1×10^{13} molecule cm^{-3} , respectively.

The HCO profiles presented in Figure 4 suggest that at room temperature and 5 Torr total pressure the HC(O)CO produced following reaction R15 dissociates too fast to distinguish the prompt and thermal HCO forming channels. However, as temperatures decrease to 250 and 212 K, the rate at which HC(O)CO thermally dissociates slows sufficiently to be able to differentiate prompt and thermal HC(O)CO decomposition.

Temperature / K	Pressure / Torr	Reaction	Rate coefficient
295	5	$\text{Cl} + (\text{HCO})_2 \rightarrow \text{HC(O)CO} + \text{HCl}$	$2.01 \times 10^{-11} \text{ cm}^3 \text{ molecule}^{-1} \text{ s}^{-1}$
		$\text{Cl} + (\text{HCO})_2 \rightarrow \text{HCO} + \text{CO} + \text{HCl}$	$1.79 \times 10^{-11} \text{ cm}^3 \text{ molecule}^{-1} \text{ s}^{-1}$
		$\text{HC(O)CO} \rightarrow \text{HCO} + \text{CO}$	91654 s^{-1}
		$\text{HCO} \rightarrow \text{loss}$	150 s^{-1}
250	5	$\text{Cl} + (\text{HCO})_2 \rightarrow \text{HC(O)CO} + \text{HCl}$	$2.01 \times 10^{-11} \text{ cm}^3 \text{ molecule}^{-1} \text{ s}^{-1}$
		$\text{Cl} + (\text{HCO})_2 \rightarrow \text{HCO} + \text{CO} + \text{HCl}$	$1.79 \times 10^{-11} \text{ cm}^3 \text{ molecule}^{-1} \text{ s}^{-1}$
		$\text{HC(O)CO} \rightarrow \text{HCO} + \text{CO}$	6566 s^{-1}
		$\text{HCO} \rightarrow \text{loss}$	150 s^{-1}
212	5	$\text{Cl} + (\text{HCO})_2 \rightarrow \text{HC(O)CO} + \text{HCl}$	$2.01 \times 10^{-11} \text{ cm}^3 \text{ molecule}^{-1} \text{ s}^{-1}$
		$\text{Cl} + (\text{HCO})_2 \rightarrow \text{HCO} + \text{CO} + \text{HCl}$	$1.79 \times 10^{-11} \text{ cm}^3 \text{ molecule}^{-1} \text{ s}^{-1}$
		$\text{HC(O)CO} \rightarrow \text{HCO} + \text{CO}$	1230 s^{-1}
		$\text{HCO} \rightarrow \text{loss}$	150 s^{-1}
212	10	$\text{Cl} + (\text{HCO})_2 \rightarrow \text{HC(O)CO} + \text{HCl}$	$2.01 \times 10^{-11} \text{ cm}^3 \text{ molecule}^{-1} \text{ s}^{-1}$
		$\text{Cl} + (\text{HCO})_2 \rightarrow \text{HCO} + \text{CO} + \text{HCl}$	$1.79 \times 10^{-11} \text{ cm}^3 \text{ molecule}^{-1} \text{ s}^{-1}$
		$\text{HC(O)CO} \rightarrow \text{HCO} + \text{CO}$	2460 s^{-1}
		$\text{HCO} \rightarrow \text{loss}$	150 s^{-1}

Table 2: Model parameters used to simulate HCO profiles following the $\text{Cl} + (\text{HCO})_2$ reaction under 5 and 10 Torr of N_2 as a function of temperature.

An experimental study of the Cl + (HCO)₂ reaction was carried out under a range of temperatures (212 – 295 K) and pressures of nitrogen (5 – 100 Torr) using laser flash photolysis coupled with LIF HCO detection, with chlorine atoms generated by 248 nm excimer photolysis of oxalyl chloride (P2). At room temperature HCO growth was observed but was attributed to the rate determining Cl + (HCO)₂ reaction and not to HC(O)CO decomposition. Indeed, the room temperature HCO growth profiles observed following reaction R15 were fit using equation E3:

$$[\text{HCO}]_t = \left([\text{HCO}] \times \left(\frac{k_g}{k_g - k_l} \right) \right) \times (\exp(-k_l t) - \exp(-k_g t)) + b \quad (\text{E3})$$

where $[\text{HCO}]_t$ is the observed HCO signal at time t , $[\text{HCO}]$ is the HCO signal height, k_g and k_l are the *pseudo-first-order* rate coefficients defining HCO growth and loss, respectively, and b is the baseline signal.

Biexponential analysis of the room temperature HCO growth profiles using equation E3 was used to quantify the Cl + (HCO)₂ reaction directly at room temperature under 5 Torr of nitrogen. A bimolecular plot of the observed *pseudo-first-order* growth coefficients against (HCO)₂ concentration is presented in Figure 5, corresponding to a k_{15} value of $(3.88 \pm 0.12) \times 10^{-11} \text{ cm}^3 \text{ molecule}^{-1} \text{ s}^{-1}$; a typical HCO profile fitted using Equation E3 included in the inset.

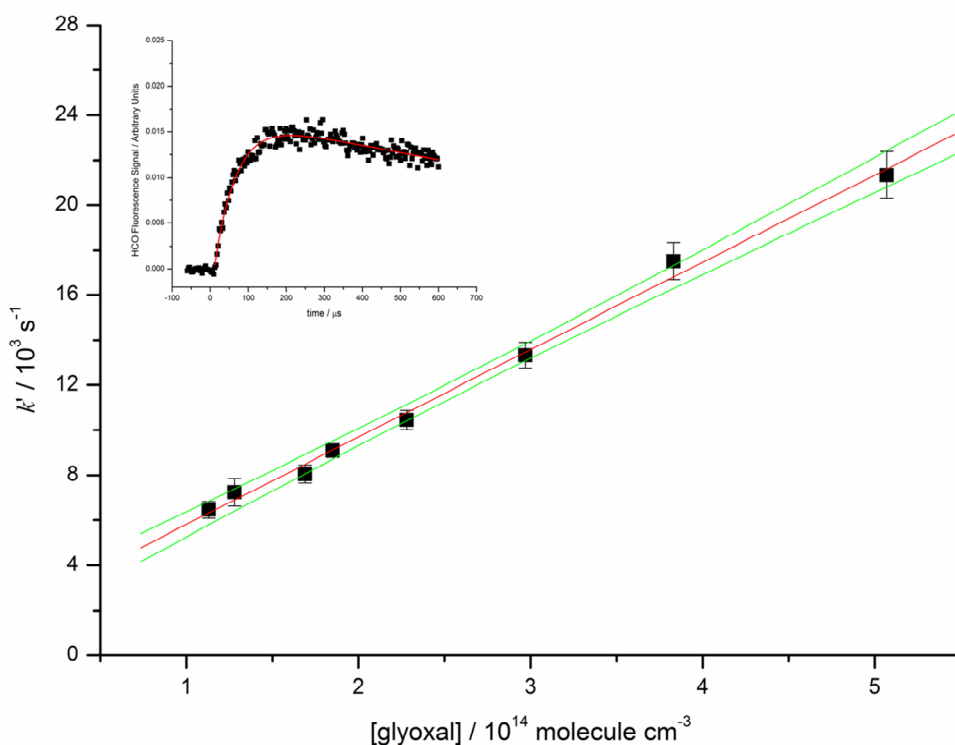


Figure 5: Bimolecular plot for the $\text{Cl} + (\text{HCO})_2 \rightarrow \text{HCO} + \text{CO}$ reaction at 295 K under 5 Torr of nitrogen, corresponding to a k_{15} value of $(3.88 \pm 0.12) \times 10^{-11} \text{ cm}^3 \text{ molecule}^{-1} \text{ s}^{-1}$; the quoted error is purely statistical at the 2σ level. Included in the inset is a typical experimental HCO growth profile measured in the presence of $3.83 \times 10^{14} \text{ molecule cm}^{-3}$ of $(\text{HCO})_2$ corresponding to a *pseudo-first-order* growth constant of $(17500 \pm 800) \text{ s}^{-1}$.

The bimolecular rate coefficient reaction R15 measured directly during this work is in excellent agreement with the relative k_{15} value of $(3.8 \pm 0.3) \times 10^{-11} \text{ cm}^3 \text{ molecule}^{-1} \text{ s}^{-1}$ reported by Niki and co-workers.⁴⁰

HCO growth profiles were not observed as temperatures were decreased under any experimental pressure, instead the HCO signal was observed to decay rapidly within a few hundred microseconds; a typical HCO decay profile observed in the presence of $\sim 3 \times 10^{14} \text{ molecule cm}^{-3}$ of $(\text{HCO})_2$ at 212 K under 10 Torr of N_2 is provided in Figure 6. Rapid removal of HCO was unexpected under these experimental conditions, and one possible explanation was that HCO was reacting with CO present as impurities in the glyoxal bulb to generate the HC(O)CO radical (R16):



The significance of reaction R16 in the Cl + (HCO)₂ reaction system was investigated by monitoring HCO decay profiles at 212 K under 10 Torr of nitrogen in the presence of varying amounts of CO (5.2 – 58.8 × 10¹⁴ molecule cm⁻³), with HCO radicals generated rapidly following the reaction of chlorine atoms with formaldehyde, HCHO (R8). However, while the *pseudo-first-order* decay constants did not exhibit a dependence on the experimental CO concentration, they were observed to scale with the HCHO concentration. Three reaction channels following reaction of HCO with HCHO (R17) were postulated, resulting in formation of either HC(O)CO and molecular hydrogen (R17a), carbon monoxide and a hydroxymethyl radical (R16b), or glyoxal and a hydrogen atom (17c). The standard enthalpies, Δ_rH_{298 K}, of reactions R17a – R17c were calculated using the thermodynamic properties published in the literature.^{42, 43}



Channel R17c can be quickly ruled out due to the endothermicity of this path. Channels R17a and R17b are both exothermic, with channel R17b the most thermodynamically favoured product path. However, if reaction R17b is the dominant channel responsible for HCO removal, then HCO would be expected to decay in the presence of HCHO at ambient temperatures, inconsistent with experimental observations. Therefore it is reasoned that reaction R17a is the dominant process responsible for HCO removal in the presence of HCHO, and that at room temperature the HC(O)CO produced rapidly dissociates to generate CO and recycle HCO (R7),⁶ leaving experiments reliant on HCO detection blind to the HCO consumed following reaction R17a.

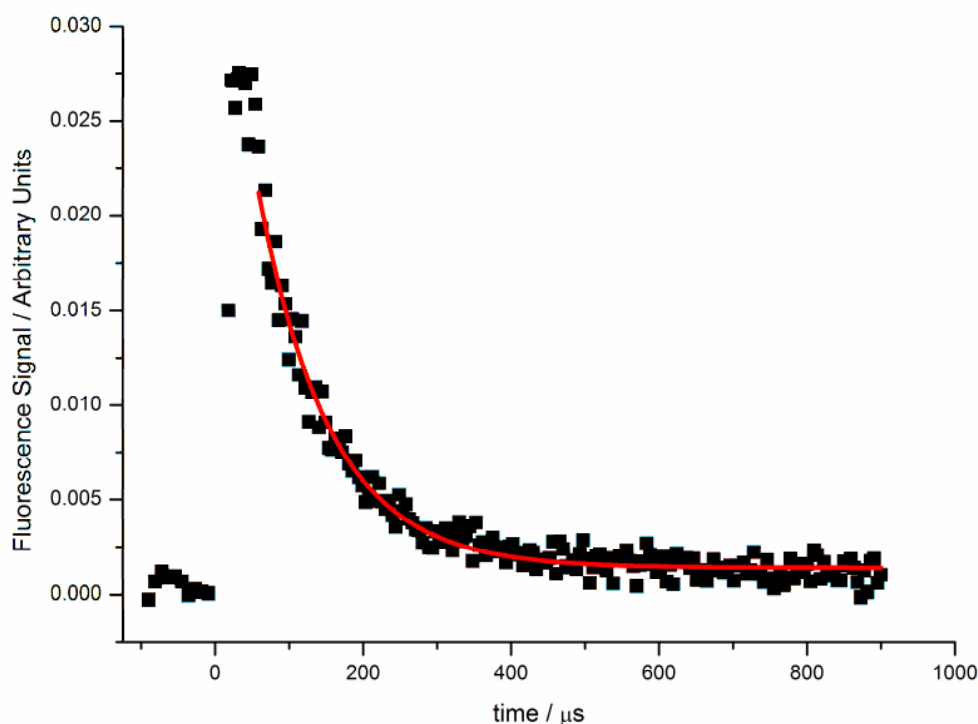


Figure 6: Experimental HCO decay profile observed in the presence of $\sim 3 \times 10^{14}$ molecule cm^{-3} of $(\text{HCO})_2$ at 212 K under 10 Torr of N_2 . Included is an exponential decay fit through these data using equation E1, corresponding to a *pseudo-first-order* decay coefficient of $(10300 \pm 265) \text{ s}^{-1}$.

7.6 Kinetics of the HCO + HCHO Reaction

The kinetics of the HCO + HCHO reaction were investigated using laser flash photolysis, coupled with LIF HCO detection at 212 K, using 10 and 30 Torr of nitrogen bath gas. HCO radicals were generated by the reaction of chlorine atoms with formaldehyde (R8), with chlorine atoms formed following 248 nm excimer laser photolysis of oxalyl chloride (P2). Quantitative kinetic measurements demand that the concentration of HCHO is known. The concentration of HCHO in the sample bulb could not be accurately determined barometrically as CO was also produced following pyrolysis of paraformaldehyde; moreover, the HCHO produced was partially lost to the walls of the gas sample bulb on consecutive days of experiments. Consequently, the HCHO concentration was determined kinetically by fitting the HCO growth profiles observed following the Cl + HCHO reaction at room temperature using equation E3 (inset of Figure 7). The *pseudo-first-order* growth constants

were then plotted against an estimation of the experimental HCHO sample bulb concentration. The HCHO sample bulb concentration could then be adjusted iteratively until the linear bimolecular plot gave a gradient equal to the Cl + HCHO rate coefficient value recommended by IUPAC ($k_8(298\text{ K}) = 7.2 \times 10^{-11}\text{ cm}^3\text{ molecule}^{-1}\text{ s}^{-1}$).⁴⁴

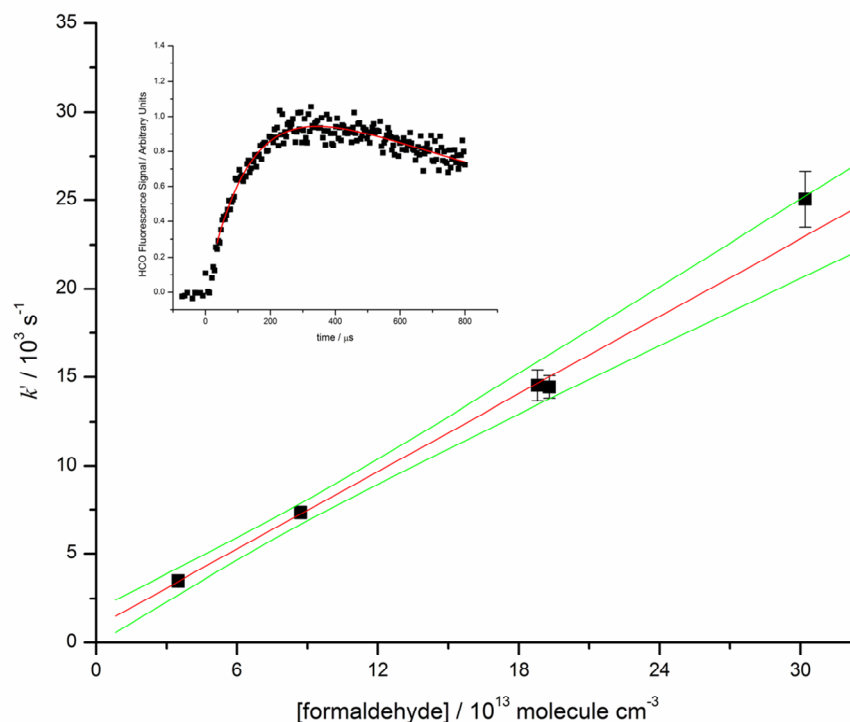


Figure 7: Bimolecular plot for the Cl + HCHO reaction at 295 K and 10 Torr total pressure used to characterize the experimental HCHO bulb concentration. A typical experimental HCO growth profile is included in the inset, measured in the presence of $8.72 \times 10^{13}\text{ molecule cm}^{-3}$ of HCHO corresponding to a *pseudo-first-order* growth constant of $(7340 \pm 350)\text{ s}^{-1}$.

A bimolecular plot showing all *pseudo-first-order* HCO decay coefficients measured in the presence of HCHO at 212 K under 10 and 30 Torr of nitrogen is presented in Figure 8. Linear least squares analysis through all data points yields the pressure independent bimolecular rate coefficient, k_{17} , $(3.44 \pm 0.15) \times 10^{-11}\text{ cm}^3\text{ molecule}^{-1}\text{ s}^{-1}$ at 212 K. A typical experimental HCO decay profile is included in the inset of Figure 8.

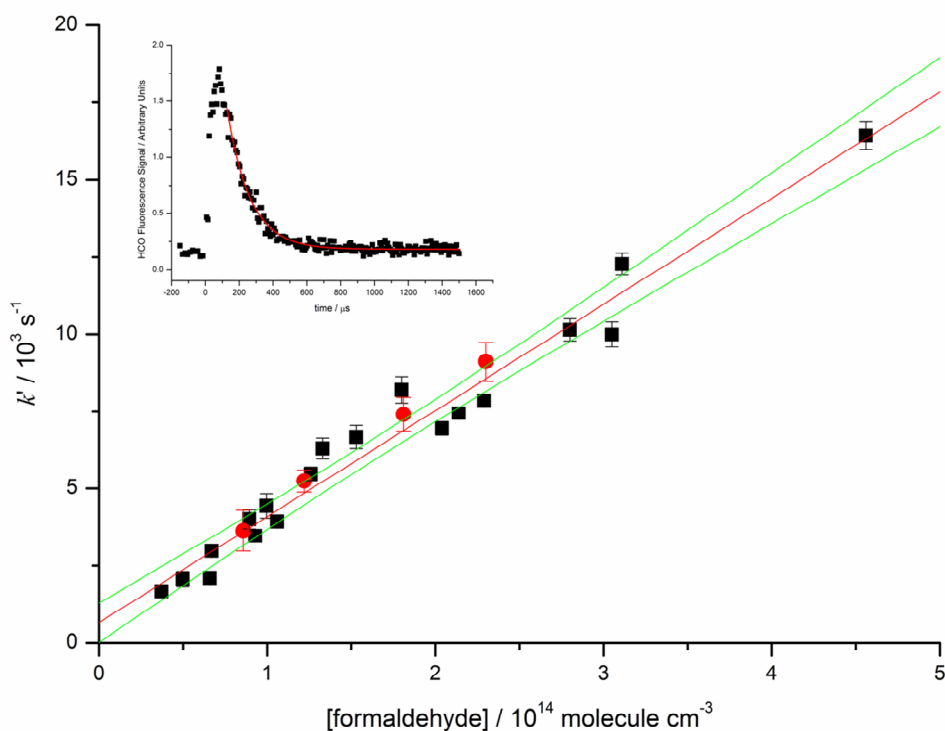


Figure 8: Bimolecular plot for the $\text{HCO} + \text{HCHO} \rightarrow \text{Products}$ reaction at 212 K under 10 (■) and 30 Torr (●) of nitrogen; corresponding to a k_{17} value of $(3.44 \pm 0.15) \times 10^{-11} \text{ cm}^3 \text{ molecule}^{-1} \text{ s}^{-1}$. Included in the inset is a typical HCO decay profile measured at 10 Torr total pressure in the presence of $2.14 \times 10^{14} \text{ molecule cm}^{-3}$ of HCHO corresponding to a *pseudo-first-order* decay constant of $(7435 \pm 180) \text{ s}^{-1}$.

7.7 Kinetics of the $\text{HCO} + \text{CH}_3\text{CHO}$ Reaction

Building on the experimental evidence supporting rapid reaction between HCO and formaldehyde, a second set of experiments were carried out to investigate whether or not HCO will react with acetaldehyde, CH_3CHO . HCO radicals were again generated by the reaction of chlorine atoms with formaldehyde (R8), with chlorine atoms produced following 248 nm excimer laser photolysis of oxalyl chloride (P2). HCO decay profiles were measured in the presence of between $(0.5 - 5) \times 10^{14} \text{ molecule cm}^{-3}$ of CH_3CHO at 212 K, under 10 Torr of nitrogen. Once again, the *pseudo-first-order* HCO decay coefficients were observed to scale with the aldehyde concentration (Figure 9), giving a bimolecular rate coefficient for

the HCO + CH₃CHO reaction of $(1.28 \pm 0.07) \times 10^{-11} \text{ cm}^3 \text{ molecule}^{-1} \text{ s}^{-1}$. A bimolecular plot intercept of $\sim 6000 \text{ s}^{-1}$ is expected given that HCHO is required to generate HCO.

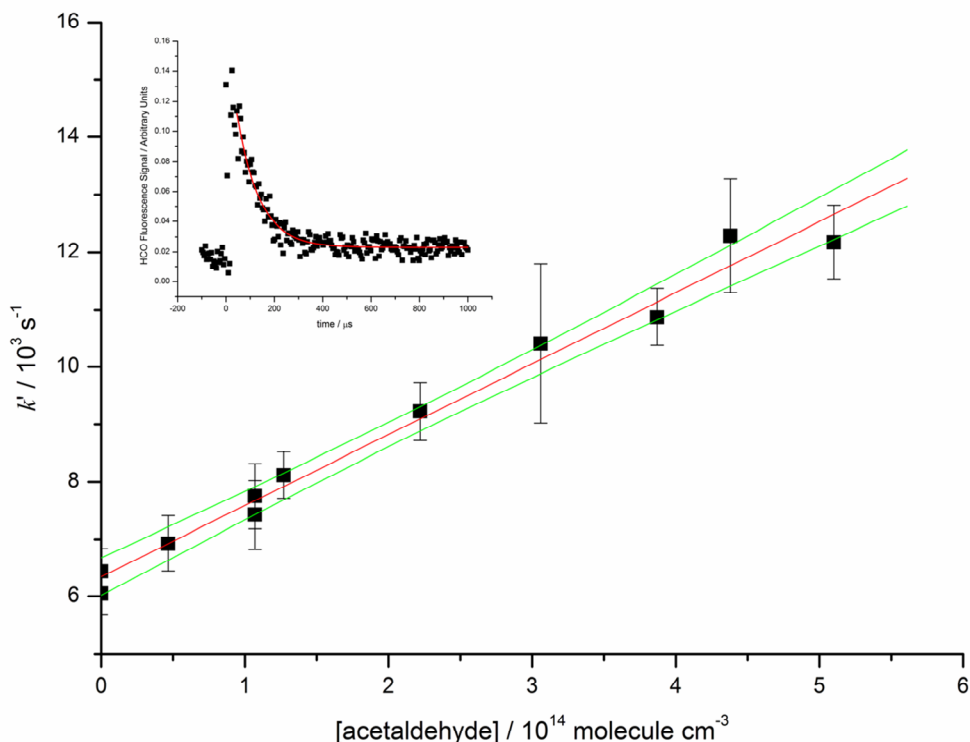


Figure 9: Bimolecular plot for the HCO + CH₃CHO → Products reaction at 212 K under 10 Torr of nitrogen, corresponding to k_{18} value of $(1.24 \pm 0.05) \times 10^{-11} \text{ cm}^3 \text{ molecule}^{-1} \text{ s}^{-1}$. A typical experimental HCO decay trace measured in the presence of $3.87 \times 10^{14} \text{ molecule cm}^{-3}$ is included in the inset. The experimental HCHO concentration used to generate HCO was $(1.6 \pm 0.1) \times 10^{14} \text{ molecule cm}^{-3}$ and consistent with the intercept observed.

Further kinetic experiments of the HCO + CH₃CHO reaction were carried out at higher temperatures (295 and 250 K), although no evidence of the HCO removal rate increasing with the acetaldehyde concentration was found; suggesting that HC(O)CO (or alternate HCO precursor) is also produced following the reaction of HCO with acetaldehyde (R18):



In order to determine whether the HCO + aldehyde chemistry presented in this chapter extends to ketone carbonyl species, additional experiments were carried out generating HCO in the presence of acetone at 212 K in 10 Torr of nitrogen. However, the observed exponential HCO decay constants were independent of the experimental acetone concentration; suggesting that HCO reactivity is limited to aldehydic carbonyl species.

7.8 Discussion

The formyl radical, HCO, has been successfully generated and monitored using pulsed laser flash photolysis coupled with laser induced fluorescence. Room temperature rate coefficients for the reactions of HCO with O₂ and NO have been measured at pressures of 10 and 30 Torr of N₂, both were found independent of pressure with values of $(5.27 \pm 0.01) \times 10^{-12} \text{ cm}^3 \text{ molecule}^{-1} \text{ s}^{-1}$ and $(1.30 \pm 0.03) \times 10^{-11} \text{ cm}^3 \text{ molecule}^{-1} \text{ s}^{-1}$, respectively, in good agreement with existing measurements reported in the literature. The HCO + NO₂ reaction was studied at room temperature under 10 Torr of N₂. Biexponential HCO decays were observed, consistent with secondary chemistry associated with the HCHO used as radical precursor. Analysis of the observed HCO decay traces yield a room temperature rate coefficient of $(6.99 \pm 0.16) \times 10^{-11} \text{ cm}^3 \text{ molecule}^{-1} \text{ s}^{-1}$. In addition, the Cl + (HCO)₂ reaction has been studied directly for the first time by monitoring the HCO produced following thermal dissociation of the nascent HC(O)CO radical, a rate coefficient of $(3.88 \pm 0.12) \times 10^{-11} \text{ cm}^3 \text{ molecule}^{-1} \text{ s}^{-1}$ was measured at 295 K, under 5 Torr of N₂; in excellent agreement with the only previous, relative measurement by Niki et al.⁴⁰

HCO chemistry has long been considered to be largely restricted to reactions with other radicals, open shell species such as O₂, NO and NO₂, or halogen molecules. The work presented in this chapter has shown for the first time that the HCO radical will also react rapidly with a range of closed-shell aldehyde species. Bimolecular rate coefficients have been measured for the reactions of HCO with formaldehyde (R17) and acetaldehyde (R18) under *pseudo-first-order* conditions in HCO, using nitrogen bath gas, with values of (3.44 ± 0.15) and $(1.24 \pm 0.05) \times 10^{-11} \text{ cm}^3 \text{ molecule}^{-1} \text{ s}^{-1}$, respectively. HCO *pseudo-first-order* rate coefficients were not observed to scale with the experimental concentration of either aldehyde at temperatures greater than 220 K, suggesting the thermally unstable HC(O)CO

radical as a likely product of reactions R17 and R18. In addition, HCO was not observed to react with acetone at 212 K, suggesting a reaction mechanism reliant on an aldehydic hydrogen atom.

HCO is produced extensively following the atmospheric oxidation of a range of volatile organics and through aldehyde photolysis,¹ but is rapidly titrated to HO₂ and CO in the troposphere through reaction with oxygen (R1). Therefore the novel HCO reactivity towards aldehyde species observed during this work has no significant implications on the chemistry of Earth's atmosphere. However, HCO, formaldehyde and acetaldehyde have all been detected in the interstellar medium (ISM).^{11, 45} Experimental and theoretical studies have long sort reactions relevant to these environments which unravel how carbon-bearing molecules form in the ISM;^{12, 46-49} the novel HCO chemistry described in this chapter could offer a way of building longer carbon-carbon chained molecules from short chained reactants in these environments.

7.9 References

1. Finlayson-Pitts, B. J.; Pitts, J. N. J., *Chemistry of the Upper and Lower Atmosphere. Theory, Experiments and Applications*. Academic Press: San Diego, 2000.
2. Miller, J. A.; Kee, R. J.; Westbrook, C. K., Chemical-kinetics and combustion modeling. *Annual Review of Physical Chemistry* 1990, 41, 345-387.
3. Herbst, E., The chemistry of interstellar space. *Chemical Society Reviews* 2001, 30, 168-176.
4. Niki, H.; Maker, P. D.; Savage, C. M.; Breitenbach, L. P., Relative rate constants for reaction of hydroxyl radical with aldehydes. *Journal of Physical Chemistry* 1978, 82, 132-134.
5. Glowacki, D. R.; Lockhart, J.; Blitz, M. A.; Klippenstein, S. J.; Pilling, M. J.; Robertson, S. H.; Seakins, P. W., Interception of Excited Vibrational Quantum States by O₂ in Atmospheric Association Reactions. *Science* 2012, 337, 1066-1069.
6. Lockhart, J.; Blitz, M.; Heard, D.; Seakins, P.; Shannon, R., Kinetic Study of the OH + Glyoxal Reaction: Experimental Evidence and Quantification of Direct OH Recycling. *Journal of Physical Chemistry A* 2013, 117, 11027-11037.
7. Horowitz, A.; Calvert, J. G., Wavelength dependence of the primary processes in acetaldehyde photolysis. *Journal of Physical Chemistry* 1982, 86, 3105-3114.
8. Salter, R. J.; Blitz, M. A.; Heard, D. E.; Pilling, M. J.; Seakins, P. W., New Chemical Source of the HCO Radical Following Photoexcitation of Glyoxal, (HCO)₂. *Journal of Physical Chemistry A* 2009, 113, 8278-8285.
9. Krasnoperov, L. N.; Chesnokov, E. N.; Stark, H.; Ravishankara, A. R., Unimolecular dissociation of formyl radical, HCO → H + CO, studied over 1-100 bar pressure range. *Journal of Physical Chemistry A* 2004, 108, 11526-11536.
10. Pilling, M. J., *Low-temperature combustion and autoignition*. Elsevier: 1997; Vol. 35.
11. Ehrenfreund, P.; Charnley, S. B., Organic molecules in the interstellar medium, comets, and meteorites: A voyage from dark clouds to the early earth. *Annual Review of Astronomy and Astrophysics* 2000, 38, 427-+.
12. Sorrell, W. H., Origin of amino acids and organic sugars in interstellar clouds. *Astrophysical Journal* 2001, 555, L129-L132.
13. Singh, A.; Shivani; Misra, A.; Tandon, P., Quantum chemical analysis for the formation of glycine in the interstellar medium. *Research in Astronomy and Astrophysics* 2013, 13, 912-920.
14. Ramsay, D. A., Absorption spectrum of free HCO radicals. *Journal of Chemical Physics* 1953, 21, 960-961.
15. Herzberg, G.; Ramsay, D. A., The 7500 to 4500 Å absorption system of the free HCO radical. *Proceedings of the Royal Society of London Series a-Mathematical and Physical Sciences* 1955, 233, 34-54.
16. Clark, J. H.; Moore, C. B.; Reilly, J. P., HCO radical kinetics - conjunction of laser photolysis and intracavity dye-laser spectroscopy. *International Journal of Chemical Kinetics* 1978, 10, 427-431.
17. Nadtochenko, V. A.; Sarkisov, O. M.; Vedenev, V. I., Study of the reactions of the HCO radical by the intracavity laser spectroscopy method during the pulse photolysis of acetaldehyde. *Bulletin of the Academy of Sciences of the USSR Division of Chemical Science* 1979, 28, 605-607.
18. Gill, R. J.; Johnson, W. D.; Atkinson, G. H., The formation and decay mechanisms of HCO in the photo-dissociation of gas-phase acetaldehyde. *Chemical Physics* 1981, 58, 29-44.
19. Tjossem, P. J. H.; Goodwin, P. M.; Cool, T. A., 2-Photon resonance REMPI detection of the formyl radical. *Journal of Chemical Physics* 1986, 84, 5334-5343.
20. Ninomiya, Y.; Goto, M.; Hashimoto, S.; Kagawa, Y.; Yoshizawa, K.; Kawasaki, M.; Wallington, T. J.; Hurley, M. D., Cavity ring-down spectroscopy and relative rate study of reactions of HCO radicals with O₂, NO, NO₂, and Cl₂ at 295 K. *Journal of Physical Chemistry A* 2000, 104, 7556-7564.

21. Hall, G.; Suits, A. G.; Whitaker, B. J., Resonant degenerate 4-wave-mixing detection of HCO. *Chemical Physics Letters* 1993, 203, 277-282.
22. Konig, R.; Lademann, J., Laser-induced-fluorescence detection of HCO produced by laser photolysis of formaldehyde. *Chemical Physics Letters* 1983, 94, 152-155.
23. Stone, B. M.; Noble, M.; Lee, E. K. C., Laser-induced fluorescence emission from HCO produced by 308 nm excimer laser photodissociation of acetaldehyde. *Chemical Physics Letters* 1985, 118, 83-87.
24. DeSain, J. D.; Jusinski, L. E.; Ho, A. D.; Taatjes, C. A., Temperature dependence and deuterium kinetic isotope effects in the HCO(DCO)+O₂ reaction between 296 and 673 K. *Chemical Physics Letters* 2001, 347, 79-86.
25. DeSain, J. D.; Jusinski, L. E.; Taatjes, C. A., Temperature dependence and deuterium kinetic isotope effects in the HCO plus NO reaction. *Journal of Photochemistry and Photobiology a-Chemistry* 2005, 176, 149-154.
26. Sappey, A. D.; Crosley, D. R., Laser-induced-fluorescence in the B-X system of the HCO radical. *Journal of Chemical Physics* 1990, 93, 7601-7608.
27. Yin, H. M.; Kable, S. H., Rotational analysis of the HCO (B) \tilde{v}_2 (A')-(X) \tilde{v}_2 (A')³(1)(1) and ³(2)(1) bands. *Journal of Molecular Spectroscopy* 2006, 237, 163-173.
28. Setokuchi, O., Trajectory calculations of OH radical- and Cl atom-initiated reaction of glyoxal: atmospheric chemistry of the HC(O)CO radical. *Physical Chemistry Chemical Physics* 2011, 13, 6296-6304.
29. Rim, K. T.; Hershberger, J. F., Product branching ratios of the HCO+NO₂ reaction. *Journal of Physical Chemistry A* 1998, 102, 5898-5902.
30. Ko, T.; Fontijn, A., High-temperature photochemistry kinetic study of the reaction H + NO₂ - OH + NO from 296 K to 760 K. *Journal of Physical Chemistry* 1991, 95, 3984-3987.
31. Shibuya, K.; Ebata, T.; Obi, K.; Tanaka, I., Rate constant measurements for the reactions of HCO with NO and O₂ in gas-phase. *Journal of Physical Chemistry* 1977, 81, 2292-2294.
32. Reilly, J. P.; Clark, J. H.; Moore, C. B.; Pimentel, G. C., HCO production, vibrational-relaxation, chemical-kinetics, and spectroscopy following laser photolysis of formaldehyde. *Journal of Chemical Physics* 1978, 69, 4380-4394.
33. Veyret, B.; Lesclaux, R., Absolute rate constants for the reactions of HCO with O₂ and NO from 298 K to 503 K. *Journal of Physical Chemistry* 1981, 85, 1918-1922.
34. Nesbitt, F. L.; Gleason, J. F.; Stief, L. J., Temperature dependence of the rate constant for the reaction HCO+O₂ -> HO₂+CO at T = 200-398 K. *Journal of Physical Chemistry A* 1999, 103, 3038-3043.
35. Nadtochenko, V.; Sarkisov, O.; Vedenev, V., Study of the reaction of radical HCO with molecular oxygen. *Doklady Akademii Nauk SSSR* 1979, 244, 152-156.
36. Dammeier, J.; Colberg, M.; Friedrichs, G., Wide temperature range (T=295 K and 770-1305 K) study of the kinetics of the reactions HCO + NO and HCO+NO₂ using frequency modulation spectroscopy. *Physical Chemistry Chemical Physics* 2007, 9, 4177-4188.
37. Atkinson, R.; Baulch, D.; Cox, R.; Crowley, J.; Hampson, R.; Hynes, R.; Jenkin, M.; Rossi, M.; Troe, J.; Subcommittee, I., Evaluated kinetic and photochemical data for atmospheric chemistry: Volume II—gas phase reactions of organic species. *Atmospheric Chemistry and Physics* 2006, 6, 3625-4055.
38. Timonen, R. S.; Ratajczak, E.; Gutman, D., Kinetics of the reactions of the formyl radical with oxygen, nitrogen-dioxide, chlorine, and bromine. *Journal of Physical Chemistry* 1988, 92, 651-655.
39. Guo, Y. L.; Smith, S. C.; Moore, C. B.; Melius, C. F., Kinetics and product branching ratios for the reaction of HCO + NO₂. *Journal of Physical Chemistry* 1995, 99, 7473-7481.
40. Niki, H.; Maker, P. D.; Savage, C. M.; Breitenbach, L. P., An FTIR study of the Cl-atom initiated reaction of glyoxal. *International Journal of Chemical Kinetics* 1985, 17, 547-558.
41. Ianni, J. C., Kintecus, Windows Version 2.80, 2002, www.kintecus.com.

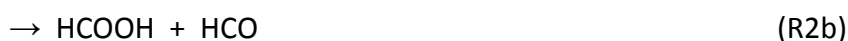
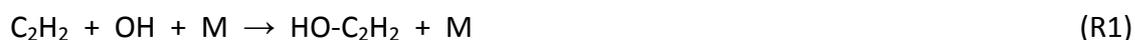
42. Baulch, D. L.; Bowman, C. T.; Cobos, C. J.; Cox, R. A.; Just, T.; Kerr, J. A.; Pilling, M. J.; Stocker, D.; Troe, J.; Tsang, W.; Walker, R. W.; Warnatz, J., Evaluated kinetic data for combustion modeling: Supplement II. *Journal of Physical and Chemical Reference Data* 2005, 34, 757-1397.
43. da Silva, G., Hydroxyl radical regeneration in the photochemical oxidation of glyoxal: kinetics and mechanism of the $\text{HC(O)CO} + \text{O}_2$ reaction. *Physical Chemistry Chemical Physics* 2010, 12, 6698-6705.
44. Atkinson, R.; Baulch, D. L.; Cox, R. A.; Crowley, J. N.; Hampson, R. F.; Hynes, R. G.; Jenkin, M. E.; Rossi, M. J.; Troe, J., Evaluated kinetic and photochemical data for atmospheric chemistry: Volume II - gas phase reactions of organic species. *Atmospheric Chemistry and Physics* 2006, 6, 3625-4055.
45. van der Marel, N.; van Dishoeck, E. F.; Bruderer, S.; van Kempen, T. A., Warm formaldehyde in the Ophiuchus IRS 48 transitional disk. *Astronomy & Astrophysics* 2014, 563.
46. Blagojevic, V.; Petrie, S.; Bohme, D. K., Gas-phase syntheses for interstellar carboxylic and amino acids. *Monthly Notices of the Royal Astronomical Society* 2003, 339, L7-L11.
47. Trixler, F., Quantum Tunnelling to the Origin and Evolution of Life. *Current Organic Chemistry* 2013, 17, 1758-1770.
48. Shivani; Singh, A.; Gupta, V.; Misra, A.; Tandon, P., Quantum-chemical approach to serine formation in the interstellar medium: A possible reaction pathway. *Astronomy & Astrophysics* 2014, 563.
49. Pilling, S.; Baptista, L.; Boechat-Roberty, H. M.; Andrade, D. P. P., Formation Routes of Interstellar Glycine Involving Carboxylic Acids: Possible Favoritism Between Gas and Solid Phase. *Astrobiology* 2011, 11, 883-893.

Chapter 8 Summary and Future Work

8.1 Synopsis

The Earth's atmosphere is often compared to a low temperature combustion system in which solar energy drives radical oxidation of trace gases. During daylight hours, this complex chain propagating chemistry is initiated predominantly through reaction with OH, resulting in the production of a wide range radical species.¹ Chemical reactions are known to generate species with excess energy, depending on the relative difference in energy between reactants and products. This excess energy is generally assumed to be removed under atmospheric conditions through non-reactive collisions, leaving the products of an initial reaction in thermal equilibrium prior to the onset of secondary chemistry. However, in chapters 3 – 6 of this thesis evidence is provided that suggests the product branching associated with OH oxidation chemistry, initiated by both addition and abstraction channels, is influenced by chemical activation.

Chapter 3 provides a complete description of the OH initiated oxidation of acetylene, C₂H₂, using a combination of experiments and theory. Briefly, the adduct formed following reaction of OH with C₂H₂, exists in two energetically distinct conformations. Subsequent rapid reaction of the adduct with O₂ results in formation of either glyoxal, (HCO)₂, and OH or formic acid and HCO, depending on the stereochemistry of the adduct at the point of association with O₂.



Reaction channel 2a dominates under atmospheric conditions, and is associated with reaction of the lower energy adduct conformer. Experimental OH yields, Φ_{OH} , for the OH + C₂H₂/O₂ system have been measured as a function of pressure and temperature in the presence of varying amounts of N₂ and/or O₂ bath gas; and modelled using master equation

(ME) analysis and variable transition state theory (VRC-TST) calculations. The nascent adduct forms with $\sim 146.6 \text{ kJ mol}^{-1}$ excess energy at 298 K, allowing the adduct conformers to interconvert rapidly over a relatively small barrier of $\sim 17 \text{ kJ mol}^{-1}$. Under low O_2 conditions the excess energy is dissipated through non-reactive collisions and the adduct conformers exist in thermal equilibrium prior to a reactive collision with O_2 . High Φ_{OH} are observed under thermal conditions as the distribution of adduct conformers shifts in favour of the more stable isomer prior to reaction with O_2 . Under high O_2 conditions, reactive collisions occur before the excess energy has been removed; lower Φ_{OH} are observed as an increased fraction of the total reactive flux is channelled through the less stable conformer to yield $\text{HCOOH} + \text{HCO}$. Theoretical analysis of the experimental Φ_{OH} measurements presented in chapter 3 suggests that under atmospheric conditions, $\sim 25\%$ of the total adduct + O_2 reaction flux occurs under non-thermal conditions.² Qualitatively similar behaviour is observed following the OH initiated oxidation of propyne and 2-butyne (chapter 4).³

The Lindemann model of association reactions is reliant on the formation of a nascent chemically activated complex. Consequently, the product branching observed for systems that include unimolecular or bimolecular exit channels for the activated complex, with critical energy barriers below the energy at which the complex is formed, are potentially influenced by chemical activation. In contrast, the widely accepted Polanyi rules state that abstraction reactions partition reaction exothermicity exclusively into the newly formed bond.⁴ Consequently, the secondary chemistry of a radical produced following oxidation initiated by a hydrogen atom abstraction channel is not expected to be influenced by chemical activation. However, chapters 5 and 6 of this thesis provide evidence of two atmospherically important hydrogen atom abstraction reactions which channel a significant fraction of the reaction exothermicity into the radical fragment.

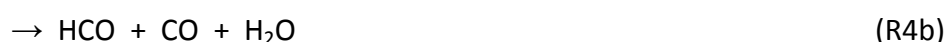
The reaction of OH with acetaldehyde, CH_3CHO , is considered to proceed via an archetypal abstraction channel (R3a). In chapter 5, direct and indirect evidence is presented which suggests $\sim 15\%$ of the acetyl population is produced following reaction with sufficient energy to dissociate directly to CO and CH_3 (R3b).





Prompt decomposition of a fraction of the nascent CH_3CO population could potentially influence the PAN and HCHO budgets in polluted regions.

The reaction of OH with glyoxal, $(\text{HCO})_2$, is an important sink for $(\text{HCO})_2$ in the atmosphere (R4); and proceeds via hydrogen atom abstraction that gives HC(O)CO and H_2O (R4a).



Initial investigations concluded that subsequent HC(O)CO chemistry was governed by a competition between unimolecular dissociation (R5) and bimolecular reaction with O_2 ;^{5, 6} with the latter proceeding via both an abstraction and association channel. However, experimental evidence presented in chapter 6 suggests that the HC(O)CO radical reacts directly with O_2 to generate OH (R6),⁷ consistent with recent calculations.⁸



The OH yield associated with the $\text{OH} + (\text{HCO})_2/\text{O}_2$ system were quantified for the first time as a function of pressure, temperature and O_2 concentration; and suggest an OH yield of ~19% under tropospheric conditions.⁷ Significantly, the OH yields were observed to converge on a maximum limiting yield, consistent with ~60% of the nascent HC(O)CO population being produced following reaction R4 with sufficient energy to promptly dissociate (R4b). In chapter 7 an HCO laser detection system was developed in an effort to confirm both prompt and growth HCO signal following the reaction of Cl atoms with $(\text{HCO})_2$ (R7), and determine the rate of thermal dissociation of HC(O)CO , at low experimental temperatures.



However, the experiments were flawed due to unexpected chemistry rapidly removing HCO from the system; further experiments were carried out that suggests the HCO radical reacts rapidly with a range of aldehydes (R8, R9, and R10):



The chemical systems investigated in this thesis provides strong evidence that chemical activation can influence the product branching associated with both bimolecular and unimolecular exit channels, following chemistry initiated by both OH addition and abstraction channels.

8.2 Implications

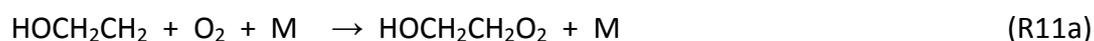
8.2.1 Combustion Chemistry

The similarity between atmospheric and combustion chemistry has been mentioned previously. The OH generating channels associated with the reactions of O₂ with HO-C₂H₂ (R2a) and HC(O)CO (R4a) both involve initial peroxy radical isomerisation to give a carbon centred radical containing a hydroperoxide function, these species are generally termed QOOH. There is a growing awareness that peroxy (RO₂) to QOOH isomerisation reactions are important under low NO_x conditions for certain radicals in the troposphere.⁹ The chemistry of RO₂ and QOOH species is of great importance in low temperature combustion (T < 900 K), as they control both chain propagation and branching, and therefore the nature of the radical pool prior to ignition.¹⁰ Consequently, the formation and reactions of RO₂ and QOOH species are central to autoignition chemistry. Recent renewed interest in autoignition stems from the next generation of engine design, such as Homogenous Charge Compression Ignition (HCCI) engines, where ignition is controlled by chemistry.¹¹⁻¹³ HCCI combustion relies on compression heating premixed fuel/air mixtures and results in lower particulate and NO_x emissions than conventional diesel engines. HCCI development requires careful

control of the combustion process and therefore demands a detailed understanding of the chemistry.

Several experimental and theoretical studies have reported the product branching following association reactions between O₂ and combustion relevant species, such as cyclic, acyclic, and oxygenated alkyl radicals, to be influenced by chemical activation.¹⁴⁻¹⁸ The product branching observed in these systems is often defined in terms of the competition between the unimolecular formally direct decomposition, and bimolecular collisional deactivating channels available to the nascent activated association complex. Recent studies have shown that for some systems, the influence of chemical activation persists to the pressures experienced inside the cylinder of an internal combustion engine. The pressure dependent branching of key combustion reactions is essential for auto-ignition modelling, yet pressure dependent chemically activated channels are rarely treated rigorously by models.¹⁰

The reaction of the β -hydroxyethyl radical, HOCH₂CH₂, with O₂ (R10) is important in the combustion of ethanol and ethylene, and has been investigated by Zador et al. using both experiment and theory.¹⁷ Calculations carried out during the study by Zador and co-workers concluded that reaction R11 proceeds across a barrierless entrance channel followed by a multi-well potential energy surface, consistent with previous theory.¹⁸ In addition to pressure dependent peroxy radical formation (R11a), Zador and co-workers reported two chemically activated channels, resulting in formation of either formaldehyde and OH (R11b), or a vinyl alcohol and HO₂ (R11c).



Zador and co-workers reported a marked pressure and temperature dependence in the product branching of reaction R11, consistent with a competition between the formally direct and deactivating channels. The impacts of chemical activation for O₂ association

reactions is likely to become most evident under the pure oxygen conditions used during oxy-fuel combustion,¹⁹ when the bath gas can also act as a reactive collision partner.

It is worthwhile to note that the nascent HOCH₂CH₂ radical produced following OH addition to ethylene (R12), forms with approximately 130 kJ mol⁻¹ excess energy;^{20, 21} under conditions relevant to oxy-fuel combustion, it is unlikely that this excess energy will be dissipated before subsequent reaction with O₂.



8.2.2 Atmospheric Chemistry

The reactions of ozone with olefins have long been considered to proceed via 1, 3 – cycloaddition across the double bond to give a primary ozonide, which then decomposes to give a carbonyl and a carbonyl biradical species, known as a *Criegee intermediate*.²² The formation of a Criegee species was first proposed by Rudolph Criegee in 1949, but these species have only recently been observed directly.²³ Nascent Criegee intermediates are known to form with substantial excess energy (~300 kJ mol⁻¹),²⁴ and it has been proposed that bimolecular reactions could intercept the activated intermediate before this energy is dissipated.²⁵ For non-thermal kinetics to influence atmospheric chemistry requires high reactivity and significant mixing ratios of co-reagent, these conditions are usually only met by O₂. Several recent experimental studies have investigated the kinetics of the simplest Criegee species, CH₂OO, following its reaction with a range of co-reagents,^{23, 26-28} although there is no evidence supporting reaction with O₂, CH₂OO has been shown to react slowly with H₂O (R12):



The thermal rate coefficient for reaction R12 has recently been contested with experimental values ranging from $(9 - 400) \times 10^{-17} \text{ cm}^3 \text{ molecule}^{-1} \text{ s}^{-1}$,^{23, 27} and a theoretical study of reaction R12 has reported a significant barrier of ~126 kJ mol⁻¹.²⁹ However, if the nascent CH₂OO biradical forms with significant excess energy, formally direct product formation might become possible for reaction R12 in high concentrations of H₂O.

8.3 Future Work

The work presented in this thesis has shown that, under atmospheric conditions, the chemically activated radicals formed following the addition of OH across an alkyne triple bond are intercepted through bimolecular reactions with O₂ before the internal quantum states of the nascent adduct have fully relaxed. Future experiments would build on work by Zador et al., and investigate whether the influence of chemical activation extends to the product branching observed during OH initiated oxidation of alkenes.

Initial experiments would aim at determining the significance of the OH forming channel reported by Zador and co-workers for the OH + C₂H₄/O₂ system. If the association reaction of O₂ with HOCH₂CH₂ (R11) was found to generate OH, then OH yields could be quantified as a function of pressure, temperature, and O₂ concentration from the ratio of rate coefficients measured in the presence and absence of O₂. Preliminary room temperature experiments, carried out under 10 Torr total pressure, suggest that OH is recycled in the OH + C₂H₄/O₂ system, with pseudo-first-order OH decays observed to slow following the addition of $\sim 1.35 \times 10^{17}$ molecule cm⁻³ of O₂ to the reaction cell (Figure 1). The bimolecular rate coefficients of (3.64 ± 0.05) and $(4.48 \pm 0.04) \times 10^{-12}$ cm³ molecule⁻¹ s⁻¹ measured in the presence and absence of O₂, respectively, correspond to an experimental OH yield of 0.19 ± 0.01 under these conditions. This analysis assumes that O₂ and N₂ quench the nascent HOC₂H₂ radical with equal efficiencies, and a relative rate study of reaction R12 could be carried out in order to test this assumption. The calculations by Zador et al. reported an active HO₂ forming channel (R11c) associated with reaction R11. The yield of HO₂ could be determined by quantifying the OH yield following addition of NO to the reaction cell. If channel R11c is significant, then a higher experimental OH yield would be expected as NO titrates the HO₂ quantitatively to OH.

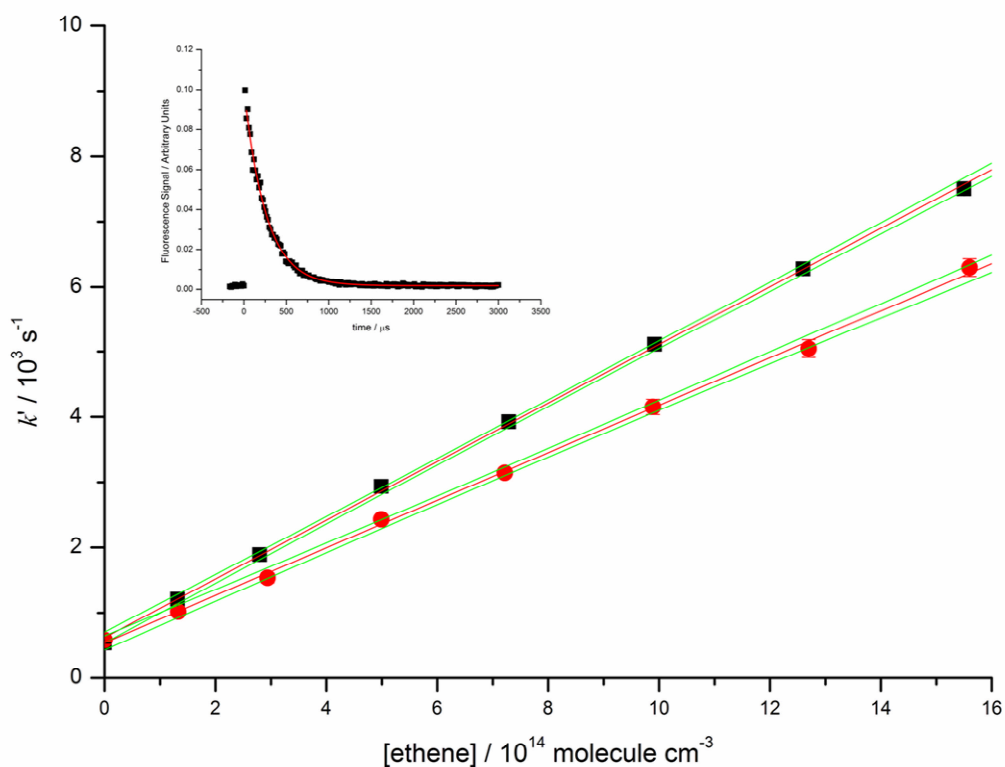


Figure 1: Room temperature bimolecular plots measured for the $\text{OH} + \text{C}_2\text{H}_4 \rightarrow \text{Products}$ reaction carried out under 10 Torr of pure N_2 bath gas (\blacksquare), and in the presence of $\sim 1.35 \times 10^{17} \text{ molecule cm}^{-3}$ of O_2 (\bullet), and correspond to bimolecular rate coefficients of (4.48 ± 0.04) and $(3.64 \pm 0.05) \times 10^{-12} \text{ cm}^3 \text{ molecule}^{-1} \text{ s}^{-1}$, respectively; (where the errors are purely statistical at the 2σ level). A typical OH decay trace measured in the presence of $\sim 7.29 \times 10^{14} \text{ molecule cm}^{-3}$ of C_2H_4 in pure N_2 bath gas, corresponding to a *pseudo-first-order* decay coefficient of $(3925 \pm 30) \text{ s}^{-1}$ is included in the inset.

8.4 References

1. Finlayson-Pitts, B. J.; Pitts, J. N. J., *Chemistry of the Upper and Lower Atmosphere. Theory, Experiments and Applications*. Academic Press: San Diego, 2000.
2. Glowacki, D. R.; Lockhart, J.; Blitz, M. A.; Klippenstein, S. J.; Pilling, M. J.; Robertson, S. H.; Seakins, P. W., Interception of Excited Vibrational Quantum States by O₂ in Atmospheric Association Reactions. *Science* 2012, 337, 1066-1069.
3. Lockhart, J.; Blitz, M. A.; Heard, D. E.; Seakins, P. W.; Shannon, R. J., Mechanism of the Reaction of OH with Alkynes in the Presence of Oxygen. *Journal of Physical Chemistry A* 2013, 117, 5407-5418.
4. Polanyi, J. C., Some concepts in reaction dynamics *Science* 1987, 236, 680-690.
5. Niki, H.; Maker, P. D.; Savage, C. M.; Breitenbach, L. P., An FTIR study of the Cl-atom initiated reaction of glyoxal. *International Journal of Chemical Kinetics* 1985, 17, 547-558.
6. Orlando, J. J.; Tyndall, G. S., The atmospheric chemistry of the HC(O)CO radical. *International Journal of Chemical Kinetics* 2001, 33, 149-156.
7. Lockhart, J.; Blitz, M.; Heard, D.; Seakins, P.; Shannon, R., Kinetic Study of the OH + Glyoxal Reaction: Experimental Evidence and Quantification of Direct OH Recycling. *Journal of Physical Chemistry A* 2013, 117, 11027-11037.
8. da Silva, G., Hydroxyl radical regeneration in the photochemical oxidation of glyoxal: kinetics and mechanism of the HC(O)CO + O₂ reaction. *Physical Chemistry Chemical Physics* 2010, 12, 6698-6705.
9. Orlando, J. J.; Tyndall, G. S., Laboratory studies of organic peroxy radical chemistry: an overview with emphasis on recent issues of atmospheric significance. *Chemical Society Reviews* 2012, 41, 6294-6317.
10. Zádor, J.; Taatjes, C. A.; Fernandes, R. X., Kinetics of elementary reactions in low-temperature autoignition chemistry. *Progress in Energy and Combustion Science* 2011, 37, 371-421.
11. Zhao, F.; Asmus, T. N.; Assanis, D. N.; Dec, J. E.; Eng, J. A.; Najt, P. M. *Homogeneous charge compression ignition (HCCI) engines*; SAE Technical Paper: 2003.
12. Dec, J. E., Advanced compression-ignition engines—understanding the in-cylinder processes. *Proceedings of the Combustion Institute* 2009, 32, 2727-2742.
13. Yao, M.; Zheng, Z.; Liu, H., Progress and recent trends in homogeneous charge compression ignition (HCCI) engines. *Progress in Energy and Combustion Science* 2009, 35, 398-437.
14. Knepp, A. M.; Meloni, G.; Jusinski, L. E.; Taatjes, C. A.; Cavallotti, C.; Klippenstein, S. J., Theory, measurements, and modeling of OH and HO₂ formation in the reaction of cyclohexyl radicals with O₂. *Physical Chemistry Chemical Physics* 2007, 9, 4315-4331.
15. Petway, S. V.; Ismail, H.; Green, W. H.; Estupiñán, E. G.; Jusinski, L. E.; Taatjes, C. A., Measurements and Automated Mechanism Generation Modeling of OH Production in Photolytically Initiated Oxidation of the Neopentyl Radical. *The Journal of Physical Chemistry A* 2007, 111, 3891-3900.
16. Fernandes, R. X.; Zádor, J.; Jusinski, L. E.; Miller, J. A.; Taatjes, C. A., Formally direct pathways and low-temperature chain branching in hydrocarbon autoignition: the cyclohexyl+ O₂ reaction at high pressure. *Physical Chemistry Chemical Physics* 2009, 11, 1320-1327.
17. Zádor, J.; Fernandes, R. X.; Georgievskii, Y.; Meloni, G.; Taatjes, C. A.; Miller, J. A., The reaction of hydroxyethyl radicals with O₂: A theoretical analysis and experimental product study. *Proceedings of the Combustion Institute* 2009, 32, 271-277.

18. da Silva, G.; Bozzelli, J. W.; Liang, L.; Farrell, J. T., Ethanol Oxidation: Kinetics of the α -Hydroxyethyl Radical+ O₂ Reaction. *The Journal of Physical Chemistry A* 2009, 113, 8923-8933.
19. Wall, T.; Liu, Y.; Spero, C.; Elliott, L.; Khare, S.; Rathnam, R.; Zeenathal, F.; Moghtaderi, B.; Buhre, B.; Sheng, C., An overview on oxyfuel coal combustion—State of the art research and technology development. *Chemical Engineering Research and Design* 2009, 87, 1003-1016.
20. Zhu, R.; Park, J.; Lin, M.-C., Ab initio kinetic study on the low-energy paths of the HO+ C₂H₄ reaction. *Chemical physics letters* 2005, 408, 25-30.
21. Senosiain, J. P.; Klippenstein, S. J.; Miller, J. A., Reaction of ethylene with hydroxyl radicals: a theoretical study. *The Journal of Physical Chemistry A* 2006, 110, 6960-6970.
22. Johnson, D.; Marston, G., The gas-phase ozonolysis of unsaturated volatile organic compounds in the troposphere. *Chemical Society Reviews* 2008, 37, 699-716.
23. Welz, O.; Savee, J. D.; Osborn, D. L.; Vasu, S. S.; Percival, C. J.; Shallcross, D. E.; Taatjes, C. A., Direct kinetic measurements of Criegee intermediate (CH₂OO) formed by reaction of CH₂I with O₂. *Science* 2012, 335, 204-207.
24. Taatjes, C. A.; Shallcross, D. E.; Percival, C. J., Research frontiers in the chemistry of Criegee intermediates and tropospheric ozonolysis. *Physical Chemistry Chemical Physics* 2014, 16, 1704-1718.
25. Olzmann, M., On the role of bimolecular reactions in chemical activation systems. *Physical Chemistry Chemical Physics* 2002, 4, 3614-3618.
26. Taatjes, C. A.; Welz, O.; Eskola, A. J.; Savee, J. D.; Scheer, A. M.; Shallcross, D. E.; Rotavera, B.; Lee, E. P.; Dyke, J. M.; Mok, D. K., Direct Measurements of Conformer-Dependent Reactivity of the Criegee Intermediate CH₃CHOO. *Science* 2013, 340, 177-180.
27. Stone, D.; Blitz, M.; Daubney, L.; Howes, N. U.; Seakins, P., Kinetics of CH₂OO reactions with SO₂, NO₂, NO, H₂O and CH₃CHO as a function of pressure. *Physical Chemistry Chemical Physics* 2014, 16, 1139-1149.
28. Buras, Z. J.; Elsamra, R. M.; Jalan, A.; Middaugh, J. E.; Green, W. H., Direct Kinetic Measurements of Reactions between the Simplest Criegee Intermediate CH₂OO and Alkenes. *The Journal of Physical Chemistry A* 2014, 118, 1997-2006.
29. Qi, B.; Chao, Y.-T., Theoretical study on the mechanism and kinetics of the reaction of Criegee radical CH₂O₂ with H₂O. *Acta Chimica Sinica* 2007, 65, 2117-2123.

Appendix A: Published Papers

As required by the regulations for thesis submission, this appendix shows the papers in which work from this thesis has been published:

Glowacki, D. R.; Lockhart, J.; Blitz, M. A.; Klippenstein, S. J.; Pilling, M. J.; Robertson, S. H.; Seakins, P. W., Interception of Excited Vibrational Quantum States by O₂ in Atmospheric Association Reactions. *Science* 2012, 337, 1066-1069.

Lockhart, J.; Blitz, M. A.; Heard, D. E.; Seakins, P. W.; Shannon, R. J., Mechanism of the Reaction of OH with Alkynes in the Presence of Oxygen. *Journal of Physical Chemistry A* 2013, 117, 5407-5418.

Lockhart, J.; Blitz, M. A.; Heard, D. E.; Seakins, P. W.; Shannon, R. J., Kinetic Study of the OH + Glyoxal Reaction: Experimental Evidence and Quantification of Direct OH Recycling. *Journal of Physical Chemistry A* 2013, 117, 11027-11037.

I carried out all of the experimental work presented in these publications, and the material from these papers is presented in detail in chapters 3, 4, and 6.